

Development of new methods for accurate estimation of tumour heterogeneity

by

Sebastian Hollizeck

[ORCID: 0000-0002-9504-3497](#)

A thesis submitted in total fulfillment for the
degree of Doctor of Philosophy

in the
The Sir Peter MacCallum Department of Oncology
Melbourne Medical School
THE UNIVERSITY OF MELBOURNE

17/04/2022

THE UNIVERSITY OF MELBOURNE

Abstract

The Sir Peter MacCallum Department of Oncology
Melbourne Medical School

Doctor of Philosophy

by [Sebastian Hollizeck](#)

ORCID: [0000-0002-9504-3497](#)

Intra-patient tumour heterogeneity is a widely accepted cause of resistance to therapy [1, 2], but the possibility to study this phenomenon is so far underexplored as the acquisition of multi region data sets is costly and ethically challenging [3]. With circulating tumour DNA (ctDNA) as a proxy it is possible to analyze a snapshot of the unified heterogeneity, but there is still an unmet need for new analysis methods to optimize the analysis of these very valuable data and drive new treatment targets [4]. In this work we will develop new methods to study genetic heterogeneity from next generation sequencing (NGS) of tumour tissue as well as ctDNA to elucidate the role of tumour heterogeneity on treatment resistance.

Declaration of Authorship

I, SEBASTIAN HOLLIZECK, declare that this thesis titled, "Development of new methods for accurate estimation of tumour heterogeneity" and the work presented in it are my own. I confirm that:

- The thesis comprises only my original work towards the DOCTOR OF PHILOSOPHY except where indicated in the preface;
- due acknowledgement has been made in the text to all other material used; and
- the thesis is fewer than the maximum word limit in length, exclusive of tables, maps, bibliographies and appendices as approved by the Research Higher Degrees Committee.

Signed:

Date:

Preface

This preface includes a summary of all chapters in this work as well as a comprehensive summary of my contributions and everyone else's contribution. This is a thesis *with* publications and each publication included in a chapter is shown here.

Hollizeck S., Wong S.Q., Solomon B., Chandrananda D.¹, Dawson S-J.¹ "Custom workflows to improve joint variant calling from multiple related tumour samples: FreeBayesSomatic and Strelka2Pass" *Bioinformatics*. 2021. DOI: [10.1093/bioinformatics/btab606](https://doi.org/10.1093/bioinformatics/btab606)

Chapter 1:

Introduction is an original work providing background and overview relevant to understanding the thesis and its relevance to the field. It includes an introduction to DNA, ctDNA, DNA sequencing, somatic variant calling and lung cancer.

Chapter 2:

Joint somatic variant calling is an original work describing two workflows for the joint analysis of multiple related tumour samples and has been published in *Bioinformatics* as "Custom workflows to improve joint variant calling from multiple related tumour samples: FreeBayesSomatic and Strelka2Pass" on 21st September 2021. In addition to the published analysis, I have added longitudinal analysis and its evaluation as well as the impact of this new method on other downstream analysis, like phylogenetic reconstruction and clonal deconvolution.

Contributions for this chapter:

- I conceptualised the work
- I implemented the workflows and containerised all required tools
- I performed the data simulation
- I performed the analysis presented in the publication

¹These authors contributed equally and are considered shared last.

- I wrote the draft of the manuscript and performed revisions
- D.C. and S-J.D. provided advice in planning and writing the manuscript
- D.C. provided guidance for method development
- S-J.D. provided guidance for method evaluation
- S.W. performed the targeted amplicon validation
- S.W. and B.S. read the draft manuscript and provided feedback
- B.S. provided clinical expertise for human data

Chapter 3:

summary plus contributions

Chapter 4:

Chapter 5:

Other publications

These publications I have contributed to in my candidature, but they are not presented in this work

Burr M.L., Sparbier C.E., Chan K.L., Chan Y-C., Kersbergen A., Lam E.Y.N., Azidis-Yates E., Vassiliadis D., Bell C.C., Gilan O., Jackson S., Tan L., Wong S.Q., **Hollizeck S.**, Michalak E.M., Siddle H.V., McCabe M.T., Prinjha R.K., Guerra G.R., Solomon B.J., Sandhu S., Dawson S-J., Beavis P.A., Tothill R.W., Cullinane C., Lehner P.J., Sutherland K.D., Dawson M.A. “**An evolutionarily conserved function of polycomb silences the MHC class I antigen presentation pathway and enables immune evasion in cancer**“ *Cancer cell.* 2019. DOI: [10.1016/j.ccr.2019.08.008](https://doi.org/10.1016/j.ccr.2019.08.008)

Solomon B.J.², Tan L.², Lin J.J.², Wong S.Q.², **Hollizeck S.**², Ebata K., Tuch B.B., Yoda S., Gainor J.F., Lecia V., Sequist L.V., Oxnard G.R., Gautschi O., Drilon A., Subbiah V., Khoo C., Zhu E.Y., Nguyen M., Henry D., Condroski K.R., Kolakowski G.R., Gomez E., Ballard J., Metcalf A.T., Blake J.F., Dawson S-J., Blosser W., Stancato L.F., Brandhuber B.J., Andrews S., Robinson B.G., Rothenberg S.M “**RET Solvent Front Mutations Mediate Acquired Resistance to Selective RET Inhibition in RET-Driven Malignancies**“ *Journal of Thoracic Oncology.* 2020. DOI: [10.1016/j.jtho.2020.01.006](https://doi.org/10.1016/j.jtho.2020.01.006)

Fennell K.A.², Vassiliadis D.², Lam E.Y., Martelotto L.G., Balic J.J., **Hollizeck S.**, Weber T.S., Semple T., Wang Q., Miles D.C., MacPherson L., Chan Y-C., Guirguis A.A., Kats L.M., Wong E.S., Dawson S-J.,

²These authors contributed equally and are considered shared first.

Naik S.H., Dawson M.A. “**Non-genetic determinants of malignant clonal fitness at single cell resolution**” *Nature*. 2021 DOI: [10.1038/s41586-021-04206-7](https://doi.org/10.1038/s41586-021-04206-7)

add more papers if they are published before the end

o.o.o.o.1 Instructions:

Where applicable, the following information must be included in a preface:

- a description of work towards the thesis that was carried out in collaboration with others, indicating the nature and proportion of the contribution of others and in general terms the portions of the work which the student claims as original;
- a description of work towards the thesis that has been submitted for other qualifications;
- a description of work towards the thesis that was carried out prior to enrolment in the degree;
- whether any third party editorial assistance was provided in preparation of the thesis and whether the persons providing this assistance are knowledgeable in the academic discipline of the thesis;
- the contributions of all persons involved in any multi-authored publications or articles in preparation included in the thesis;
- the publication status of all chapters presented in article format using the descriptors below;
 - Unpublished material not submitted for publication
 - Submitted for publication to [publication name] on [date]
 - In revision following peer review by [publication name]
 - Accepted for publication by [publication name] on [date]
 - Published by [publication name] on [date]
- an acknowledgement of all sources of funding, including grant identification numbers where applicable and Australian Government Research Training Program Scholarships, including fee offset scholarships.

Acknowledgements

I first want to acknowledge the Wurundjeri people of the Kulin nation, the traditional custodians of the land on which my work was conducted. I want to pay respects to their elders: past, present and emerging and all other elders that might happen to read this work. In my time in Australia I was lucky to get a glimpse of this mysterious and special continent and country through their eyes and I am grateful for their ongoing work in keeping the legends and teachings alive.

People

fill this in with people

Software and packages

think of where to put the package citations; Probably at the end as appendix

This section is dedicated to all the software that usually gets un-cited because they are "standard" or backbone

Lots of figures in the introductory Chapter 1 were created with the help of BioRender.com

Most analysis in a prototype state was done on a linux cluster running Centos 7 [5] with Bash [6] and due to the high amount of data, parallel [7] was used of the multi-cpu architecture of HPCs.

R

In depth data analysis and visualisation was done with R [8] with the help of packages listed below.

Most of the parallelisation in R was performed with BiocParallel [9], which is available through BiocManager [10].

Colour shemes and manipulation was performed with colorspace [11, 12].

Copynumber analysis was performed with sequenza [13], FACETS [14, 15] and PURPLE [16]. Some analysis was also directly performed with copynumber [17, 18].

Variant effect prediction was performed with VEP [19].

Table manipulation was performed with data.table [20].

Violin plots were generated with vioplot [21].

Heatmaps and UpSet plots were generated with ComplexHeatmap [22]

Phylogenetic analysis was performed with both ape [23] and phangorn [24] followed by dendextend [25].

Google sheets and its built in scripts were used to collect stats on docker pull requests and the data was then read in R through googlesheets4 [26].

Additional libraries, which were used for a multitude of things are listed in no particular order below: Rsamtools [27], GenomicRanges [28], optparse [29], VariantAnnotation [30], MultiAssayExperiment [31], circlize [32], BioQC [33], Biostrings [34], deconstructSigs [35], BSgenome [36], QDNAseq [37], RColorBrewer [38], pheatmap [39], ensemblVEP [40], stringdist [41], Rsubread [42], svglite [43], grImport [44], XML [45], kableExtra [46], lsa [47], irlba [48], ggplot2 [49]

maybe itemize over just a blob

python

Analysis for Chapter 4 was mostly done through python [50] with the help of many different packages, which are listed here in no particular order: numpy [51], ncls [52], pysam [53, 54, 55], zarr [56], pandas [57, 58], quadprog [59] as well as scipy [60].

latex

Of course, finally the typesetting of the thesis itself was done with L^AT_EX. With these additional packages in no particular order: babel, csquotes, lmodern, CrimsonPro, fontenc, xcolor, hhline, siunitx, biblatex, hyperref, quotchap, todonotes, float, afterpage, multicol, enumitem, array, tocloft, caption, appendix, xurl, graphicx, epstopdf, subfigure, booktabs, rotating and listings. The bese class is ‘book’ and all packages are available on CTAN and the source code is available at my GitHub repository <https://github.com/SebastianHollizeck/PhDThesis>.

Contents

Abstract	iii
Declaration of Authorship	iv
Preface	v
Acknowledgements	ix
List of Figures	xv
List of Tables	xix
List of Equations	xxi
Listings	xxi
Abbreviations	xxv
1 Introduction	1
1.1 DNA	1
1.1.1 Ploidy	3
1.1.2 Mutations	4
1.2 cfDNA	5
1.3 DNA sequencing	6
1.3.1 Library preparation	7
1.3.2 Next generation sequencing	8
1.3.3 Long read sequencing	8
1.4 DNA analysis	8
1.4.1 Mapping	10
1.4.2 Variant calling	10
1.4.3 Germline	11
1.4.4 Somatic	11
1.5 Cancer	12
1.6 Overview	20

2 Joint somatic variant calling	21
2.1 Introduction	21
2.2 Publication	23
2.2.1 Summary	23
2.2.2 FreeBayesSomatic workflow	23
2.2.3 Strelka2Pass workflow	24
2.2.4 Validation	25
2.3 Effects on downstream analysis	29
2.3.1 Phylogenetic reconstruction	29
2.4 Longitudinal analysis	32
2.4.1 Clonal deconvolution	35
2.4.2 Longitudinal enriched phylogeny	37
2.5 Usage	37
3 CASCADE	39
3.1 Introduction	39
3.1.1 Lungcancer	40
3.2 Publications	41
3.3 Patient level analysis	41
3.3.1 Analysis workflow	42
3.3.2 Patient CA-A	46
3.3.3 Patient CA-I	55
3.3.4 Patient CA-J	63
3.3.5 Patient CA-K	71
3.3.6 Patient CA-L	79
3.4 Cohort level analysis	87
3.4.1 Phylogenetic reconstruction	87
3.5 Mitochondrial phylogenetic reconstruction	87
3.5.1 Method	88
3.5.2 Results	90
3.5.3 Summary	93
3.6 Outlook	93
4 Mismatchfinder	95
4.1 Introduction	95
4.1.1 Mutational signature analysis	95
4.1.2 Restrictions and pitfalls of standard signature analysis	96
4.1.3 Overview	97
4.2 Methods	97
4.2.1 Mathematical concept	97
4.2.2 Data preprocessing	99
4.2.3 Mismatch detection	99
4.2.4 Filtering steps	99
4.2.5 Consensus reads	100
4.2.6 Germline filtering	101
4.2.7 Count normalisation	101
4.2.8 Signature deconvolution	102
4.2.9 Signature detection	104
4.2.10 Tumour detection	105
4.3 Results	105

4.3.1	Simulated Data - the validation promised land	106
4.3.2	Real world data - the only things that matters	112
4.3.3	Summary	119
5	Conclusion	121
 Appendices		147
A	Strelka2Pass and FreeBayesSomatic publication	149
A.1	Introduction	150
A.2	Materials and methods	151
A.2.1	FreeBayesSomatic workflow	151
A.2.2	Strelka2Pass workflow	152
A.3	Validation	153
A.3.1	Simulated data	153
A.3.2	Clinical data	155
A.4	Discussion	156
A.5	Supplementary methods	169
A.5.1	Alignment of clinical data	169
A.5.2	Validation of clinical data	169
A.5.3	Purity estimation with sequenza	170
A.5.4	Performance of individual steps in Strelka2Pass	170
A.5.5	Ensemble workflows – user suggestions	170
B	CASCADE - supplementary methods	177
B.1	Patient CA-A	181
B.2	Patient CA-I	189
B.3	Patient CA-J	195
B.4	Patient CA-K	199
B.5	Patient CA-L	205
C	MisMatchFinder - supplementary methods	209
C.1	ROI bed files generation	209
C.2	Oligo-nucleotide context normalisation	209
C.3	Germline filtering with zarr	212
C.3.1	Zarr conversion with scikit-allel	212
C.3.2	MisMatchFinder filtering - the zarr API	213
C.3.3	Data simulation	213
C.3.4	Signature simulation - we can spike this punch	213
C.3.5	Patient data subsampling	216

List of Figures

1.1	Overview DNA structure	2
1.2	Overview Chromosome structure	3
1.3	Overview DNA structure	5
1.4	Library preparation for NGS	7
1.5	Sequencing by synthesis (Illumina)	9
1.6	Drawing of central nervous system metastasis	16
1.7	Original hallmarks of cancer	18
1.8	Newest hallmarks of cancer	19
2.1	Comparison of joint multi-sample and single tumour-normal paired variant calling methods	26
2.2	Reconstructed phylogenies of joint samples	31
2.3	Tanglegram of the reconstructed phylogenies	32
2.4	Timeline from diagnosis till death for patient CA-F	33
2.5	Improved somatic variant calling in longitudinal data	34
2.6	Longitudinal data informs diagnostic variant calling	35
2.7	Reconstructed clonal trees for joint and pairwise variant calling	36
2.8	Reconstructed phylogeny with longitudinal ctDNA samples	37
2.9	Usage statistics joint workflows	38
3.1	Timeline of patient CA-A from diagnosis until death	46
3.2	Allelic frequencies of driver and emerging resistance mutations	47
3.3	PET scans of patient CA-A before and during Selpercatinib treatment	47
3.4	Schematic of tumour lesions in patient CA-A	48
3.5	Phylogeny of autopsy samples from patient CA-A	49
3.6	Heatmap of driver gene variants in patient CA-A	51
3.7	Circos plot of patient CA-A sample 11	52
3.8	Circos plot of patient CA-A sample 11 without allele frequency filter	53
3.9	Timeline of patient CA-I from diagnosis until death	55
3.10	Schematic of tumour lesions in patient CA-I	56
3.11	Phylogeny of autopsy samples from patient CA-I	57
3.12	Heatmap of driver gene variants in patient CA-I	59
3.13	Circos plot of patient CA-I sample dx	60
3.14	Circos plot of patient CA-I sample 557	61
3.15	Clonal evolutionary tree CA-I	62
3.16	Cancer cell fraction of mutation clusters of clonal tree for patient CA-I	62
3.17	Timeline of patient CA-J from diagnosis until death	63
3.18	Schematic of analysed tumour lesions in patient CA-J	64
3.19	Phylogeny of autopsy samples from patient CA-J	65
3.20	Heatmap of driver gene variants in patient CA-J	67
3.21	Circos plot of patient CA-J sample 2	68
3.22	Circos plot of patient CA-J sample 20	69
3.23	Timeline of patient CA-K from diagnosis until death	71

3.24	Schematic of analysed tumour lesions in patient CA-K	72
3.25	Phylogeny of autopsy samples from patient CA-K	73
3.26	Heatmap of driver gene variants in patient CA-K	75
3.27	Circos plot of patient CA-K sample 1	76
3.28	Circos plot of patient CA-K sample 8	77
3.29	Timeline of patient CA-L from diagnosis until death	79
3.30	Schematic of analysed tumour lesions in patient CA-L	80
3.31	Phylogeny of autopsy samples from patient CA-L	81
3.32	Heatmap of driver gene variants in patient CA-L	83
3.33	Circos plot of patient CA-L sample P.1	84
3.34	Circos plot of patient CA-L sample P.2	85
3.35	Clonal evolutionary tree CA-L	86
3.36	Cancer cell fraction of mutation clusters of clonal tree for patient CA-L	86
3.37	Average coverage of mitochondrial DNA of CASCADE patients	89
3.38	Mitochondrial and somatic phylogenetic reconstruction of CA-A	90
3.39	Mitochondrial and somatic phylogenetic reconstruction of CA-I	91
3.40	Mitochondrial and somatic phylogenetic reconstruction of CA-J	91
3.41	Mitochondrial and somatic phylogenetic reconstruction of CA-K	92
3.42	Mitochondrial and somatic phylogenetic reconstruction of CA-L	92
4.1	Trinucleotide count contributions for single base substitution (SBS) signature 7a . .	96
4.2	Schematic of consensus computation method for overlapping reads	101
4.3	Distance of deconvolution methods from truth	103
4.4	Mismatchrate of different filtering methods	106
4.5	Signature analysis of spike-in somatic variants	108
4.6	Signature weight differences for different deconvolution methods	108
4.7	Signature weights differences from normal for SBS7a spike-in	109
4.8	Signature weights differences from normal for SBS3 spike-in	110
4.9	Signature analysis without germline variant filtering	110
4.10	Percent increase of mismatches in analysis with and without germline filter	111
4.11	Signature weights of the normal sample with and without germline filter	111
4.12	PCA of tri-nucleotide mismatch counts of real world data (PC1 and PC2)	113
4.13	Signature weights for the WGS of two MBCB patients	118
4.14	Signature weights for the WES of two melanoma patients	119

Appendices**147**

A.1	Comparison of joint multi-sample variant calling and single tumour-normal paired calling methods	154
A.2	Characteristics of simulated data	159
A.3	Performance of workflows using simulated data	159
A.4	Variant allele frequencies (VAF) of variants detected by joint sample analysis . . .	160
A.5	Performance of individual steps in the Strelka2pass workflow using the simulated data	161
A.6	Summary of variant filters assigned by Mutect2	162
A.7	Assessing the performance of different workflows using tumour samples with different evolutionary relationships in the simulated data	163
A.8	Correlation of variant allele frequencies in validation	164

A.9	Performance of the different workflows using clinical samples from eight cancer patients	165
A.10	Correlation between cellularity and proportion of variants found only with joint calling using FreeBayesSomatic	166
A.11	Improvement in recall using FreeBayesSomatic and Strelka2pass over Mutect2 in the clinical samples	166
A.12	Performance of ensemble variant calling strategies	167
A.13	Schematic of analysed tumour lesions in patient CA-F	175
B.1	Circos plot of patient CA-A sample 26	181
B.2	Circos plot of patient CA-A sample 31	182
B.3	Circos plot of patient CA-A sample 41	183
B.4	Circos plot of patient CA-A sample 47	184
B.5	Circos plot of patient CA-A sample 55	185
B.6	Circos plot of patient CA-A sample 57	186
B.7	Circos plot of patient CA-A sample 59	187
B.8	Number of somatic variants per sample in patient CA-I	189
B.9	Phylogeny of samples from patient CA-I with diagnostic sample	189
B.10	Circos plot of patient CA-I sample 559	190
B.11	Circos plot of patient CA-I sample 566	191
B.12	Circos plot of patient CA-I sample 573	192
B.13	Circos plot of patient CA-I sample 579	193
B.14	Circos plot of patient CA-I sample 583	194
B.15	Circos plot of patient CA-J sample 24	195
B.16	Circos plot of patient CA-J sample 28	196
B.17	Circos plot of patient CA-J sample 32	197
B.18	Circos plot of patient CA-J sample 42	198
B.19	Circos plot of patient CA-K sample 4	199
B.20	Circos plot of patient CA-K sample 5	200
B.21	Circos plot of patient CA-K sample 6	201
B.22	Circos plot of patient CA-K sample 9	202
B.23	Circos plot of patient CA-K sample 13	203
B.24	Circos plot of patient CA-L sample 8	205
B.25	Circos plot of patient CA-L sample 17A	206
B.26	Circos plot of patient CA-L sample 26	207
C.1	Trinucleotide count contributions for single base substitution (SBS) signature 3	217
C.2	Signature weights differences from normal for SBS7a spike-in	217
C.3	Signature weights differences from normal for SBS3 spike-in	217
C.4	PCA of tri-nucleotide mismatch counts of real world data (PC ₂ and PC ₃)	218
C.5	Fitted beta distribution for Signature SBS3 in healthy samples	219
C.6	Fitted beta distribution for Signature SBS17a in healthy samples	220
C.7	Fitted beta distribution for Signature SBS12 in healthy samples	221
C.8	Fitted beta distribution for Signature SBS46 in healthy samples	222

List of Tables

3.1	Autopsy samples sequenced for patient CA-A	48
3.2	Copy number analysis results for patient CA-A	50
3.3	Autopsy samples sequenced for patient CA-I	55
3.4	Copy number analysis results for patient CA-I	58
3.5	Autopsy samples sequenced for patient CA-J	64
3.6	Copy number analysis results for patient CA-J	66
3.7	Autopsy samples sequenced for patient CA-K	72
3.8	Copy number analysis results for patient CA-K	74
3.9	Autopsy samples sequenced for patient CA-L	79
3.10	Copy number analysis results for patient CA-L	82
4.1	Germline variants retained after germline filtering	117
A.1	Sample name mapping	168
A.2	Runtime of different workflows on simulated data	169
B.1	Lung cancer genes for CASCADE analysis	180
C.1	Dinucleotide counts of GRCh38	210
C.2	Trinucleotide counts of GRCh38	211

List of Equations

2.1	FreeBayesSomatic: LOD _{normal}	23
2.2	FreeBayesSomatic: LOD _{tumour}	23
2.3	FreeBayesSomatic: somaticLOD definition	23
2.4	FreeBayesSomatic: VAF _{tumour}	24
2.5	FreeBayesSomatic: somaticVAF definition	24
2.6	Strelka2Pass: pairwise error probability	25
2.7	Strelka2Pass: joint error probability	25
2.8	Strelka2Pass: joint SomEVS	25
3.1	Inclusion criteria for cluster of PhylogicNDT analysis	45
3.2	Selective pressure with effective population size	87
3.3	Mitochondrial variants based distance function of two samples	89
4.1	MisMatchFinder: number of mismatches	98
4.2	MisMatchFinder: sequencing error	98
4.3	MisMatchFinder: germline variants	98
4.4	MisMatchFinder: number of mismatches with distributions	98
4.5	MisMatchFinder: number of mismatches correlation with somatic variants	98
4.6	MisMatchFinder: optimisation for signature weights	102
4.7	MisMatchFinder: optimisation function restrictions	102
4.8	MisMatchFinder: quadratic programming formula	102
4.9	Beta distribution probability density function	104
4.10	Beta distribution cumulative density function	104
4.11	Inverse beta distribution cumulative density function	104
4.12	MisMatchFinder: CDF-score calculation per signature and patient	105

Listings

4.1	Blacklist postprocessing	115
A.1	parse strelka VCF	173
A.2	annotate variants with copy number calls	173
A.3	convert to maf format	174
B.1	Preprocessing of mitochondrial reads and variants for analysis in R	177
C.1	scikit-allel conversion vcf_to_zarr	212
C.2	field options for reduced memory	213
C.3	spike-in variant selection	214
C.4	bamsurgeon spike-in	215

Abbreviations

BAM	Binary Alignment Map
bp	base pair
BQ	Base Quality
CCF	Cancer Cell Fraction
cfDNA	cell free DNA
ChIP	Chromatin ImmunoPrecipitation
ctDNA	circulating tumour DNA
DBS	Double Base Substitution
DNA	DeoxyriboNucleic Acid
F81	Felsenstein 1981 model
GATK	Genome Analysis ToolKit
HKY85	Hasegawa, Kishino and Yano 1985 model
HPC	High Performance Computing
ILM	Iterative Linear Models
InDel	Insertion or Deletion
MQ	Mapping Quality
MRCA	Most Recent Common Ancestor
NGS	Next Generation Sequencing
NJ	Neighbour Joining
NSCLC	Non-Small Cell Lung Cancer
PCA	Principal Component Aanalysis
PCx	Principal Ccomponent number x
PET	Positron Emission Tomography
PON	Panel Of Normals
QP	Quadratic Programming
RAID	Redundant Array of Independent Disks

Abbreviations

RNA	RiboNucleic Acid
ROI	Region Of Interest
RPRS	Read Position Rank Sum
SBS	Single Base Substitution
SCLC	Small Cell Lung Cancer
SNP	Single Nucleotide Polymorphism
SV	Structural Variant
TAS	Targeted Amplicon Sequencing
TKI	Tyrosine Kinase Inhibitor
TNBC	Triple Negative Breast Cancer
UPGMA	Unweighted Pair Group Method with Arithmetic mean
UV	Ultra Violet light
VCF	Variant Call Format
VEP	Variant Effect Predictor
WES	Whole Exome Sequencing
WGS	Whole Genome Sequencing
WPGMA	Weighted Pair Group Method with Arithmetic mean

“Begin at the beginning,” the King said, very gravely, “and go on till you come to the end: then stop.”

— Lewis Carroll, *Alice in Wonderland*



Introduction

This first introduction chapter contains all the necessary background information as well as an overview for the work discussed in this thesis. It summarised basic biological properties of DNA and cell biology as well as the respective technologies to read, analyse and measure these biological concepts and then how to evaluate the output of these methods. [Section 1.1](#) delineates the role DNA plays for the cell and then [section 1.2](#) shows how these standards are changed in the tumour and cell free context. [Section 1.3](#) introduces the current technologies used to measure and detect DNA and its variations. With [section 1.4](#) covering the computational analysis methods to read out changes in the DNA. Then [section 3.1.1](#) relates how these changes lead to cancer and what we can learn from them. The introduction concludes with [section 1.6](#) as an overview over the thesis aims and my work in addressing them in the following chapters.

1.1 DNA as a information storage unit

It is a widely accepted fact, that Deoxyribonucleic acid (DNA) serves as the long term information storage molecule of our cells. This information is protected and allows correction of simple errors through its double helix structure [61, 62]. The nucleotides, which consist of a deoxyribose sugar (hence the name), a phosphate group and the nitrogenous base, are joined together by phosphate groups. Even though there are six common naturally occurring nitrogenous bases: Adenine (A), Thymine (T), Guanine (G), Cytosine (C), Uracil (U) and nicotinamide, only the first four are used to encode the genetic information into DNA. Each of the strands mirrors the other, so that an adenine will be paired up with a thymine forming two hydrogen bonds. Similarly, cytosine will pair with guanine forming an even stronger bond with three hydrogen bonds. While other pairings which do

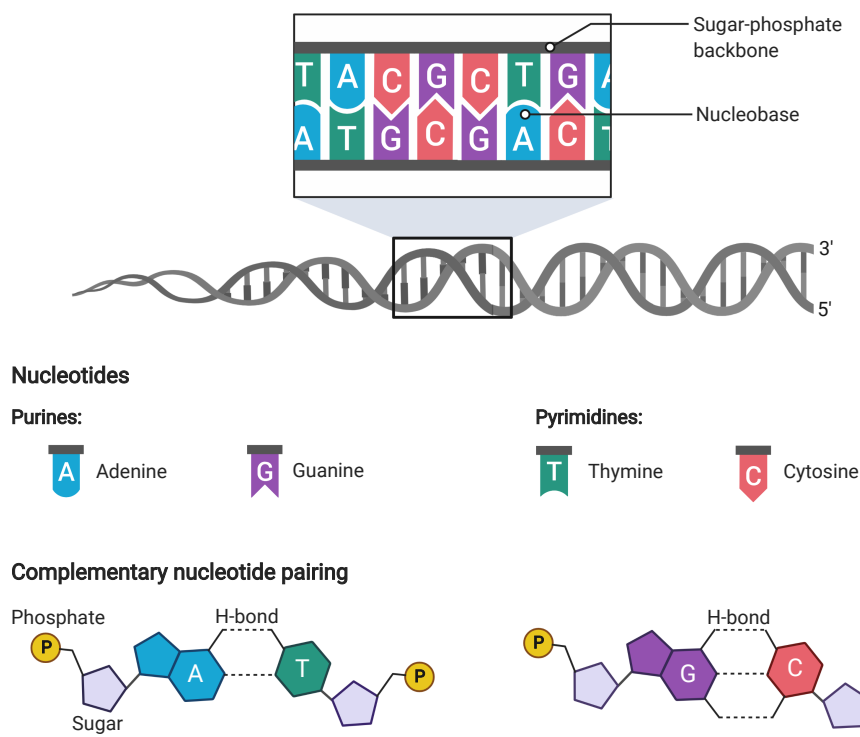


Figure 1.1: Overview of DNA structure and the nucleobases, which form DNA strands. Nucleotides are split into Purines and Pyrimidines by the structure of the nitrogen ring; complementary pairing of bases is shown as shapes of the bases as well as with 2D structures; Hydrogen (H) bonds are shown as dotted lines; Phosphates are shown as P; 3' and 5' ends are defined by the internal number of the carbon atom of the sugar which is exposed; Adapted from “DNA structure” by BioRender.com (2021) Retrieved from <https://app.biorender.com/biorender-templates>

not follow those rules are chemically possible, they are mostly observed in ribonucleic acid (RNA) [63]. These very strict bonding rules enable the DNA to be similar to a hard drive with backup on a computer. And as only one strand contains all the information, the DNA polymerase enzyme does only need access to one strand, which allows parallel replication during cell division, but also error corrections, by proof reading the newly synthesised strand with the template. In order to be able to distinguish the two strands, they were assigned the names 3' and 5' depending on the numbering of the carbon atom in the sugar, which is exposed (Figure 1.1).

The entirety of the DNA encoding the organism is commonly called “the genome” with all genes, which consist of introns and exons are called exome. Unicellular organisms usually only have a very small amount of introns, which to current knowledge only provide limited information and are only responsible for structure. In vertebrates introns as well as intergenic DNA (the DNA between genes) contribute most of the DNA in the genome. For example in humans, only 1% of the genetic

material is considered to be exonic, whereas introns contribute $\approx 24\%$ and the rest is intergenic ($\approx 75\%$)[64].

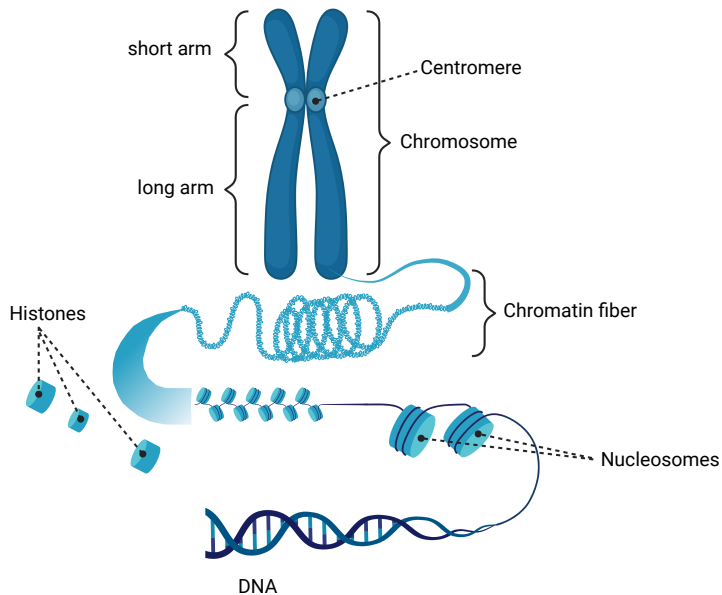


Figure 1.2: Structural overview of the metaphase condensed chromosome: DNA is first wrapped around Histones to form nucleosome, which then associate with each other to form the chromatin fiber, which in the metaphase of the cell cycle is condensed even more into the X-shaped chromosome

The DNA in eukaryotes however is not free floating around in the nucleus of a cell, but rather in most eukaryotic organisms, it is highly condensed and structured, first wrapped around nucleosomes like thread on a spool, then organised around histones, into either open (accessible) or closed chromatin, which then can be even further condensed into chromosomes, which have a X-like shape, with two shorter and two longer arms (Figure 1.2). This allows some DNA to be accessible where the use of other areas can be restricted[65]. Through this restriction, the availability of certain genes, which are the sections of the DNA, which encode for short term storage molecules like RNA. This restriction plays an important role in cell fate and cell viability. Ultimately, all information stored to create a new highly complex organism is stored in just the DNA of one cell. Whichever parts are used and how they are used decides the function and the identity of the cell[66].

1.1.1 Ploidy - it is good to have a backup, if you do it right

Similar to the already discussed RAID-like setup of the DNA in two strands, another concept of data security, a spatial different storage is also implemented. Most eukaryotic organisms have at least

two of each chromosome (diploid) with some species reaching up to septaploid [67]. However, this concept is not the only reason for the ploidy of somatic cells. For sexually reproducing organisms, at least a diploid set of chromosomes is necessary to enable information to be joined from both parents. Germline cells (sperm and egg) are generally monoploid, such that the resulting cell will be diploid, but the ploidy of the somatic cells is not as uniform within a species, where it can vary between organisms based on gender or rank [68]. In most organisms, a change in ploidy is fatal [69] and only partial ploidy changes like extra copies of chromosome 17 [70], chromosome 18 [71] and chromosome 21 [72] are tolerated. These syndromes can occur when there is an uneven split of chromosomes during cell division. The additional advantage, apart from sexual reproduction, is that a second almost identical copy of a chromosome allows repair of DNA, even when both strands are damaged, for example in a double strand break. In this case, the information from the sister chromosome will be used, by first cutting the double strand break ends to have an overhang (resection). This overhang will then merge with the sister chromosome's mirrored strand. In this state, the two chromosomes are fused together in a Holliday junction, which allows the missing part from the resection and the double strand break to be synthesised [73]. During this process, which is part of the homology directed repair (HDR) machinery, the sister chromosomes exchange parts of their DNA, when resolving the Holliday junction. As these stretches of DNA do not need to be 100% identical, this plays an important role in evolution and diversity [74, 75].

Even though this X-like structure is the most commonly used and known structure, the DNAs 3D structure is usually very different and only takes this shape for the very short time of the cell cycle. Most of the time, the chromosomes are unravelled into something resembling a ball of yarn, where the "open" chromatin regions are on the outside and the "closed" regions are "hidden" in the inside and each chromosome establishes its own "territory" inside the nucleus (Figure 1.3). This structure allows another DNA cross over with non-sister chromosomes, which is called a chiasma.

1.1.2 Phantastical mutations and where to find them

However even though the DNA is highly stable, and error correction methods are constantly working to not introduce any changes in the DNA, the source of evolution and adaptation of species is sourced in a steady mutation rate [76, 77]. These changes in normal tissue are mostly irrelevant to the organism as a whole and will not be passed on to the next generation. These changes are known as somatic mutations. This type of mutation accumulates in a cell linearly over the course of the lifespan of the cell and is not bound to just cell divisions [78, 79]. In contrast, if one of those

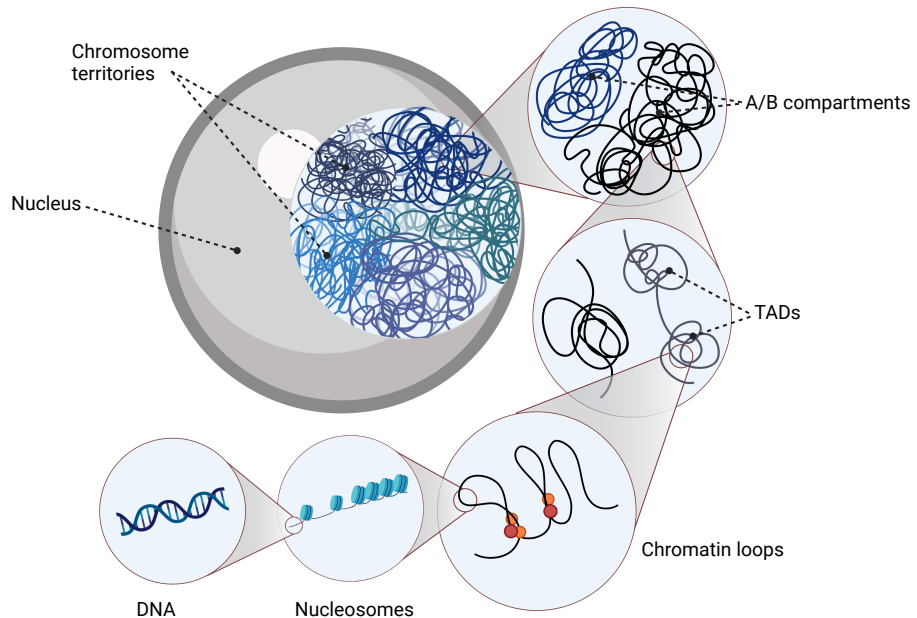


Figure 1.3: Individual chromosomes occupy a subspace in the nucleus called chromosome territories. Chromosome territories can be further partitioned to distinct A and B compartments, which are enriched for active and repressed chromatin, respectively. Genomic regions within topologically associating domains (TADs) display increased interactions, while their interactions with neighbouring regions outside the TADs are rather limited.

mutations occurs in the germline cell, e.g. sperm or egg producing cells, these mutations will be propagated to all offspring and be present in all cells of that organism and in term all its offspring. These mutations are called germline mutations. These mutations are also called germline variants, as they establish in the population and represent a variation of the organism. Mutations can also be classified depending on either their size, ranging from single nucleotide polymorphisms (SNPs) over small insertions or deletions (InDels) to large structural changes, like the deletion of parts of or even a whole chromosome arm. Like previously described with ploidy changes, usually smaller changes have less impact on the overall fitness of the organism, however even SNPs can lead to changes which are not compatible with life[80, 81].

1.2 Cell free DNA is more than just bits and pieces

When a cell from a multicellular organism dies, through which ever method, there will be numerous enzymes involved, which clear the debris and recycle material. This means that proteases digest proteins into amino acids, which will later be used for either building new proteins or possibly

even digested further for energy production. The same happens with the DNA in the cell. However, as discussed in the previous section 1.1 the DNA is wrapped around histones and organised in structures called nucleosomes. These protect the DNA from being cut by DNases by hindering the access to the DNA, similar to how they stopped the access for transcription into RNA. This then in turn leads to the DNA being cut into pieces mainly in the length of 167 base pairs (bp). These DNA fragments, which are called cell free DNA (cfDNA), can then be detected in bodily fluids, like blood or even stool. By analysing these fragments, non invasive tests for prenatal care have been possible, as the DNA of the foetus is detectable in the mother's blood [82, 83]. Similar to the process, a cancer also sheds DNA, titled circulating tumour DNA (ctDNA), when its cells die, either through intervention of the immune system or through other forcefull processes. These ctDNA fragments can also be analysed and molecular properties measured, without even knowing the exact location of the tumour. As a blood test can be routinely performed in the clinic or even a general practitioner, the monitoring of cancer progression is significantly easier and safer than through other measures. Of course, it is, similar to the prenatal test, only a proxy for the cells which are still alive, as these have not shed their DNA. Additionally, the amount of shedded DNA is highly variable between tumours, with a general higher amount for later stages, so that sometimes there is almost no ctDNA present, even though the cancer is fairly advanced [84, 85].

include the length of ctDNA

1.3 DNA sequencing - when is next generation sequencing the current generation?

As we know the building blocks, that make DNA as well as the process and the enzymes responsible, we can synthesise DNA in vitro. By chemically modifying the nucleotides supplied to the synthesis process, the sequence of the copied strand can be analysed. The first method to make use of this used the lambda phage to fuse known ends for the primers needed for the reaction to the piece of DNA and supplied labelled nucleotides [86]. This method was then superseded by "Sanger sequencing" after Frederick Sanger who with colleagues published this method in 1977, by adding dideoxynucleotides in a low concentration, the polymerase chain reaction would terminate trying to integrate these nucleotides and by labelling them radioactively or fluorescently, a gel can be used to determine the sequence of a piece of DNA [87, 88], which made the method better suited for larger scale projects.

However, this method has multiple issues for modern research questions. Mostly, that it is fairly labour and time consuming to analyse multiple pieces of DNA at the same time, and it is very challenging to sequence all the DNA of an organism. The human genome project, which was started in 1990 used machines which automated the Sanger sequencing procedure and it still took hundreds of researchers 13 years to complete the DNA sequence of just one human [89, 64]. Even though this was a very long project, it laid the ground work for the usage of the current sequencing technologies.

1.3.1 Library preparation - what we learned from using phages

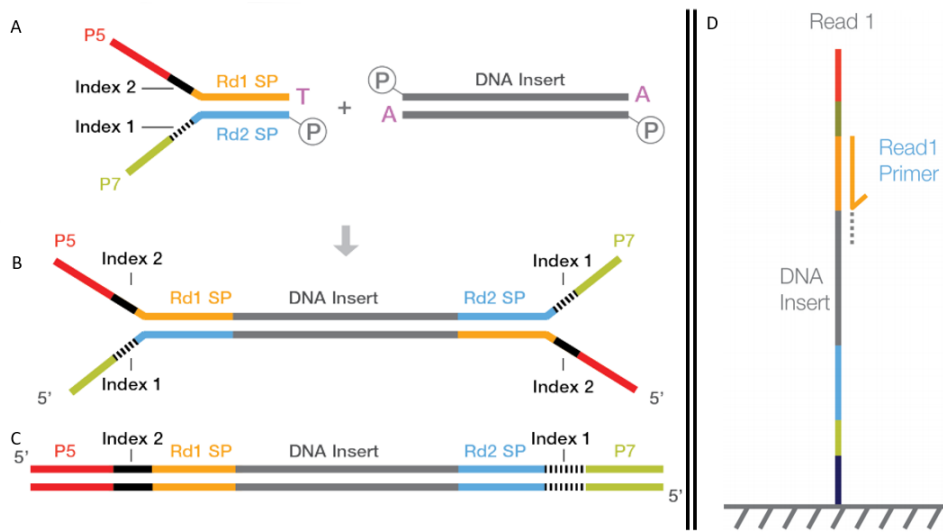


Figure 1.4: Adapter ligation during library preparation. The adapters are added to the DNA insert during library preparation. A. The DNA insert is prepared by adding an A-tail and phosphorylation. B. The adapter complex which includes the P5/P7 flow cell binding adapter is added to the DNA insert. C. The DNA insert is ready for sequencing. D. The DNA insert binds to the flow cell for sequencing. Primers bind to the DNA insert to generate reads;

Figure adapted from "[How short inserts affect sequencing performance](#)" [90]

Library preparation is the name of the preprocessing step, which is done before it is sequenced with the current technologies. The first step to sequence DNA is to obtain the DNA, which is done by lysing the cells of interest, which disrupts the cell membrane and therefore spills all its contents. The then spilled DNA is fragmented into smaller pieces, by either restriction enzymes or sonication, to have a size of about between 200-800bp. These steps are not necessary when preparing sequencing of ctDNA, as discussed in [Section 1.2](#), the DNA is unbound and already digested into short fragments. Once the DNA is ready, it is phosphorelated and an A-tail is added, before the adapter complex is ligated. This enabled the DNA to bind to the flow cell which is covered with the reverse complement of the adapter ([Figure 1.4](#)).

1.3.2 Next generation sequencing

Next generation sequencing (NGS) is the coined term for basically any standard high-throughput sequencing performed, which includes exome, genome, transcriptome, protein-dna interactions (ChIP) and other epigenome studies. The term NGS is still widely used, even though it has been more than 10 years since the first NGS approach was commercially available. While in the beginning of next generation sequencing there were multiple approaches, the current lion share (80% of sequencing data) of protocols use the Illumina short read sequencing by synthesis approach ([Figure 1.5](#))[\[91, 92\]](#), which is based on the concept of alternating integration of fluorescently labelled nucleotides and imaging with a microscope ([Figure 1.5](#)) as well as multiplexing, where a DNA fragment is ligated to an index, which allow to sequence multiple samples at once [\[93, 94\]](#) as it is shown in [Figure 1.4](#). This method allows highly accurate determination of the sequence of a DNA fragment and depending on the flow cell and sequencing machine allows to sequence a whole genome in just 24h.

1.3.3 Long read sequencing - the "third" generation sequencing

By now, multiple methods which broke free of the size limitations of NGS exist, which are commonly referred to as long read sequencing. Most of the current methods trade the very high accuracy of the second generation NGS methods for the capability of sequencing huge continuous strands of DNA (current record 2.3 Million bp [\[95\]](#)) with normal library preparation ranging between 10-30 Kbp. These methods are expected to revolutionise our understanding of the highly repetitive elements that exist in the genome, such as the centromeres of chromosomes. Methods such as the direct molecule sequencing approach by Oxford Nanopore are even able to distinguish post transcriptional modifications on RNA[\[96\]](#). So far, these methods however are still very expensive and as this work is dealing with ctDNA, which is highly fragmented, these methods offer only limited advantages over the short read sequencing, while being much more expensive.

1.4 DNA analysis - what to do with the sequence

The types of analysis that can be done with the output from the sequencing machine stretches far, however, all methods need to first infer the location in the genome, the sequenced piece of DNA

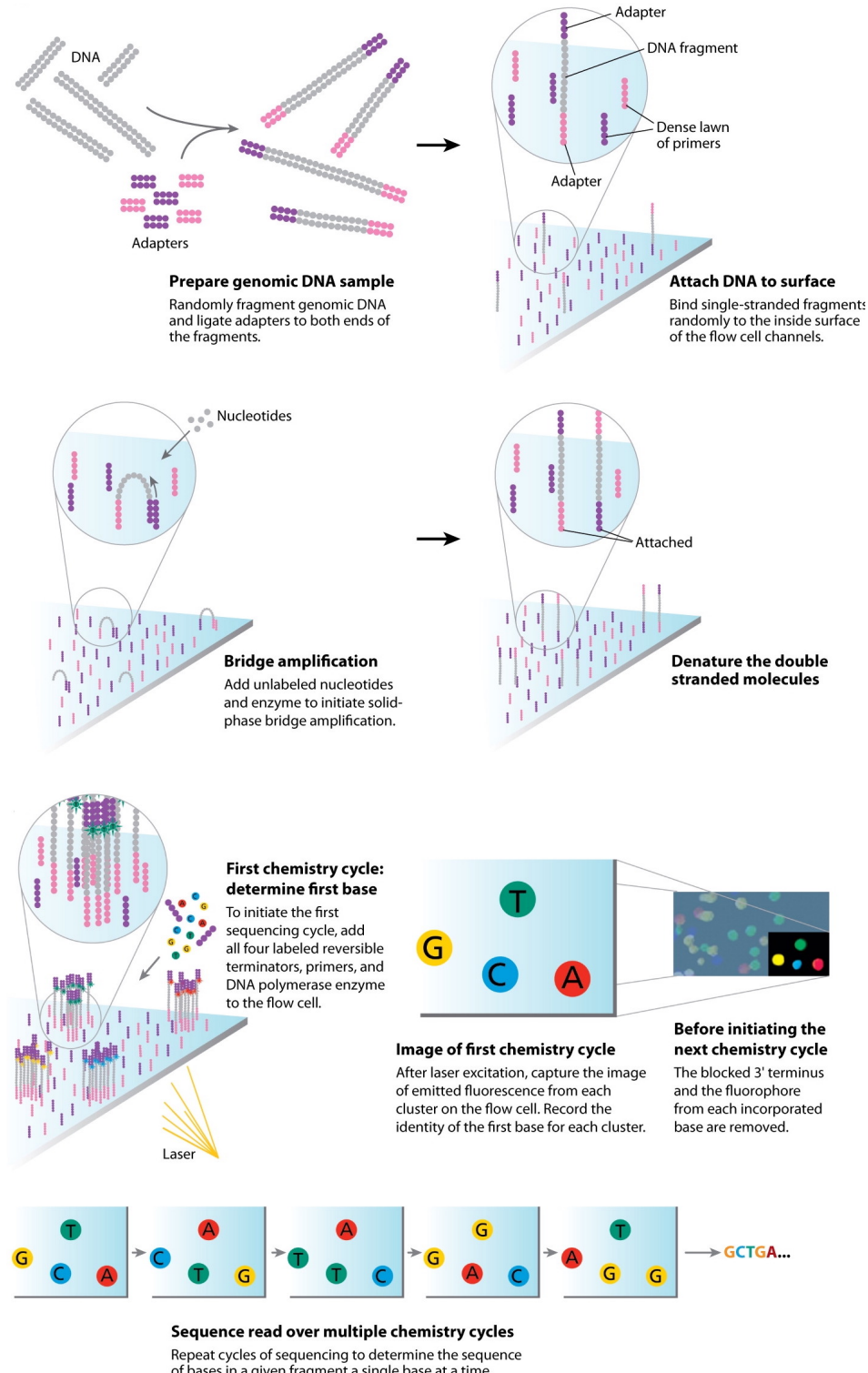


Figure 1.5: The Illumina sequencing-by-synthesis approach. Cluster strands created by bridge amplification are primed and all four fluorescently labeled, 3'-OH blocked nucleotides are added to the flow cell with DNA polymerase. The cluster strands are extended by one nucleotide. Following the incorporation step, the unused nucleotides and DNA polymerase molecules are washed away, a scan buffer is added to the flow cell, and the optics system scans each lane of the flow cell by imaging units called tiles. Once imaging is completed, chemicals that effect cleavage of the fluorescent labels and the 3'-OH blocking groups are added to the flow cell, which prepares the cluster strands for another round of fluorescent nucleotide incorporation; Figure adapted from Mardis[91]

originated from. As the current methods randomly fragment the DNA ([Section 1.3.1](#)), the genomic location information is completely lost. This process is referred to as mapping.

1.4.1 Mapping - Ey man, where is my genomic location?

In this process, the fragments of DNA, which were sequenced, are assigned a genomic coordinate on the reference genome. This is only possible, due to the fact, that we have a resolved genome sequences ([Section 1.3](#)) for a high number of species. The location a sequenced piece of DNA fits to the reference genome might be unique, but it could also fit to multiple locations, due to highly repetitive regions or due to the existence of pseudo genes with almost 100% identity. In addition to this, the reference genome might not accurately reflect the genome of the organism that has been sequenced. Each mapping position is therefore assigned a quality score, which reflects how likely it is the actual position of the sequence. As Illumina sequencers have the ability to sequence both ends of the DNA fragment, the position of the ends (read 1 and read 2) to each other can also be used to infer the quality, as they should be within a reasonable distance to each other ([Figure 1.4](#))

As this process is time-consuming and the exact location of the fragment might not be as important, there exists a subset of tools called pseudo-mapper, which are based on k -mers, which are predefined DNA sequences of length k , which help to identify certain regions of interest. These tools are especially common for RNAseq, where the exact location of a read does not matter, only that the read is within a gene [[97](#), [98](#)], but also for methods that estimate similarity between sequences (DNA, RNA or protein) [[99](#), [100](#)].

For this work however, the exact position of reads is crucial, so only real mapping methods like BWA [[101](#)] or Bowtie 2 [[102](#)], which are optimised for short reads from Illumina systems, provide the necessary functions.

add things about alternative contigs and reference genome?

1.4.2 Variant calling - spot the difference

As intra-species genetic variation is intended for adaptation and evolution, there will be places where the DNA sequence of the subject will differ from the sequence of the reference (see [Section 1.1.2](#)). These variants give insight into medical background as well as treatment options for patients and can even be used to guide family planning. Depending on the type of variation that is

of interest, a different set of computational methods are needed, as germline and somatic variants have different properties.

1.4.3 Germline variant calling - the cards you have been dealt at birth

The most common source of DNA used for germline variant analysis is the mono nuclear layer from the blood of the subject, but really almost any cell can be used for this process, as all cells in the organism will share all germline variants ([Section 1.1.2](#)). The only important input on top of the DNA sequence from the sequencer are the reference genome of the organism, as all variant nomenclature is based on the reference and the ploidy of the organism ([Section 1.1.1](#)). The ploidy is key to infer, at which ranges of allele frequency a variant can biologically occur. For example in a human diploid genome, germline variants can occur either in one or both chromosomes, which mean we assume reads should show an allele frequency of around 50% and 100%, where the hexaploid commercial wheat [[103](#)] allele frequency for variants would be 16%, 33%, 50%, 66%, 0.83% and 100%. Due to the random sampling and possible sequencing errors, the observed allele frequencies will differ from the theoretical values. Most state of the art germline variant calling method will also use haplotype reconstructions through de-Brujin graphs, which features a remapping of reads in relation to each other [[104](#), [105](#), [106](#), [107](#), [108](#)] where the original mapping location assigned by the aligner ([Section 1.4.1](#)) is only used as a guideline. This allows to resolve even complex haplotypes of the sample by not restricting the method to the linear setup of the reference genome.

1.4.4 Somatic variant calling - life is ever-changing

In contrast to germline variant calling, somatic variant calling methods cannot rely on allele frequency, as not all cells sequenced are expected to have the change in nucleotide. The allele frequency is instead a measure of the sub clonal size. A subclone is here defined as the set of cells, which were derived from the cell, which originally acquired the somatic mutation. Depending on the selective advantage, just random drift and also the time point when the variant was introduced, these clones can be very variable in size and therefore their contribution to the DNA in the sequencing. As not all cells have the variants, the selection of the tissue for library preparation is very important, unlike for germline calling. The main use of somatic variant calling is the genetic diagnosis and research of cancer samples, where the main question is, which changes are present in the tumour, which lead to the disease.

The ideal scenario for tumour somatic variant calling is when a biopsy of the tumour as well as a normal sample of the patient is available. In most clinical cases, this will be the diagnostic biopsy as well as the mono nuclear layer from blood, just like for germline calling ([Section 1.4.3](#)). This needs to be adjusted depending on the type of malignancy, because if the tumour is a leukemia, the mono nuclear layer of the blood might contain tumour cells, but for solid tumours, the blood is a routine, minimally invasive option. These two samples are then analysed together and only changes that are only in the somatic tumour sample and not in the normal sample are reported. Even though this concept sounds simple, there are some pitfalls [[109](#)]. First, there might be some tumour contamination in the normal sample, which needs to be adjusted for [[106, 110](#)]. Second, there might be normal “contamination” in the tumour sample, this means that not all cells in the tumour sample are actually tumour. This means that the signal of the tumour changes is reduced and harder to find.

All of these issues are amplified in the case, when there is no “normal” sample available, either because the patient didn't consent, due to other medical issues, or because for diagnostic tests there usually is no need for a germline sample. In this case, there is the option for “tumour only” variant calling, which requires a database of germline variants in the population, to distinguish between somatic and germline variants, as the variant calling is very similar to just germline variant calling ([Section 1.4.3](#)) without the restriction of the ploidy. However, even with an extensive database like gnomAD [[111](#)] it is unlikely to be able to remove all germline variants from the analysis and as there is no direct comparison, the precision of the “tumour only” method is significantly lower [[112](#)].

1.5 Cancer

For a long time in human history, the origin of cancer as a disease was a mystery and a multitude of theories, starting in ancient Egypt, were developed. These theories ranged from a curse to chemical imbalance over parasites to trauma. In this section I will outline both the history of cancer as a disease and the treatments starting with ancient times leading up right until the current times. While the first steps are very wide, because the biology itself was not understood, it is quite curious how often people with more knowledge came to worse conclusions and theories, than were already known thousands of years ago.

Around 3000BC the Egyptians describe the bulging tumour of the breast as an incurable disease [[113](#)], even then they already had some ointments, which were used, including resection, cauterisation

and salting of the affected areas, all of which were still used up until the 19th century [114]. This papyrus document is considered the oldest evidence of cancer in humanity.

When the ancient Greeks laid the foundation for modern medicine with Hippocrates, the first hypothesis about natural causes of cancers was formulated and the terms “cancer” and “carcinoma” were coined. The abundance and accumulation of “black bile” in the body was thought to be the cause of the cancers. However, the treatment was still the same as before, with resection and lotions [115].

Following Hippocrates, the Roman physician Celsus progressed the understanding of cancers significantly, by describing metastatic relapse of treated breast cancer in neighbouring armpits and even the spread to distant organs. He also was aware, that the outcome of patients was better, if the tumours were removed early and aggressively [116].

With the destruction of the western Roman Empire, the Middle East became well known for their strong advances towards modern medicine and the court physician to the Emperor of Constantinople Aetius had success with the first total mastectomy and generally was an advocate of the total excision of tumours [117].

Sadly, while both the understanding of cancer and the treatment were steadily improving, the Pope prohibited bloodshed as well as surgeries and therefore lead to a slow-down of advances, especially because autopsies were also forbidden a hundred years later in 1305. However, there were still illegal experiments conducted and the general classification which is still used up to date was started, by Henri de Mondeville, who started classifying tumours by their anatomical site[118].

After the end of the “dark ages”, the wide availability of older medical works from both Greek and Roman due to the book print invention, led to the re-emergence of the use of chemical ointments and lotions on cancer lesions. With Paracelsus promoting the usage of chemicals, which he himself warns are poisonous in the wrong concentration, for the treatment of cancer, he laid the groundwork for the modern Chemotherapy [119].

As the dissection of corpses was no longer banned by the church, more and more cases of “hidden” causes of death were found post mortem, which were often cancers on internal organs, like the brain but also the detection of malignant and benign tumours was a major breakthrough. This lead to the understanding, that benign tumours might turn malignant after some time and many physicians suggested removal of the benign growths [120].

Due to genetic disposition of cancer, especially breast cancer, two independent physicians (Zacutus Lusitani and Nicholas Tulp) came to the conclusion, that cancer is contagious and proposed isolation of patients [121, 122] which shows, that while the treatment of cancer was improving steadily, but the origin of the disease was still a mystery. It took until 1700 when Deshaies-Gendron described cancer as a transformation of a normal body part, which continues to grow without control and while he was aware of metastatic disease, he suggested no treatment, as he did not believe cancer to be curable with drugs [123].

Another ground-breaking work published in the same year was the collection of almost three thousand autopsy reports and their clinical history, which contain a number of detailed cancer cases including: brain, head and neck, lung, breast, esophagus, stomach, colon, liver, pancreas, kidney, uterus, cervix, bladder, and prostate. Many of the terms used by Theophilus Boneti to describe the cases are still in use and the work itself was the first step toward tumour pathology [124]

However, it took almost 150 years after the theory of cancer being contagious for Nooth [125] to conduct experiments trying to infect himself with cancer pieces resected from another person, which proved that cancers generally are not infectious.

With the invention and consequently common use of the microscope in the pathology, more and more causes of deaths were identified as caused by cancer. An example is the connection of a chronic cough to lung cancer and swollen joints with sarcoma [126].

After more and more autopsies of cancer patients, surgeons like Heister [127] found that breast cancer resection needs to include the breast, the axillary lymph node and the pectoralis major muscle which got to be known as the Halsted radical mastectomy and was the standard of care for a long time.

While the treatment of cancers (mostly surgical) was getting more and more advanced, but the origin and cause of cancer in patients was still very much debated. As there are a manifold of causes as we now know, it is maybe not surprising that it took longer, but by the middle of the 18th century chronic inflammation as a cause of cancer initiation was hypothesised [128].

The next big step was taken, when in 1838 the concepts of cells as fundamental building blocks of organisms was published. In the following years, many cancers were dissected and microscopically analysed. This revealed that tumour cells look vastly different from normal cells, and it was thought that they morphological features could serve to identify their fate [129] and became known

for defining the cellular origin of benign and malignant tumours. And while he described the tumours as a collection of abnormal cells with stroma, he thought cancer to arise from newly generated cells from a diseased organ and thought the underlying cause to be “amorphous embryonal blastema”.

With this foundation, over the next hundred years, lots of advances were made into the morphology of different tumours and many previously undetected ones, like leukemia, were found and extensively characterised. However, even then, there were researchers, which understood that the heterogeneity of cancers is so vast, that while he was convinced that the microscope will be a mandatory instrument to diagnose cancers, more effort to collect and study specimen is necessary to have a complete picture [130].

As many shared the view of Bennett, the second half of the 19th century was a rich source of surgical pathology and the oncology literature in general. Most outstanding was Rudolf Virchow’s “Die krankhaften Geschwülste” [131] which is a first landmark book on the classification of cancers, and is still a well of knowledge. From his work, the terms “hyperplasia” and “metaplasia” we derived, as pre-cancerous states of cells. He also was one of the first to hypothesis the presence of growth stimulating substances around cancers, which lead to their uncontrolled growth. While he also was the first to again oppose the “amorphous embryonal blastema” theory and instead was convinced that tumour cells were just abnormally changed cells, which he called “chronic irritation theory” and had a theory that metastasis were seeded by the original lesion (like in this melanoma Figure 1.6), he also had major scientific impact in a number of other fields like Parasitology, Forensic and Anthropology¹.

While the search of possible cancer causing substances started to get more and more interest, only one real cause was thought to be found in the ore of the central European mountains, where miners would have a higher prevalence of lung cancers. Nevertheless, this was later found to be caused by radio active material and not by the inhaled dust of minerals as expected. Similar, many parasites and bacteria were found as potential causes of cancer, but none of the findings could produce proof.

While all these steps were getting closer together in time up until the beginning of the 20th century, they were still fairly minor in the contrast to the high speed and throughput results that the last hundred years brought with it. While technically Willhelm Röntgen discovered the X-rays just before the change of the century [132], both its impact on the body and cancer were only clear a few

¹Maybe surprising to hear, that he was strongly opposed to Darwin’s theory of evolution. In his own words: “The intermediate form is unimaginable save in a dream... We cannot teach or consent that it is an achievement that man descended from the ape or other animal.”

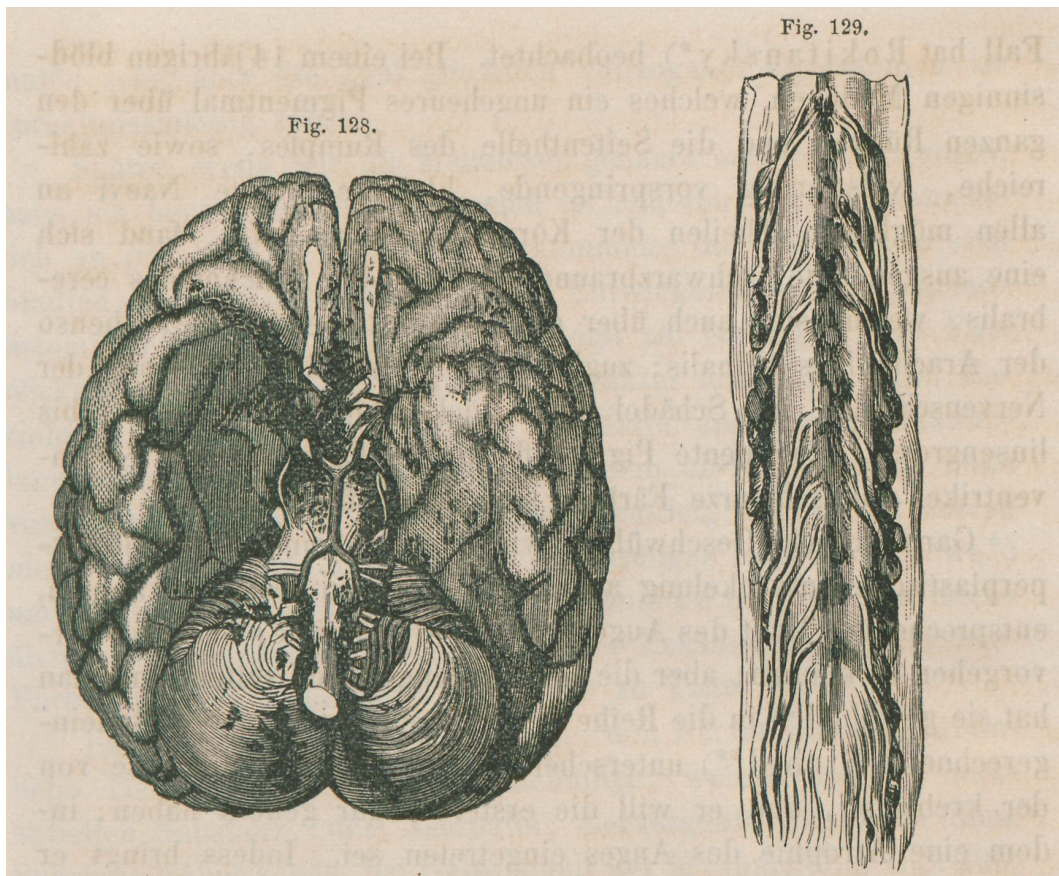


Figure 1.6: Drawing of central nervous system metastasis from page 121, Volume 2 of “Die krankhaften Geschwülste” Virchow [131]; translated original caption: Fig. 128: Multiple melanoma of the Pia mater basilaris, most pronounced around the Medulla oblongata, the Pons, the Fossa Sylvii, Fissura longit (sample No. 256a from 1858); Fig. 129: Lower end of spinal cord of Fig. 128 with multiple melanoma of the soft skin with node like growths at the nerve roots (sample No. 256b from 1858)

years into the last century [133, 134]. However, similar to how X-rays can cause cancers, researchers also found quickly, that it can also treat cancer and thus the field of radiotherapy was created. This then was the first major change in cancer treatment for around five thousand years, which also could treat inoperable cancers.

The next invention, that I want to highlight in the vast amount of advances made in the advent of the 20th century, is the cutting needle aspiration syringe, which allowed a non-traumatic biopsy of internal organs for microscopy study. Which made it possible to not have exploratory surgery and instead allow planning of necessary operations.

The next major step in the treatment of cancers comes in the form of chemotherapy, when Ehrlich [135] published his work “Beiträge zur experimentellen Pathologie und Chemotherapy” where he injected animals with different toxins in order to destroy cancer cells. Although, it still took another

30 years till after the second world war when the discovery, that a chemical design for warfare also had potent anti-tumour effect.

In the meantime, the first long term tissue cultures of animal cancer cell lines were established and further insights like the Warburg effect [136] found, which showed, that cancer cells use glucose at a higher rate than healthy cells. This effect ultimately led to the discovery of the positron emission tomography (PET) scan, which allowed a significantly more granular diagnosis and localisation of cancerous lesions than before.

With the success of growing human cell lines in vitro, the USA embarked on a massive experiment to test any potential source of chemical carcinogenesis. But at the same time, multiple viruses were identified to cause cancers in the 1950s, when electron microscopy was invented [137].

Only a few more years later, the biggest advance in the understanding of biology was made, when the structure of DNA was discovered [61] ([Section 1.1](#)) and subsequently lead to numerous new experiments and breakthroughs. When studying how viruses are able to reverse transcribe their RNA and insert a new gene into a healthy cell, which then transformed into a cancer cell, the term “oncogene” was coined[138, 139, 140] and the foundation for the understanding of how genes influence the emergence of cancers was laid. This also lead to the understanding, that heritable changes in the genome could predispose a person to cancer, which was previously hypothesised [141]. And while the discovery of DNA was a substantial boost for the understanding of cancer, the diagnostic capabilities increased at a similar speed, with urine tests for biomarkers of certain cancers as well as antigen detection.

And this is when we arrive at the “current” times, when a few years ago next generation sequencing (NGS) ([Section 1.3](#)) was introduced and sped up data generation on genomic and non-genomic diagnostic tests, from targeted amplicon sequencing to whole genome sequencing. These highly specific tests then allowed the application of highly specific drugs, like tyrosine kinase inhibitors (TKI)s, which are tailored to target a specific alteration in the genome of a cancer cell, and genetically engineered antibodies which can be homed in on the cancer. And while the therapeutic world is quickly evolving, many of the questions from previous times are still the same. We still don’t know how and when the heterogeneity in cancers occurs, we just know it is a major source of resistance to treatment. We also still do not have an answer to the “cell of origin” question that has been asked for so long, but we do know that some cancers can de-differentiate and morph between cell types.

So instead of trying to answer these questions directly, there has been an effort to define fundamental features malignancies have to be considered cancers, very similar to the early pathology descriptions. The original characteristics comprise 1. Sustaining proliferative signalling 2. Evading growth suppressors 3. Activating invasion and metastasis 4. Enabling replicative immortality 5. Inducing angiogenesis 6. Resisting cell death ([Figure 1.7](#)).

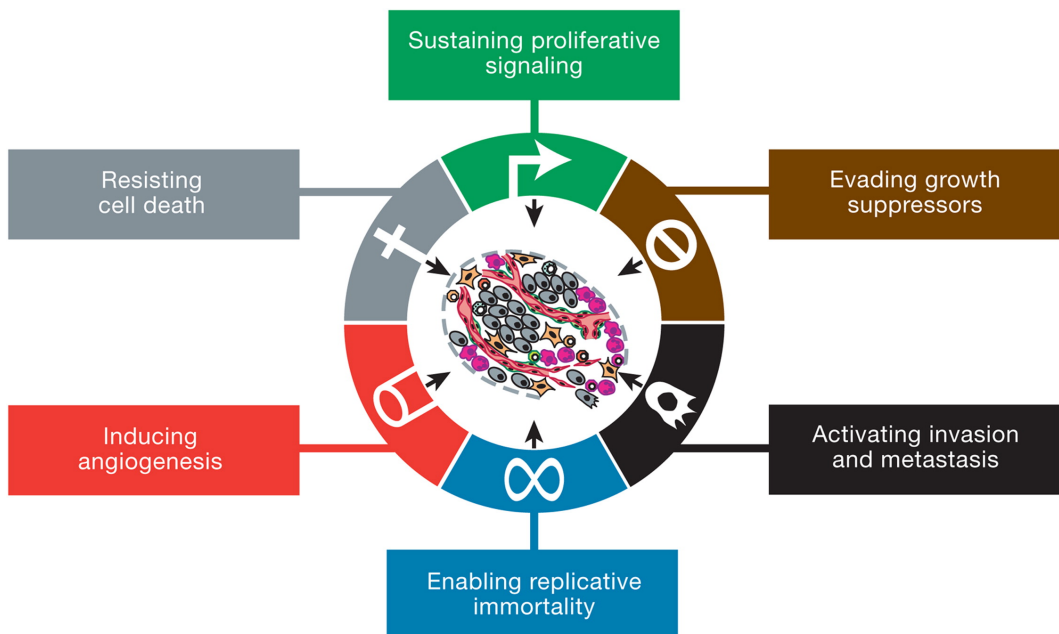


Figure 1.7: Acquired capabilities of cancer; Functional capabilities acquired by most cancers during their development; Figure adapted from Hanahan et al.[\[142\]](#)

These hallmarks were for a while considered the core of tumour development and the authors themselves hypothesised, that these core mechanics allow us to condense the complexity that cancer displays, both in the clinic and in labs, with a small set of rules, which all cancers have to obey [\[142\]](#). In their exact words: “We foresee cancer research developing into a logical science, where the complexities of the disease, described in the laboratory and clinic, will become understandable in terms of a few underlying principles”

However, with 11 years of additional research into the topic, more hallmarks have been found, and the original list was revised by the authors to contain additional characteristics, namely 1. Avoiding immune destruction 2. Tumour-promoting inflammation 3. Genome instability and mutation 4. Deregulating cellular energetics [\[143\]](#). And even then a few years later, even more hallmarks e.g. metabolic rewiring are now considered a part of the characteristics of cancer [\[144\]](#).

And even during the time of my PhD, further research revealed additional hallmarks, which got

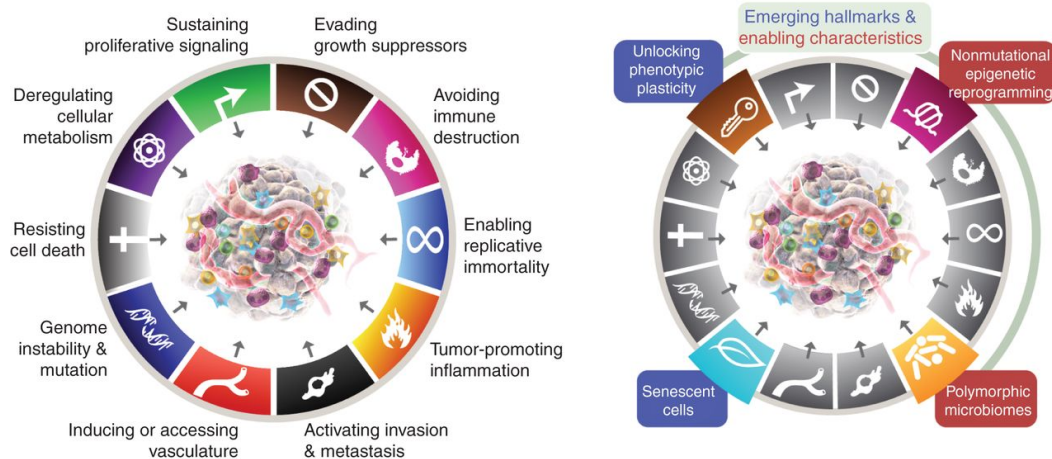


Figure 1.8: Emerging hallmarks and enabling characteristics of cancer; updated version of the hallmarks figure (Figure 1.7,[142]); Figure adapted from Hanahan[145]; Left, the Hallmarks of Cancer currently embody eight hallmark capabilities and two enabling characteristics. In addition to the six acquired capabilities – Hallmarks of Cancer – proposed in 2000 (Figure 1.7), the two provisional “emerging hallmarks” introduced in 2011 ([143]) –cellular energetics (now described more broadly as “reprogramming cellular metabolism”) and “avoiding immune destruction” – have been sufficiently validated to be considered part of the core set. Given the growing appreciation that tumors can become sufficiently vascularized either by switching on angiogenesis or by co-opting normal tissue vessels [146], this hallmark is also more broadly defined as the capability to induce or otherwise access, principally by invasion and metastasis, vasculature that supports tumor growth. The 2011 sequel further incorporated “tumor-promoting inflammation” as a second enabling characteristic, complementing overarching “genome instability and mutation,” which together were fundamentally involved in activating the eight hallmark (functional) capabilities necessary for tumor growth and progression. Right, this review incorporates additional proposed emerging hallmarks and enabling characteristics involving “unlocking phenotypic plasticity,” “nonmutational epigenetic reprogramming,” “polymorphic microbiomes,” and “senescent cells.”

characterised by Hanahan [145]. The newest version adds another two characteristics and hallmarks, specifically: 1. unlocking phenotypic plasticity 2. nonmutational epigenetic reprogramming 3. polymorphic microbiomes 4. senescent cells (see Figure 1.8).

These evolution of these hallmarks shows, why even though lots of time and effort was invested into cancer research for multiple centuries, there still is no unifying definition and treatment for cancer. The vast heterogeneity not only between cancer types, but also between patients makes it very hard to study. But even within patient there is third type of heterogeneity, which is the main cause of treatment resistance and relapse [1]. And while we know, that this diversity exists and efforts have been made to measure and classify them [147], there is still a lack of methods, which deal with the heterogeneity in their models to inform clinical approaches directly.

Write how this shows that the heterogeneity of cancer is the reason we still havent found a unifying description and treatment

1.6 Overview

add short description of each chapter

“It is the main source of our mistakes, when making making decision, that we only look at life piece by piece and not as a whole.“

— Lucius Annaeus Seneca, *Epistulae morales ad Lucilium*

2

Joint somatic variant calling - if germline can do it,
so can we

2.1 Introduction

In 2018, at the start of the work presented in this thesis, we observed a difference in methodology between germline and somatic variant calling methods. Where all "modern" germline variant callers, like Strelka2 [106], HaplotypeCaller [148], DRAGEN [149] and DeepVariant [150], have the built-in capability to jointly call multiple related samples, for example from family trios, virtually no somatic variant caller had this functionality.

The joint analysis of smaller cohorts improves the performance of germline variant calling methods significantly, by allowing to assess technical artefacts, which might be unique for the individual sequencing machine or the researcher handling the DNA [151, 152]. Additionally, as certain parts of the genome are more problematic to sequence (Section 1.3) and map (Section 1.4.1), a “control“ sample can help to distinguish if a certain observed change occurring frequently is a technical issue or in fact a real change.

For somatic variant calling, this concept has been adopted on in the genome analysis toolkit (GATK) [153] to allow the use of panel of normals (PON), which contains frequently seen changes in healthy (“normal“) individuals analysed with the same sequencing technology [154]. Although, in contrast to the more intricate model for the germline equivalent, this is a post processing step of the analysis. Mutect2, which is the most recent somatic variant calling algorithm provided by the Broad institute, also provides a multi-sample mode, for which all tumour samples need to be from the same patient, either related longitudinally or spatially [155]. However, this mode is not very well publicised and

all tutorials released by the developers state that “there is currently no way to perform joint calling for somatic variant discovery” [109]. So while all methods in the GATK are considered a beta feature, the multi sample mode needs to be used with care.

There are only two methods currently, which have documented and published capabilities to jointly analyse tumour samples from the same patient to call somatic variants. The first one is a specialised method built on a joint bayesian model for SNVs that occur in multiple samples called multiSNV [156]. However, it has multiple shortcomings, which make it not usable for our data. First, as the name suggests, the method can only jointly evaluate SNVs and completely ignores INDELS and structural variants, which would be acceptable for the superior performance it provides. However, multiSNV was optimised only for WES and not for the very deep WGS that is now available and part of this thesis. This mismatch of input types means exceptionally high runtimes on our data. Even with custom parallelisation that was attempted in this work, the predicted runtime for just one multi sample patient would have been longer than 3 years. This shows, that while multiSNV was a great step forward at the time, there is a real need for new methods to stem the tide of sequencing data available due to the ever decreasing sequencing cost.

multiSNV has been the only software available for multi sample analysis for almost five years, but during this work, superFreq [157] was published. It combines all standard analysis steps for tumour analysis, like quality assessment, variant calling, copy number analysis and clonal deconvolution, into one program and is even able to jointly analyse samples. However, similar to multiSNV, its focus during optimisation and development was on WES and RNAseq data, so when applied to our data, we could not find a server node with enough memory to execute the workflow.

This then prompted us to investigate possible workflows to enable the analysis of high depth WGS, which we estimate to become more and more normal, with the ever dropping prices of sequencing. The following sections will show the development and validation of the joint variant calling methods as described in Hollizeck et al. [158] (Section 2.2), additional analysis on the impact of the joint variant calling on downstream analysis (Section 2.3), longitudinal analysis (Section 2.4) and clonal deconvolution (Section 2.4.1) and lastly information on the usage of the methods by others in the research community (Section 2.5).

2.2 Publication

The full publication about joint somatic variant calling can be found at <https://doi.org/10.1101/bioinformatics/btab606> and non-journal formatted version is also attached as [Appendix A](#) with all supplementary methods.

References to supplementary data will be prefixed with the letter [A](#) in the text.

2.2.1 Summary

To enable highly sensitive, fast and accurate variant detection from multiple related tumour samples, we have developed joint variant calling extensions to two widely used single-sample algorithms, FreeBayes [104] and Strelka2 [106]. Using both simulated and clinical sequencing data, we show that these workflows are highly accurate and can detect variants at much lower variant allele frequencies than other commonly used methods.

2.2.2 FreeBayesSomatic workflow

The original FreeBayes algorithm can jointly evaluate multiple samples, but routinely it does not perform somatic variant calling on tumour-normal pairs. We introduce FreeBayesSomatic which allows concurrent analysis of multiple tumour samples by adapting concepts from SpeedSeq [159] which differentiates the likelihood of a variant between tumour and normal samples instead of imposing an absolute filter for all variants called in the normal. Hence, for each genotype (GT) at SNV sites, FreeBayesSomatic first calculates the difference in likelihoods (LOD) between the normal ([Equation 2.1](#)) and the tumour ([Equation 2.2](#)) samples genotype likelihoods (GL) with g_0 describing the reference genotype.

$$\text{LOD}_{\text{normal}} = \max_{g_i \in \text{GT}} (\text{GL}(g_0) - \text{GL}(g_i)) \quad (2.1)$$

$$\text{LOD}_{\text{tumour}} = \min_{s \in \text{Samples}} \left(\min_{g_i \in \text{GT}} (\text{GL}_s(g_i) - \text{GL}_s(g_0)) \right) \quad (2.2)$$

$$\text{somaticLOD} := (\text{LOD}_{\text{normal}} \geq 3.5 \wedge \text{LOD}_{\text{tumour}} \geq 3.5) \quad (2.3)$$

Next, the variant allele frequencies (VAF) in both the tumour and the normal samples are compared at each site.

$$\text{VAF}_{\text{tumour}} = \max_{s \in \text{Samples}} (\text{VAF}_s) \quad (2.4)$$

$$\begin{aligned} \text{somaticVAF} := & (\text{VAF}_{\text{normal}} \leq 0.001 \vee \\ & (\text{VAF}_{\text{tumour}} \geq 2.7 \cdot \text{VAF}_{\text{normal}})) \end{aligned} \quad (2.5)$$

A variant is classified as somatic when both somatic LOD as well as somatic VAF pass the criteria somaticLOD ([Equation 2.3](#)) and somaticVAF ([Equation 2.5](#)).

The thresholds chosen for both LOD and VAF calculations were previously fitted by the blue-collar bioinformatics workflow for the “DREAM synthetic 3” dataset using the SpeedSeq likelihood difference approach [[160](#)] and were selected to identify high confidence variants.

2.2.3 Strelka2Pass workflow

In contrast to FreeBayes, whilst Strelka2 has a multiple-sample mode for germline analysis and tumour-normal pair somatic variant calling capabilities, it cannot jointly analyse multiple related tumour samples. We enable this feature by adapting a two-pass strategy previously used for RNA-seq data [[161](#)]. First, somatic variants are called from each tumour-normal pair. All detected variants across the cohort are then used as input for the second pass of the analysis, where we re-iterate through each tumour-normal pair but assess allelic information for all input genomic sites.

The method re-evaluates the likelihood of each variant, by integrating every genotype from each tumour-normal pair. This step can “call” a variant (v) in a sample that initially did not present enough evidence to pass the Strelka2 internal filtering using two conditions: 1) if this variant was called as a proper “PASS” by Strelka2 in any other tumour sample, or 2) if the integrated evidence for this variant across all tumour-normal pairs reached a sufficiently high level. The second condition was based on the somatic evidence score (SomEVS) reported by Strelka2, which is the logarithm of the probability of the variant v being an artefact.

$$p_{error}(v) = 10^{\left(\frac{-\text{SomEVS}(v)}{10}\right)} \quad (2.6)$$

While the germline sample is shared between all processes, we can approximate these individual probabilities as being independent, since one variant calling process is agnostic of the other. Hence, we derive the following:

$$p_{error}(v_{s_1}, v_{s_2}, \dots, v_{s_n}) = \prod_{s \in \text{Samples}} p_{error}(v_s) \quad (2.7)$$

And therefore:

$$\text{SomEVS}(v_{s_1}, v_{s_2}, \dots, v_{s_n}) = \sum_{s \in \text{Samples}} \text{SomEVS}(v_s) \quad (2.8)$$

This allows the summation (Equation 2.8) of the SomEVS score across all supporting variants to assign a "PASS" filter, if it reached a joint SomEVS score threshold. This threshold can be set by the user and is 20 by default, which corresponds to an estimated error rate of 1%. These "recovered" variants need to pass a set of additional quality metrics related to depth of coverage, mapping quality and read position rank sum score.

As an additional improvement, we also built multiallelic support into Strelka2 which originally only reports the most prevalent variant at a specific site. Within the two-pass analysis, we reconstruct the available evidence for a multiallelic variant at a called site from the allele-specific read counts and report the minor allele at this site, if there is sufficient support from other samples. This method allows recovery of minor alleles only if another sample has this variant called by Strelka2, as SomEVS scores are not available for minor alleles.

2.2.4 Validation

While the development of new methods can challenge previous assumptions and allow to challenge previous ruled, all methods need be validated against the current gold standard methods in the field with data which allows objective measurements. For germline variant calling, there have

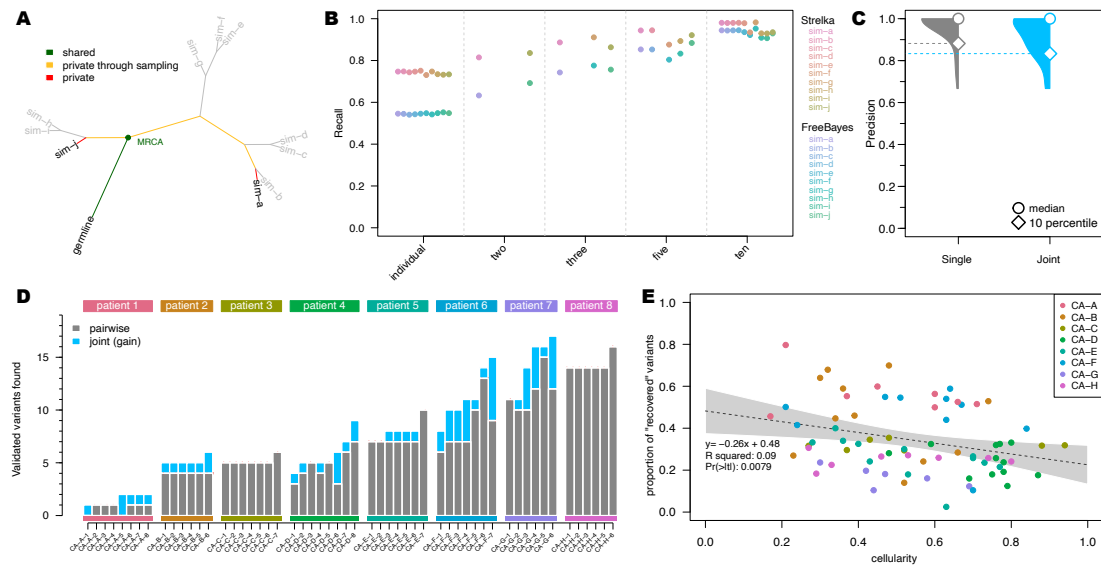


Figure 2.1: Comparison of joint multi-sample variant calling and single tumour-normal paired calling methods; A) Simulated phylogeny highlighting two samples with high evolutionary distance (sim-a and sim-j) where MRCA denotes the most recent common ancestor. B) Recall estimates of FreeBayes and Strelka2, run in individual tumour-normal paired and joint calling configurations using two (sim-a and sim-j), three (sim-a, sim-g and sim-j), five (sim-a, sim-c, sim-f, sim-h and sim-j) and all ten tumour samples. C) Precision of Strelka2 and D) Number of variants called by Strelka2 run in both tumour-normal paired (grey) and added with joint calling configurations (blue), which have been validated by targeted amplicon sequencing (TAS). E) Correlation between cellularity and proportion of variants found only with joint calling using Strelka2Pass for clinical samples; grey area shows the "95%" confidence interval for the linear model fit (dotted line).

been multiple community lead challenges and specifically designed test datasets, but there is currently no somatic variant calling equivalent. This issue is even more pronounced for our method, as we do not only need a tumour-normal pair, but we need the multiple tumour samples in the dataset to be related. To allow a fair comparison, we first generated a fully synthetic dataset, where every variant is known and fully defined (Section 2.2.4.1) to allow a general performance assessment of the methods. Then to ensure that these metrics also hold true in real world data, we then re-analysed previously published datasets which have orthogonal validation in the form of targeted amplicon sequencing (TAS) (Section 2.2.4.2).

2.2.4.1 Simulated data

We first simulated a phylogeny with somatic and germline variants from ten tumour samples and one normal (Figure 2.1A and Figure A.2A, B). Germline variants were simulated at a uniform allele frequency of 0.5. Somatic VAFs were sampled from a custom distribution, modelled to favour low allele frequency variants to closely represent real world data (min VAF: 0.001; max VAF: 1; Fig. S1C, D). Paired-end sequencing reads with realistic error profiles were simulated for WGS data at 160X

average coverage using the ART-MountRainier software [162]. The simulated reads were aligned to GRCh38 and both germline and somatic variants from the phylogeny were spiked into the aligned reads using Bamsurgeon [163]. We compared the workflows for FreeBayes and Strelka2 with and without our extensions for joint variant calling on the simulated datasets. The performance of Mutect2 joint variant calling was also assessed using its proposed best practice workflow. As both Mutect2 and FreeBayes do not return a verdict for each individual sample, we needed to assign each sample in the multi-sample VCF its own FILTER value. We called a somatic variant as present in a sample, if there were at least two reads supporting it for this sample and the overall FILTER showed a “PASS”, which was the same cut-off used in the refiltering step in the Strelka2-pass workflow.

While the precision of each method without our extensions was greater than 99.8%, they all missed at least 25% of all variants in the samples (i.e. recall $\leq 75\%$). In contrast, the recall of the modified workflows increased to $\approx 95\%$ with only a minute decrease in the precision for both FreeBayes and Strelka2 (Figure A.3). Mutect2 had virtually no change in precision, but the recall actually decreased from $\approx 75\%$ to $\approx 41\%$ when analysing the samples jointly (Figure A.3B). Additionally, with our modified workflows, true positive variants were called with VAFs as low as 0.008 (median detected VAF ≥ 0.14 for joint sample analysis and ≥ 0.21 for single tumour-normal pair analysis), enabling improved distinction between true variants and technical errors (Figure A.4). This improvement in performance for Strelka2 is only achieved after the refiltering step and not just a result of the second pass (Figure A.5, Section A.5.4).

The performance of joint variant calling in Mutect2 was inferior compared to all other methods (Figure A.3A, B). This was primarily due to the "clustered_events" filter in Mutect2, which excluded the majority of false negative variants, with negligible contribution to the exclusion of true negative variants (Figure A.6A, B). This result was unexpected as the simulated variants were evenly distributed along the genome and the corresponding allele frequencies were sampled randomly (Figure A.2D).

Since the extent of the improvement in our joint calling workflows is bound by the number of shared variants between samples, we sub-sampled the simulated dataset, to show the effect of incomplete sampling on our methods, which is more likely in clinical settings. Furthermore, the evolutionary distance between the related samples in addition to the number of samples, has a major impact on the number of shared variants, as only variants acquired between the germline and the most recent common ancestor (MRCA), will benefit from the joint analysis. Therefore, we selected three sample subsets which included two, three and five samples with high evolutionary distance to show the

minimum expected improvement ([Figure 2.1A, B](#)). There was a clear linear improvement for both FreeBayesSomatic and Strelka2Pass when increasing the number of samples, even if they had a distant evolutionary relationship. In contrast, when using only two samples with a small evolutionary distance, the increase in performance was almost as large as when jointly analysing all 10 available samples. This shows that samples with a high number of shared variants will perform better in joint calling workflows ([Figure A.7](#)).

2.2.4.2 Clinical data

To validate the performance of our new workflows, we then analysed WGS and whole-exome sequencing (WES) data of multi-region tumour samples from eight patients, with multiple tumour sites (average 7 samples per patient; total number of samples 55), enrolled in a rapid autopsy program conducted at the Peter MacCallum Cancer Centre ([Table A.1](#) and [Section A.5.2](#)) [[164, 165](#)]. The published studies had multiple somatic variants from the clinical samples orthogonally validated through targeted amplicon sequencing (TAS). We used these TAS-validated variants as the gold standard to evaluate the performance of different workflows, acknowledging that the technical biases inherent to TAS data are different to those present in WGS and WES ([Figure A.8](#)) and that there would be sampling biases depending on different tumour cells analysed in each data type.

In concordance with the results of the simulated data, our improved workflows found additional variants in all but one patient ([Figure 2.1D, Figure A.9](#)) (total additional variants Strelka2Pass: 64; FreeBayesSomatic: 85) with only a slight drop in precision for FreeBayesSomatic (mean: 0.94 vs. 0.88) and Strelka2Pass (mean: 0.97 vs. 0.92). Since the panel of variants validated by TAS was limited (7108 bp for patients CA-B through -H), this increase in detected variants suggests that a high number of shared variants in samples are missed with current approaches, which in turn leads to an overestimation of tumour heterogeneity between samples, as these variants are thought to not be present rather than undetected.

Even though the number of shared variants is a major influencing factor when jointly calling variants, low cellularity samples benefit more from the joint calling, as conventional methods cannot reliably distinguish low allele frequency variants from noise. Through a joint analysis approach, the number of recovered variants is higher in low cellularity samples, which indicates, that especially for clinical samples with variable tumour purity, joint analysis can have a major impact on improving performance ([Figure 2.1E, Figure A.10](#)).

Mutect2 in contrast, did not show significant improvement in any sample in its joint calling configuration, but showed inferior performance compared to the tumour-normal pairwise approach in two samples ([Figure A.9E](#)), similar to its decreased performance in the simulated data ([Figure A.3](#)). This was due to true variants being removed by the internal filters of the tool ([Figure A.6C, D](#)). This is in stark contrast to our novel workflows, where the joint analysis preserves all called sites from the pairwise method and finds additional variants. Overall, Mutect2 found less validated variants in all patients than both Strelka2Pass (mean: 2.2) and FreeBayesSomatic (mean: 2.5) with comparable levels of precision ([Figure A.9](#), [Figure A.11](#)) but longer run times ([Table A.2](#)).

Our improved workflow also enabled the discovery of multiallelic variants with Strelka2, which led to the discovery of on average 42 additional variants (min: 1; max: 535) in the analysed WES and 987 additional variants in the WGS (min: 81; max 2329). These variants are strong indicators of sub clonal structure and are invaluable for the study of evolutionary trajectories in cancer, as shown in the following sections.

2.3 Effects of additional somatic variants on downstream analysis

The ability to find additional shared variants has significant impact on our understanding of cancer evolution and the timing of initiation and metastatic seeding. Recent work has shown, that similar to the well known genetic heterogeneity, there is heterogeneity when it comes to the timing of metastatic seeding. While traditionally it was thought that tumours only metastasise after they reach a certain size, to escape the restrictions of the niche, like reduced nutrition, recent publications showed, there is also very early metastatic seeding [[166](#)]. But all methods analysing heterogeneity, evolutionary timing and history are fully reliant on the somatic variants found in the data. Therefore, if we improve the input provided to these analysis methods, we can expect a clearer and possibly more granular result.

The following section will quantify the effect of additionally found variants on phylogenetic reconstruction and clonal decomposition, which use somatic variants as input.

2.3.1 Phylogenetic reconstruction

As this work is not about the advantages and shortcomings of different phylogenetic reconstruction tools, we have not performed a comprehensive comparison of these tools, but rather focused on the

results of using additional variants. For this reason, we chose to use neighbour joining (NJ) [167], because it is fast, readily available in most phylogenetic reconstruction tool kits and if the input distance is correct, the output will be correct. And even, if the distance is not 100% correct, if the distance is “nearly additive” and the input distances are not far off from the real distance, the tree topology will still be reconstructed correctly [168]. Lastly, in contrast to many other methods like UPGMA and WPGMA [169], NJ does not assume an equal mutation rate of each sample, because we know, that the molecular clock hypothesis [170] is not valid for different lineages of cancers [171].

The only thing that NJ requires as an input is a distance matrix of all samples, so the next step was the selection of the right distance metric. While there are many distance measures for DNA sequences, which allow accounting for different probabilities of transitions and transversions as well as uneven base composition, models like F81 [172] or HKY85 [173] are only really designed for germline mutations and are not easily applicable for subclonal somatic mutations, which is why we decided to first transform the variants present in all samples into a binary occurrence vector and then calculating the Hamming distance [174] between all samples. This generates a maximum parsimony approach and the branch length of the trees will be directly translatable to the amount of variants which are different between samples.

Figure 2.2 shows both the reconstructed phylogenies of the autopsy samples of the late stage melanoma patient “CA-F“ from the manuscript (Appendix A, Table A.1), using the variants found with the default tumour-normal method on the left and our improved joint method on the right. The exact same reconstruction methodology was used otherwise, such that only the different inputs lead to the final difference.

Maybe adjust the font size in the trees to make it more readable

There are several obvious changes, first in the longer edge connecting the germline to all other samples, which we consider as the state of no somatic variants. This shows that there are many more shared mutations in all samples, than what would have been anticipated with the default method, which corresponds to an overestimation of the heterogeneity of the samples. As the accumulation of somatic variants is still used as a proxy for timing and cell divisions, when assuming a high mutation rate for lung cancer ($5.3 \cdot 10^{-8}$ from Werner et al. [175]) this difference of ≈ 36000 variants is equivalent to ≈ 2000 cell divisions. While the cell doubling rate of lung cancers is highly dependent on the type [176], this change makes a substantial difference when assessing the timing of the tumour initiation and further evolution.

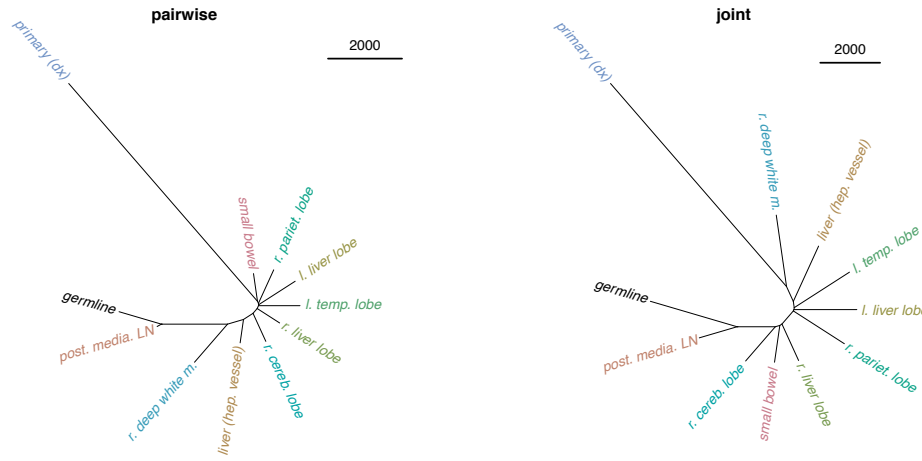


Figure 2.2: Reconstructed phylogenies of a patient with multiple spatially distinct samples; Neighbour joining on Hamming distance on variant occurrence vector. Tip labels describe the location of the sample in the patient. Trees are shown as unrooted with germline as fixated origin point; black line ruler shows the length of an edge with 2000 mutations

Secondly, there have been topological changes, which generate a longer bifurcating edge between the olive coloured “r. liver lobe” and the “r. pariet. lobe” showing a bottle neck in cancer evolution, which fits very well with the clinical history, where the patient lived with stable disease for almost ten years, before progressing and dying. The extreme distance of the primary/diagnostic sample from the rest of the samples could be either a difference in sequencing quality, or due to the exposure to FFPE for the ten years between tumour diagnosis and death. However, as this feature is preserved between both the joint and the pairwise analysis, it does not appear to be an effect of our new method.

maybe increase the line width of the edges

Figure 2.3 shows a topology focused view of the two trees, which highlights the breaks which are needed to morph one tree into the other with dotted edges [177]. The common subtrees are coloured the same on both sides and connecting lines show identical labels. This format shows that while the trees look quite similar at first glance, they show vastly different topologies.

One example of this is “small bowel” which was connected to the red common subtree, but is now much closer to the “r. cereb. lobe” and forms a parallel clade with the “r.liver lobe”. In general, where the pairwise tree shows a very linear topology, which leaves only branching out of the main with no disjunct subclades, which are clearly present in the joint reconstruction. (Figure 2.3).

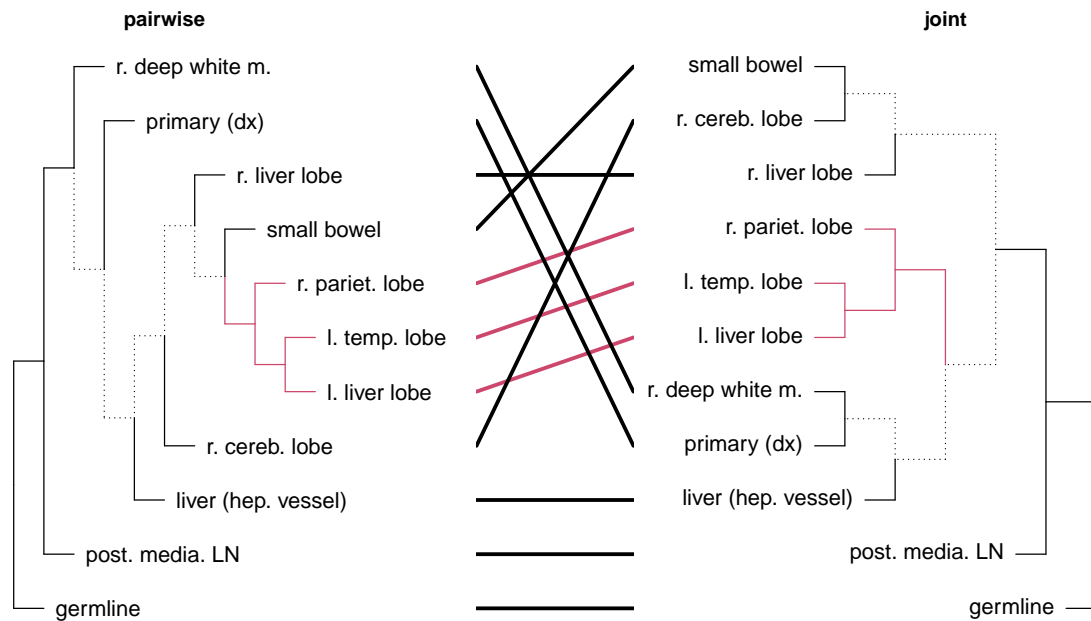


Figure 2.3: Side by side view of the reconstructed trees from Figure 2.2; internal edges, which are distinct between trees are shown as dotted lines; common subtree is shown in red Tree labels have been sorted to minimise distance between labels; Visualisation generated with dendextend [25]

2.4 Longitudinal analysis

The initial motivation for the development of our workflows was the analysis of multi-region, or spatial, samples from the same patient coming from the CASCADE rapid autopsy program. However, we were very interested on applying the methods on longitudinal samples from patients, for example, for the joint analysis of diagnostic and relapse sample, or even the repeated testing of ctDNA are quite worth thinking about. In this part, we present work using the published workflows on a longitudinal dataset, which highlights the flexibility and widespread usability of the new methods.

In addition to their autopsy which resected nine distinct metastatic sites (Figure A.13), Patient “CA-F” also had three longitudinal blood samples taken, from which ctDNA was extracted and WES performed. These blood samples were taken as non-invasive surveillance seven, five and two months before the death of the patient (Figure 2.4). In a study of late stage melanoma patients, Tan et al. identified ctDNA sequencing as a way to stratify patients into high and low risk of relapse and therefore inform adjuvant therapy [178]. This makes patient “CA-F” a very good test dataset to showcase

the improvement with joint variant calling. Similar to the spatially related samples, the joint analysis can improve the performance, which then in turn enable the detection of lower allele frequency variants, either through lower tumour burden or through the limited availability of DNA fragments from brain lesions due to the blood brain barrier [179].

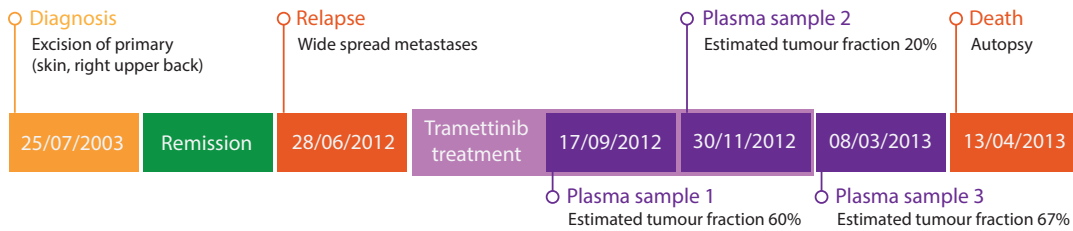


Figure 2.4: Timeline from diagnosis till death for patient CA-F: 1.9mm melanoma removed after diagnosis Friday 25th July, 2003 but with negative sentinel lymph node biopsy; Thursday 28th June, 2012: PET scan and subsequent liver biopsy confirm relapse with wide spread metastases; trametinib treatment from Oct. 2012 till Jan. 2013 with minor response; blood plasma samples during treatment (1 and 2) as well as after progression (3); death and rapid autopsy of nine metastatic sites (Saturday 13th April, 2013, [Figure A.13](#)); Tumour fraction in plasma samples was estimated via the original driver mutation (BRAF:K601E)

To show that even in longitudinal data, the joint analysis can boost the signal, we jointly variant called the diagnostic biopsy sample with the three ctDNA samples and compared them with the results from the pairwise analysis. On average, we found 2905 additional variants in each of the ctDNA samples, which is more than doubles the average number of variants found with the pairwise analysis (2414). Out of those, we found 534 variants in the ctDNA samples, which were found as a high confidence variant in the diagnostic sample, indicating that these findings are high quality calls.

Exactly like in the spatially different samples, in longitudinal data lower tumour purity samples benefit more from the joint analysis. We see that time point 2 (T2) has the highest amount of recovered variants (377) which are found as high confidence variants in both other time points ([Figure 2.5 A vs. B vs. C](#)) and T2 also has the lowest tumour purity in the cfDNA recorded (T1: 60%; T2: 20%; T3: 60%) however, there are still 106 variants, which were not found in the ctDNA samples at all with the pairwise analysis at all, even though they were high confidence variants in the primary sample ([Figure 2.5 F](#)). These variants usually show a lower depth of coverage (dp) in the ctDNA samples, which may possibly indicate a problematic region in the genome, but rather than it not being called a variant, it is just a sign of incomplete data, which can be used with our joint approach.

Finally, we can also find 398 additional variants in the primary sample. 398 were discarded due to missing data in the tissue sequencing, but could be found with a high confidence in the longitudinal

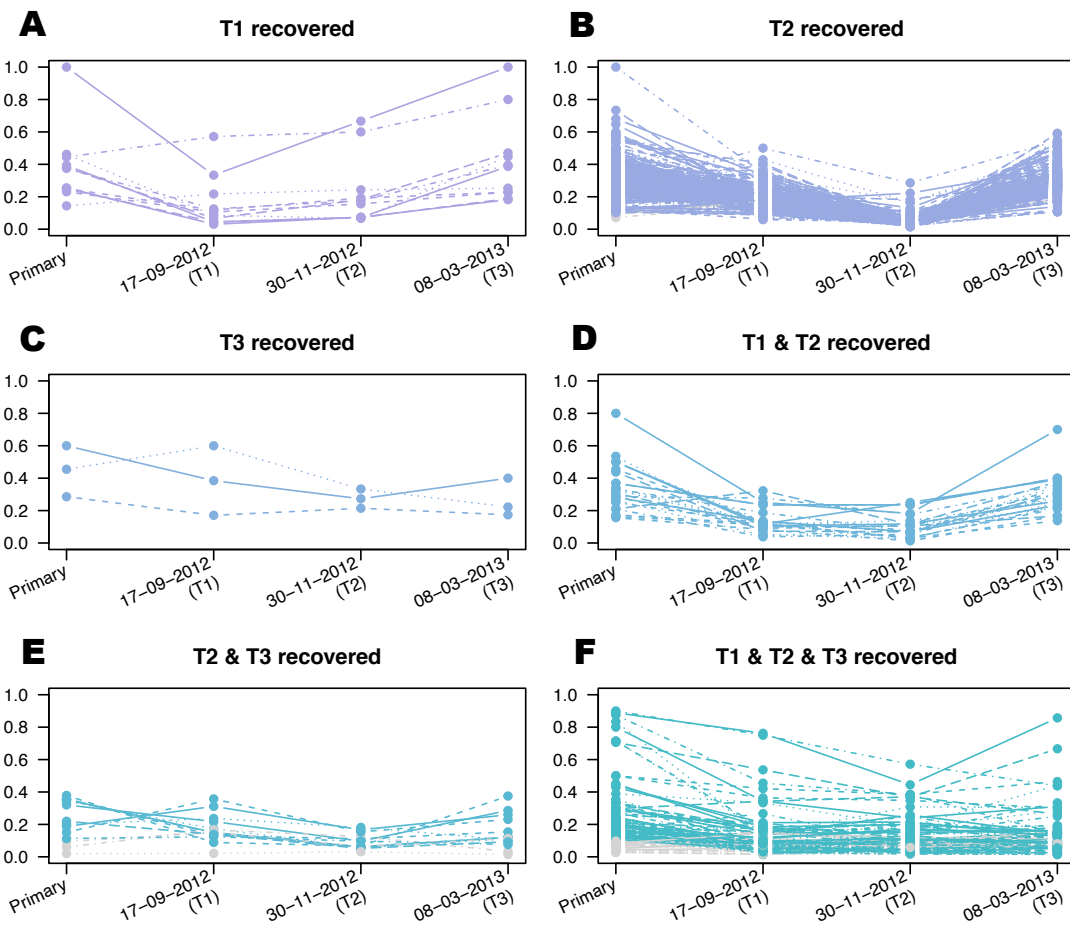


Figure 2.5: Improved somatic variant calling in longitudinal data: Variant allele frequency (VAF) of variants found additionally through joint variant calling which were found as high confidence variants in the primary sample; Variants with less than 0.1 VAF in the primary are coloured grey; “T1 recovered“ shows variants, which were high confidence in all ctDNA samples but T1 and were only found through joint calling there; Axis label show the date of blood collection

data and two of the variants were included, as all 4 samples had this variant below the detection threshold (Figure 2.6). The missing depth in the primary also leads to the occasional very high allele frequency of the variant, as all available reads show the variant, but their numbers are below the threshold normal variant callers will report variants.

This shows that both spatially and longitudinal related samples should be analysed jointly, as it substantially increases the amount of true variants found, which as shown before, can have a large impact on downstream analysis of the samples.

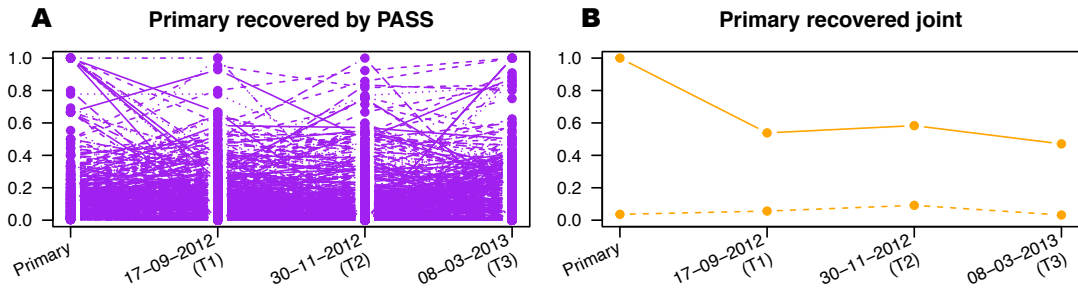


Figure 2.6: Longitudinal data informs diagnostic variant calling: Vafs of variants additionally found through joint calling in the primary samples; Primary recovered by PASS shows variants which were high confidence in at least one ctDNA sample; Primary recovered joint shows variant which were low confidence in all samples in the pairwise analysis; Axis label show the date of blood collection

2.4.1 Clonal deconvolution

One of the most important information derived from multiple related samples from the same patient is the clonal deconvolution, where subclonal reoccurring patterns of mutations (clones) are resolved both spatially and longitudinally. These reoccurring clones can be linked to either parallel evolution through positive selection pressure, like a targeted drug, or to the process of developing metastases where a piece of the cancer “breaks” off and grows at a different site. In contrast to the lack of options for joint somatic variant calling, there is a plethora of algorithms and methods available for clonal deconvolution. Since 2015 PhyloWGS [180], Canopy [181], CLOE [182], CloneFinder [183], MACHINA [184] and MOBSTER [185] were published, to name a few. Underlying all these models is a form of clustering variants with similar variant allele frequency together, to reduce the combinatorial space and enhance the confidence in the signal [186]. Due to the high number of tools, it is very challenging to select the right tool, especially since all of them have advantages and disadvantages [187]. In this work we decided to use PhylogicNDT [188] as it has been shown to work well on clinical samples [189] and does not have the restriction for the input to be from copy number neutral areas which many of the other tools have.

Both the variants found with the default pairwise as well as with the new joint workflows were annotated with their local allele specific copy number to form a MAF like file format which is required by PhylogicNDT. While PhylogicNDT allows the user to supply the cancer cell fraction for every variant, the program can also estimate them from the supplied allelic counts and the copy number. Local copynumber calls were derived from copy number segment calls made by sequenza by intersecting chromosomal location of each variant with the copy number segment containing

the variants location. This requires multiple steps and the source code is shown in [Listing A.1](#) (parsing VCF), [Listing A.2](#) and [Listing A.3](#) (convert to MAF format). Variants which couldnt be annotated with copy number information, because their genomic location did not overlap with any called copy number segment, were discarded for this analysis.

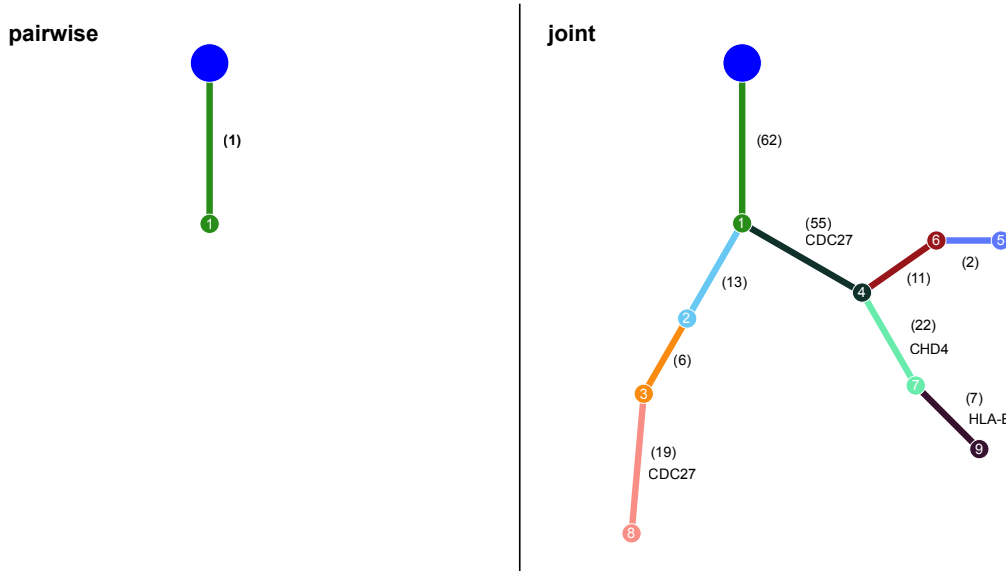


Figure 2.7: Reconstructed clonal trees from PhylogicNDT; Blue circle at top depicts the germline/normal state. The coloured edges with the same coloured circle represents a distinct subclone of the parent from which the edge emerges; The number in braces next to the edge is the number of mutations which define this subclone with an added gene symbol added, if there is a cancer driver gene mutation. The left part shows the result when using the default pairwise method of Strelka2 and the right side uses the results from the Strelka2Pass workflow

[Figure 2.7](#) shows the highest parsimony clonal tree reconstructed by PhylogicNDT for the pairwise as well as the joint variant calling. As the copynumber calling information is the same for both inputs, the only difference is in the called variants. While there was no subclonal structure detected at all for the pairwise analysis, there is a highly variable structure detected using the jointly called variants. As this is a clinical sample, we cannot be certain that the more branched model is the actual truth, but it's biologically more logical that a late stage cancer has developed several subclones, rather than it being a very homogeneous disease at all of the 10 sites at autopsy with no evolution over ten years of disease [189]. It is of particular interest, that the *CDC27* gene got mutated at different time points in different clones (clone 8 vs. clone 4), which is a clear sign of parallel evolution, which would definitely be missed without the joint analysis.

2.4.2 Longitudinal enriched phylogeny

Of course it is finally also possible to build a phylogeny with the spatial tissue samples and the longitudinal ctDNA samples. However, as the ctDNA give a holistic view of all cancer metastases ([Section 1.2](#)) the interpretation needs to accommodate for that.

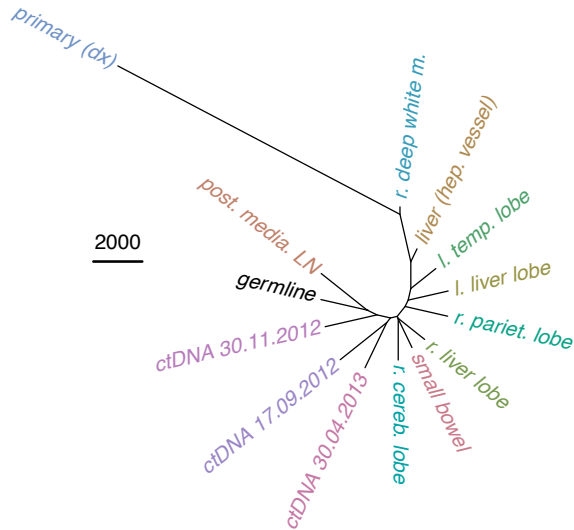


Figure 2.8: Reconstructed phylogeny with longitudinal ctDNA samples: Tree from [Figure 2.2](#) with three additional ctDNA samples from different time points about one year prior to death. The ruler shows the equivalent of 2000 mutations

The maybe most surprising thing is that the more temporally distant ctDNA samples from 17.09.2012 and 30.04.2013 are in a subclade together, away from the “ctDNA 30.11.2012“ sample. Secondly, the addition of the ctDNA samples also lead to a further bipartition edge, which separates “r. liver lobe“, “small bowel“ and “r. cereb. lobe“ from the rest of the tree ([Figure 2.8](#)). This was already inferable from the topology of the previous tree in [Figure 2.3](#) “joint“, but is even more pronounced with the inclusion of the ctDNA samples.

This shows that the addition of more samples helps to refine and improve the trajectory and history of cancer samples and it is vital to do this analysis jointly to generate the optimal result.

2.5 Usage statistics and uptake

Ultimately when choosing research software, publication and citations are not a good metric to evaluate the quality of a method [190]. Many published software packages are not maintained or

not even functional even though they are published. While we developed these joint somatic variant calling workflows to deal with a challenge we faced, the interest of others was continuously expressed by both members of the bioinformatics community whenever we presented this work.

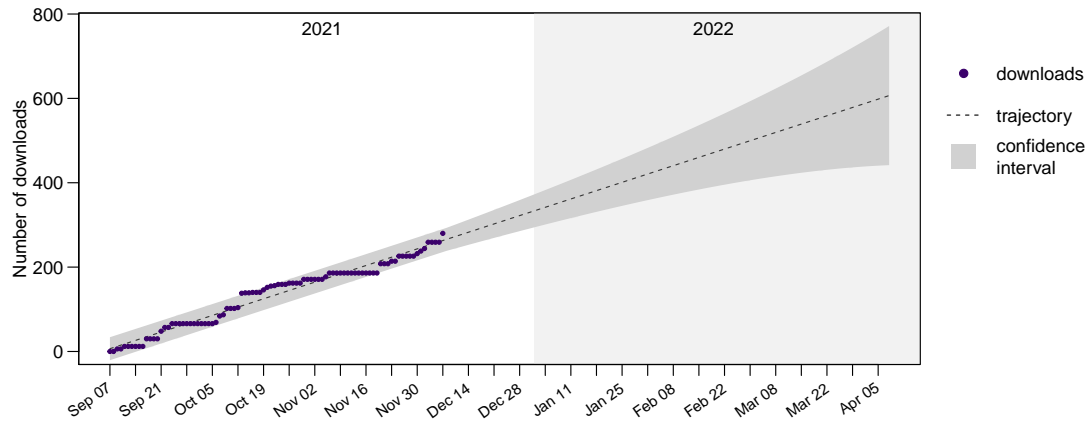


Figure 2.9: Cumulative download numbers of the “dawsontoolkit” docker container since publication of the manuscript; Actual counts are shown as dots, with smoothed trajectory depicted as dotted line with the 95% confidence interval shown as a grey background; confidence interval has been adjusted with exponential decay of prediction accuracy with distance from the last data point; Start date 7th September 2021 (publication of method); End point prediction 8th April 2022 (End of candidature); Numbers were recorded daily from the DockerHub API

To have some proxy of the usage statistics of the workflows, we recorded the download numbers of the “dawsontoolkit” docker container after the publication of the manuscript. The container only consists of software for refiltering and joint analysis of the workflows . Obviously, this is an imperfect measurement, as people can reuse a downloaded container as often as they want, which would not appear in the count and similarly, just because the container was downloaded, the analysis might not have been used. Nevertheless, it still shows an interaction and an interest in the methods. The download numbers show a sustained and stable increase in downloads (Figure 2.9). This suggests, that there is a need in the methods, rather than a simple curiosity after publication, which hopefully will facilitate a higher quality analysis of future projects and therefore lead to a better understanding of cancer evolution and heterogeneity.

“Death is a release from and an end of all pains: beyond it our sufferings cannot extend: it restores us to the peaceful rest in which we lay before we were born”

— Lucius Annaeus Seneca, *De Consolatione ad Marciam*

3

CASCADE - Late stage lung cancer in the spotlight

3.1 Introduction

As tumour heterogeneity is seen as one of the major causes of resistances to treatment and ultimately relapse, much cell line based research has been conducted to solve tissue of origin and evolutionary trajectories via bulk and single cell sequencing paired with cell barcoding [191, 192]. However while cell line models are a great resource for high throughput methods and allow easier reproducibility of results, they are no real substitute for primary patient cells. With the increased availability of patient samples through bio-banking efforts like the UK BioBank [193] and the Victorian Cancer BioBank [194], both patient derived xenografts (PDX) and organoids have gained more and more traction [195]. Both of which are specialised models to grow primary patient cells in an environment which closer resembles the body of the patient. While this method is superior in many aspects, there are some significant drawbacks. The culturing of the cells requires more effort and is not as easily scalable. These method also require fresh patient samples, which are not always readily available.

While it is fairly easy to collect diagnostic specimen from tumour biopsies for storage and research, late stage tumour biopsies are rare. Due to the deteriorating health status of the patient biopsies are dangerous and often an unnecessary burden for the patient. However these samples are especially critical when answering the question of how the cancer was able to avoid treatment and kill the patient, as it may reveal an unappreciated insight into spatial, temporal and genomic heterogeneity.

To try to combat this issue the CASCADE program was initiated. It recruits cancer patients close to the end of life and enrolls them in a rapid autopsy program. These autopsies are carried out at any

Do I need
to cite the
hetero-
geneities
here?

time of the day to minimise the impact on the sample to allow high quality assessment like RNA sequencing of the frozen cells [196]. While the program collects cancer patients unconditionally of their type of disease, the analysis of this thesis is restricted to the five lung cancer patients available at the time of my PhD. Currently there are no further lung cancer patients enrolled, but recruitment is still ongoing. Four of these five patients had an Epidermal growth factor receptor (*EGFR*) based cancer and one had a RET Proto-Oncogene (*RET*) fusion with *KIF5B*. Each of those patients had on average 30 specimens resected and put into a bio bank. We then continued to sequence, on average, eight of these samples with either whole genome sequencing (WGS) or whole exome sequencing (WES) to deeply analyse and classify the underlying resistance and driver mechanisms of each patient and their heterogeneity.

3.1.1 Lungcancer

With around 1.6 million deaths world-wide each year, lung cancer is the number one cause of cancer death [197]. Every year about twelve thousand Australians get diagnosed with lung cancer. These cases can be generally split into two groups: small cell lung cancers (SCLC) and non-small cell lung cancers (NSCLC), which account for around 15% and 85% of cases, respectively. The majority of NSCLC are either lung adenocarcinoma or lung squamous cell carcinoma [198]. Even though smoking is highly associated with lung cancers, there is a big group of never smokers, with a high risk of lung cancers in East Asia, especially women, which is correlated with outside influences like pollution and occupational carcinogens and paired with genetic susceptibility [199]. This group usually shows *EGFR* (epidermal growth factor receptor) driven tumours. *EGFR* is a transmembrane receptor tyrosine kinase, which is usually only expressed in epithelial, mesenchymal, and neurogenic tissue, but its overexpression in other tissues is a hallmark of many human malignancies, not just NSCLC.

Even with those strict classifications in place, it is widely accepted, that cancer is a heterogeneous disease, which needs to be accounted for when developing treatments [200]. The ongoing research of lung cancer has led to a shift from cytotoxic chemotherapy to a more personalized approach by accounting for the genetic background of each patient's disease [201]. But not only the inter-patient heterogeneity needs to be taken into account, but also the heterogeneity between different sites of the disease in the same patient [3, 202]. This makes the choice of treatment for one single patient more and more difficult, as some sites might respond to treatment, where another might not. This means, in order to design the perfect treatment regime for a patient, a deep understanding of the

overall complexity of the disease is needed. By studying a diverse background of driver mechanisms of lung cancers and their respective treatment and resistance modes, a general insight in the biologic background is possible. Analysing not only one, but several metastases of the same patients paints a much clearer picture of disease progression and the process behind the resistance to treatment that ultimately lead to death.

3.2 Publications

This chapter includes and reproduces data analysis also shown in two publications, however due to the restriction of the university for sole first author, they are only mentioned here instead of included. The first publication features the resistance mechanism of small cell transformation (“*An Evolutionarily Conserved Function of Polycomb Silences the MHC Class I Antigen Presentation Pathway and Enables Immune Evasion in Cancer*” Burr et al. [203]) of one of the patients and the second shows the discovery of an emerging novel resistance to a targeted RET-fusion driven cancer (“*RET Solvent Front Mutations Mediate Acquired Resistance to Selective RET Inhibition in RET-Driven Malignancies*” Solomon et al. [164]).

3.3 Patient level analysis

This section outlines the work performed for each patient and highlight work specifically done for certain patients due to their unique clinical features. However most of the analysis is streamlined and the workflow applied the same way to each patient. The following sections expand on the individual steps.

1. **Quality control:** Each sample of a patient is checked for kinship and sequencing quality
2. **Read mapping**
3. **Joint somatic variant calling:** SNPs, InDels and SVs are called jointly
4. **Copy number calling**
5. **Variant effect annotation:** short and structural variants are annotated with possible biological effects
6. **Phylogenetic reconstruction**

7. Clonal deconvolution

3.3.1 Analysis workflow

This section summarises the primary analysis performed for each patient in detail. Specific analysis, like RNA analysis are discussed in the individual patient sections.

3.3.1.1 Quality control

When multiple samples per patient are available, the possibility of sample mix-ups and issues is higher than when just dealing with a tumour normal pair, so in addition to the standard read depth, sequencing quality and reads-on-target analysis that is routinely performed after sequencing, we performed an additional step of kinship detection. We use concepts commonly employed in germline cohort analysis, like child and parents (trio) or even large databases (gnomAD). As most germline variants are due to mendelian inheritance, we can use the percentage of shared homo- and heterozygous germline variants to estimate the relatedness of two samples. For our analysis we used NGSCheckMate [204] and all the results shown in later sections are based on it, however we also used Somalier [205] on two patient samples with surprising kinship results but Somalier confirmed the result.

While this analysis is very useful to detect samples which do not belong to a patient, either through mislabelling or similar, it does not protect from mix-ups within a patients samples. However nothing but orthogonal validation will be able to discern these errors.

Other quality controls were performed with fastQC [206] for read integrity and ‘*CollectWgsMetrics*’ from Picard [207] for WGS samples and ‘*samtools flagstat*’ [55] for on-target estimation for WES samples.

3.3.1.2 Read mapping

For highest mapping performance, reads were aligned alternative contig aware with BWA [101] (v0.7.17) to GRCh38 (*GCA_000001405.15*) with alternative contigs but no decoy regions. Initial mapping was post-processed with ‘*bwa-postalt.js*’ from bwa-kit to adjust the mapping assignment and quality mapping both to alternative and canonical contigs. Finally reads were duplicate marked with ‘*MarkDuplicates*’ from the Picard-toolkit.

3.3.1.3 Joint somatic variant calling

For short variants (SNPs and InDels), the workflows presented in [Chapter 2](#) were used and while the Strelka2Pass workflow generates structural variants calls, they are not jointly called over all samples. Instead for the structural variants (SVs) we used GRIDSS2 [208], which has a calling model for multiple related tumour samples and as GRIDSS2 is also a prerequisite for copy number calling with PURPLE ([Section 3.3.1.4](#)) using the same structural variants allows a higher conformity of analysis.

3.3.1.4 Copy number analysis

After somatic variant calling, copy number analysis is a stable when dissecting the resistance and driver alterations of a tumour sample. While lung cancers are known for their high mutational burden [209], often genetic amplifications can be found as driver or resistance mechanism. One of the more common resistance mechanisms is a high *EGFR* or *MET* amplification which significantly affect transcription [210]. And while copy number alterations are often shared between metastases [211], the same heterogeneity that can be found in variant calling analysis also affects copy number analysis. Many modern copy number calling method will use the B-allele frequency , the allele frequency of a heterozygous germline variant, to gain allele specific copy number calls [13, 212, 16]. However each of those methods will only use the input of one tumour and one germline sample, very similar to [Chapter 2](#) we can actually improve the performance by analysing all tumour samples jointly. So far only HATCHet [213] has a joint copy number calling method, requires significant time investment for installation and subjective manual parameter optimisation on a per patient basis. In contrast both sequenza and PURPLE have very easy installation and usage procedures.

Explain why we didnt use hatchet in the end? subjective parameter tuning?

Explain purple vs sequenza for WGS vs WES

3.3.1.5 Variant effect annotation

For small variants (SNPs and InDels) “Variant Effect Predictor“ (VEP) version 92 [19] was used to assign possible effects. As a variant can affect multiple genes due to overlapping gene boundaries, effects within a curated list of lung cancer related genes ([Table B.1](#)) were assigned an ‘IMPACT’ of ‘HIGHEST’ in order with the VEP provided impact values of ‘LOW’, ‘MODERATE’ and ‘HIGH’ . To only have one effect per variant, only the variant with the highest impact was returned. In case of

multiple transcripts being affected with the same impact level, the putative canonical transcript result is used.

For structural variants, the effect annotation depends on the type of the structural variants. For amplifications and deletions, the genes within the variant are compiled and returned as a list. The effect of inversions and similar structural changes are assumed to be fusion based, so the breakpoint is annotated with the gene hit by both breakpoints and a potential fusion gene is returned.

3.3.1.6 Phylogenetic reconstruction

Variants called in any sample were transformed into a binary presence/absence vector with a pure absence vector as the germline native state. The vectors were then concatenated into a string representation, and for each pair the Hamming distance were computed [174]. The distance matrix was used as input for the neighbour joining algorithm and visualised with ape [23].

3.3.1.7 Clonal deconvolution

Clonal deconvolution for each patient was done with PhylogicNDT Cancer cell fractions (CCF) were left to PhylogicNDT with the option ‘*-maf_input_type calc_ccf*’ by supplying the allele specific local copy number call for each variant the same way as shown in [Section 2.4.1](#) with the copy number calls from [Section 3.3.1.4](#). If no copy number was reported for a variant, it was removed from the analysis.

For the clustering of variants all variants with no known protein changing function were included, by removing all variants with the VEP consequence “intergenic_variant”, “intron_variant”, “upstream_gene_variant”, or “downstream_gene_variant”. While these variants certainly might distinguish clones within the sample, they could only arise through random genetic drift and did not relate to resistance mechanisms.

As PhylogicNDT can only visualise 58 distinct clusters, due to the limit of distinct colours, we restricted the analysis after clustering all mutations. Clusters with a variant in one of the 319 driver genes suggested by PhylogicNDT were always retained. All other clusters were automatically removed, if the number of variants n supporting the cluster was smaller than 10, or the CCF value in each sample was too homogeneous, or the confidence interval CI of the CCF value was too high.

The homogeneity of the CCF value of a cluster c was assessed by calculating the z-score of each sample s CCF in respect to all other samples CCF. If one samples z-score indicated a fold change of less than 1.5, the cluster was removed ([Equation 3.1](#)).

$$Inclusion(c) = \begin{cases} \text{FALSE, } & \text{for } n_c(vars) < 10 \\ \text{FALSE, } & \text{for } \forall s : |\text{z-score}(CCF_s)| < 1.5 \\ \text{FALSE, } & \text{for } \forall s : CI(CCF_s) < 0.1 \\ \text{TRUE, } & \text{else} \end{cases} \quad (3.1)$$

3.3.2 Patient CA-A

This patient was a 61 year old male with a metastatic *RET-KIF5B* fusion positive NSCLC. After failure of Carboplatin, Pemetrexed, and Pembrolizumab as well as Lenvatinib, with compassionate access to Selpercatinib (Figure 3.1) he experienced almost immediate improvement with decreased levels of carcinoembryonic antigen and almost 100% reduction of fusion positive ctDNA after one month (Figure 3.2). Similar to the ctDNA analysis, Positron emission tomography-computed tomography imaging revealed significantly reduced tracer uptake in multiple sites and partial response (Figure 3.3).

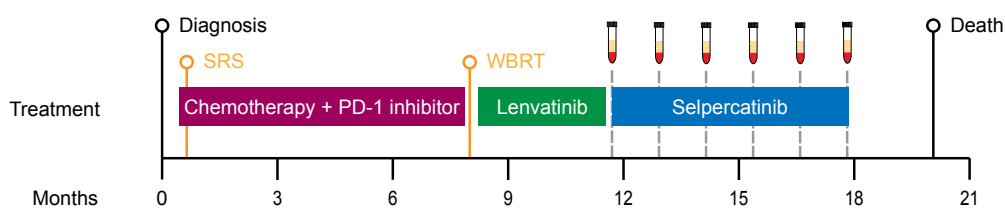


Figure 3.1: Timeline of patient CA-A from diagnosis until death: Diagnostic biopsy detected *KIF5B-RET* positive lung adenocarcinoma; SRS: stereotactic radiosurgery; WRBT: whole brain radiation therapy; a total of six blood samples were taken just before and during the selpercatinib treatment.

Serial sampling of the plasma of the patient and analysis with the commercial Guardant360 assay [214] revealed the previously undetected RET G810S resistance mutation after three months of treatment. While at this point the driver mutation allele frequency was still dropping in the plasma, by month four the abundance of RET G810S had increased and was accompanied by additional mutations in the same site (RET G810R, C and V). In addition with the increase of fusion positive ctDNA this suggests that any mutation in this site affects the efficiency of Selpercatinib. While the patient initially was responsive to the treatment, repeat PET scans showed a progressive disease after six months, which ultimately lead to the death of the patient (Figure 3.3).

At autopsy, 24 tumour tissue biopsies and a post mortem blood sample were collected and eight of them were selected for WGS at 130x coverage (Figure 3.4, Table 3.1) and analysed with the standard workflow (Section 3.3.1).

Somatic variant calling revealed substantial spatial heterogeneity, where both the occipital and the right pleura sample only contained RET G810S, the right liver lobe harboured predominantly RET G810R with either G810S and G810C as minor clones and lastly, the left liver samples showed almost even mix between G810C and G810S clones but no G810R presence. The emergence of these

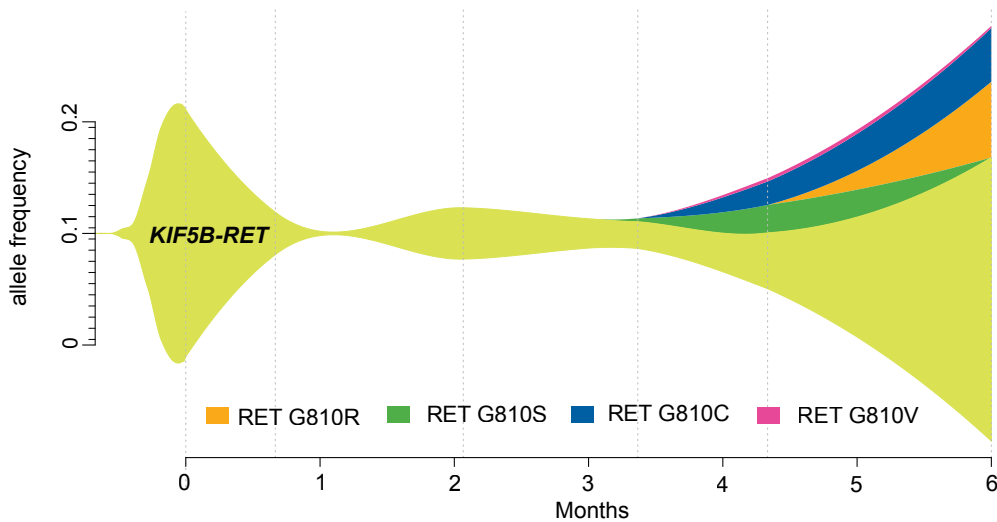


Figure 3.2: Allelic frequencies of driver and emerging resistance mutations during Selpercatinib treatment (11 months after diagnosis); *KIF5B-RET* fusion is the initiating driver with *RET* G810R/S/C/V the emerging resistance SNPs

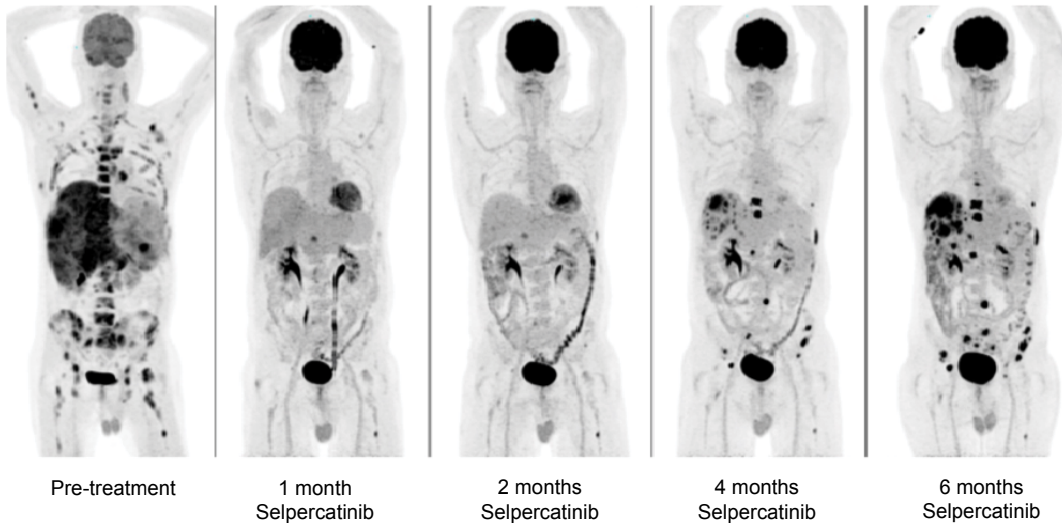


Figure 3.3: PET scans of patient CA-A before and during Selpercatinib treatment

mutations in multiple different sites at different allele frequencies, especially in already established sites in the liver, suggests that these mutations are the result of parallel evolution under positive selection through therapy, rather than seeding from one resistant clone. Apart from the mutations changing RET G810 no other variants affecting *RET* or any other lung cancer genes were found in multiple samples. The occipital sample also contained a BRCA1 V939A mutation and one left liver sample (47) showed a synonymous KIT S967%3D mutation. Additionally, no other variant found in non cancer related genes allowed the same explanation of resistance ([Figure 3.6](#)).

Phylogeny based on the short variants shows a nice clustering into right (26 and 57) and left liver

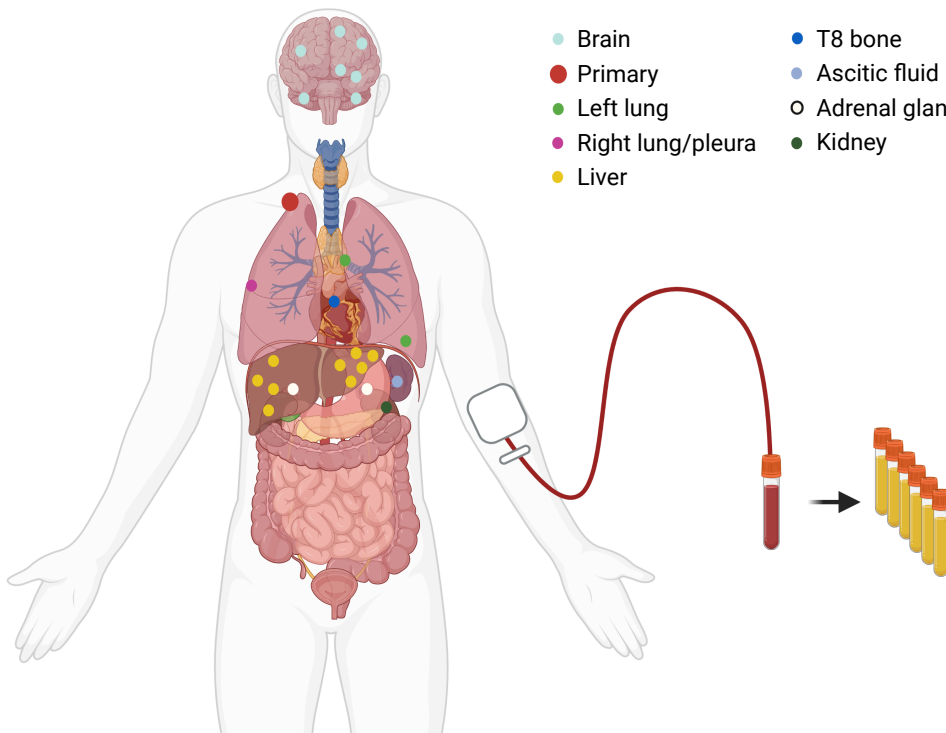


Figure 3.4: Schematic of tumour lesions in patient CA-A: Primary diagnostic sample shown in red; All 24 autopsy samples were coloured by organ they were collected from: Brain (7), left lung (2), right lung (1), liver (9), T8 bone (1), ascitic fluid (1), adrenal gland (2), kidney (1); Additionally to the post mortem blood sample, six serial blood samples were taken ([Figure 3.1](#))

Table 3.1: Autopsy samples sequenced for patient CA-A: Sample number is the internal sample collection during CASCADE autopsy, the organ of the sample, the fraction of tumour cell from H& E stain and the pathology of the tumour sample.

Sample number	Organ	H & E	Type
11	right occipital lobe	0.75	lung adenocarcinoma
26	right liver lobe	0.6	
31	left lower lung	0.2	
41	left liver lobe	0.2	
47	left liver lobe	0.5	
55	left liver lobe	0.4	
57	right liver lobe	0.6	
59	right pleura	0.7	

(41, 47, and 55) with occipital and pleural sample sharing the most mutations as a hint towards the longest evolutionary trajectory and final progression. There also exists a bifurcating line separating progression (11, 41, 47, 55; top right) and stable disease sites. The much lower and higher number of both samples 31 and 41 were due to the low tumour purity of those samples (Tables 3.1 and 3.2, [Figure 3.5](#)).

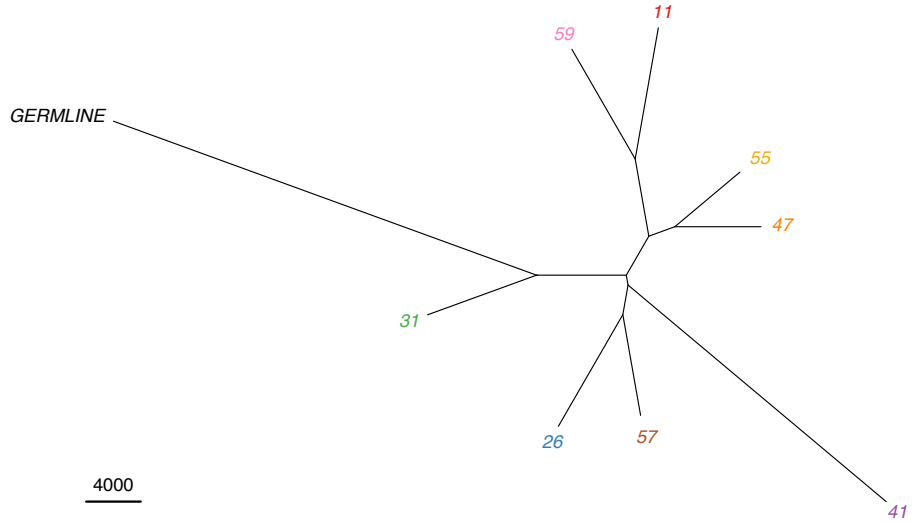


Figure 3.5: Phylogeny of autopsy samples from patient CA-A; reconstructed with all somatic SNVs and InDels. Ruler symbolises 4000 Variants difference

The structural variant calling with GRIDSS showed consistent presence of the *KIF5B-RET* fusion at high allele frequency (min: 0.27 max: 0.535), consistent with cancer cell fraction of 1 when correcting for local copy number changes (min: 2 max: 3; [Figure 3.7](#)), in all but sample 31, which might be due to the low purity of the sample ([Table 3.1](#)). While there is a high number of structural variants present in each sample, consistent with genomic instability in late stages of cancer [189] and wide spread chromosomal rearrangement as a hallmark of cancer [145], most of these rearrangements are sub-clonal and therefore not the main cause of resistance or cancer initiation and rather the result of rampant tumour evolution. To allow a more focused look at structural events and their effect, we restricted the visualisation to events with an allele frequency of 0.2 or higher ([Figures 3.7 and 3.8](#)).

While this change also have a minute effect on the PURPLE copy number calls, which are informed by structural variants, these structural variants will also be sub-clonal and therefore removal will result in a cleaner clonal copy number profile.

[Figures 3.7, B.1, B.3, B.4, B.5, B.6](#) and [B.7](#) show very similar copy number profiles of all tumour samples of patient CA-A, with loss of heterozygosity on almost all chromosomes apart from chromosome 5 and 9, only [Figure B.1](#) shows a less granular mix of gain and loss of the minor allele, which is most likely due to the lower tumour purity of the sample. However, all samples exhibit high copy number gain levels consistent with whole genome duplication ([Tables 3.1 and 3.2](#)). All samples show a copy number gain in chromosome 7 at the *EGFR* locus leading to *EGFR* amplification (min: 3.9 max: 9.9), which is a known resistance mechanism to Levantinib [216] and was therefore most likely a result of previous treatment ([Figure 3.1](#)). Just as expected from the results of the

Guardant360 ctDNA results leading up to the death of the patient, there is no *MET* amplification present in the patient at any site.

Do i need more genes here?

With the absence of any other plausible mechanism, of SNV, SV or CNV nature, the only possible explanation of resistance to Selpercatinib in the patient are the solvent front mutations RET G810C/R/S/V as described in Solomon et al. [164]. However, the autopsy revealed substantial spatial heterogeneity of the emerged resistance mechanisms within the patient which was previously unappreciated.

Table 3.2: Copy number analysis results for patient CA-A: results are taken from the best fit result of PURPLE; WG: whole genome

Sample number	purity	ploidy	polyclonal %	WG duplication
11	0.73	2.86	29.75	True
26	0.61	3.00	26.57	
31	0.21	5.40	49.86	
41	0.28	4.30	42.43	
47	0.46	2.86	29.72	
55	0.38	2.86	38.41	
57	0.61	3.00	28.55	
59	0.69	2.60	37.11	

With the high percentage of likely sub-clonality of samples (Table 3.2) we used PhylogicNDT to

add the phylogicNDT results

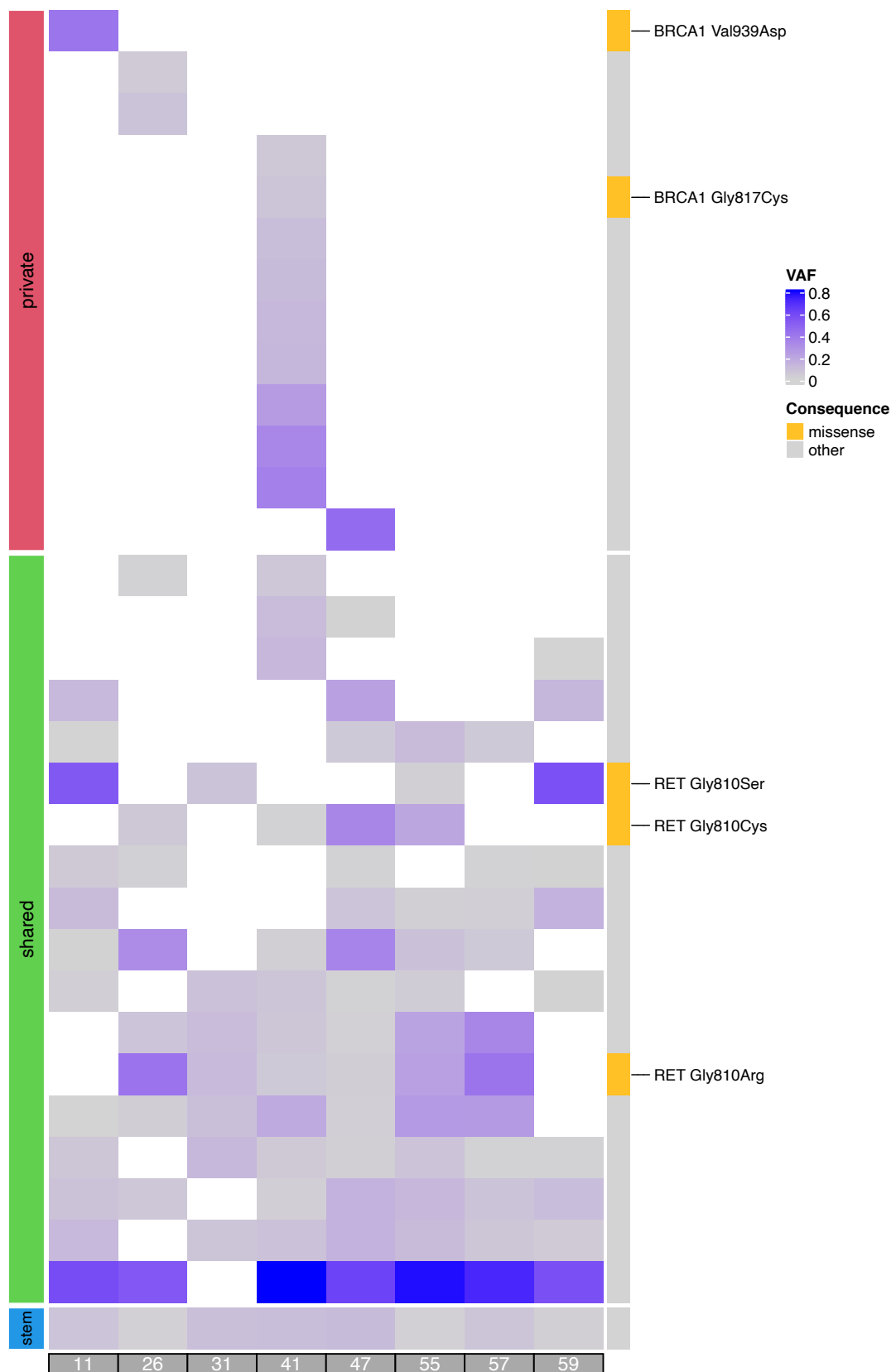


Figure 3.6: Heatmap of driver gene variants in patient CA-A: Protein altering mutations are highlighted with their HGVS notation; non protein altering mutations are grouped as “other“.

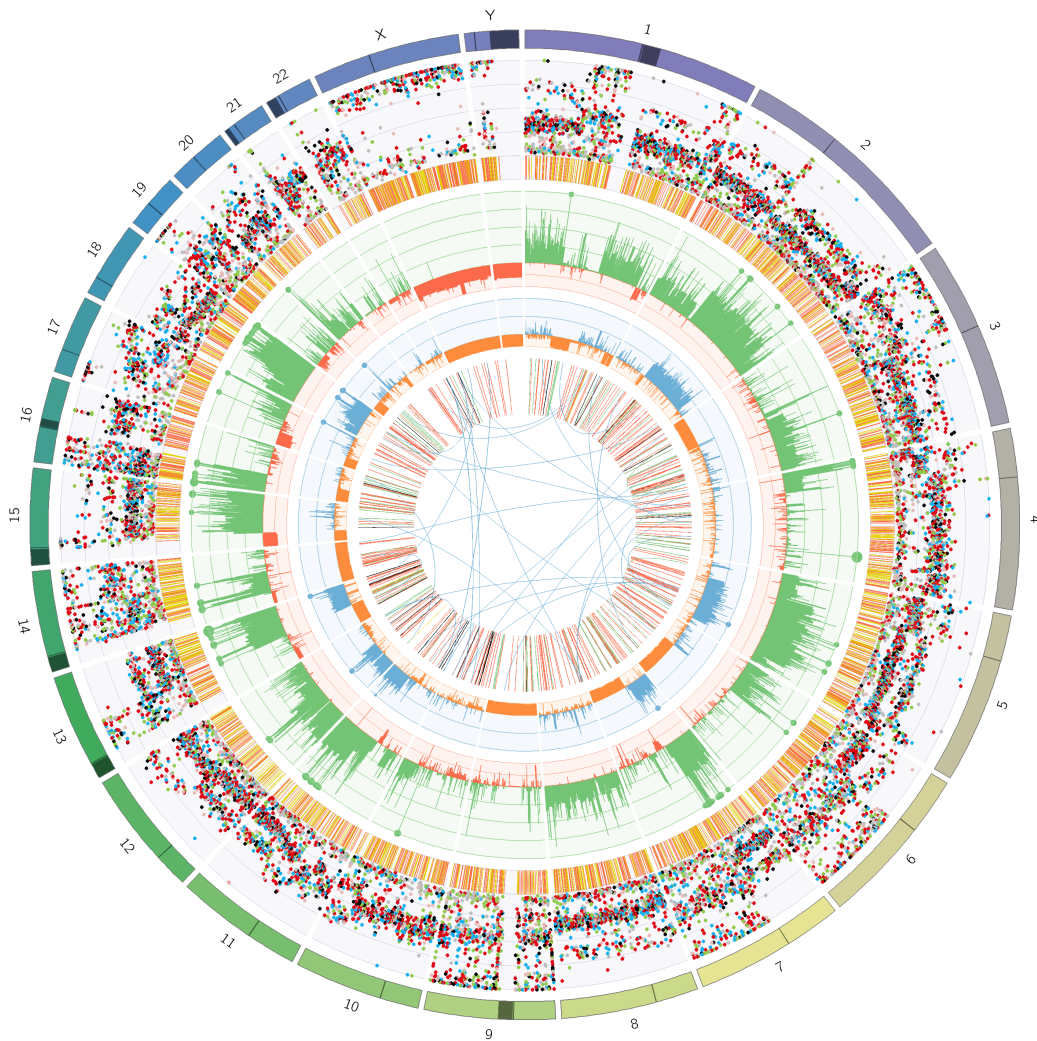


Figure 3.7: Circos plot of patient CA-A with somatic structural variants with allele frequency > 0.2 : outer first ring shows the canonical chromosomes with gaps (centromere, heterochromatin,...) highlighted as darker areas; second ring visualises all somatic SNVs corrected for tumour purity and scaled from 0 to 1, the colour representing the base change of SNV like in Alexandrov et al. [215]; vertical lines directly under the SNVs symbolise InDels, with yellow for insertions and red for deletions; the third ring shows the total copy number alterations, with green showing a copy number gain and red a loss, dots at the outer border show a copy number greater than four; the last ring shows the minor copy number, with blue depicting a gain and orange a loss, this ring allows the detection of copy number neutral changes, like loss of heterozygosity; the center shows all structural variants: translocations in blue, deletions in red, insertions in yellow, tandem duplications in green and inversions in black.



Figure 3.8: Circos plot of patient CA-A with all somatic structural variants: outer first ring shows the canonical chromosomes with gaps (centromere, heterochromatin,...) highlighted as darker areas; second ring visualises all somatic SNVs corrected for tumour purity and scaled from 0 to 1, the colour representing the base change of SNV like in Alexandrov et al. [215]; vertical lines directly under the SNVs symbolise InDels, with yellow for insertions and red for deletions; the third ring shows the total copy number alterations, with green showing a copy number gain and red a loss, dots at the outer border show a copy number greater than four; the last ring shows the minor copy number, with blue depicting a gain and orange a loss, this ring allows the detection of copy number neutral changes, like loss of heterozygosity; the center shows all structural variants: translocations in blue, deletions in red, insertions in yellow, tandem duplications in green and inversions in black.

3.3.3 Patient CA-I

This 56 year old female never smoker presented with *EGFR* exon 19 deletion positive lung cancer in stage with metastatic involvement. After initially good response with Gefitinib treatment, the patient showed progressive nodal disease and was moved to Carboplatin/Gemcitabine chemotherapy with mixed response. After the change to Afatinib small intra-cranial metastases were detected and biopsy of the parasternal mass revealed small cell transformation in addition to the *EGFR* T790M resistance mutation. Subsequent treatment change to Carboplatin/Etoposide as well as CAV (cy clophosphamide, doxorubicin, vincristine) and finally Nivolumab were not successful and the patient died 40 months after diagnosis (Figure 3.9).

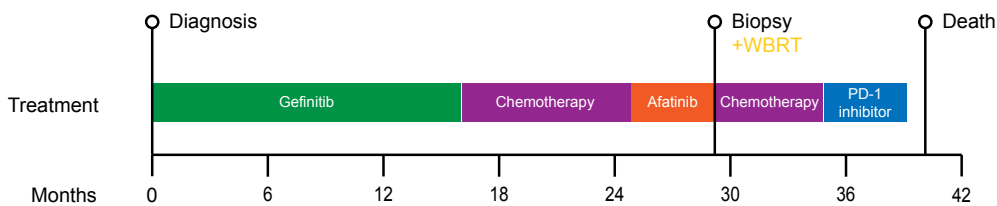


Figure 3.9: Timeline of patient CA-I from diagnosis until death: Diagnostic biopsy detected *EGFR* exon 19 deletion lung adenocarcinoma; Second biopsy after 24 months revealed additional *EGFR* T790M mutation and small cell transformation

At autopsy six lesions and one blood sample were collected and biobanked (Figure 3.10). After quality assessment by pathology with H& E stain, all autopsy samples and the initial diagnostic biopsy were sequenced as WES (Table 3.3) and analysed with the standard workflow (Section 3.3.1). The secondary small cell confirmation biopsy at 29 months did not contain enough tissue for sequencing.

Table 3.3: Autopsy samples sequenced for patient CA-I: Sample number is the internal sample collection during CASCADE autopsy, the organ of the sample, the fraction of tumour cell from H& E stain and the pathology of the tumour sample. Dx: diagnostic sample

Sample number	Organ	H & E	Type
Dx	right VATS	-	adenocarcinoma
557	parasternal mass	0.9	
559	left diaphragm	0.9	
566	right liver lobe	0.6	small cell
573	right hilar lymph node	0.9	
579	left lung lobe	0.8	
583	left pleura	0.9	

Somatic variant calling showed very little genetic heterogeneity. The original *EGFR* exon 19 deletion was present in all sequenced samples from the diagnostic to the 40 months later autopsy samples.

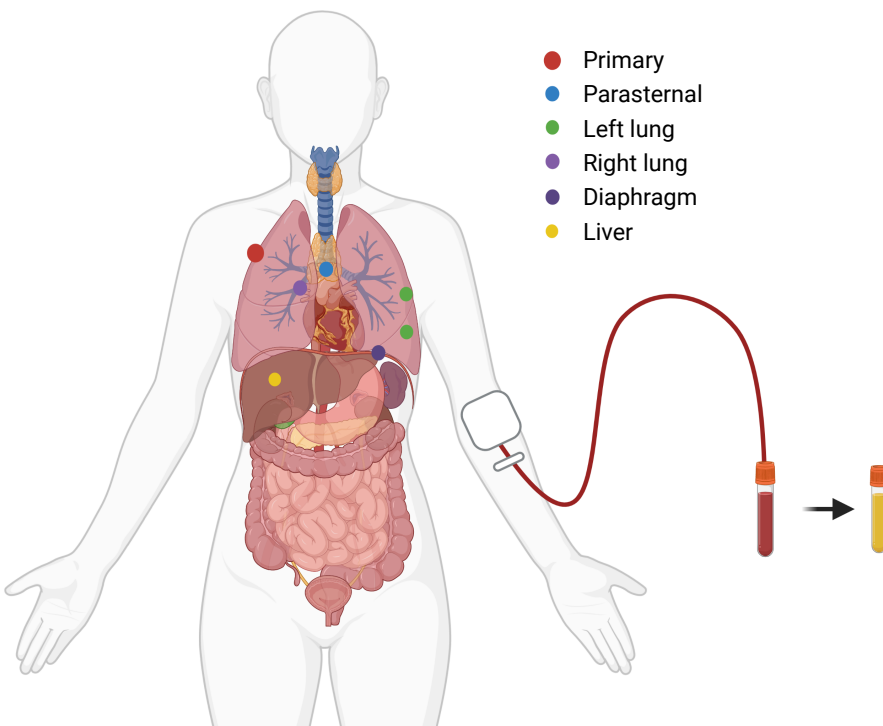


Figure 3.10: Schematic of tumour lesions in patient CA-I: Primary diagnostic sample shown in red; All six autopsy samples were coloured by organ they were collected from: Parasternal (1), left lung (2), right lung (1), diaphragm (1), liver (1); Additionally a post mortem blood sample was taken

No other protein altering somatic mutations were detected at a purity corrected allele frequency ≥ 0.33 . While the diagnostic sample presented with TERT H687Q at 25% VAF with sufficient local copy number amplification, none of the autopsy samples showed any support for this variant. Generally, the number of somatic protein altering SNVs and InDels (min: 988 max: 1236 mean: 1090.5) is very close to the average lung adenocarcinoma with an observed tumour mutational burden of 18.75 [215]. In contrast, the diagnostic sample showed a much higher number of mutations, which we attribute to the formalin-fixed paraffin-embedded (FFPE) preservation, which is known to cause DNA damage [217]. This DNA damage could have led to a higher rate of called somatic variants (Figure B.8). In order to appreciate the relationship of the autopsy samples, we removed the diagnostic sample from the phylogenetic analysis. The full phylogeny can be seen in Figure B.9. The phylogeny of SNVs and InDels shows no internal hierarchical structure, but rather shows that both stem of tumour initiation and additional private mutations accumulated during the disease progression are approximately equal in number, with the stem being slightly longer. Only a very limited amount of somatic variants are shared between cancer samples, which are not part of the initial stem (Figure 3.11). Which is consistent with the clinical history, where there never was any remission, but

only mixed response of already established lesions.

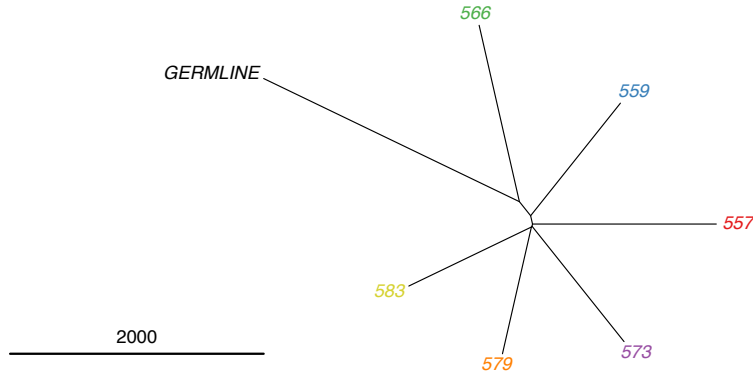


Figure 3.11: Phylogeny of autopsy samples from patient CA-I; reconstructed with all somatic SNVs and InDels. Ruler symbolises 2000 Variants difference. The phylogeny with diagnostic sample can be found in [Figure B.9](#)

Due to the pathology information of small cell transformation, we could highlight an intronic *TP53* mutations, which is present at almost 100% VAF in all autopsy samples. However the same variant was also found in the diagnostic sample, which was reportedly adenocarcinoma. The variant was therefore not sufficient to drive the transformation, but could have been a predisposition for the patient ([Figure 3.12](#)).

When comparing the diagnostic sample with the samples at autopsy the most striking difference is the lower overall copy number gain. The cause of this difference is the amplified minor allele in the diagnostic sample, which is almost completely absent in all autopsy samples. However this amplification in the diagnostic sample could be rooted in the FFPE DNA damage combined with the lower purity of the sample, which in term was used as a sign of amplification of the minor allele after purity correction through sequenza. The consistent feature between all samples, diagnostic and autopsy, is the loss of heterozygosity on chromosomes 2, 4, 10 through 13, and 19. With consistent copy number gains at the end of chromosome 1, 3 and 7 and all of chromosome 5 and 6. The high amplification of chromosome 7 is consistent with the origin of *EGFR* driven primary tumour and the copy number loss of the start of chromosome 17 for all autopsy samples, but only a loss of heterozygosity in the primary sample is consistent with the genetic prerequisites for small cell transformation. ([Figure 3.13](#) vs. Figures [3.14](#), [B.10](#), [B.11](#), [B.12](#), [B.13](#) and [B.14](#) and [Table 3.4](#)).

Clonal deconvolution of somatic variants with PhylogeneticNDT revealed a linear, most likely longitudinal, development of clones adjusting to the changing treatment of the initial clone 1 containing the exon 19 deletion with individual subclones branching off. While the HLA-A disrupting variant in cluster 13 was observed at high frequency in the diagnostic sample, it was out-competed by other

what more
do i write
here? other
drivers?

Table 3.4: Copy number analysis results for patient CA-I: results are taken from the best fit result of sequenza

Sample number	purity	ploidy	WG duplication
Dx	0.29	5.5	True
557	0.93	2.6	False
559	0.96	2.6	False
566	0.69	2.7	False
573	0.94	2.6	False
579	0.95	2.6	False
583	0.95	2.6	False

clones at autopsy, seen as transient cluster 4. Due to the small cell transformation, which correlates with down regulation of major histocompatibility complex (MHC) components, a direct disruption of *HLA-A* was not necessary anymore. Some clones also were only observed in specific sites, like cluster 15 or not found at certain sites (cluster 5) which pointed to high heterogeneity of disease at autopsy (Figures 3.15 and 3.16).

These results agree with the phylogenetic reconstruction which showed initial shared somatic evolution of all sites, with strong individual evolution and limited substructure.

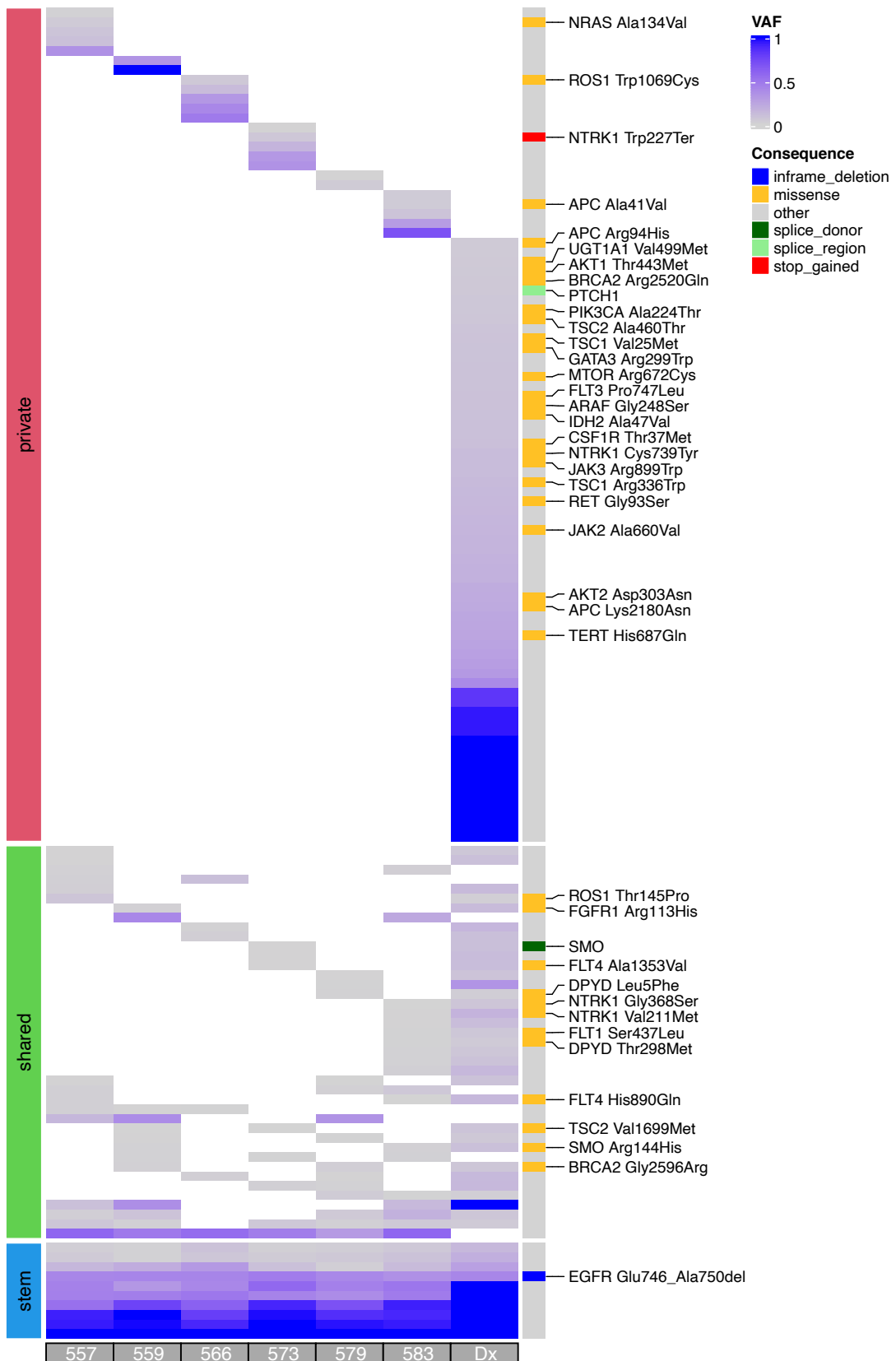


Figure 3.12: Heatmap of driver gene variants in patient CA-I: Protein altering mutations are highlighted with their HGVSp notation; non protein altering mutations are grouped as “other“.

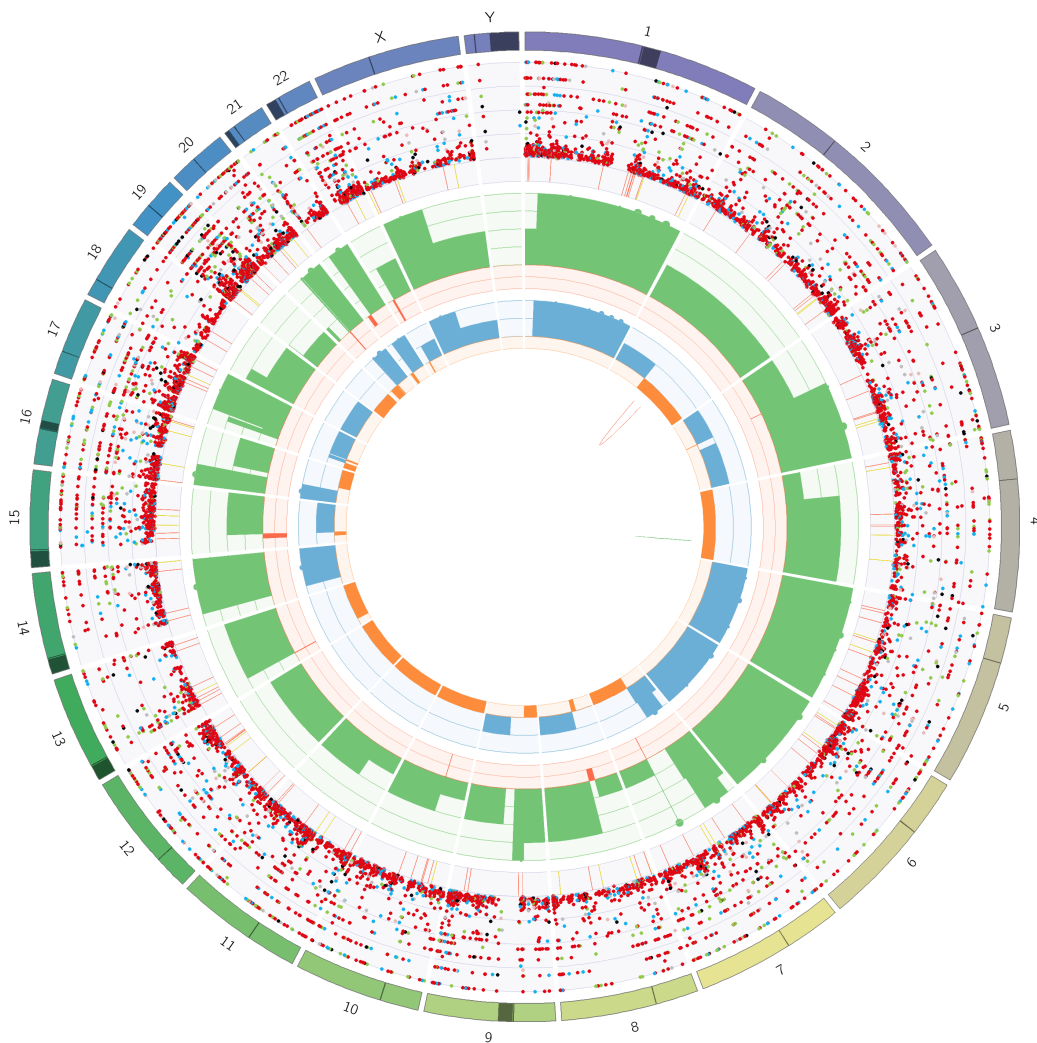


Figure 3.13: Circos plot of patient CA-I sample dx with somatic structural variants: outer first ring shows the canonical chromosomes with gaps (centromere, heterochromatin,...) highlighted as darker areas; second ring visualises all somatic SNVs corrected for tumour purity and scaled from 0 to 1, the colour representing the base change of SNV like in Alexandrov et al. [215]; vertical lines directly under the SNVs symbolise InDels, with yellow for insertions and red for deletions; the third ring shows the total copy number alterations, with green showing a copy number gain and red a loss, dots at the outer border show a copy number greater than four; the last ring shows the minor copy number, with blue depicting a gain and orange a loss, this ring allows the detection of copy number neutral changes, like loss of heterozygosity; the center shows all structural variants: translocations in blue, deletions in red, insertions in yellow, tandem duplications in green and inversions in black.

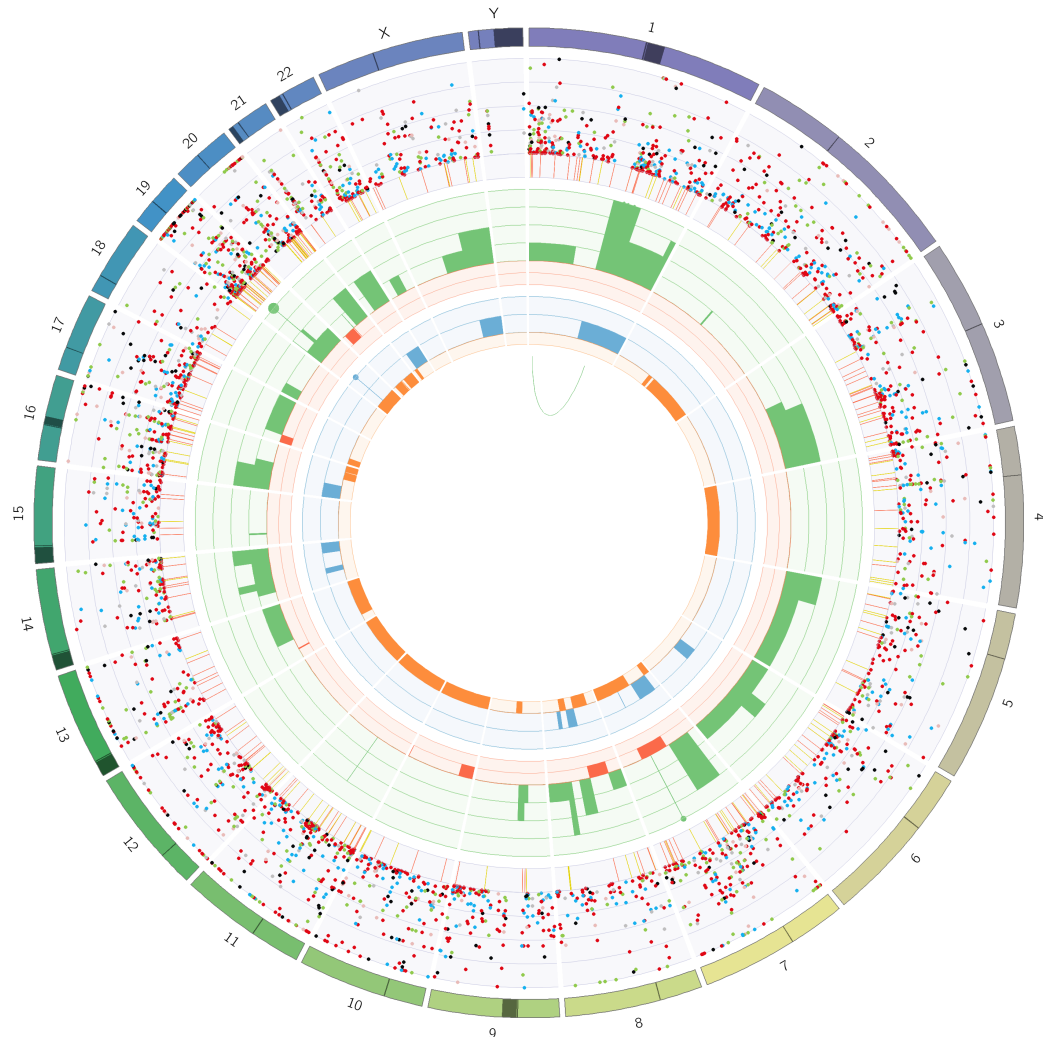


Figure 3.14: Circos plot of patient CA-I sample 557 with somatic structural variants: outer first ring shows the canonical chromosomes with gaps (centromere, heterochromatin,...) highlighted as darker areas; second ring visualises all somatic SNVs corrected for tumour purity and scaled from 0 to 1, the colour representing the base change of SNV like in Alexandrov et al. [215]; vertical lines directly under the SNVs symbolise InDels, with yellow for insertions and red for deletions; the third ring shows the total copy number alterations, with green showing a copy number gain and red a loss, dots at the outer border show a copy number greater than four; the last ring shows the minor copy number, with blue depicting a gain and orange a loss, this ring allows the detection of copy number neutral changes, like loss of heterozygosity; the center shows all structural variants: translocations in blue, deletions in red, insertions in yellow, tandem duplications in green and inversions in black.



Figure 3.15: Clonal evolutionary tree of patient CA-I; Highest support tree for clustered ccf clones generated with PhylogeneticNDT; Support for clone is shown in parenthesis; Major driver alterations of clones were annotated; Clusters with less than 5 supporting variants were discarded; Cluster with 2000 supporting variants only present in sample Dx was discarded as FFPE artefact

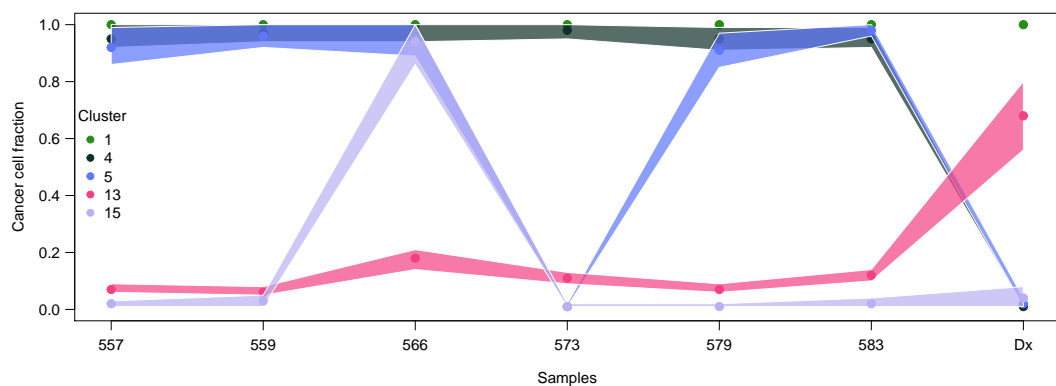
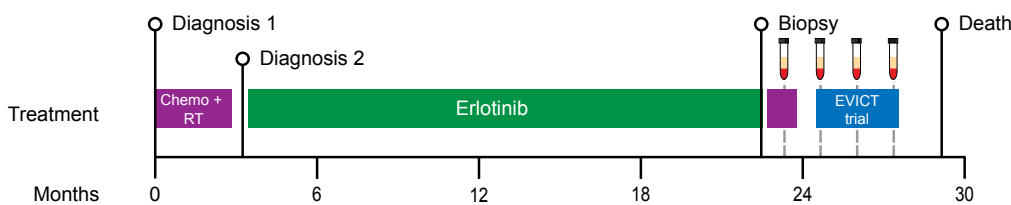


Figure 3.16: Cancer cell fraction of mutation clusters of clonal tree for patient CA-I; transparent polygons show the 95% confidence intervals. Clusters and cluster colours are taken from [Figure 3.15](#)

3.3.4 Patient CA-J

Patient CA-J was a 65 year old female never smoker, who presented with moderately differentiated lung adenocarcinoma (Stage IIIB). Molecular pathology revealed metastatic EGFR L858R positive disease in both the left and the right lungs, the surrounding lymph nodes, the left adrenal gland, multiple bones (T₃, scalp and dura). Initial treatment with both Carboplatin/Paclitaxel and radiotherapy was halted after detection of additional brain, bone and lung lesions and changed to Erlotinib. Progressive pulmonary disease and subsequent left lung core biopsy showed an additional BRAF V600E mutation. Treatment was adjusted to Carboplatin and Pemetrexed however disease still progressed in distant metastasis and recurred in the primary site. The patient was finally enrolled in the EVICT trial treating with both Vemurafenib and Erlotinib, which lead to stable bone metastasis after one month, but ultimately led to progression in both pulmonary and bone metastasis. The patient died 29 months after initial diagnosis ([Figure 3.17](#)).



[Figure 3.17](#): Timeline of patient CA-J from diagnosis until death: Diagnostic biopsy detected EGFR L858R positive stage IIIB lung adenocarcinoma; Second diagnosis after 3 months revealed additional brain, bone and lung metastasis with a reclassification to stage IV; Biopsy at the end of erlotinib treatment revealed additional BRAF V600E mutation; one blood sample was taken during the second round of chemotherapy and three more during the time the patient was enrolled in the EVICT trial

At autopsy 18 sites of disease were resected and biobanked. A representative six samples from different organs and sites were selected and WGS performed after H& E staining confirmed high enough tumour purity ([Table 3.5](#), [Figure 3.18](#)). All WGS samples were analysed with the standard analysis workflow ([Section 3.3.1](#)).

Somatic variant calling revealed heterogeneity of resistance and driver mutations. While the initial driver variant EGFR L858R was present in all autopsy samples at varying allele frequency (min: 0.12, max: 1, median: 1), the secondary BRAF V600E mutation, which was detected in the progression biopsy 22 months after diagnosis, was not present in sample 28 and only at very low allele frequency (0.03) in sample 24. Sample 42 showed the *BRAF* mutation at only 0.61 VAF. While the absence in sample 28 could be explained by the overall low tumour purity of the sample, both 24 and 42

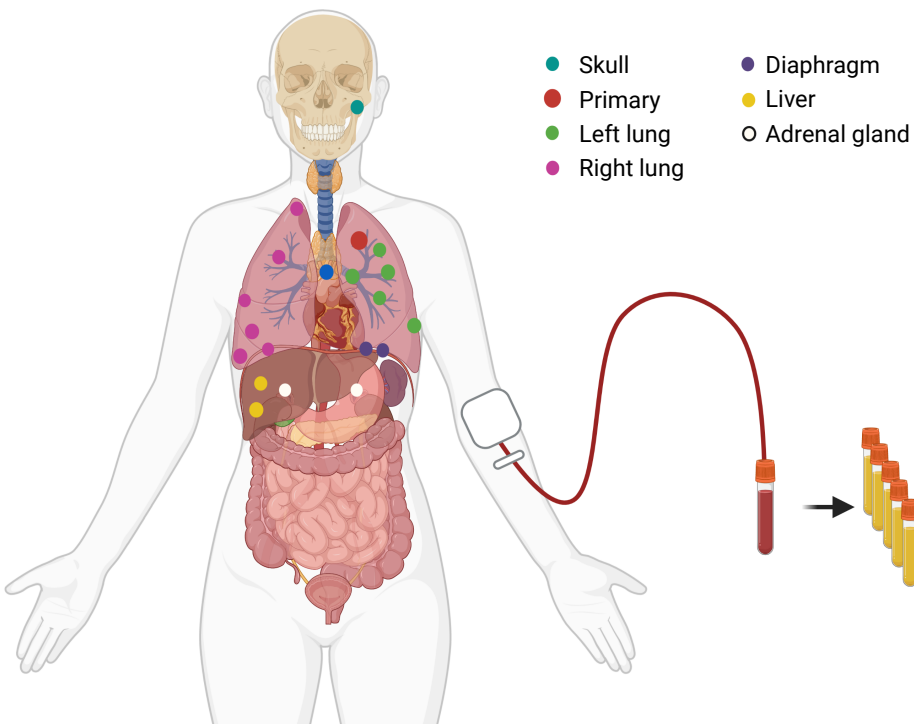


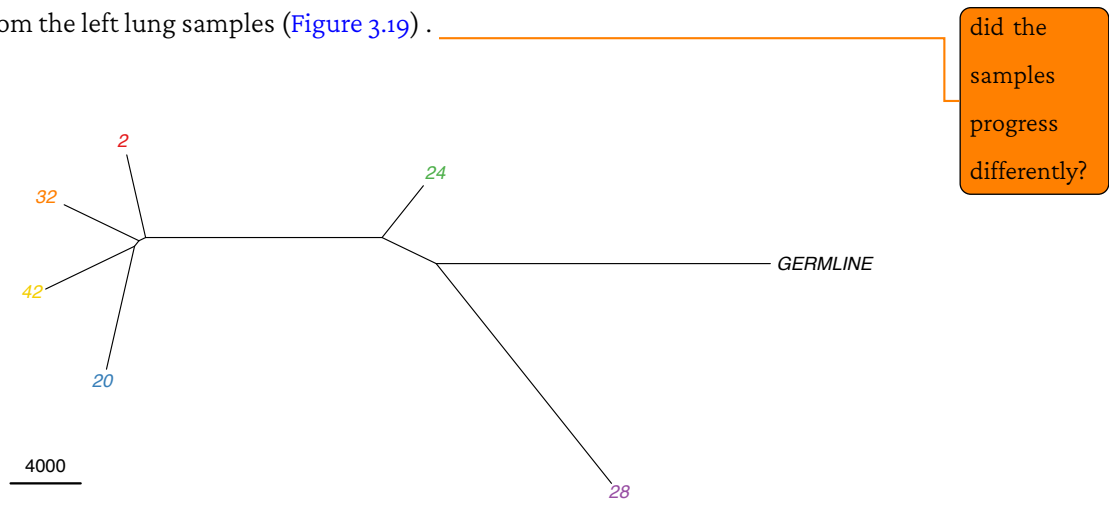
Figure 3.18: Schematic of analysed tumour lesions in patient CA-J: Primary diagnostic sample shown in red; All 18 autopsy samples were coloured by organ they were collected from: skull (1), left lung(5), right lung (6), diaphragm (2), liver(2), adrenal gland (2); Additionally to the post mortem blood sample, four serial blood samples were taken ([Figure 3.17](#))

Table 3.5: Autopsy samples sequenced for patient CA-J: Sample number is the internal sample collection during CASCADE autopsy, the organ of the sample, the fraction of tumour cell from H& E stain and the pathology of the tumour sample. Dx: diagnostic sample

Sample number	Organ	H & E	Type
Dx	left lung core	-	
2	adrenal gland	0.5	
20	right lower lung	0.7	
24	left upper lung	0.9	adenocarcinoma
28	left middle lung	0.5	
32	right upper lung	0.5	
42	base of skull	0.4	

had a higher than 50% tumour purity. The subclonal nature of the *BRAF* shows the importance of accurately measuring the heterogeneity of the disease, as a *BRAF* targeted treatment would have only affected half of the sites analysed in this work. Additionally to the *BRAF* mutation, some sites (2, 20, 32 and 42) developed a “stop gained” mutation in *TP53* (*TP53* G38Ter) at 100% VAF. While both the *BRAF* and *TP53* mutations were present at similar allele fractions in the diagnostic sample (Dx) suggesting a clonal structure, the *TP53* variant was more prevalent at autopsy all samples. So

while *BRAF* and *TP53* mutations were correlated in the diagnostic sample, the *TP53* “stop gained” developed independently. Sample 24 in spite of showing traces of *BRAF* V600E did not develop a *TP53* mutation and sample 28, which did not contain a *BRAF* change instead exhibited two different additional putative driver events (*FLT4* V1097M and *KEAP1* Q282H) which were not observed in any other sample. Finally, Sample 32 also contained a subclonal *KRAS* L5Q mutation in addition to both *BRAF* and *TP53* mutations (Figure 3.20).

The emergence of the *TP53* mutations was a expansion event for samples 2, 20, 32, and 42 differentiating them from the left lung samples (Figure 3.19). 

did the samples progress differently?

Figure 3.19: Phylogeny of autopsy samples from patient CA-J; reconstructed with all somatic SNVs and InDels. Ruler symbolises 4000 Variants difference.

Similar to the short variants, there are some structural variants present in all samples. The inversions on chromosome 12 as well as the co-located break and fusion with the start of chromosome 5 could be observed in all samples, even those with very low tumour purity, but the inversions and fusions of chromosome 7, 8, 9, and 11 can only be seen in the high purity samples 20, 24, 32, and 42 and most were subclonal, as they only have a median allele frequency of 14.3% (min: 10.3%, max: 99.7%). While multiple samples exhibited gene fusions with lung cancer driver and resistance genes like *BRAF*, *FGFR1* and *GNAS* these fusions were only present at subclonal levels $\leq 10\%$.

All samples apart from sample 2 showed whole genome duplication and high polyclonality, which suggests that in addition to the heterogeneity observed through short and structural variants, there was an additional level of heterogeneity of copy number alterations. The lower purity of sample 2 might have been a confounding factor, however both sample 28 and 32 showed lower purities, but a much higher polyclonality. While sample 2 had several minor focal amplifications in *PMS2*, *STK11* and *GADD45B*, no major copy number amplification was found. All other samples showed

amplifications in *KRAS* (min: 2.9, max: 5.0, median: 4.6), *CDK4* (min: 3.2, max: 24.4, median: 21.7) and *BRAF* (min: 2.1, max: 6.0, median: 3.9) in addition to the highly amplified *EGFR* (min: 10.6, max: 266.7, median: 197.4) and *MET* (min: 4.2, max: 6.3, median: 4.6) locus. Both *EGFR* and *MET* copy number gain most likely were the resistance mechanism to the initial treatment with the tyrosine kinase inhibitor Erlotinib. (Figures 3.21, 3.22, B.15, B.16, B.17 and B.18 , Table 3.6).

Table 3.6: Copy number analysis results for patient CA-J: results are taken from the best fit result of PURPLE; WG: whole genome

Sample number	purity	ploidy	polyclonal %	WG duplication
2	0.24	2.00	15.72	False
20	0.40	4.80	44.62	
24	0.73	3.70	32.41	
28	0.18	3.90	42.62	True
32	0.25	4.75	49.71	
42	0.52	3.35	42.16	

Both the somatic variants as well as copy number analysis showed clear signs of a *BRAF* driven tumour with both *BRAF* mutations and amplifications and amplification of *CDK4*. However the patient also displayed potential alternative methods of resistance, like *KEAP1* and *FLT4* mutations

which could only be appreciated analysing multiple sites of the cancer.

add the phylogeneticNDT results when done

maybe include phylogenetic tree?

maybe include ddPCR data during EVICT phase

do i mention the
TP53 mutation here?

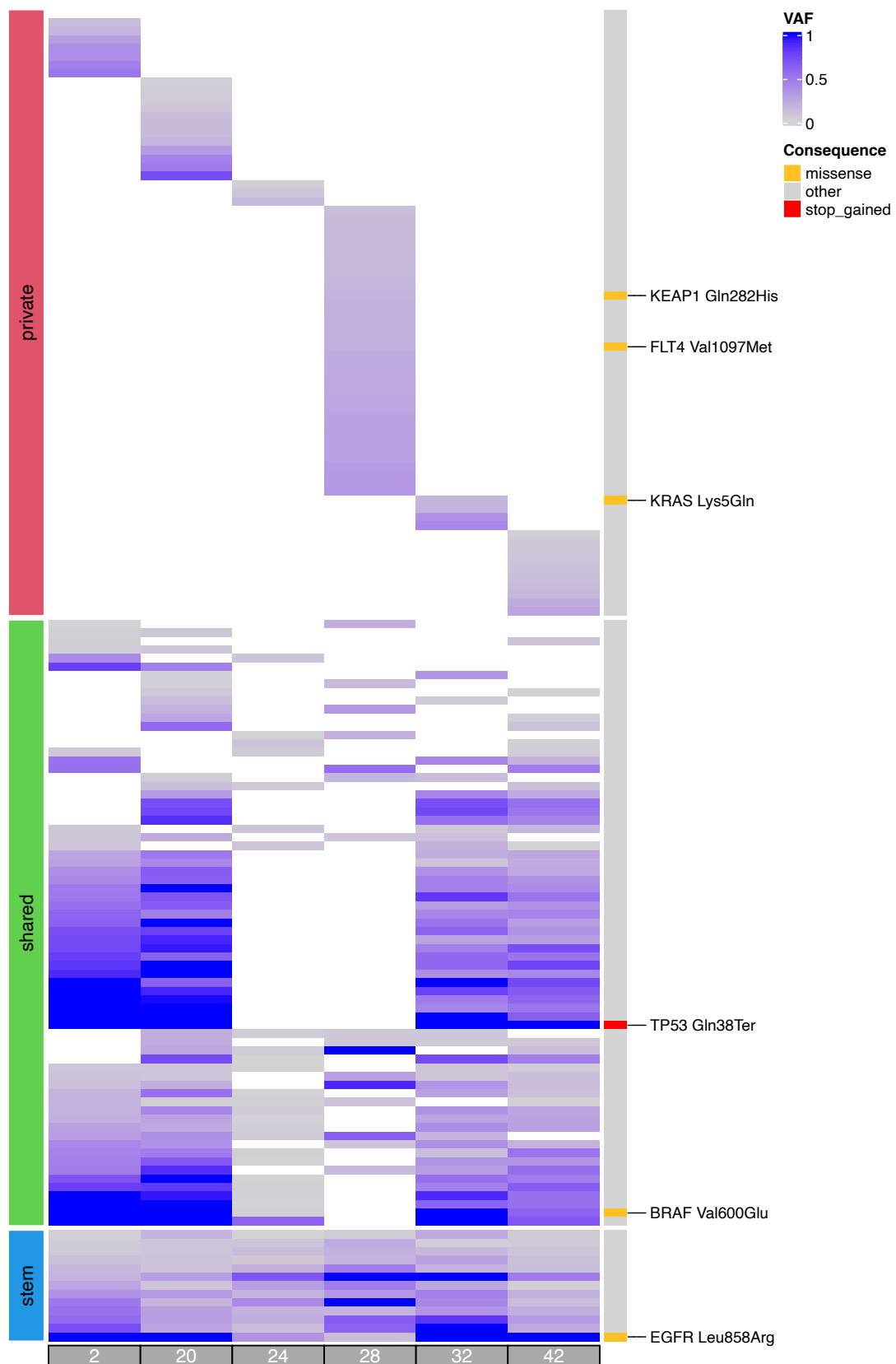


Figure 3.20: Heatmap of driver gene variants in patient CA-J: Protein altering mutations are highlighted with their HGVSp notation; non protein altering mutations are grouped as “other“.



Figure 3.21: Circos plot of patient CA-J sample 2 with somatic structural variants with allele frequency ≥ 0.1 : outer first ring shows the canonical chromosomes with gaps (centromere, heterochromatin,...) highlighted as darker areas; second ring visualises all somatic SNVs corrected for tumour purity and scaled from 0 to 1, the colour representing the base change of SNV like in Alexandrov et al. [215]; vertical lines directly under the SNVs symbolise InDels, with yellow for insertions and red for deletions; the third ring shows the total copy number alterations, with green showing a copy number gain and red a loss, dots at the outer border show a copy number greater than four; the last ring shows the minor copy number, with blue depicting a gain and orange a loss, this ring allows the detection of copy number neutral changes, like loss of heterozygosity; the center shows all structural variants: translocations in blue, deletions in red, insertions in yellow, tandem duplications in green and inversions in black.

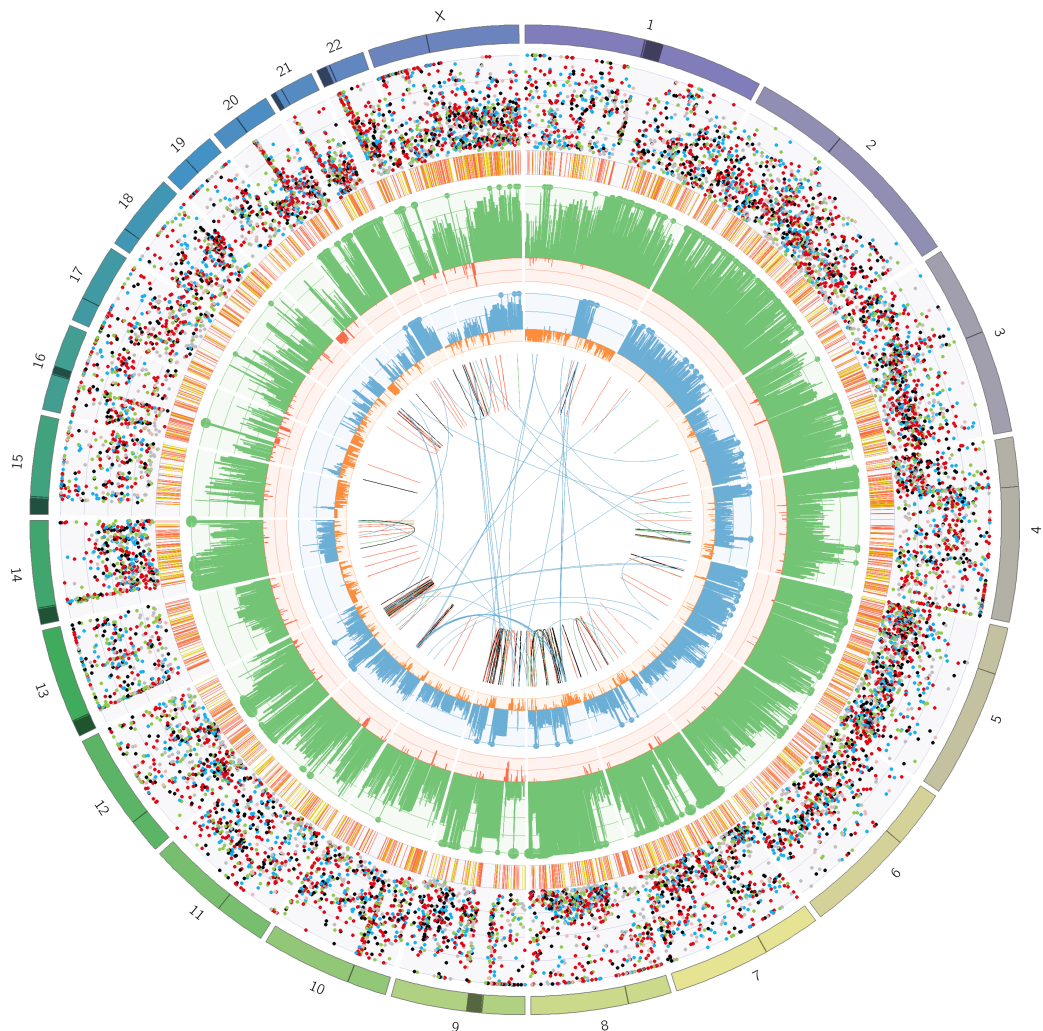


Figure 3.22: Circos plot of patient CA-J sample 20 with somatic structural variants with allele frequency ≥ 0.1 : outer first ring shows the canonical chromosomes with gaps (centromere, heterochromatin,...) highlighted as darker areas; second ring visualises all somatic SNVs corrected for tumour purity and scaled from 0 to 1, the colour representing the base change of SNV like in Alexandrov et al. [215]; vertical lines directly under the SNVs symbolise InDels, with yellow for insertions and red for deletions; the third ring shows the total copy number alterations, with green showing a copy number gain and red a loss, dots at the outer border show a copy number greater than four; the last ring shows the minor copy number, with blue depicting a gain and orange a loss, this ring allows the detection of copy number neutral changes, like loss of heterozygosity; the center shows all structural variants: translocations in blue, deletions in red, insertions in yellow, tandem duplications in green and inversions in black.

3.3.5 Patient CA-K

69 year old male patient presented with multifocal adenocarcinoma without distant metastasis. The most PET avid location (left upper lung) was designated the primary site over the two other less avid locations (right upper lung and left lower lung). Initial treatment with Gefitinib was stopped when the dominant lung lesion and a hilar node lesion showed signs of progression and changed to Afatinib. A CT scan after 50 months showed a mild increase at the primary site, stable disease in satellite nodules and no new metastatic sites. After short treatment with Erlotinib, molecular pathology of a biopsy revealed the acquired EGFR T790M resistance mutation. Enrolment in the CLOVIS trial with Rociletinib and Chemotherapy was ceased due to disease progression. Biopsy 2 confirmed the T790M mutation and therapy with Osimertinib was started, which led to slowly progressive disease. Due to new intracranial disease, increase in lung and renal disease treatment was switched to Nivolumab, but no remission was achieved and the patient died after 103 months (Figure 3.23).

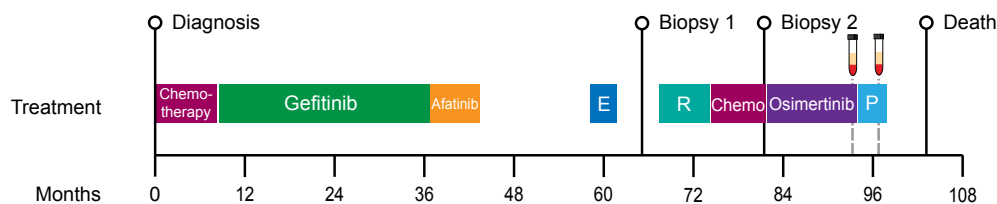


Figure 3.23: Timeline of patient CA-K from diagnosis until death: Diagnostic biopsy detected EGFR L858R positive lung adenocarcinoma; Biopsy 1 after 66 months showed additional EGFR T790M mutation; Biopsy 2 showed no additional variants; one blood sample was taken towards the end of Osimertinib treatment and one second one during PD-1 checkpoint blockade treatment. E: Erlotinib; R: Rociletinib; P: PD-1 inhibitor

At autopsy 18 sites were resected and biobanked and seven high quality representative samples from different organs were selected for WGS (Figure 3.24, Table 3.7) and analysed with the standard workflow (Section 3.3.1).

ddPCR/AVENIO on plasma with AKT1?

Joint somatic variant calling on all autopsy samples revealed significant genetic heterogeneity on Resistance mechanisms present at each site. While the initial EGFR L858R mutation was still present in all sequenced lesions, the left lower lung sample (8) was the only one with a homozygous variant. All other samples presented with 50% VAF for the activating mutation. Biopsy 1, 66 months after diagnosis, showed additional EGFR T790M mutation, but at autopsy sample 1 (adrenal gland) did

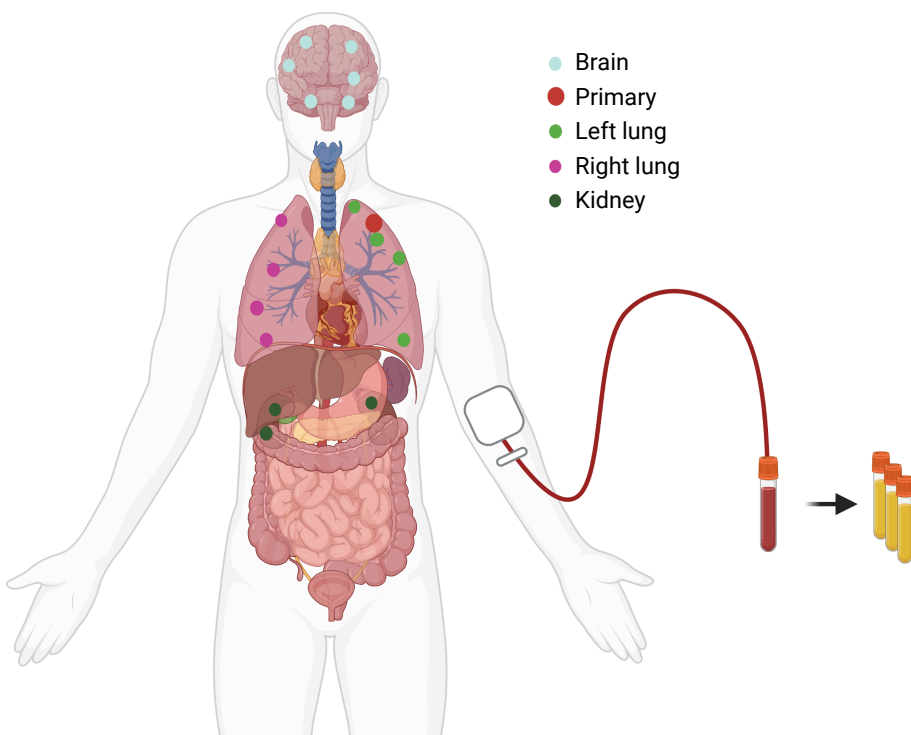


Figure 3.24: Schematic of analysed tumour lesions in patient CA-K: Primary diagnostic sample shown in red; All 17 autopsy samples were coloured by organ they were collected from: Brain (6), left lung (4), right lung (4), kidney (3); Additionally to the post mortem blood sample, two serial blood samples were taken (Figure 3.23)

Table 3.7: Autopsy samples sequenced for patient CA-K: Sample number is the internal sample collection during CASCADE autopsy, the organ of the sample, the fraction of tumour cell from H& E stain and the pathology of the tumour sample. Dx: diagnostic sample

Sample number	Organ	H & E	Type
Dx	left lung core	?	
1	right kidney	?	
4	right upper lung	?	
5	right lower lung	?	
6	right middle lung	?	adenocarcinoma
8	left lower lung	?	
9	left upper lung	?	
13	left brain	?	

not show evidence of the mutation at all and samples 8, 9, and 13 (left lung and brain) only exhibit the variant at subclonal (< 30% VAF). Either the mutation was already subclonal at biopsy, or the resistance was out-competed by a different clone due to the Osimertinib treatment which targets T790M. The adrenal gland lesion, which did not contain the T790M mutation, instead presented

with two other clonal EGFR mutations (S720T and L718Q) which are both known resistant mechanisms to Osimertinib and Dasatinib [218, 219].

Additionally the mutations AKT1 G17L and APC E190Ter bifurcate the the autopsy samples into two groups, because the variants are mostly mutually exclusive, where only samples 8 and 9 showed both the stop gained APC mutation at 100% VAF with very low VAF of the *AKT1* mutation. Furthermore, several *EGFR* mutations also showed different spatial clonal abundance. Multiple samples exhibited different C797 substitutions both of which are known resistance mechanisms to Osimertinib [220, 221]: Sample 4 contained the EGFR C797G mutation at 7% VAF whereas samples 6, 8, and 9, had a C797S mutation at 1%, 14%, and 22% VAF respectively. However, while 8 shared the sample protein change (C797S) the genomic change is different to both sample 6 and 9. Only sample contained EGFR L792H as subclonal mutation at 11% VAF and both sample 1 and 6 contained a minor clonal EGFR S720T, known resistance mechanisms [218, 222]. Additionally to the adrenal sample both lower and middle lower lung samples contained EGFR L718Q. Lastly, all but sample 8 contain the *SMAD4* frameshift mutation at a median cancer cell fraction of 73% (min: 16%, max: 100%) (Figure 3.26).

These splits nicely grouped the samples according to their organ of origin right kidney (1) and left brain (13) as outliers and left (8 and 9) and right lung (4, 5, and 6) (Figure 3.25).

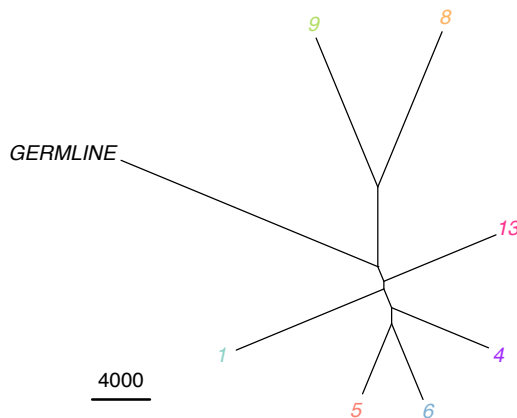


Figure 3.25: Phylogeny of autopsy samples from patient CA-K; reconstructed with all somatic SNVs and InDels. Ruler symbolises 4000 Variants difference

Similar to the short variants, structural variants and copy number changes also showed a difference between samples 8 and 9 with the rest. While all samples show inversions on chromosome 6, 8 and 9 with fusions between chromosome 1 and 18, chromosome 6 and 8 and chromosome 8 and 9, samples 8 and 9 also showed a fusion of chromosome 3 with 18 and additional inversions on chromosome 18. The additional inversions and haploinsufficiency directly affect *SMAD4*. These

structural changes complemented the “missing” *SMAD4* frameshift mutation in these samples and suggested a key role of *SMAD4* in the resistance to treatment.

Samples 8 and 9 were the only samples in the patient with significantly amplified copy numbers resulting in a whole genome duplication, however they still exhibited the same pattern of loss of heterozygosity. In all samples we observed a copy number gain in the q arm of chromosome 1 amplifying both *NTKR1* and *DDR2* with a loss of heterozygosity for *NRAS* and *MTOR* on the p arm of the same chromosome. The loss of heterozygosity presented in all samples on chromosome 3 reduces the representation of *TM4SF1*, *PIK3CA*, and *USP13*, however in both sample 8 and 9 the other chromosome is amplified leading to a copy number neutral area. The loss of heterozygosity on chromosome 5 leads to a haploinsufficiency for *APC*, *PIK3R1*, *CSF1R*, *PDGFRB*, and *FLT4* for all samples, which combined with the stop mutation in samples 8 and 9 is suggestive of a common resistance pathway. The loss of heterozygosity on chromosome 8 affected *TUSC3* and *FGFR1*. No lung cancer driver genes were affected by the loss of heterozygosity on chromosome 15. The seemingly heterozygous loss of chromosome X had the loss of *ARAF* and *AR* as a consequence, but the loss must be subclonal given the sex of the patient was male. Lastly, the additional copy number loss only present in both samples 8 and 9 affected *JAK2*, *CD274*, and *PDCD1LG2* and these samples also show *EGFR* amplification in contrast to all other samples (Figures 3.27, B.19, B.20, B.21, 3.28, B.22 and B.23, Table 3.8).

Table 3.8: Copy number analysis results for patient CA-K: results are taken from the best fit result of PURPLE; WG: whole genome

Sample number	purity	ploidy	polyclonal %	WG duplication
1	0.78	1.84	7.62	False
4	0.48	1.84	4.80	False
5	0.58	1.88	1.02	False
6	0.79	1.86	6.93	False
8	0.30	3.40	6.44	True
9	0.69	3.45	8.32	True
13	0.47	1.90	0.05	False

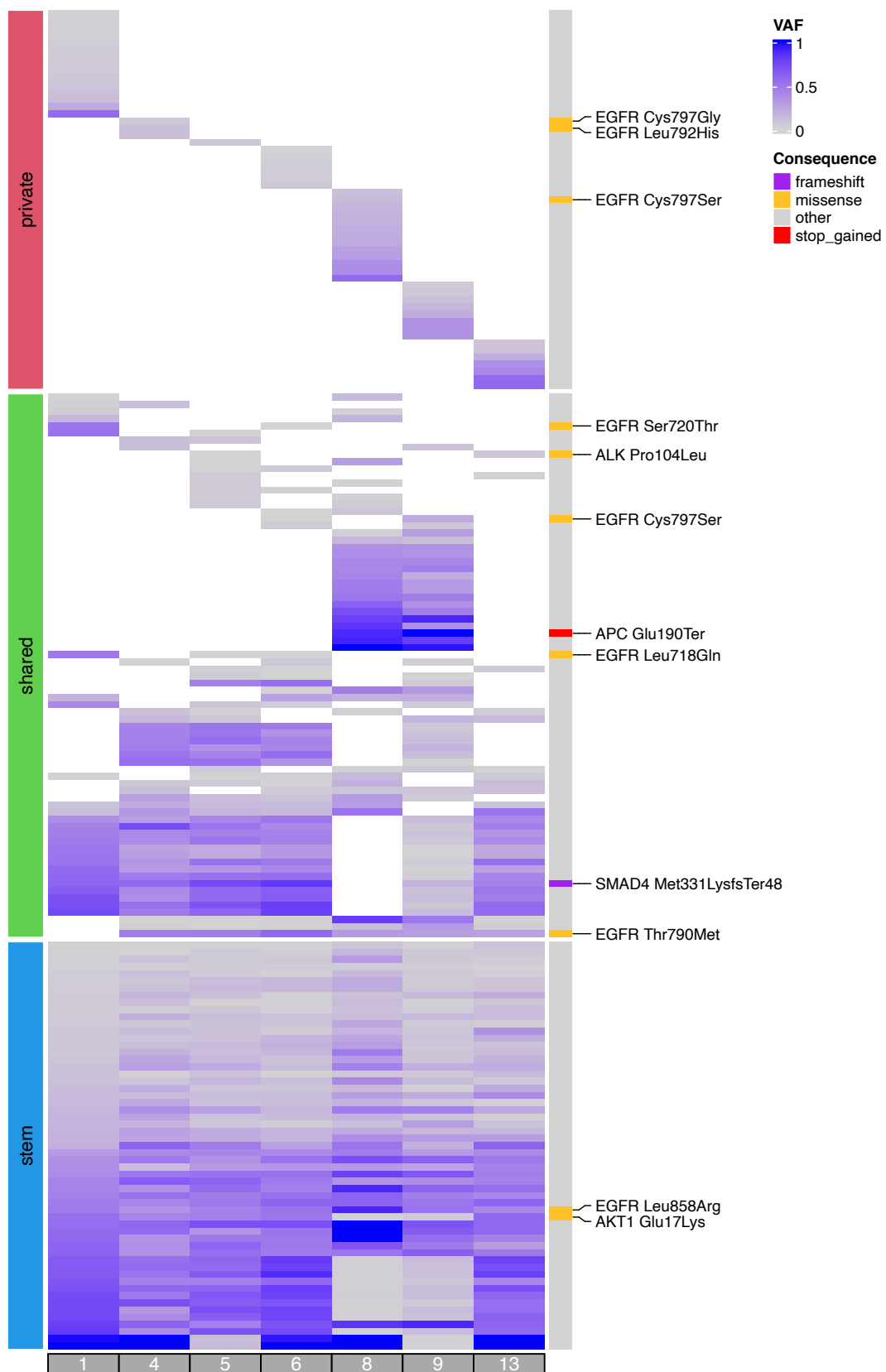


Figure 3.26: Heatmap of driver gene variants in patient CA-K: Protein altering mutations are highlighted with their HGVSp notation; non protein altering mutations are grouped as “other“.



Figure 3.27: Circos plot of patient CA-K sample 1: outer first ring shows the canonical chromosomes with gaps (centromere, heterochromatin,...) highlighted as darker areas; second ring visualises all somatic SNVs corrected for tumour purity and scaled from 0 to 1, the colour representing the base change of SNV like in Alexandrov et al. [215]; vertical lines directly under the SNVs symbolise InDels, with yellow for insertions and red for deletions; the third ring shows the total copy number alterations, with green showing a copy number gain and red a loss, dots at the outer border show a copy number greater than four; the last ring shows the minor copy number, with blue depicting a gain and orange a loss, this ring allows the detection of copy number neutral changes, like loss of heterozygosity; the center shows all structural variants: translocations in blue, deletions in red, insertions in yellow, tandem duplications in green and inversions in black.



Figure 3.28: Circos plot of patient CA-K sample 8: outer first ring shows the canonical chromosomes with gaps (centromere, heterochromatin,...) highlighted as darker areas; second ring visualises all somatic SNVs corrected for tumour purity and scaled from 0 to 1, the colour representing the base change of SNV like in Alexandrov et al. [215]; vertical lines directly under the SNVs symbolise InDels, with yellow for insertions and red for deletions; the third ring shows the total copy number alterations, with green showing a copy number gain and red a loss, dots at the outer border show a copy number greater than four; the last ring shows the minor copy number, with blue depicting a gain and orange a loss, this ring allows the detection of copy number neutral changes, like loss of heterozygosity; the center shows all structural variants: translocations in blue, deletions in red, insertions in yellow, tandem duplications in green and inversions in black.

3.3.6 Patient CA-L

This 68 year old female ex-smoker presented with *EGFR* mutant NSCLC, however after 12 months of the treatment with the *EGFR* inhibitor Erlotinib a transformation to small cell lung cancer (SCLC) was detected. While previously it was thought that the different subsets of lung cancers are distinct, more and more evidence is found showing neuroendocrine transformation as a resistance mechanism to targeted therapies not only in lung but also in prostate cancers [223, 224]. The treatment was altered to chemotherapy and PD-1 inhibitors, however due to the loss of MHC-I antigen presentation of small cell lung cancer, the tumour failed to respond [203] and the patient died after 29 months (Figure 3.29).

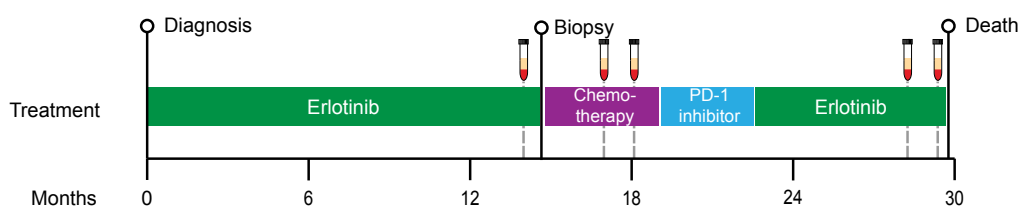


Figure 3.29: Timeline of patient CA-L from diagnosis until death: Diagnostic biopsy detected *EGFR* exon 19 deletion positive lung adenocarcinoma; Biopsy after 15 months Erlotinib treatment showed signs of small cell transformation; blood samples were taken at the end of the first Erlotinib treatment, during the chemotherapy treatment and 28 and 29 months after the initial diagnosis.

During autopsy 25 lesions were resected and biobanked and representative samples, both adenocarcinoma and small cell carcinoma according to histology, were selected for WES (Figure 3.30, Table 3.9) and analysed with the standard workflow (Section 3.3.1). For granular analysis of the transition from adenocarcinoma to small cell carcinoma, the progression sample after 15 months (P) was dissected to the individual types based on histology staining.

Table 3.9: Autopsy samples sequenced for patient CA-L: Sample number is the internal sample collection during CASCADE autopsy, the organ of the sample, the fraction of tumour cell from H&E stain and the pathology of the tumour sample. P.1/2: micro-dissected progression biopsy (80% small cell, 20% adenocarcinoma)

Sample number	Organ	H & E	Type
P.1	right lung core	>0.9	small cell
P.2	right lung core	>0.9	adenocarcinoma
8	right upper lung	0.9	small cell
17A	left lower lung	-	poorly differentiated adenocarcinoma
26	right kidney	1	adenocarcinoma

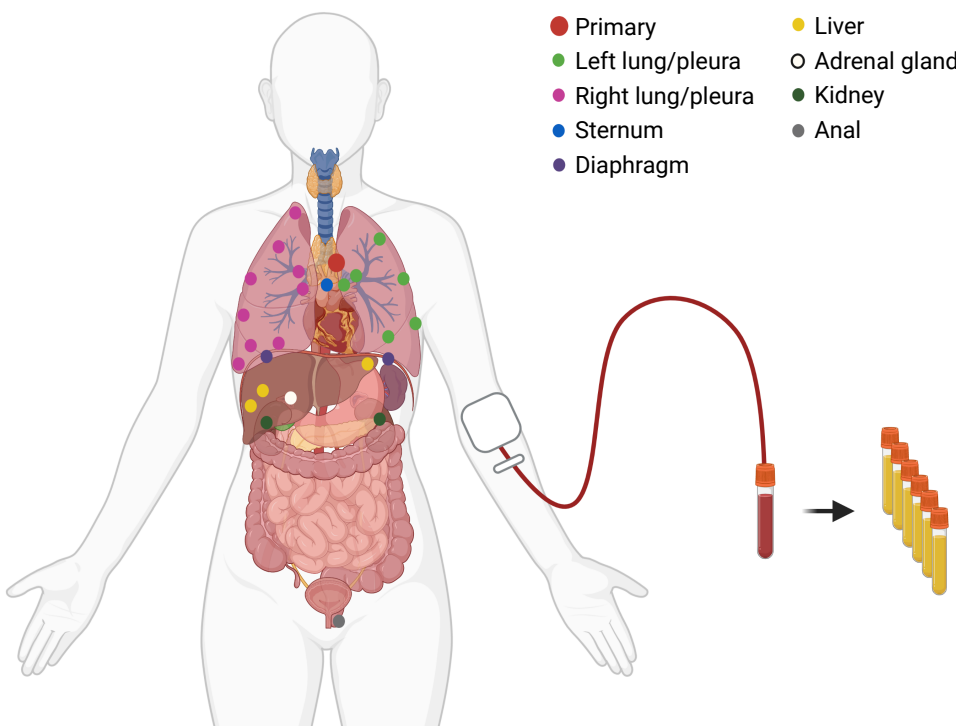


Figure 3.30: Schematic of analysed tumour lesions in patient CA-L: Primary diagnostic sample shown in red; Samples are coloured by organ they were collected from: left lung (6), right lung (9), sternum (1), diaphragm (2), liver (3), adrenal gland (1) kidney (2), anal (1); Additionally to the post mortem blood sample, five serial blood samples were taken ([Figure 3.29](#))

Even though not all samples had changed from adeno- to small cell carcinoma, all samples showed the *TP53* “stop gained” mutation at 100% VAF. This shows, that while a *TP53* mutation was not sufficient for the histological transformation [225]. Unsurprisingly, the samples that remained adeno (17A and 26) show a higher dependency on *EGFR* which led to higher clonal abundance of the initial *EGFR* exon 19 deletion and a subsequently higher VAF of EGFR T790M, while the small cell transformed lung sample (8) acquired a secondary *TP53* M40I mutation. No additional variants were close to clonal representation ([Figure 3.32](#)).

Surprisingly even though the samples were taken at different times (one at progression and one at autopsy) the small cell transformed samples P.1 and 8 were evolutionary closer related and shared more variants, than to the samples taken at the same time. In contrast, the two adenocarcinoma samples taken at autopsy were clustered together. Additionally, the split of sites of small cell transformation and adenocarcinoma already had happened before the progression sample and the small cell transformed samples appeared to be evolutionary different from samples 17A and 26, seen by the split in two directions following split into small cell and non-small cell samples after the edge

leading to P.2. In general, the phylogeny suggested the presence of at least 3 distinct trajectories: one giving rise to the adeno sample at progression (P.2), one resulting in the small cell sample P.1 and its longitudinal successor sample 8 and lastly the two adenocarcinoma samples 17A and 26 (Figure 3.31).

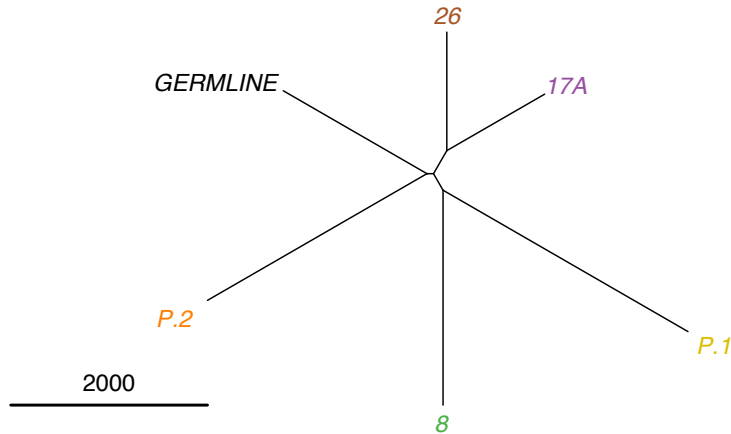


Figure 3.31: Phylogeny of samples from patient CA-L; reconstructed with all somatic SNVs and In-Dels. Ruler symbolises 2000 Variants difference.

Copy number analysis with sequenza revealed a high prevalence of loss of heterozygosity in all samples, but both sample P.2 and 8 showed almost no copy number gains on chromosome 9 and 10 with 8 even extending through to 12. In general small cell transformed samples showed a higher level of copy number gain than the original adenocarcinoma. The difference in copy number in the two spatially intertwined types of cancers can only be attributed to the small cell transformation. Additionally to the increased overall ploidy of the small cell sample P.1 over P.2 (Table 3.10), P.2 also lost chromosome X completely (Figure 3.33 vs. Figure 3.34). Interestingly, the small cell samples still have the same high amplification level of EGFR seen in the adenocarcinoma samples (min: 6 max: 13) suggesting the transformation did not remove EGFR based signalling. While commonly small cell transformation is associated with RB1 loss, the locus was amplified in all samples with a loss of heterozygosity. As this patient's sequencing was restricted to exonic regions, we could not rule out a regulatory defect. Interestingly, while the small cell transformed part of the progression sample (P.1) showed a heterozygous loss of chromosome X, the adenocarcinoma part (P.1) showed an almost complete loss of chromosome X, which could not be observed in any of the autopsy samples, which instead show and amplification. This indicated, that the small cell transformation happened at multiple sites instead of being spread after the transformation (Figures 3.33, 3.34, B.24, B.25 and B.26), .

Table 3.10: Copy number analysis results for patient CA-L: results are taken from the best fit result of sequenza

Sample number	purity	ploidy	WG duplication
P.1	0.86	3.3	True
P.2	0.27	2.1	False
8	0.96	3.1	True
17A	0.18	4.2	True
26	0.28	3.7	True

Clonal deconvolution with PhylogicNDT showed a presence of cluster 7, which is barely present at autopsy showing a massive clonal restructure in the time between the progression samples P.1 and P.2 and the autopsy. The two small cell samples also share cluster 5, which was also present in the adeno part of the progression sample, but not in the adenocarcinoma samples at autopsy. Additionally cluster 8 with the EGFR T790M mutation was present at progression and was still a major clone at autopsy in samples 17A and 26 due to the adenocarcinomas dependence on EGFR. For P.2, the mixture of both Cluster 5 and 8 suggested, that even though the dissection was histologically guided, the supposedly adenocarcinoma sample P.2 still had genetical small cell carcinoma markers. the almost 100% cancer cell fraction (CCF) clusters 11 and 12 show that each site had accumulated and selected somatic mutations distinguishing the autopsy samples from each other and the progression samples. Due to the low abundance and high amount of supporting variants of both cluster 16 and 14 and their exclusivity to P.1 and P.2 respectively, we contributed these clusters to the FFPE preservation of the samples (Figures 3.35 and 3.36).

maybe talk about the RNAseq data with RB1 loss in some areas

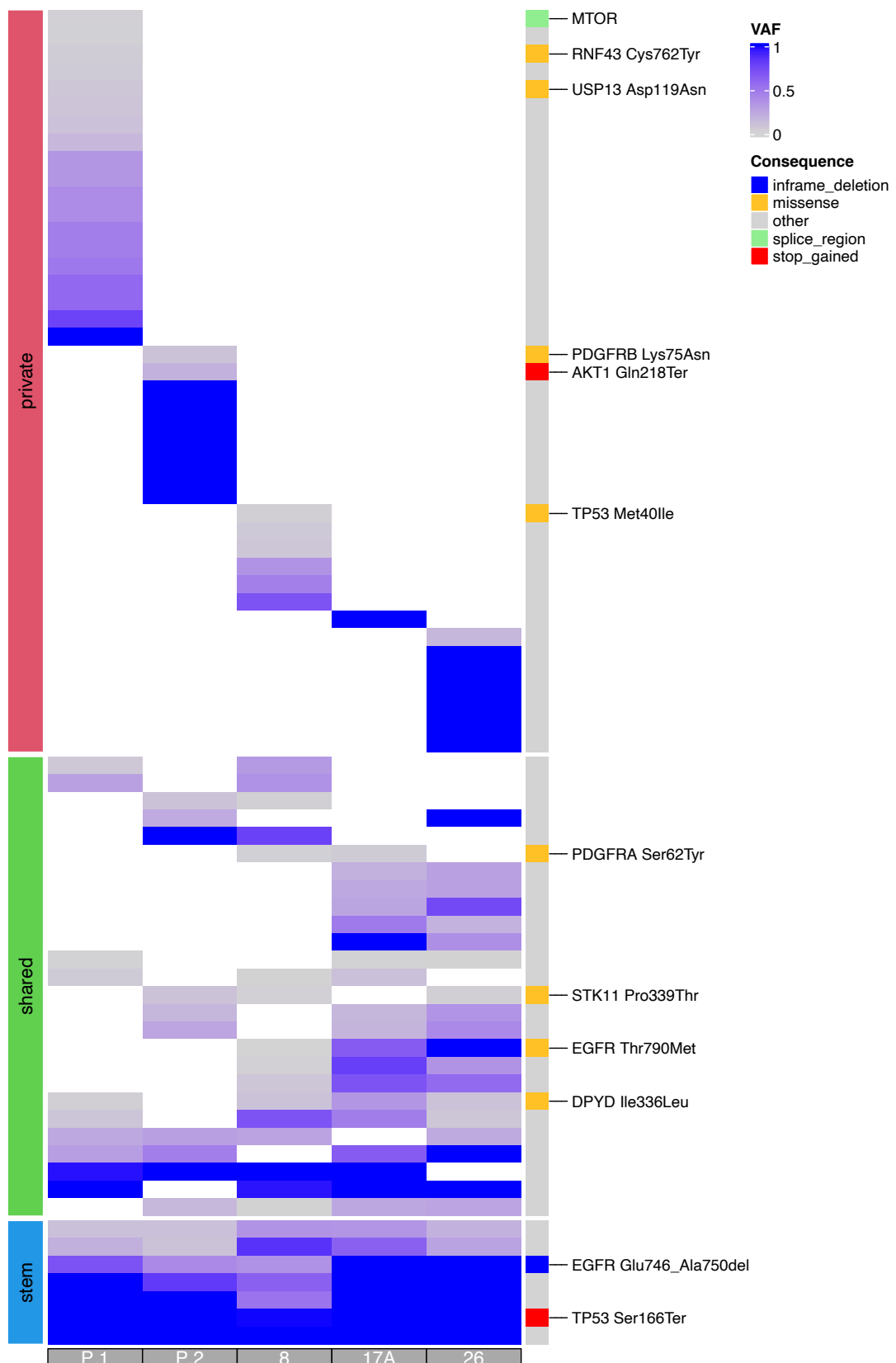


Figure 3.32: Heatmap of driver gene variants in patient CA-L: Protein altering mutations are highlighted with their HGVSp notation; non protein altering mutations are grouped as “other”.

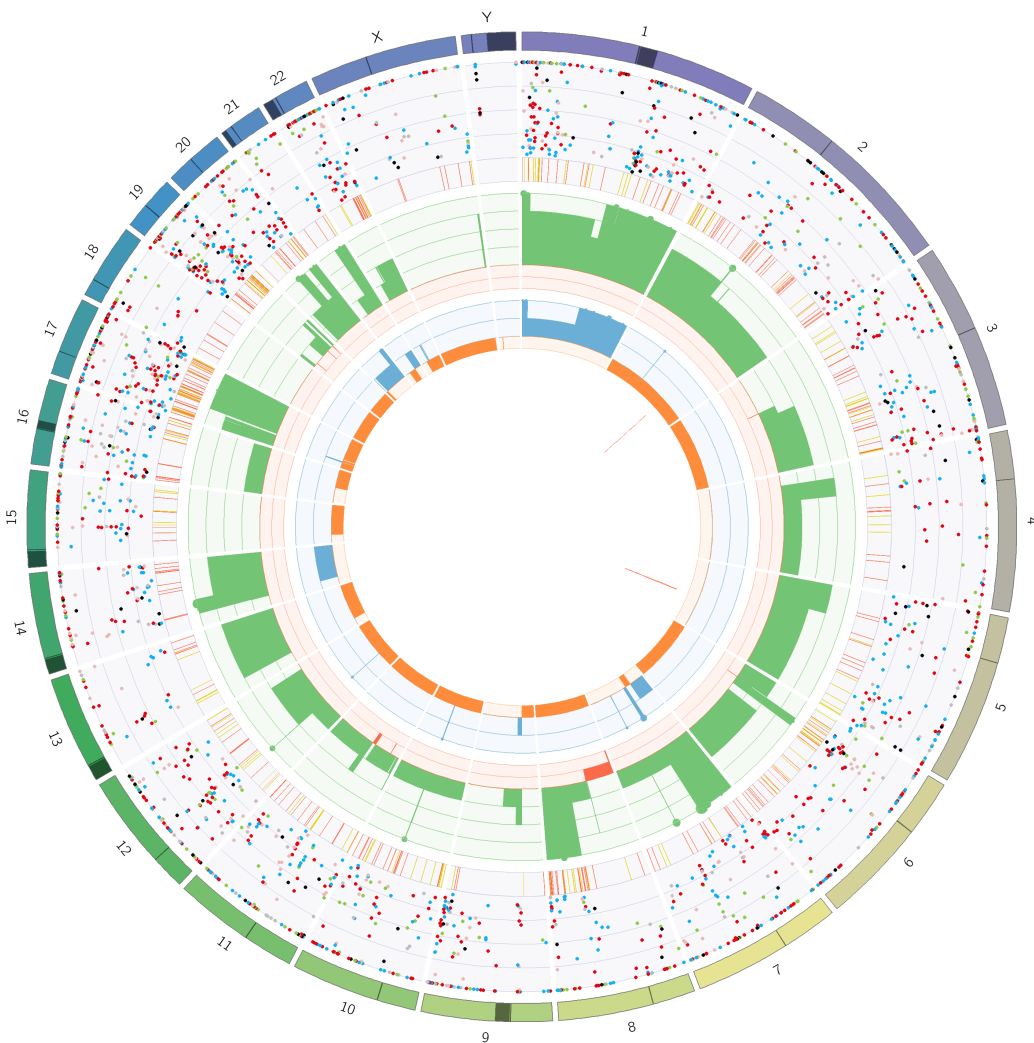


Figure 3.33: Circos plot of patient CA-L sample P.1: outer first ring shows the canonical chromosomes with gaps (centromere, heterochromatin,...) highlighted as darker areas; second ring visualises all somatic SNVs corrected for tumour purity and scaled from 0 to 1, the colour representing the base change of SNV like in Alexandrov et al. [215]; vertical lines directly under the SNVs symbolise InDels, with yellow for insertions and red for deletions; the third ring shows the total copy number alterations, with green showing a copy number gain and red a loss, dots at the outer border show a copy number greater than four; the last ring shows the minor copy number, with blue depicting a gain and orange a loss, this ring allows the detection of copy number neutral changes, like loss of heterozygosity; the center shows all structural variants: translocations in blue, deletions in red, insertions in yellow, tandem duplications in green and inversions in black.

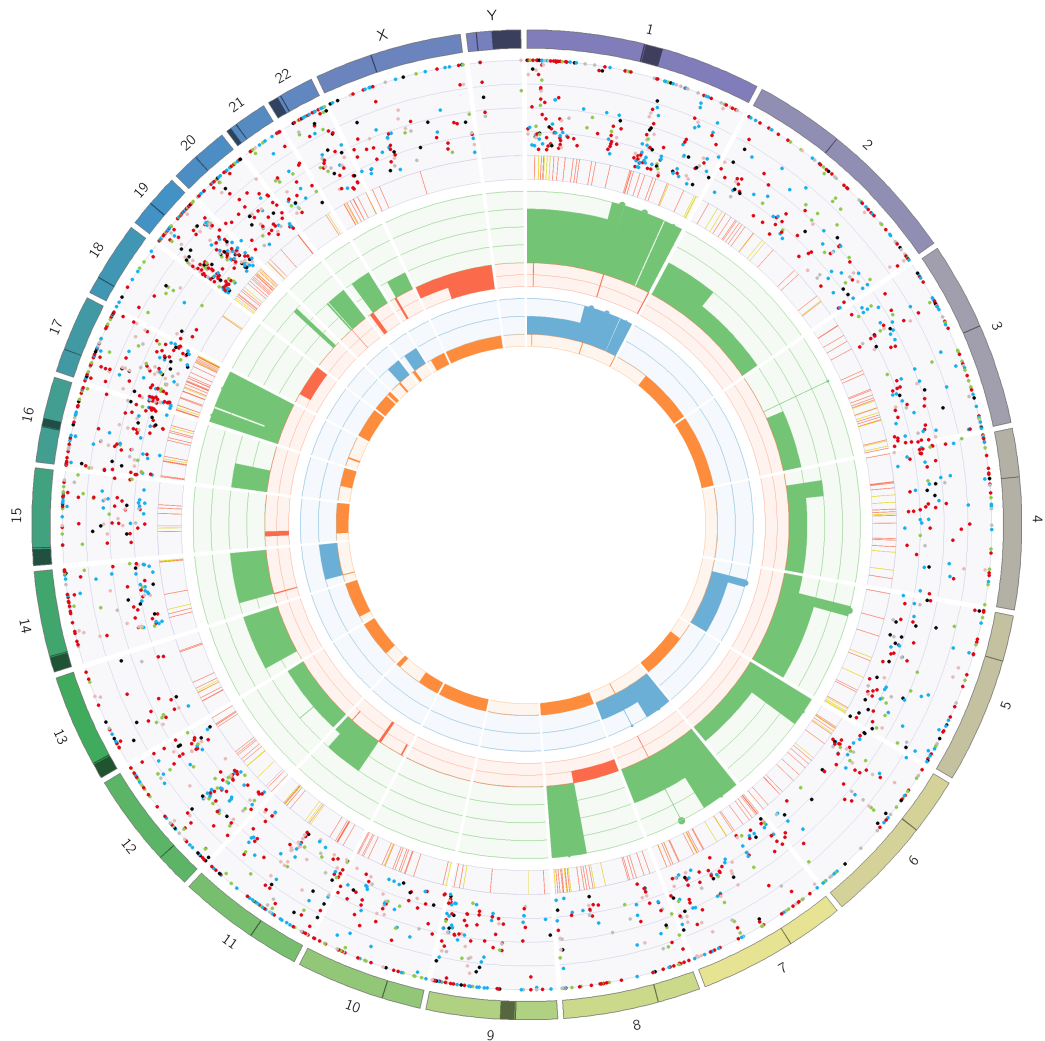


Figure 3.34: Circos plot of patient CA-L sample P.2: outer first ring shows the canonical chromosomes with gaps (centromere, heterochromatin,...) highlighted as darker areas; second ring visualises all somatic SNVs corrected for tumour purity and scaled from 0 to 1, the colour representing the base change of SNV like in Alexandrov et al. [215]; vertical lines directly under the SNVs symbolise InDels, with yellow for insertions and red for deletions; the third ring shows the total copy number alterations, with green showing a copy number gain and red a loss, dots at the outer border show a copy number greater than four; the last ring shows the minor copy number, with blue depicting a gain and orange a loss, this ring allows the detection of copy number neutral changes, like loss of heterozygosity; the center shows all structural variants: translocations in blue, deletions in red, insertions in yellow, tandem duplications in green and inversions in black.



Figure 3.35: Clonal evolutionary tree of patient CA-L; Highest support tree for clustered ccf clones generated with PhylogicNDT; Support for clone is shown in parenthesis; Major driver alterations of cluster were annotated; Clusters with less than 5 supporting variants were discarded.

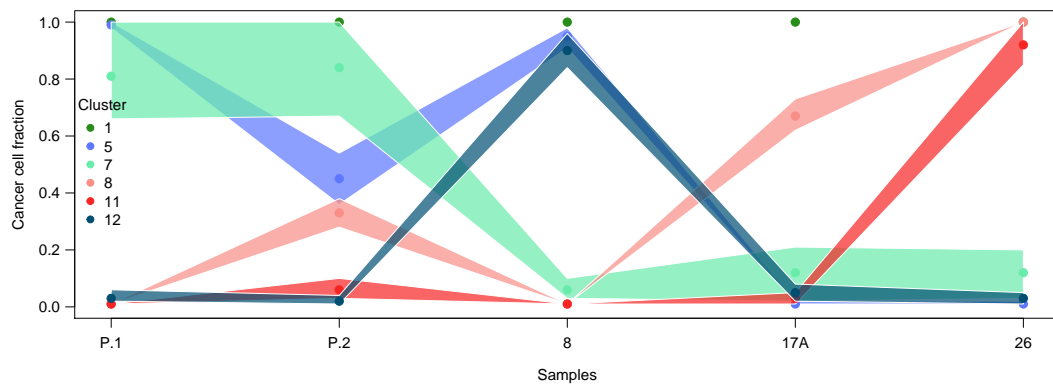


Figure 3.36: Cancer cell fraction of mutation clusters of clonal tree for patient CA-L; transparent polygons show the 95% confidence intervals. Clusters and cluster colours are taken from Figure 3.35

3.4 Cohort level analysis

fill this

ideas:

loss of heterozygosity

long stem and explosion of small cell transformation

potentially move this after the mitochondrial analysis to put that in as well.

3.4.1 Phylogenetic reconstruction

Phylogenies differences and similarities

3.5 Mitochondrial phylogenetic reconstruction - the power house of the phylogenies

While phylogenetic reconstruction is a well established method for genetic variants from canonical chromosomes to study metastatic progression and timing of evolutionary divergence [180, 226, 166], there are multiple issues. In [Section 2.3.1](#) and [Section 2.4.1](#) we showed how important the proper variant calling method is to accurately recover phylogenies and clonal patterns. In addition, using somatic variants to reconstruct phylogenies is a flawed concept flawed to begin with. Most models studying genetic variation assume neutral evolution of the sites [227, 228], but cancers almost exclusively exhibit positive selection [229]. And while passenger mutations might not directly affect fitness of the cell, they only exist due to the link to the driver mutation and therefore has little to no additional information gain in addition to the driver. In addition, while in small populations genetic drift as a stochastic process overpowers selective processes (fitness coefficient s) and can therefore be assumed to be neutral, in larger populations N_e (effective population size) where [Equation 3.2](#) does not hold true, mutations are under selective pressure [230].

$$N_e \cdot s \ll 1 \quad (3.2)$$

All in all we can assume that with cancer growing, positive selection through treatment and tumour micro environmental niches, almost all assumptions of the coalescent theory are not applicable for

tumour samples and therefore methods using somatic variants and their respective results need to be selected and evaluated carefully.

To tackle this issue, and assist with the interpretation of phylogenetic reconstruction results, we adjusted a method used in single cell sequencing to track clonal expansion with mitochondrial somatic mutations [231] to be usable for standard bulk sequencing. Mitochondrial variants are an ideal source of clonality information, because the mutation rate is significantly higher than nuclear DNA, due to the missing proof reading and repair mechanisms, which allows very granular separation in a shorter time period. Additionally, while there are several diseases caused by defects in mitochondria such as Kearns-Sayre syndrome [232], MERRF [233] and MELAS [234], they usually follow a mendelian inheritance pattern and are hereditary and not somatically acquired. In the cancer context, somatic mutations in mitochondrial DNA are assumed to be approximately neutral with a possible selection pressure towards healthy ageing and negatively selecting cancer [235, 236].

3.5.1 Method

First a pileup of all mitochondrial positions is performed. Before the pileup we preselect reads which uniquely map to the mitochondrial genome and only retain high mapping quality reads. Then the nucleotide counts in each position is transformed into a MultiEssayExperiment [31] for final analysis in R. The preprocessing code can be found in [Listing B.1](#).

The final MultiEssayExperiment is then read into R and quality metrics applied to exclude samples with not enough coverage on the mitochondrial contig. usually WGS samples will show an extensive coverage of mitochondrial DNA, however WES will require a library preparation with probes in this area. Patient CA-I has a coverage of more than 100x for all but the germline sample which only has an overall coverage of 17x. Similar, patient CA-L shows lower depth for the germline sample (127x) but a generally high coverage for all tumour samples. All other Patients (CA-A/J/K) where samples are sequenced as WGS show a coverage of more than 200 even for low performing samples with a median depth of 67 916, 45 603 and 49 726 per sample ([Figure 3.37](#)).

This shows, that even without specifically enriching for mitochondrial DNA, most samples will contain enough tumour reads for this analysis.

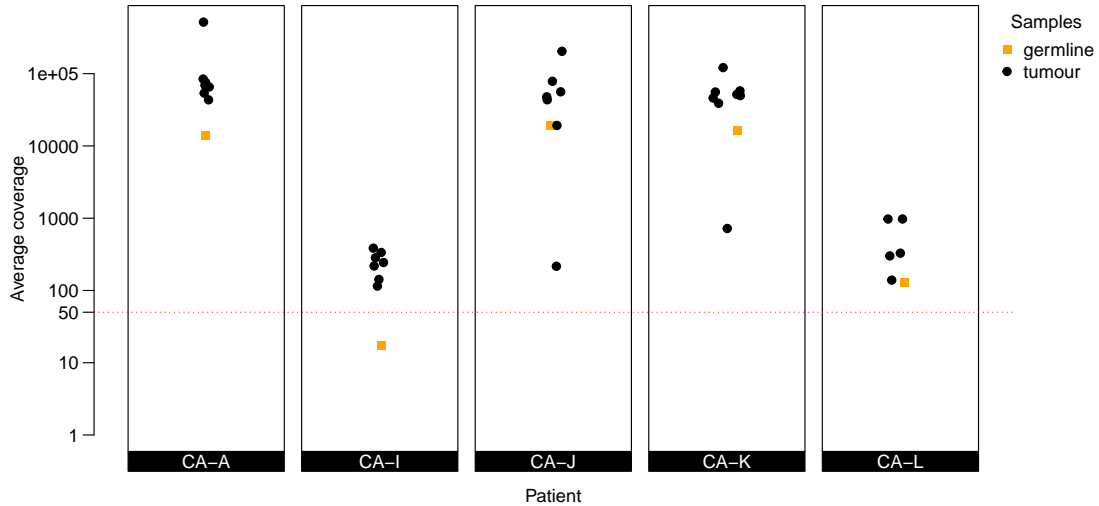


Figure 3.37: Average coverage of mitochondrial DNA of CASCADE patients: Orange squares show germline sample for each patient; black points show tumour samples; horizontal red dotted line shows quality cut off suggested by Ludwig et al. [231]

To ensure optimal results, we excluded all samples with an average coverage of less than 50x. This means we remove the germline sample for patient CA-I, however as we expect the germline sample to be the ancestral state for all samples, so it can be reconstructed. Secondly, we were more interested in the relation of tumour samples with each other, which is still possible.

In contrast to the simple hamming distance used for the presence-absence vector representation of canonical somatic variants (Section 3.3.1.6) for mitochondrial variants we employed a allele frequency (vaf) based distance (Equation 3.3) of two samples s_i and s_j . The difference in read support is normalised with the product of the total allelic depth cov and summed up at all sites of variation v .

$$mitoDist(s_i, s_j) = \sum_{v \in Variants} \left| \frac{vaf_{s_i}(v) \cdot cov_{s_i}(v) - vaf_{s_j}(v) \cdot cov_{s_j}(v)}{cov_{s_i}(v) \cdot cov_{s_j}(v)} \right| \quad (3.3)$$

This distance was only calculated for variant sites where both samples had at least a coverage of 100x to have a representative sampling of the allelic prevalence in each sample as a human cell usually has more than 100 mitochondria [237].

3.5.2 Results

While the mitochondrial variants analysis only uses a fraction of the size of the genomic DNA loci and therefore most likely breaks the infinite sites assumption [238], it was still able to generate a second viewing angle at the heterogeneity and trajectory of the multi-regional samples in each patient.

3.5.2.1 Patient CA-A

While the separation of progression ((11, 47, 55, and 59) and stable (26, 31, 41, and 57) disease sites was already visible in the somatic phylogeny, the bottle neck of treatment and new metastasis is more obvious in the mitochondrial phylogeny. However the individual resolution of splits appeared to be lower for the mitochondrial reconstruction (Figure 3.38).

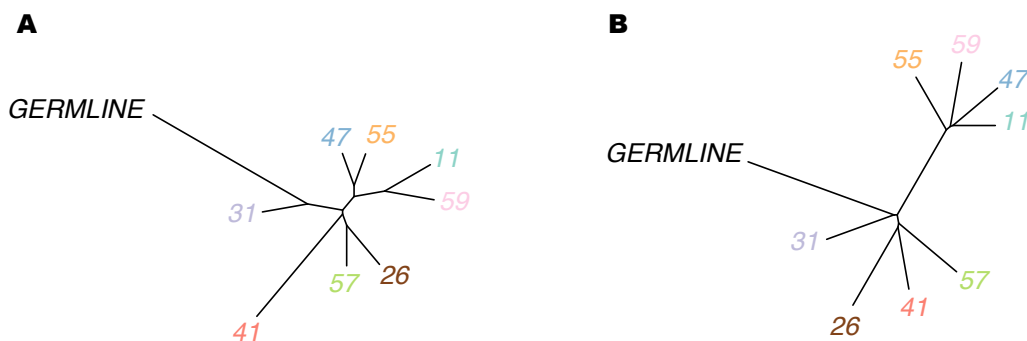


Figure 3.38: Mitochondrial and somatic phylogenetic reconstruction of CA-A: Somatic variants based reconstruction (A) and mitochondrial variants based reconstruction (B)

3.5.2.2 Patient CA-I

Neither the somatic variants nor the mitochondrial variants resolved the evolutionary trajectory in a granular fashion. The slightly long stem of shared variants was most likely due to the low coverage of the germline sample. Similar to all other patients, the substructure of the samples was changed. While on the somatic variants showed sample 566 as the closest to the germline sample, mitochondrial variants instead indicated sample 559 as the closest (Figures 3.37 and 3.39).

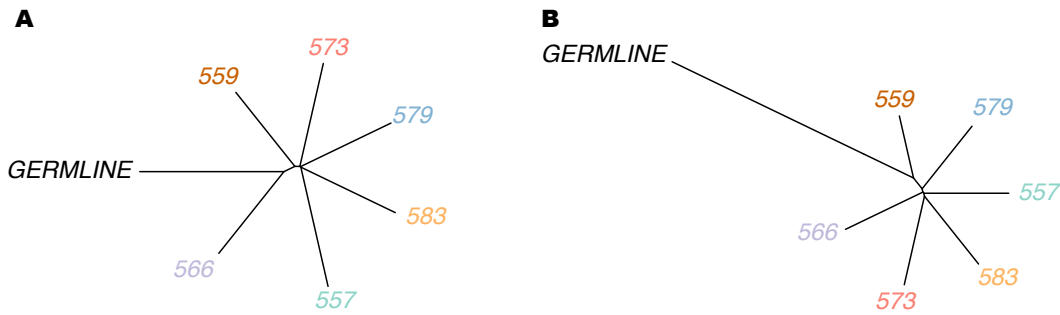


Figure 3.39: Mitochondrial and somatic phylogenetic reconstruction of CA-I: Somatic variants based reconstruction (A) and mitochondrial variants based reconstruction (B)

3.5.2.3 Patient CA-J

In contrast to the somatic variant phylogeny, the mitochondrial reconstruction showed sample 2 as a substantial outlier and instead of the two samples 24 and 28 only sample 28 was grouped closely with the germline sample. The low distance to the germline sample can be attributed to its very low tumour purity. However sample 24, which was also evolutionary close to the germline sample when using somatic variants, is now grouped with the other samples with similar copy number profile, even due to the lower purity (Table 3.6, Figure 3.40)

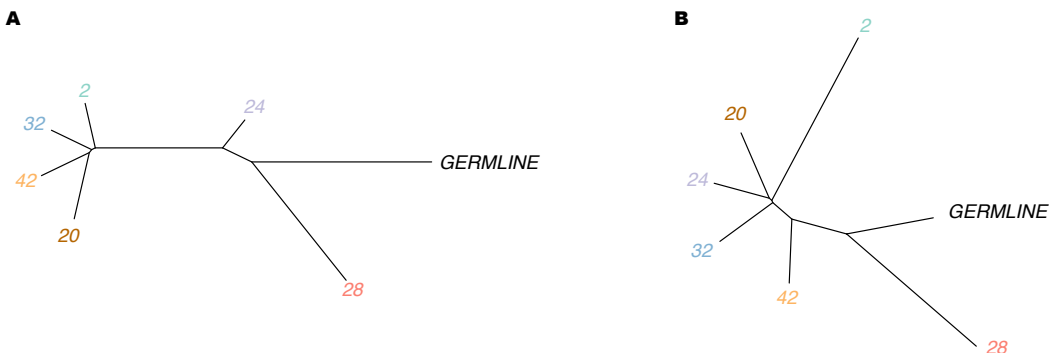


Figure 3.40: Mitochondrial and somatic phylogenetic reconstruction of CA-J: Somatic variants based reconstruction (A) and mitochondrial variants based reconstruction (B)

3.5.2.4 Patient CA-K

In contrast to the somatic variant phylogeny, which showed a outgroup of samples 8 and 9, with a second cluster of samples 4, 5, and 6, the mitochondrial data supported a half way split into two groups. These groups almost perfectly split the samples into the left and right body half with sample 6 being the only sample from the right side clustered with the left lung and brain samples 8, 9, and 13. These data suggested that while only samples 8 and 9 showed a whole genome duplication and

the *APC* “stop gained” mutation, they were closer related to the other samples than assumed from the somatic variant analysis (Table 3.8, Figures 3.26 and 3.41).

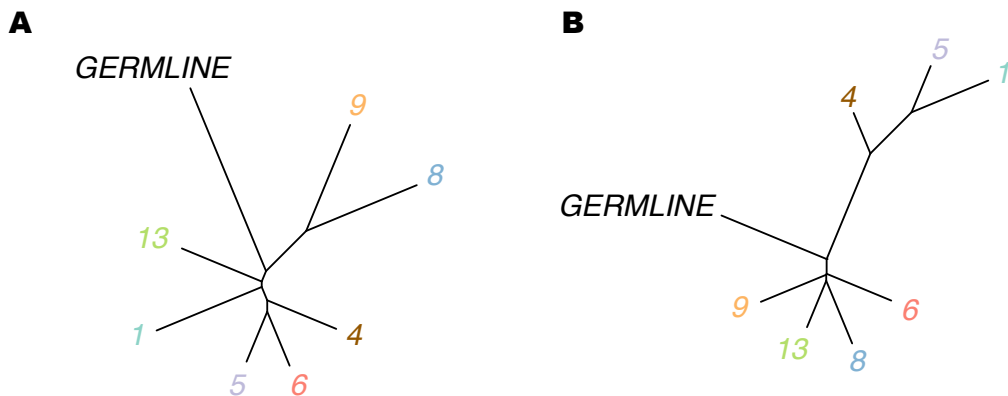


Figure 3.41: Mitochondrial and somatic phylogenetic reconstruction of CA-K: Somatic variants based reconstruction (A) and mitochondrial variants based reconstruction (B)

3.5.2.5 Patient CA-L

While the somatic variants linked the small cell carcinoma samples P.1 and 8 together, the mitochondrial analysis shows that the closest relative to P.1 was P.2. as both of the Progression samples were taken 14 months ahead of the death of the patient, this fitted the clinical history of the samples better. Additionally instead of grouping the adenocarcinoma sample 17A and 26 together, the mitochondrial phylogeny suggests, that while they share a common resistance mechanism (EGFR T790M), it might have been acquired in parallel instead of being seeded from the same lesion, as all samples other than the P.1/2 samples are not grouped together. Lastly, the closeness of sample 8 and the germline sample possibly indicated a presence of small cell disease already “before” the progression samples. However the FFPE conservation of the P samples could have altered the molecular clock and influenced the branching site on the tree (Figures 3.32 and 3.42).

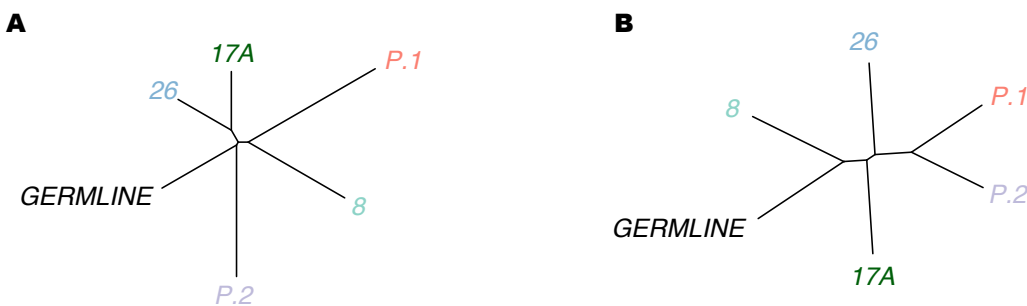


Figure 3.42: Mitochondrial and somatic phylogenetic reconstruction of CA-L: Somatic variants based reconstruction (A) and mitochondrial variants based reconstruction (B)

3.5.3 Summary

With the analysis of the mitochondrial history of samples, we could shed some light on the timing of lesions and the development of resistance mechanisms, which is not heavily influenced by the treatment and its selection pressure. While the infinite sites hypothesis does not hold true for mitochondrial DNA, due to the limited sites and reduced repair mechanisms, the selection pressure of treatment and their resistance mechanisms parallel evolution biased the analysis of multiple related tumour sample when using somatic variants.

This method could offer an alternate view on the history of samples and their kinship with data that was previously discarded but was abundantly available at no extra cost. Ideally both somatic variants and mitochondrial variants would be integrated into a holistic approach, however due to the substantial difference in scale between nuclear DNA and mitochondrial DNA, the process is intricate and outside the scope of this work.

3.6 Outlook

“When the sum is already greater than the parts, there is room to make it greater still.”

— Navalí, Hatungo of the Karui

4

MisMatchFinder - hope springs eternal

4.1 Introduction

While even very early on, researchers realised, that cancers have different morphologies and clinical progression depending on the primary occurrence of the tumour ([Section 1.5](#)), with the extensive sequencing of cancer specimen over the last decade, the mutational signatures of cancers came into focus. These signatures are specific and characteristic combinations of mutations, which stem from distinct biological processes. These processes include exposure to DNA damaging agents like Chemotherapy treatment, tobacco and UV, as well as biological intrinsic pathways errors in DNA-replication or -repair. As each of those processes has a more or less distinct profile of mutations [[239](#), [240](#)] the analysis and deconvolution of the signatures involved in a patients mutational landscape can help diagnosing and treating a patient. While many signatures occur at a background level and are related to “normal” cellular processes like ageing [[215](#)], others can point to defective mismatch repair or gain of function mutations in specific pathways, which then lead to new avenues of therapy for the patient [[241](#)].

Supplementary information and plots for this chapter are attached in the appendix and prepended with [C](#).

4.1.1 Mutational signature analysis

Traditionally the cancer mutational signature analysis entails a somatic variant calling process ([Section 1.4.2](#)) followed by a counting and deconstructing step, which assigns weights to the individual signatures. These signatures are precompiled list of mutation count relations ([Figure 4.1](#)). While

the individual SNP already contains valuable information, there is an improvement in granularity when also counting the base up and downstream of the change. This expands the feature space of counts from the six base classes of SNPs ($C>A$, $C>G$, $C>T$, $T>C$, $T>A$, and $T>G$) to 96 unique trinucleotide contexts [215]. While there technically are six more base changes and many more trinucleotide contexts combinatorially possible, they can be collapsed into the afore mentioned ones by using the reverse complement.

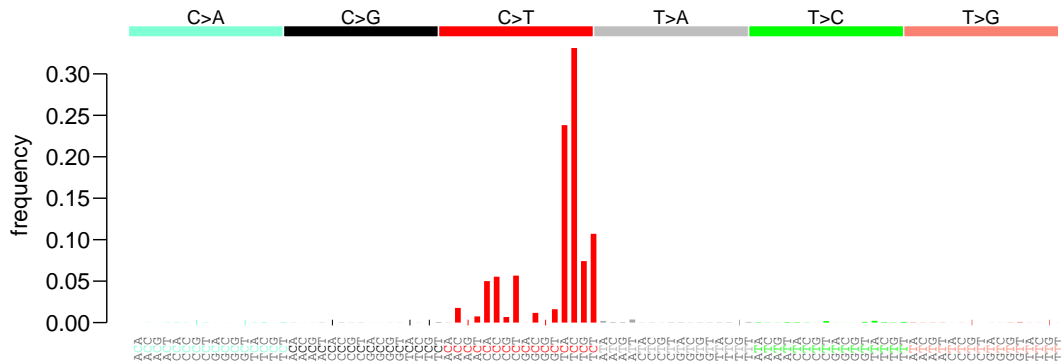


Figure 4.1: Trinucleotide count contributions for SBS signature 7a (UV exposure); values taken from Alexandrov et al. [209]

Additionally to the single base substitution (SBS) there now exist doublet base substitution signatures and InDel signatures for somatic mutations of cancers [209], which are all based on the same principle and enable a higher precision for stratification of similar cancer subtypes and DNA damaging agents.

4.1.2 Restrictions and pitfalls of standard signature analysis

Especially for cancer samples, the focus is usually on somatic variants of the sample. This requires a fairly deep sequencing of the tumour sample with at least WES, better WGS, and for optimal results, a germline sample for tumour-normal variant calling is required as well to not have noise from potentially missed germline variants (Section 1.4.4). This means the cost of the data of the analysis is surprisingly high for a fairly diffuse result of signatures that contribute to the variants found. This is especially relevant when it comes to clinical diagnostic tools, where every biopsy of the patient is valuable and a germline sample might not always be available. For an analysis, which is based on the averaged and aggregated somatic variants to require a high quality input seems counter-intuitive. Especially as the analysis will always report signatures, even if there are virtually

no variants reported, it will still suggest a mixture of potentially clinically relevant signatures, even if the patient is healthy.

4.1.3 Overview

These reasons make the actual analysis, which should come as a first step to inform both clinicians and pathology what to look out for more of a side arm, which is nice to have but not significant or informative. This chapter describes a newly developed method, which allows the detection of somatic signatures from low coverage WGS of cfDNA. This allows the non-invasive monitoring of patients and possibly screening of at-risk individuals with very little cost.

4.2 Methods

With the change from a variant focused approach to a read based method, this new method will call “mismatches” of a read from the reference genome, rather than a variant. This has the advantage of not requiring a matched normal and its use for virtually any sequencing data source, be it TAS, WES, WGS or even nanopore sequencing⁴. However it also means, that the error suppression method, which are usually used by variant calling methods like read position ranks sum (RPRS) or strand bias are not usable, which leads to a higher degree of background noise. In the following sections I will describe how we filter and curate the found mismatches to retain as much signal as possible.

4.2.1 Mathematical concept

With the change from site based method, the concept of a mismatch from the reference needs to be introduced. A mismatch in the following is any position in an aligned read, which does not show the same base as the reference at the aligned position. The mismatch will inherit all the metrics of the read such as mapping quality, base quality and read position.

This then means, there are three sources of mismatches in a read, which are somatic variants, germline variants and sequencing errors ([Equation 4.1](#)).

$$n(\text{mismatches}) = n(\text{somatic var.}) + n(\text{germline var.}) + n(\text{seq. error}) \quad (4.1)$$

⁴however nanopore is not really usefull due to the short fragments naturally occurring in cfDNA

With the sequencing error being a function of the sequencing machine and chemistry, the error rate should be a stable almost constant, when using the same sequencing machine and chemistry [151, 152]. We can therefore reduce [Equation 4.1](#) to

$$n(\text{mismatches}) = n(\text{som. var.}) + n(\text{germ. var.}) + c_{\text{seq. err.}} \quad (4.2)$$

Secondly, the number of germline variants is approximately the same between two people [242], which again simplifies [Equation 4.2](#) by replacing $n(\text{germline var.})$.

$$n(\text{mismatches}) = n(\text{som. var.}) + c_{\text{germ. var.}} + c_{\text{seq. err.}} \quad (4.3)$$

Of course, [Equation 4.3](#) is a crude approximation and instead the constants are not real constants, but instead are better approximated with Gaussian distributions which leads to the following equation

$$n(\text{mismatches}) = n(\text{som. var.}) + \mathcal{N}(\mu_{\text{germ. var.}}, \sigma_{\text{germ. var.}}^2) + \mathcal{N}(\mu_{\text{seq. err.}}, \sigma_{\text{seq. err.}}^2) \quad (4.4)$$

However, both [Equation 4.3](#) and [4.4](#) allow to make the conclusion, that with small enough values for either $c_{\text{germ. var.}}/c_{\text{seq. err.}}$ or $\mu_{\text{germ. var.}}/\mu_{\text{seq. err.}}$ and $\sigma_{\text{germ. var.}}/\sigma_{\text{seq. err.}}$ respectively, there is a linear correlation between the amount of mismatches on a read and the somatic variants it contains:

$$n(\text{mismatches}) \sim n(\text{som. var.}) \quad (4.5)$$

With the help of [Equation 4.5](#) we can approximate tumour mutational burden and signatures from individual reads. This method is therefore independent from read depth and requires no matched normal sample for somatic variant calling.

4.2.2 Data preprocessing

As this new method has sophisticated internal measures to filter and process sequencing data, the steps for preprocessing are minimal: The reads only need to be aligned to a reference genome ([Section 1.4.1](#)). For optimal mapping and additional noise reduction, paired end sequencing of at least 75 bp is suggested. This ensures a few bases overlap on the standard fragment length of less than 150bp of ctDNA ([Section 1.2](#)). Another optional suggested step is the duplication marking of the BAM file.

4.2.3 Mismatch detection

In contrast to conventional variant calling approaches, which find regions of interest through pile-ups (position wise) and then realign reads in the surrounding area, to accurately estimate the most likely event that lead to the observed haplotype ([Section 1.4.2](#)), with this new method, we take every individual read as a separate entity to fully span the heterogeneity of all cells and their genetic background. A sequencing reads “MD“- and “CIGAR“- tag from the preprocessed BAM file are used to reconstruct the sequence of the read and the positions, where the read shows a different base than the reference. These potential mismatch sites will then be filtered in multiple steps to reduce the impact of both germline variants as well as sequencing errors

4.2.4 Filtering steps

Apart from the filters, which most variant callers will employ, like mapping quality (MQ) and base quality (BQ), which are used to ignore reads as well as positions respectively, the method also internally filters out common sequencing errors next to homopolymer regions [[243](#)]. While these cutoffs were preselected by me for optimal performance on our data (MQ=20, BQ=55, homopolyLength=5), the program allows the user to adjust them to their liking. This is also possible for both the region of interest (ROI) bed-file which was used to restrict the analysis to only highly mappable regions of the genome ([Section C.1](#)), as well as for multiple other parameters which are unique to our method, like minimum average base quality, minimum and maximum number of mismatches per read and/or

fragment, and the minimum and maximum length of a fragment [244]. If any of these values are not within the specified range a read will be discarded in the analysis. This is also the default for reads which have a secondary alignment position or are considered duplicates of any kind.

4.2.5 Consensus reads - what happens when the sequencer isn't sure

When paired end sequencing of ctDNA is analysed, the fraction of fragments where reads overlap is higher, than with “normal” tissue based sequencing, due to the shorter fragment length of ctDNA ([Section 1.2](#)). This allows an fragment internal consensus generation, by adjusting for differences between forward and reverse read. In many variant calling methods, these differences are used by measuring the “strand bias” [245, 246, 247] or “strand balance probability” [104] by looking at a specific locus and evaluating the discrepancy of all forward and all reverse reads. As our method evaluates each read/fragment independently, the bias cannot be calculated, however in the overlapping region of both reads, a consensus can be generated. If both reads agree on the mismatch, the BQ of both reads will be added together to emphasise the increased evidence for this variants. However, if they disagree the base of the higher quality will be used and its quality will be decreased by half of the BQ of the lower quality base ([Figure 4.2](#) bottom). To increase the stringency of the method, the user can also enable the ‘*–strictOverlap*’ option, which will only consider a mismatch, if both reads agree with each other and decrease the BQ to zero otherwise. As we are only interested in mismatches from the reference, all positions where both agree with the reference are irrelevant for the analysis and will be discarded ([Figure 4.2](#) top). For the most stringent analysis, MisMatchFinder can additionally be configured to only use mismatches in the overlap part of a fragment (‘*–onlyOverlap*’), which significantly reduces the number of sequencing errors which end up in the final analysis ([Section 4.3.1.1](#)).

This method however also reduces the available data by restricting the analysis to areas where reads are overlapping. Due to the fragment size distribution of ctDNA a paired end sequencing with 100bp read length will in most cases lead to an overlap of at least 45 nucleotides ([Section 1.2](#)) and with 150bp most ctDNA fragments will be almost entirely covered by both reads in theory. However due to soft-clipping and incomplete alignment, this number will be lower in reality. In our tests, the restriction leads to on average 18 nucleotides (min: 14bp max: 25bp std.dev.: 1.45) being retained in the analysis from a read on average for a 100bp read in real world data. This however means that with a read depth of 8-10x ≈80% of the genome will be covered by the overlap of at least one read pair.

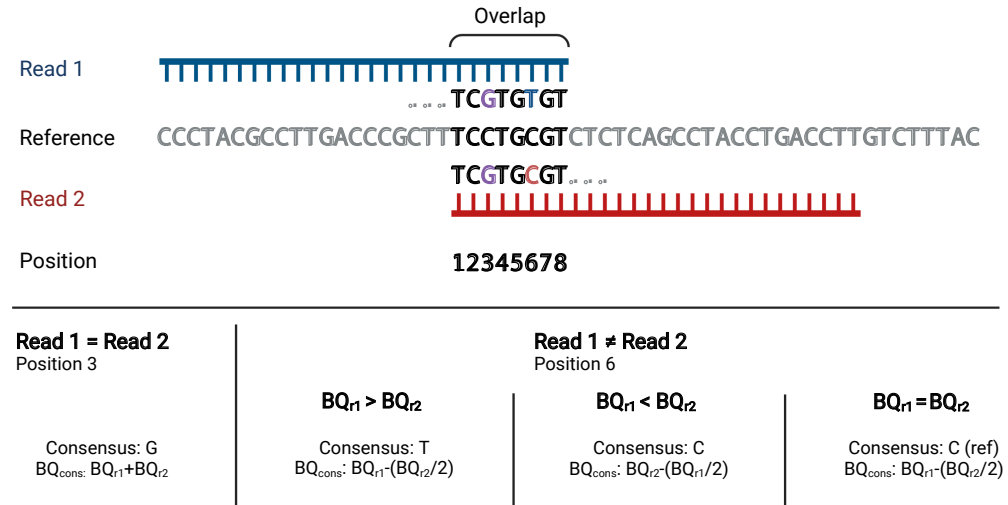


Figure 4.2: Schematic of consensus computation method for overlapping reads in Mis-MatchFinder; Read 1 and Read 2 depict two overlapping paired end reads aligned to the reference sequence; Positions in the overlap are numbered for later referral; Read positions agreeing with the reference are coloured black, positions differing from the reference but agreeing in both reads are coloured purple (position 3) and differences between reads are coloured in the respective read colours (blue and red, position 6); Calculation for the resulting base quality (BQ_{cons} for each possibility is shown as formulas)

4.2.6 Germline filtering - exclusion of normal variation

To further enable the [Section 4.2.1](#) claim that the germline is a very small constant, we need to remove as many mismatches as possible, which stem from germline variants. For this purpose, I built a zarr [56] based storage system from the gnomAD database (v.3.1) [111] using scikit-allel [248]. A in-depth explanation of the generation as well as a script for for an end user can be found in [Section C.3](#).

This then allows very precise filtering of known germline variants sites from the analysis. The method allows the specification of an allele frequency to consider a variant to be filtered, however as baseline, it will filter all sites, which were detected in any sample in gnomAD. This even includes sites with low quality variants, as these are signs for sequencing or mapping complications, which will most likely interfere with our method as well.

4.2.7 Count normalisation - not everyone has the same chances

Finally when having filtered all “noise” mismatches from the dataset, we can aggregate all mismatches to oligo-nucleotide counts. With this step also comes the classification of directly neighbouring mismatches as DBS, which are counted as separate entities. SBS and DBS both can be used

to identify underlying biological mutational processes, but they have very different signatures associated with them [209]. The counts formed this way are influenced by the background frequency of their reference oligo-nucleotides in the analysed genomic region. As the frequencies of di- and tri-nucleotides are not uniform in the genome, the chance for a mismatch found in an “AAA” reference context is almost seven times higher than a mismatch in “CGC” (Table C.2, Table C.1). To reduce this bias towards high frequency oligo-nucleotides, I implemented a count normalisation step.

First the di- and tri-nucleotides in the analysed regions are counted using the supplied reference without any black-listed and/or only in white-listed regions. These counts are then either used to directly weight the observed mismatch counts, which leads to a more uniform distribution of mismatches, or by building a fraction of observed oligo-nucleotides and the total counts in the genome (Table C.2, Table C.1), the weighting achieves an approximation of how the counts would be distributed over the whole genome. These two options are available with ‘*–normaliseCounts*’ for the approximation to full genome. By also adding ‘*–flatNormalisation*’ only the observed counts are used for normalisation.

4.2.8 Signature deconvolution - find the original signal

The deconvolution of the involved signatures from known set of signatures is equivalent to finding the minimal distance between m as the observed number of mismatches in each oligo-nucleotide context (a vector of length 96) and $\mathbf{S}w$, where \mathbf{S} is the matrix of oligo-nucleotide defined contributions for each signature, resulting in a matrix of $96 \times k$ with k being the number of known signatures. Lastly, w is the vector of weights of each signature, which we want to estimate.

$$\text{minimise: } (m - \mathbf{S}w)^T(m - \mathbf{S}w) = m^T m - w^T \mathbf{S}^T m - m^T \mathbf{S}w + w^T \mathbf{S}^T \mathbf{S}w \quad (4.6)$$

$$\text{with: } \sum_j w_j = 1 \quad \text{and} \quad \forall j \quad w_j \geq 0 \quad (4.7)$$

Equation 4.6 can then be written as

$$\text{minimise: } -m^T \mathbf{S}w + \frac{1}{2} w^T \mathbf{S}^T \mathbf{S}w \quad (4.8)$$

With the same restrictions as shown in [Equation 4.7](#). These equations and the idea to solve it with quadratic programming (QP) have been taken from Lynch [249], the iterative linear models (ILM) solving approach was adapted from deconstructSigs [35]. Both methods are reimplemented in python in MisMatchFinder, using the quadprog package [59] for QP and a translation of the R code of deconstructSigs for ILM.

MisMatchFinder allows the use of either QP or ILM, as they in many cases produce very similar results [249]. The default method is QP however, even though ILM is the more interpretable method and is the more parsimonious method, because with the increased number of signatures, in the latest work by Alexandrov et al. [209], ILM does not lead to the right signatures if the signal is not strong enough but QP seems to be more stable ([Figure 4.3](#)).

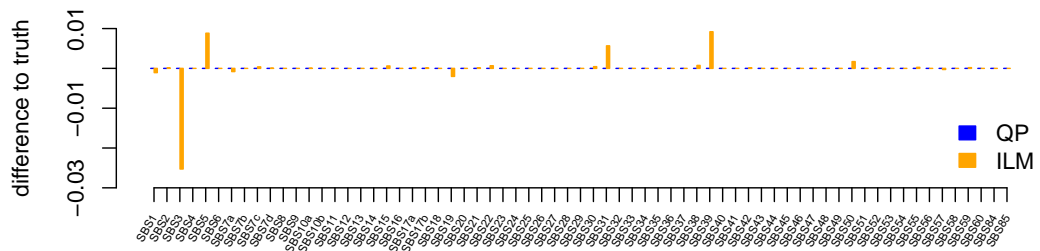


Figure 4.3: Distances of the estimated weights generated with ILM and QP from the true weight used as input; Truth is a synthetic count sample with (SBS1: 0.25; SBS3: 0.05; SBS5: 0.46; SBS7a: 0.1; SBS19: 0.03; SBS21: 0.01; SBS31: 0.08; SBS57: 0.02;)

The combinatorial problem in ILM, already shown by Lynch [249], seems to be especially strong with “wide” signatures like SBS3 ([Figure 4.1](#)) and low signature contribution. That makes it less useful for our approach, as we expect low tumour purity and therefore low somatic signature signals in cfDNA, but even with ILM as deconvolution method impacts the detection of SBS7a less than the detection of SBS3. especially for SBS3 the weight for ILM will only be assigned with sufficient signal (15 and 20 mutations per megabase respectively for SBS7a and SBS3) where QP allows a more linear increase in signal, even at lower levels. In contrast ILM will assign more weight overall than QP once the signal reaches a certain threshold ([Figure 4.6](#)). This means, that ILM will be better for high powered signal, but less effective for the more subtle differences we expect from ctDNA.

The deconvolution method might be a spot for further optimisation by creating a custom deconvolution system adjusted for ctDNA detection.

For the rest of this chapter, unless specified differently, the results shown will use the QP deconvolution method.

maybe move the simulation description here

4.2.9 Signature detection

Signature deconvolution with QP will lead to non negative signature weights for almost all of the signatures when using MisMatchFinder derived counts, however a positive signature does not necessarily signal the activity of this process in a tumour capacity due to the normal somatic mutation background and germline residual signal ([Section 4.3.2.3.1](#)). To enable calling of significantly active signatures in samples, we developed a z-score like system, which uses the distribution of each signature weight in the healthy population as a background.

As the weight values after deconvolution were between 0 and 1 inclusive, with a high enrichment for 0 and 0-adjacent weights, we chose the beta distribution with probability density function (PDF, [Equation 4.9](#)) with shape parameters α and β and normalisation constant B to ensure the cumulative density function (CDF) sums up to 1.

$$f(x; \alpha, \beta) = \frac{1}{B(\alpha, \beta)} x^{\alpha-1} (1-x)^{\beta-1} \quad (4.9)$$

To enable a z-score like estimation, we calculate the λ -quantile of the cumulative density function of the beta distribution ([Equation 4.10](#)) for each patient samples p signature weight w of signature s with healthy sample fitted shape parameters α_s and β_s per signature by solving for λ resulting in the inverse beta cumulative density function ([Equation 4.11](#)).

$$F(x; \alpha, \beta) = \frac{\int_0^x t^{\alpha-1} (1-t)^{\beta-1} dt}{B(\alpha, \beta)} \quad (4.10)$$

$$x = F^{-1}(\lambda; \alpha, \beta) = \{x : F(x; \alpha, \beta) = \lambda\} \quad (4.11)$$

This allows us to estimate how many healthy samples would have a signature weight less than the patient sample for the respective signature s (Equation 4.12). While we did not see significant down regulation of signatures from the background, the method supports both over- and under-representation analysis. Ten percent of all samples were removed from both tails the distribution of each signature before fitting the shape parameters to minimise the impact of outliers.

$$\forall s \in \text{Signatures}, \forall p \in \text{Patients} : \text{CDF-score}(s, p) := \frac{w_s(p)}{F^{-1}(\lambda; \alpha_s, \beta_s)} \quad (4.12)$$

We used a $\lambda = 0.99$ to calculate CDF-scores for all signatures and assumed a CDF-score of more than 2 to be significantly different.

This allowed the prioritization of significantly changed signatures in the tumour samples with regards to our healthy background depending on the desired application. A higher CDF-score cut off will increase specificity at the cost of sensitivity.

While most signature weights could be estimated very well with the moment matching estimation of fitdistrplus [250] some signatures did not show an ideal fit. However in these cases, the fit resulted in a wider distribution with higher theoretical quantiles than empirically observed, which reduced the predictive power of the signature. These signatures also showed a double peak distribution indicative of a population sub structure in the healthy population (Figures C.5 and C.6 vs. Figures C.7 and C.8).

4.2.10 Tumour detection

write about the glmnet and compare to ichorCNA

ichorCNA tumour purity > 3% vs GLMnet

4.3 Results

In this section I will present the results when applying MisMatchFinder to various different datasets. First the evaluation of the method on simulated data, which allows accurate and definitive insight

into the sensitivity and a proof of concept ([Section 4.3.1](#)). Then the analysis of real world applications is displayed in [Section 4.3.2](#) demonstrating that the method does not only work in cleanly simulated data, but find clinically relevant insight in patient samples.

4.3.1 Simulated Data - the validation promised land

Just like in [Chapter 2](#), the novelty of the approach leads to the issue of no gold standard dataset, with which to evaluate the performance of a new method. While there are low coverage WGS datasets of cancer patients, none of them have validated signatures associated with them. So again simulated data is the optimal starting point to allow both optimisation of parameters as well as granular detection of artefacts which can originate from any step starting from sequencing over mapping to the signature deconvolution.

4.3.1.1 Sequencing errors - there is always a cleaner data

To judge the ability of our approach to filter out sequencing errors, we first simulated “clean” sequencing reads with neither germline or somatic variants with the ART simulation suite [[162](#)]. As current estimates of Illumina sequencing is in the range of 1 in 666 to 1 in 1149 [[152](#)] which is significantly higher than even the highest tumour mutational burdens of cancers (melanoma: 1 in 5k; tobacco smoking lung cancer: 1 in 100k) it is very important to be able to eliminate as much of the background noise of sequencing errors as possible.

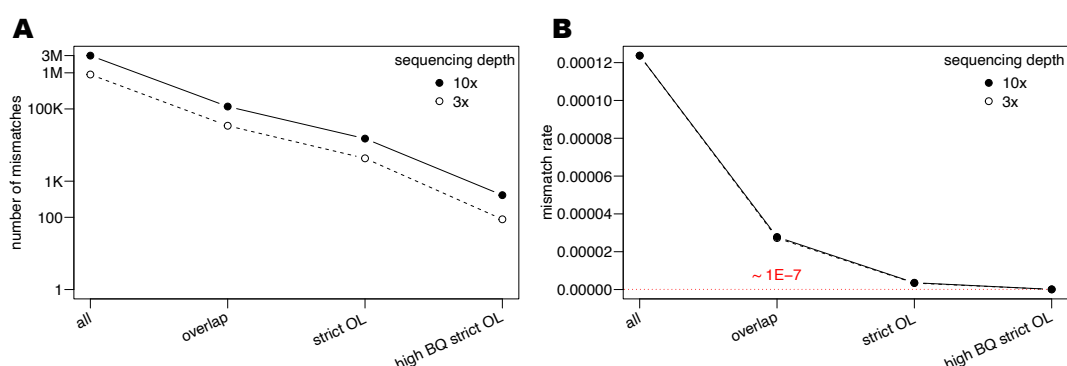


Figure 4.4: Mismatchrate of different filtering methods on sequencing data simulated with ART [[162](#)] for both 10x and 3x coverage; Mismatches correspond to simulated sequencing errors; all: no filters, overlap: only use the overlapping parts of paired end reads with consensus building ([Section 4.2.5](#)), strict OL: overlap but reads *must* agree, high BQ strict OL: strict OL with high BQ in both variants; A) Absolute counts B) counts from A normalised by the number of analysed bases
all: all aligned bases, other: number of bases in read overlap

By only using high base quality mismatches, where both reads agree on the mismatch 99.98% of all sequencing errors can be eliminated and only 1 in 10M bases will be wrongly counted as a variant ([Figure 4.4](#)). This false discovery rate is multiple orders of magnitude lower than before and in a similar range to normal mutationally driven cancers tumour mutational burden [[209](#), [251](#)].

4.3.1.2 Spike-in signature detection

With the technical error eliminated in simulated data, the question was would our method work in a real world data, however to establish a baseline for detection limit and sensitivity of the method, we decided to first use a hybrid approach, were we spike-in somatic variants into a genuine low coverage WGS sequencing of a healthy control. That reduces the amount of unknown variability from other published datasets.

While it would be possible simulate the variants completely de novo, without any prior knowledge, we know that somatic mutations follow a certain pattern and there are mutational hotspots [[252](#), [79](#)], so we decided to instead use the COSMIC database [[253](#), [254](#)] as the to select mutations from. This allows us to select mutations, which definitely occurred in a specific cancer subtype, which leads to a simulation which closer resembles real data. The in-depth protocol is shown in [Section C.3.4](#). The downside of this method is that the spike-in will not predominantly happen on shorter fragments, as it would be the case with ctDNA.

In the following section I will discuss the results for the simulation of the very prominent SBS7a signature (see [Figure 4.1](#)) which is predominantly present in Melanoma (see [Section 4.3.1.2.1](#)) and secondly the much flatter and more uniform SBS3 (see [Figure C.1](#)), which is a sign of defective homologous recombination in breast cancers ([Section 4.3.1.2.2](#)).

The spike-in was done at multiple different ratios, to simulate varying tumour purity and tumour mutational burden (TMB). [Figure 4.5](#) shows the signature analysis result of the lowest spike-in ratio “ro.1“ which corresponds to 0.1 somatic variants per mega base and results in approximately 300 variants for the whole genome. As the spike-in process has to satisfy certain quality measures, not all candidate variants can be used. As such, the final simulated BAM contains 264 additional variants for the SBS3 simulation and 287 for the SBS7a equivalent. That corresponds to 304 and 364 “tumour“ reads respectively within the ≈ 261 million reads of the simulated BAM. With increasing ratio, the spike-in signatures show decreasing weights for other signatures, which likely got introduced due to the incomplete spike-in ([Section C.3.4](#)).

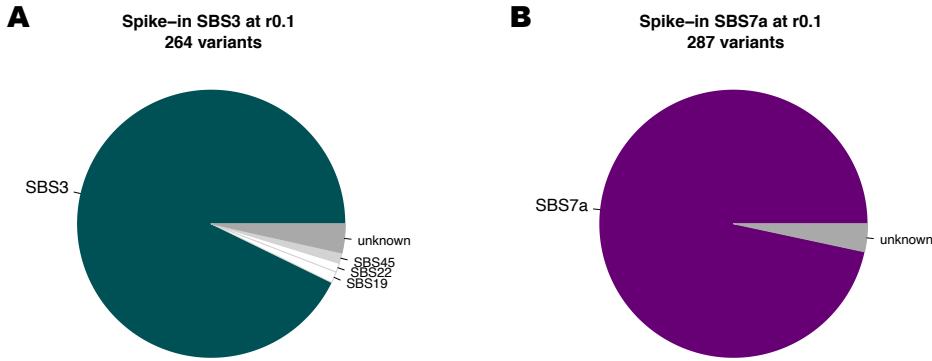


Figure 4.5: Signature analysis results of spiked-in somatic variants; signatures with a weight less than 1% were collated into “unknown”; The original spike-in signature was coloured in green (SBS3) and purple (SBS7a), unrelated signatures are coloured white and signatures corresponding to sequencing artefacts are coloured in lightgrey; r0.1 corresponds to approximately 0.1 variants per mega base; Weights were generated with deconstructSigs [35]

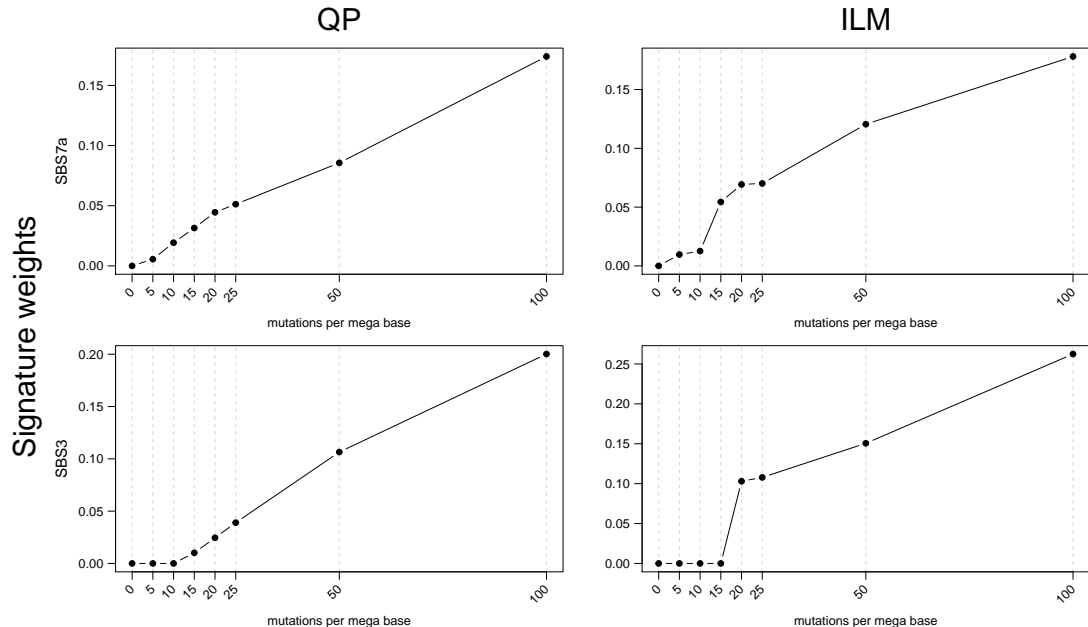


Figure 4.6: Signature weight differences for different deconvolution methods; Methods are the quadratic programming (QP) and iterative linea model (ILM); deconvolution was performed on the same counts generated with MisMatchFinder on 7 simulated dataset with increasing mutational burden from 5 to 100 mutations per mega base spike-in; for 0 mutations per mega base, the normal sample used for the spike-in was used

4.3.1.2.1 Melanoma - UV exposure (SBS7a)

With melanoma, TMB ranges from 0.1 to 100 mutations per mega base [209], however Melanoma is usually seen as a very cancer with very high mutational load, which makes it the ideal target for this new mutational based tool. With only the strict overlap (Section 4.2.5) and the germline

([Section 4.3.1.3](#)) filtering enabled, we can see that already from r₅, which represents 16899 mutated reads (of 260 Mio.), we see an increase in signature SBS7a. While this signal is likely too low to trust this in a real world setting, with r₁₀, the weight is already 2% and well established. Secondly, the method is very specific on this dataset, where only SBS7a shows an increase with higher spike-in, which minor leaks to other heavily $C > T$ signatures like SBS2 and SBS30 ([Figure 4.6](#),[Figure 4.7](#)), which partly already stem from the spike-in process, which slightly enriched for SBS2 ([Figure 4.5B](#) “unknown”). All other signatures, which are present in the normal show a decrease, which is to be expected, as all signature weights need to sum up to one.

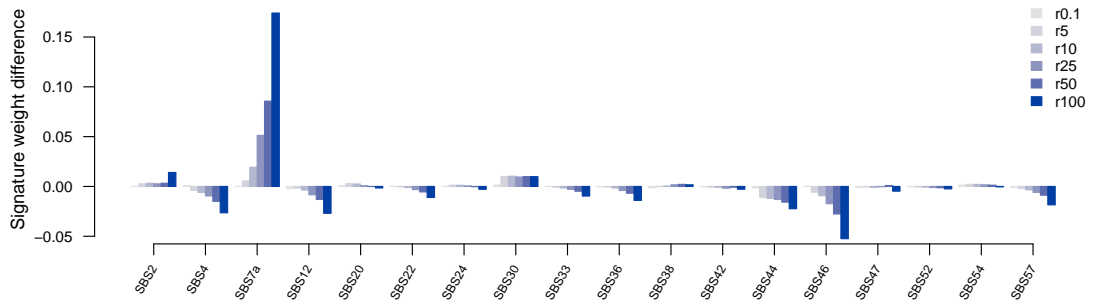


Figure 4.7: Signature weights differences from normal for SBS7a spike-in; Weights were deconstructed with QP method in MisMatchFinder and the weights assigned to the normal sample used for the spike-in were subtracted; Only Signatures with original weight $\geq 1\%$ or a minimum difference of 0.5% are shown. The full weights can be seen in [Figure C.2](#); r_{0.1} corresponds to 0.1 mutations per mega base (287 variants) and r₁₀₀ is the equivalent of 100 mutations per mega base (286974 variants)

4.3.1.2.2 Defective homologous recombination-based DNA damage repair (SBS3)

Just as with the SBS7a signatures, even for the much less specific signature SBS3, MisMatchFinder specifically picks out the spike-in signature and does not assign it to any other signature. There is a small increase in SBS4 for the very low mutation rate simulations, where no SBS3 is detected. Not surprisingly, the detection limit for SBS3 is slightly higher than for SBS7a (5 vs. 15 mutations per mega base), because it is a more uniform signal. Exactly as with SBS7a, all other signatures show a slight decrease, to accommodate the additional signature weight which sums to one ([Figure 4.6](#), [Figure 4.8](#)). While this is slightly higher than the currently assumed median TMB in breast cancer, especially triple negative breast cancer (TNBC) has shown a higher TMB, which is at comparable levels to the limit of detection we see in this simulated dataset [[255](#)].

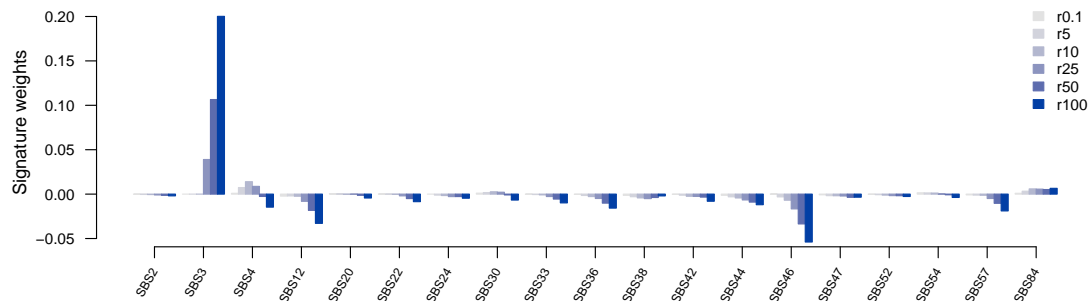


Figure 4.8: Signature weights differences from normal for SBS3 spike-in; Weights were deconstructed with QP method in MisMatchFinder and the weights assigned to the normal sample used for the spike-in were subtracted; Only Signatures with original weight $\geq 1\%$ or a minimum difference of 0.5% are shown. The full weights can be seen in [Figure C.3](#); r_{0.1} corresponds to 0.1 mutations per megabase (264 variants) and r₁₀₀ is the equivalent of 100 mutations per megabase (285367 variants)

4.3.1.3 Germline filtering

With real patient data, we can evaluate the effect of removing germline variants from the analysis is. For this I used the same simulated samples from above ([Section 4.3.1.2](#)), where the reads are original ctDNA sequencing reads from a healthy person. These reads will have a natural background germline variant signature.

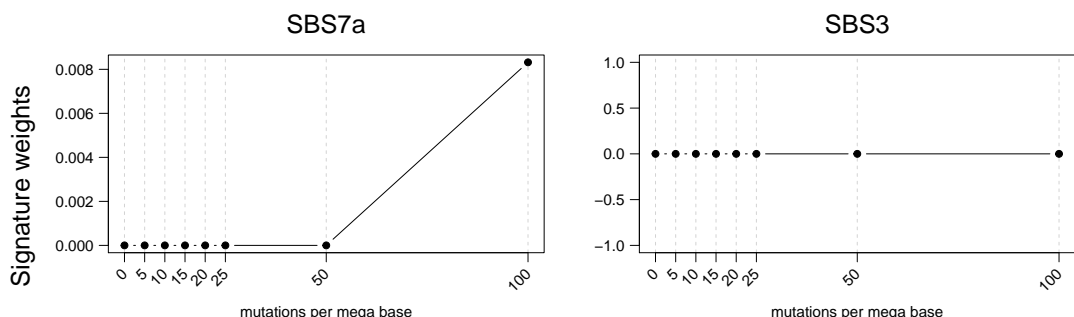


Figure 4.9: Signature analysis without germline variant filtering; Weights were deconstructed with QP method in MisMatchFinder, but in contrast to [Figure 4.6](#), the filter removing all known germline variants was disabled

In stark contrast to the previous analysis ([Figure 4.6](#)), when retaining mismatches in known germline variant sites, the sensitivity of the method reduces significantly. Only for the SBS7a spike-in at the very highest mutation frequency (100 mutations per mega base) a signal is detected. This signal is still weaker than what was previously found with just 10 mutations per mega base. Unsurprisingly SBS3 performs worse, just as before, and no signal is detected at all ([Figure 4.9](#)).

This extreme change is caused by the much higher number of mismatches which were used in the

analysis (≈ 1.8 Mio without germline filter and $\approx 130K$ with germline filter). This increase in mismatches in the analysis dilutes the spike-in variants. Figure 4.10 shows that without the germline filter the additional found mismatches never exceeds 5% which seems to be the detection threshold for SBS7a, as with germline filtering this threshold corresponds nicely with the arise of SBS7a weight in those samples (Figure 4.6).

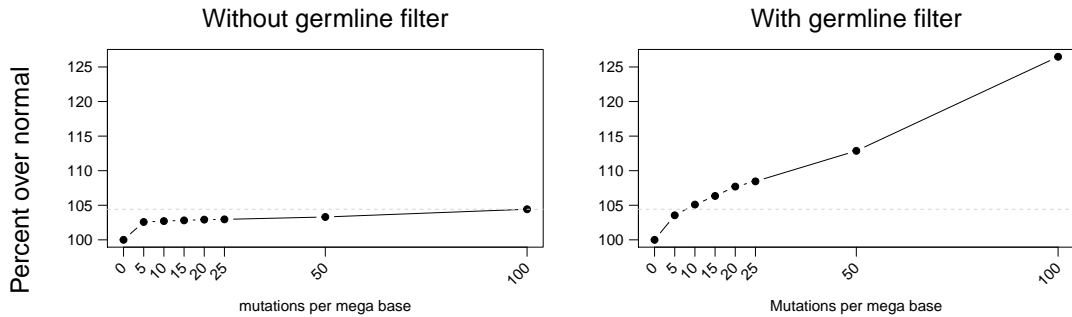


Figure 4.10: Percent increase of mismatches in analysis with and without germline filter; Values are normalised to the number of mismatches found in the normal sample (depicted as 0 mutations per mega base); dotted grey line shows the maximum increase in the left panel (without germline filter)

While we already know that the spike-in variants were not detected when retaining germline variant sites, the signatures detected in the normal sample are vastly different as well. Without the germline filter, the most prevalent signatures are SBS1 and SBS5 which are thought to be molecular clock like signatures, related to the age of the individual [209]. In the germline filtered analysis the most prevalent signatures are SBS4 (tobacco smoking), SBS12 (unknown) and SBS46 (sequencing artefact). In general it seems like the germline filter removes predominantly SBS1 and SBS5, while most other signatures remain the same (Figure 4.11).

As the sample was acquired through a healthy donor blood bank, we have no way to verify if the sample was or is a smoker.

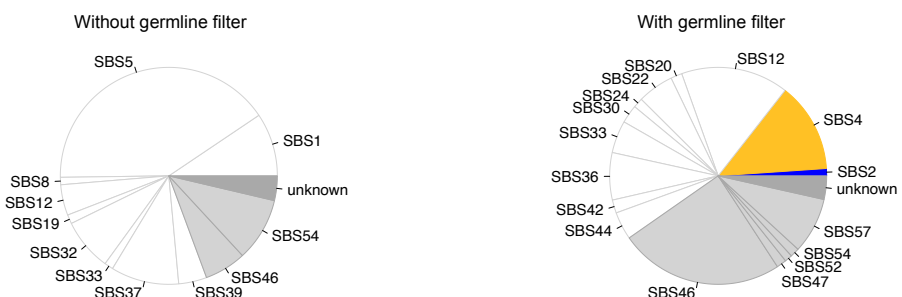


Figure 4.11: Signature weights of the normal sample with and without germline filter; MisMatchFinder derived signature weights with and without germline filter; weights below 1% contribution are accumulated in “unknown” (darkgrey), lightgrey signatures show sequencing artefact signatures, yellow shows smoking related signatures and blue depicts APOBEC signatures

This shows that germline filtering similar to the consensus overlap analysis is fundamentally important for the method to recover signal. In the following sections, unless further specified, the germline filter will be enabled for all analysis.

4.3.2 Real world data - the only things that matters

While simulated data is perfect to ensure the method performs as expected in edge cases and to estimate detection limits, only real world data allows the final examination if the model used for analysis can mirror biological concepts. To show our new method is usable for a variety of datasets, we used a mixture of different cancer types from various different sequencers. In [Section 4.3.2.2](#) I present the dataset of healthy individuals to show specificity of our method. Then in [Section 4.3.2.3](#) I present the analysis for metastatic breast cancer patients with matched tumour and germline sequencing. First how efficient germline filtering is in [Section 4.3.2.3.1](#) and then how accurate and sensitive our method is when compared to the current gold standard of tumour-normal tissue analysis ([Section 4.3.2.3.2](#)) and then the envisioned approach of tumour only analysis for clinical samples in [Section 4.3.2.3.3](#). These analysis were also performed on their melanoma equivalent in [Section 4.3.2.4.1](#) for the matched analysis and [Section 4.3.2.4.2](#) to show that the detection is not cancer specific.

4.3.2.1 Bias detection

This dataset of healthy samples is ideal to detect biases, because any variability that cannot be accounted to either age or gender is unwanted and will affect the cancer samples in the same way. We expect an increased mismatch rate in the older individuals due to the accumulation of somatic mutations due to “clock like signatures” [[256](#)]. In contrast, the tumour samples should show a bias with respect to higher tumour purities, as higher amount of tumour reads would lead to a higher amount of mismatches from somatic mutations. To verify that our assumptions are correct, we performed a principle component analysis (PCA) of the raw tri-nucleotide mismatch count numbers of each sample which MisMatchFinder can report alongside the weights of signatures.

Neither age, nor sex of the sample seemed to have any influence on the mismatches of the sample [Figure 4.12A, B](#). That age of the patient does not seem to influence the result could be a side effect of the germline filtering, where a somatic variant is filtered, if it happens at a known germline site ([Section 4.3.1.3](#)). However age not being a confounding factor is positive. In contrast, there seems

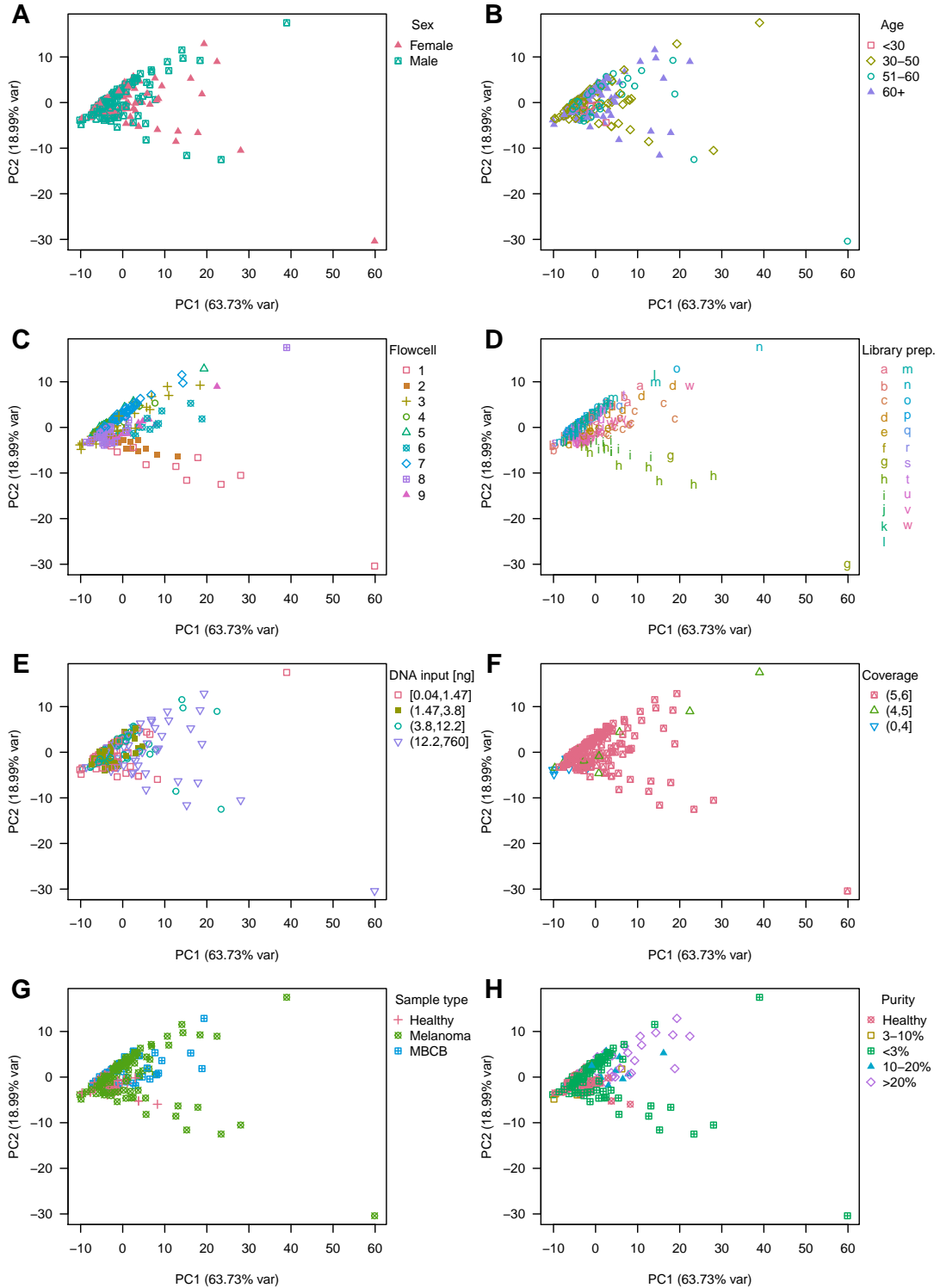


Figure 4.12: PCA (PC1 and PC2) of tri-nucleotide mismatch counts of healthy donor and tumour samples (melanoma and metastatic breast cancer) of varying purity; PCA was conducted on scaled and centered data

to be a batch effect like structure with regards to the used flowcell on the sequencer and library preparation (Figure 4.12C, D). As these two are fairly intertwined, it is almost impossible to tease

the two apart, however it seems like the flowcell bias is overarching multiple library preparations. Flowcell 1 contains samples from both 'g' and 'h' and flowcell 3 both 'a' and 'd', suggesting that the flowcell has more influence than the preparation. This is consistent with recent literature, which suggests, that there are more and less error prone flow cells [152].

While there is a slight bias towards higher PC1 values for higher DNA input samples, which might be due to a higher library complexity when sequencing, it is fairly minor and this bias exists for every other method using de-duplicated sequencing data as it might have an effect on the non-redundant data available (Figure 4.12E). Similarly, the very low coverage samples are at the very left of PC1, there is a substantial spread along the axis for the higher coverage samples as well (Figure 4.12F).

And just as we expected from the model and the biology, there is a hint of a separation for both tumour type and tumour purity, with the higher purity samples oriented toward the top right and the healthy and lower purity samples at the left (Figure 4.12G, H).

These tendencies can also be observed when looking at PC2 and PC3 (Figure C.4). PC3 still accounts for $\approx 9\%$ of the observed variability and PC6 is the first component with an eigenvalue smaller than 1 suggesting that only the first five components should be retained for further analysis (explaining a cumulative 97.3% of the variance). However, as we use the counts for signature deconstruction the PCA analysis only served as a quality control.

4.3.2.2 Healthy cohort

We sequenced the 60 healthy samples, from varying age groups (24 yrs.-70 yrs. median: 48.5 yrs.) with 24 males and 36 females, in the exact same way as the tumour only samples for MBCB and melanoma (Section 4.3.2.3.3 and Section 4.3.2.4.2 respectively) to an effective average coverage of 8x WGS, with mixed healthy samples and cancer samples on sequencing flow cells to account for batch effects.

add the age via mismatchrate plot

[257]

4.3.2.2.1 Black list generation

With the strong influence filtering our both technical errors (Section 4.3.1.1) and germline variants (Section 4.3.1.3) as background noise had on our method, we hypothesised that a blacklist of mismatches found in our healthy individuals would help us further cut down on unwanted background signal and refine the somatic mismatch calls. I therefore ran mismatchfinder with significantly relaxed quality cut-offs to capture as much variation as possible. This includes a reduction in mapping quality and base quality as well as not restricting the analysis to the highly accurate overlap part of the paired end reads. However we still restricted the analysis to the same highly mappable areas of the genome the same as for the tumour analysis as well as filtering already known germline variants for a better estimation of the impact of this filter step.

The site files generated through MisMatchFinder were then concatenated and aggregated to multiple blacklists with cut-offs of a variant present in at least 3, 5 or 10 times. The bash code used for the post processing of MisMatchFinder site files can be found in Listing 4.1.

Listing 4.1: Blacklist postprocessing

```

1 awkCounting=$(cat << 'AWK '
2 {
3     key=$1"\t"$2"\t"$3"\t"$4
4     counts[key]++;
5 }
6 END{
7     for(i in counts){
8         occ = counts[i]
9         if(occ >= 3){
10            print i"\t"counts[i] > "healthy_blacklist_sites_m3.tsv"
11        }
12        if(occ >= 5){
13            print i"\t"counts[i] > "healthy_blacklist_sites_m5.tsv"
14        }
15        if(occ >= 10){
16            print i"\t"counts[i] > "healthy_blacklist_sites_m10.tsv"
17        }
18    }
19 }
20 AWK
21 )

```

```
23 cat *_sites.tsv | awk "$awkCounting"
```

Add the health cohort in there/ possible age

4.3.2.3 MBCB patient samples

are they
actually
published?

The first dataset of patients is two previously published BRCA1/2 positive breast cancers. The data contains matched tumour, germline and ctDNA sequencing as high depth WGS for both patients. With the matched normal, we can use the current standard protocol of somatic mutational pattern analysis ([Section 4.1.1](#)) and compare it with our new method ([Section 4.3.2.3.2](#)).

As the sequencing data of the ctDNA is much higher depth than what is used in standard clinical practice, we down sample the data to 10x coverage, which is also the coverage of the simulated data. By using numerous different seeds for the sampling, we can generate pseudo technical replicates of the sequencing ([Section C.3.5](#)), which then in term can give an approximation of the stability of the results for both the tissue and the ctDNA samples .

And secondly we analysed a set of tumour only sequencing samples, how they would be available in clinical testing, e.g. copy number analysis [[258](#), [259](#)]. To show that our method can be applied to supply additional clinically relevant information from already available data ([Section 4.3.2.3.3](#)).

add the subsampled data

4.3.2.3.1 Germline artifacts

As I have pointed out above, how important the germline filter step is to boost the signal of somatic variants ([Section 4.2.6](#)), we were interested how many germline variants were not filtered out with our method. The high depth matched healthy WGS samples of the breast cancer dataset is ideal for this analysis. I called germline variants on the matched normal using Strelka2 and compared the called variants with the sites which MisMatchFinder found to be somatic (retained after germline filtering) on the sub-sampled data. All variants with any quality filter assigned by Strelka2 were considered for this analysis, such that possible clonal hematopoiesis (CH) variants are still considered. [Table 4.1](#) shows that on average 2100 germline variants are not filtered out. However, this only equates to 0.9% for MBCB196 and 1.5% for MBCB298 of all sites found to be mutated. The exact numbers depend on the strictness of the parameters of the analysis as well as the mutation rate of the

Table 4.1: Germline variants retained after germline filtering with in MisMatchFinder analysis; Default parameters were used when running MisMatchFinder with gnomAD zarr for filtering. seed column shows the seed used to subsample the high depth sequencing BAM, “mismatch sites” column contains number of sites found to be changed, “germline sites” contains the number of sites also found with germline variant calling, fraction shows fraction of column 4 and 3

Patient ID	seed	mismatch sites	germline sites	fraction
MBCB196	1007	216 950	2107	0.0097
	1234	217 145	2073	0.0095
	1337	216 823	2080	0.0096
	1717	217 593	2089	0.0096
	2358	217 317	2097	0.0096
	3311	217 219	2046	0.0094
	5229	216 876	2062	0.0095
	6060	217 388	2080	0.0096
	9876	217 656	2008	0.0092
	1756	148 495	2168	0.0146
MBCB298	3599	149 901	2224	0.0148
	4117	149 382	2277	0.0152
	4306	149 549	2248	0.0150
	4359	149 805	2205	0.0147
	5788	150 103	2241	0.0149
	5887	150 099	2287	0.0152
	8387	149 533	2248	0.0150
	9754	149 547	2229	0.0149

sample, but with default parameters a similar result should be expected with other samples. The germline variant removal is very effective filtering the 3.75 (MBCB196) and 3.76 (MBCB298) million germline SNPs called by Strelka2 to less than 0.05% of the original. As the genetic background in gnomAD is not balanced and shows a lack of non-european ancestry data [260], this filtering could become less effective when analysing samples from indigenous or otherwise genetically less characterised patients, as their germline variants might not be recorded yet.

Nevertheless, this result combined with the effective filtering of technical errors (Section 4.3.1.1) suggests, that the remaining sites are somatic mutations of either the healthy tissue or the cancer.

add section about somatic variants that are wrongfully filtered

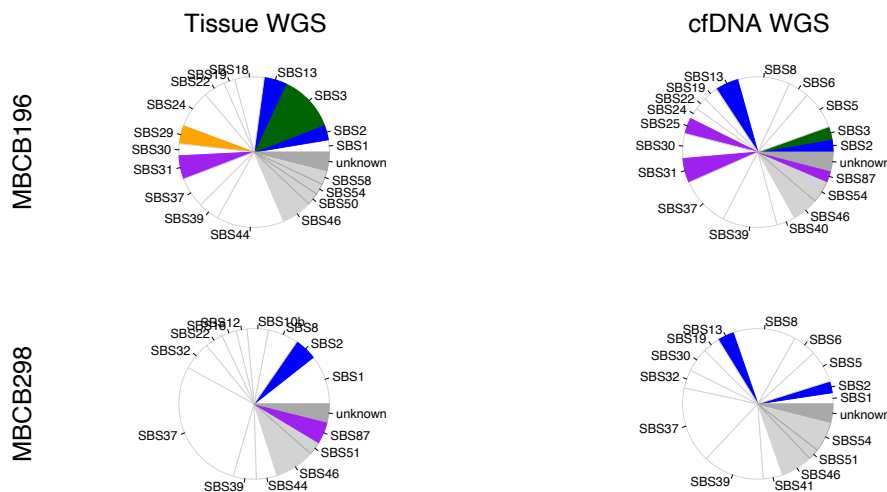


Figure 4.13: Signature weights for the WGS of two MBCB patients; Colours show cancer associated signatures: blue (APOBEC), red (UV exposure), orange (tobacco), purple (chemotherapy), light grey (sequencing artefacts), dark grey (everything below 1% weight)

4.3.2.3.2 Matched WGS samples - when you know what the results should be

4.3.2.3.3 Tumour only WGS samples - the large scale clinical approach

4.3.2.4 Melanoma patients

For melanoma real world data, we analysed multiple datasets, which allowed to highlight and dissect specific aspects of signature detection from lcWGS when dealing with melanoma. First I will show the results on a set of two patients, were WES of tumour tissue, normal tissue and both cfDNA samples is available on top of lcWGS of the cfDNA ([Section 4.3.2.4.1](#)) and then I will highlight the results of the analysis of a bigger dataset of melanoma patients without matched normals but with varying tumour fraction ([Section 4.3.2.4.2](#)).

4.3.2.4.1 Matched WES samples - when you know what the results should be

With the help of the WES of both the tissue and the cfDNA samples, we know what the expected outcome for each of the lcWGS samples is, as the standard procedure for signature detection starts with somatic variants. Strelka2 was used to call somatic variants and the high confidence somatic SNPs were then used in R to generate signature weights with sigminer using default parameters for the GRCh38 genome build and the QP deconstruction method [[261](#)].

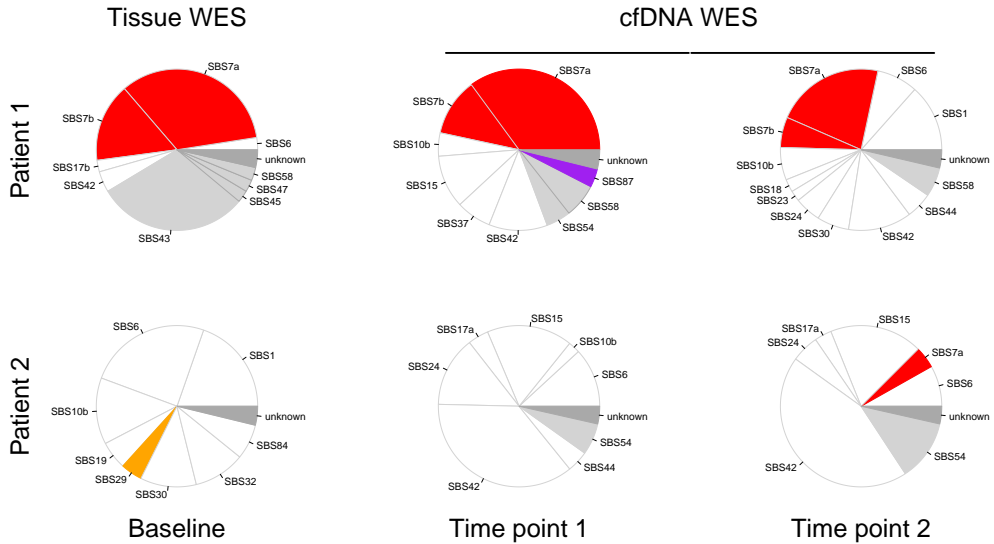


Figure 4.14: Signature weights for the WES of two melanoma patients; First column shows the results for the tissue baseline and middle and right column show the cfDNA; Colours show cancer associated signatures: blue (APOBEC), red (UV exposure), orange (tobacco), purple (chemotherapy), light grey (sequencing artefacts), dark grey (everything below 1% weight)

For Patient 1, both the tissue as well as the cfDNA samples show a very high signature weight related to UV radiation SBS7a and SBS7b (combined $\geq 30\%$ however patient 2 only shows very little SBS7a in only the cfDNA samples.

4.3.2.4.2 Large detection level cohort - how sensitive can we be?

4.3.3 Summary

Dont know if we need this

“As you think, so you become. Our busy minds are forever jumping to conclusions, manufacturing and interpreting signs that aren’t there.“

— Epictetus, *The Enchiridion*

5

Conclusion

we should have some stuff to write here in the end

Bibliography

- [1] Ibiayi Dagogo-Jack and Alice T. Shaw. "Tumour heterogeneity and resistance to cancer therapies". In: *Nature Reviews Clinical Oncology* 15.2 (Nov. 2017), pp. 81–94. doi: [10.1038/nrclinonc.2017.166](https://doi.org/10.1038/nrclinonc.2017.166).
- [2] R. Fisher, L. Pusztai, and C. Swanton. "Cancer heterogeneity: implications for targeted therapeutics." In: *British journal of cancer* 108 (3 Feb. 2013), pp. 479–485. issn: 1532-1827. doi: [10.1038/bjc.2012.581](https://doi.org/10.1038/bjc.2012.581). ppublish.
- [3] Tracy L. Leong et al. "Deep multi-region whole-genome sequencing reveals heterogeneity and gene-by-environment interactions in treatment-naive, metastatic lung cancer". In: *Oncogene* 38.10 (Oct. 2018), pp. 1661–1675. doi: [10.1038/s41388-018-0536-1](https://doi.org/10.1038/s41388-018-0536-1).
- [4] Ting Yan et al. "Multi-region sequencing unveils novel actionable targets and spatial heterogeneity in esophageal squamous cell carcinoma". In: *Nature Communications* 10.1 (Apr. 2019). doi: [10.1038/s41467-019-109255-1](https://doi.org/10.1038/s41467-019-109255-1).
- [5] The Centos Project. *Centos* 7. July 2014. url: <https://www.centos.org/> (visited on 10/26/2021).
- [6] Free Software Foundation. *Bash (3.2.48)*. [Unix shell program]. Version 5.1.8(1)-release. 2007. url: <http://ftp.gnu.org/gnu/bash/bash-3.2.48.tar.gz>.
- [7] Ole Tange et al. "GNU Parallel - The Command-Line Power Tool". In: *login: The USENIX Magazine* 36.1 (Feb. 2011), pp. 42–47.
- [8] R Core Team. *R: A Language and Environment for Statistical Computing*. R Foundation for Statistical Computing. Vienna, Austria, 2021. url: <https://www.R-project.org/>.
- [9] Martin Morgan et al. *BiocParallel: Bioconductor facilities for parallel evaluation*. R package version 1.24.1. 2020. url: <https://github.com/Bioconductor/BiocParallel>.
- [10] Martin Morgan. *BiocManager: Access the Bioconductor Project Package Repository*. R package version 1.30.10. 2019. url: <https://CRAN.R-project.org/package=BiocManager>.
- [11] Achim Zeileis, Kurt Hornik, and Paul Murrell. "Escaping RGBland: Selecting colors for statistical graphics". In: *Computational Statistics & Data Analysis* 53.9 (July 2009), pp. 3259–3270. doi: [10.1016/j.csda.2008.11.033](https://doi.org/10.1016/j.csda.2008.11.033).
- [12] Achim Zeileis et al. "colorspace: A Toolbox for Manipulating and Assessing Colors and Palettes". In: *Journal of Statistical Software* 96.1 (2020). doi: [10.18637/jss.v096.i01](https://doi.org/10.18637/jss.v096.i01).
- [13] F. Favero et al. "Sequenza: allele-specific copy number and mutation profiles from tumor sequencing data". In: *Annals of Oncology* 26.1 (Jan. 2015), pp. 64–70. doi: [10.1093/annonc/mdu479](https://doi.org/10.1093/annonc/mdu479).

- [14] Ronglai Shen and Venkatraman E. Seshan. “FACETS: allele-specific copy number and clonal heterogeneity analysis tool for high-throughput DNA sequencing”. In: *Nucleic Acids Research* 44.16 (June 2016), e131–e131. doi: [10.1093/nar/gkw520](https://doi.org/10.1093/nar/gkw520).
- [15] Venkatraman E. Seshan and Ronglai Shen. *facets: Cellular Fraction and Copy Numbers from Tumor Sequencing*. R package version 0.6.0. 2018. url: <https://github.com/mskcc/facets> (visited on 09/29/2021).
- [16] Daniel L. Cameron et al. “GRIDSS, PURPLE, LINX: Unscrambling the tumor genome via integrated analysis of structural variation and copy number”. In: *bioRxiv* (Sept. 2019). doi: [10.1101/781013](https://doi.org/10.1101/781013).
- [17] Gro Nilsen et al. “Copynumber: Efficient algorithms for single- and multi-track copy number segmentation”. In: *BMC Genomics* 13.1 (Nov. 2012). doi: [10.1186/1471-2164-13-591](https://doi.org/10.1186/1471-2164-13-591).
- [18] Gro Nilsen, Knut Liestol, and Ole Christian Lingjaerde. *copynumber: Segmentation of single- and multi-track copy number data by penalized least squares regression*. R package version 1.29. 2021.
- [19] William McLaren et al. “The Ensembl Variant Effect Predictor”. In: *Genome Biology* 17.1 (June 2016). doi: [10.1186/s13059-016-0974-4](https://doi.org/10.1186/s13059-016-0974-4).
- [20] Matt Dowle and Arun Srinivasan. *data.table: Extension of ‘data.frame’*. R package version 1.14.0. 2021. url: <https://CRAN.R-project.org/package=data.table>.
- [21] Daniel Adler and S. Thomas Kelly. *vioplot: violin plot*. R package version 0.3.5. 2020. url: <https://github.com/TomKellyGenetics/vioplot>.
- [22] Zuguang Gu, Roland Eils, and Matthias Schlesner. “Complex heatmaps reveal patterns and correlations in multidimensional genomic data”. In: *Bioinformatics* 32 (May 2016), pp. 2847–2849. doi: [10.1093/bioinformatics/btw313](https://doi.org/10.1093/bioinformatics/btw313).
- [23] Emmanuel Paradis and Klaus Schliep. “ape 5.0: an environment for modern phylogenetics and evolutionary analyses in R”. In: *Bioinformatics* 35.3 (July 2018). Ed. by Russell Schwartz, pp. 526–528. doi: [10.1093/bioinformatics/bty633](https://doi.org/10.1093/bioinformatics/bty633).
- [24] Klaus Schliep et al. “Intertwining phylogenetic trees and networks”. In: *Methods in Ecology and Evolution* 8.10 (Apr. 2017). Ed. by Richard Fitzjohn, pp. 1212–1220. doi: [10.1111/2041-210X.12760](https://doi.org/10.1111/2041-210X.12760).
- [25] Tal Galili. “dendextend: an R package for visualizing, adjusting and comparing trees of hierarchical clustering”. In: *31.22* (July 2015), pp. 3718–3720. doi: [10.1093/bioinformatics/btv428](https://doi.org/10.1093/bioinformatics/btv428).

- [26] Jennifer Bryan. *googlesheets4: Access Google Sheets using the Sheets API V4*. R package version 1.0.0. 2021. url: <https://CRAN.R-project.org/package=googlesheets4>.
- [27] Martin Morgan et al. *Rsamtools: Binary alignment (BAM), FASTA, variant call (BCF), and tabix file import*. R package version 2.8.0. 2021. url: <https://bioconductor.org/packages/Rsamtools>.
- [28] Michael Lawrence et al. “Software for Computing and Annotating Genomic Ranges”. In: *PLoS Computational Biology* 9.8 (8 Aug. 2013). Ed. by Andreas Prlic, e1003118. doi: [10.1371/journal.pcbi.1003118](https://doi.org/10.1371/journal.pcbi.1003118).
- [29] Trevor L Davis. *optparse: Command Line Option Parser*. R package version 1.6.6. 2020. url: <https://CRAN.R-project.org/package=optparse>.
- [30] Valerie Obenchain et al. “VariantAnnotation: a Bioconductor package for exploration and annotation of genetic variants”. In: *Bioinformatics* 30.14 (2014), pp. 2076–2078. doi: [10.1093/bioinformatics/btu168](https://doi.org/10.1093/bioinformatics/btu168).
- [31] Marcel Ramos et al. “Software for the integration of multi-omics experiments in Bioconductor”. In: *Cancer Research* 77(21); e39-42 (June 2017). doi: [10.1101/144774](https://doi.org/10.1101/144774).
- [32] Zuguang Gu et al. “circlize implements and enhances circular visualization in R”. In: *Bioinformatics* 30.19 (19 June 2014), pp. 2811–2812. doi: [10.1093/bioinformatics/btu393](https://doi.org/10.1093/bioinformatics/btu393).
- [33] Jitao David Zhang et al. “Detect tissue heterogeneity in gene expression data with BioQC”. In: *BMC Genomics* 18.1 (Apr. 2017), p. 277. doi: [10.1186/s12864-017-3661-2](https://doi.org/10.1186/s12864-017-3661-2). url: <http://accio.github.io/BioQC/>.
- [34] H. Pagès et al. *Biostrings: Efficient manipulation of biological strings*. R package version 2.58.0. 2020. url: <https://bioconductor.org/packages/Biostrings>.
- [35] Rachel Rosenthal. *deconstructSigs: Identifies Signatures Present in a Tumor Sample*. R package version 1.8.0. 2016. url: <https://CRAN.R-project.org/package=deconstructSigs>.
- [36] Hervé Pagès. *BSgenome: Software infrastructure for efficient representation of full genomes and their SNPs*. R package version 1.58.0. 2020. url: <https://bioconductor.org/packages/BSgenome>.
- [37] Ilari Scheinin et al. “DNA copy number analysis of fresh and formalin-fixed specimens by shallow whole-genome sequencing with identification and exclusion of problematic regions in the genome assembly”. In: *Genome Research* 24.12 (Sept. 2014), pp. 2022–2032. doi: [10.1101/gr.175141.114](https://doi.org/10.1101/gr.175141.114).

- [38] Erich Neuwirth. *RColorBrewer: ColorBrewer Palettes*. R package version 1.1-2. 2014. url: <https://CRAN.R-project.org/package=RColorBrewer>.
- [39] Raivo Kolde. *pheatmap: Pretty Heatmaps*. R package version 1.0.12. 2019. url: <https://CRAN.R-project.org/package=pheatmap>.
- [40] Valerie Obenchain and Lori Shepherd. *ensemblVEP: R Interface to Ensembl Variant Effect Predictor*. R package version 1.32.0. 2020.
- [41] M.P.J. van der Loo. “The stringdist Package for Approximate String Matching”. In: *The R Journal* 6.1 (1 2014), pp. 111–122. doi: [10.32614/rj-2014-011](https://doi.org/10.32614/rj-2014-011). url: <https://CRAN.R-project.org/package=stringdist>.
- [42] Yang Liao, Gordon K. Smyth, and Wei Shi. “The R package Rsubread is easier, faster, cheaper and better for alignment and quantification of RNA sequencing reads”. In: *Nucleic Acids Research* 47.8 (8 Feb. 2019), e47–e47. doi: [10.1093/nar/gkz114](https://doi.org/10.1093/nar/gkz114).
- [43] Hadley Wickham et al. *svglite: An 'SVG' Graphics Device*. R package version 2.0.0. 2021. url: <https://CRAN.R-project.org/package=svglite>.
- [44] Paul Murrell. “Importing Vector Graphics: The grImport Package for R”. In: *Journal of Statistical Software* 30.4 (2009), pp. 1–37. doi: [10.18637/jss.v030.i04](https://doi.org/10.18637/jss.v030.i04). url: <http://www.jstatsoft.org/v30/i04/>.
- [45] Duncan Temple Lang. *XML: Tools for Parsing and Generating XML Within R and S-Plus*. R package version 3.99-0.5. 2020. url: <https://CRAN.R-project.org/package=XML>.
- [46] Hao Zhu. *kableExtra: Construct Complex Table with 'kable' and Pipe Syntax*. R package version 1.3.4. 2021. url: <https://CRAN.R-project.org/package=kableExtra>.
- [47] Fridolin Wild. *lsa: Latent Semantic Analysis*. R package version 0.73.2. 2020. url: <https://CRAN.R-project.org/package=lsa>.
- [48] Jim Baglama, Lothar Reichel, and B. W. Lewis. *irlba: Fast Truncated Singular Value Decomposition and Principal Components Analysis for Large Dense and Sparse Matrices*. R package version 2.3.3. 2019. url: <https://CRAN.R-project.org/package=irlba>.
- [49] Hadley Wickham. *ggplot2: Elegant Graphics for Data Analysis*. Springer-Verlag New York, June 8, 2016. 260 pp. isbn: 978-3-319-24277-4. url: <https://ggplot2.tidyverse.org>.
- [50] Guido VanRossum. *The Python language reference*. Hampton, NHRedwood City, Calif: Python Software FoundationSoHo Books, 2010. isbn: 9781441412690.

- [51] Charles R. Harris et al. “Array programming with NumPy”. In: *Nature* 585.7825 (Sept. 2020), pp. 357–362. doi: [10.1038/s41586-020-2649-2](https://doi.org/10.1038/s41586-020-2649-2).
- [52] Endre Bakken Stovner and Pål Sætrom. “PyRanges: efficient comparison of genomic intervals in Python”. In: *Bioinformatics* (Aug. 2019). Ed. by John Hancock. doi: [10.1093/bioinformatics/btz615](https://doi.org/10.1093/bioinformatics/btz615).
- [53] Andreas Heger, Kevin Jacobs, et al. *pysam: htslib interface for python*. Oct. 25, 2021. url: <https://github.com/pysam-developers/pysam> (visited on 10/26/2021).
- [54] James K Bonfield et al. “HTSlib: C library for reading/writing high-throughput sequencing data”. In: *GigaScience* 10.2 (Jan. 2021). doi: [10.1093/gigascience/giaboo7](https://doi.org/10.1093/gigascience/giaboo7).
- [55] Petr Danecek et al. “Twelve years of SAMtools and BCFtools”. In: *GigaScience* 10.2 (Jan. 2021). doi: [10.1093/gigascience/giaboo8](https://doi.org/10.1093/gigascience/giaboo8).
- [56] Alistair Miles et al. *zarr-developers/zarr-python: v2.10.2*. 2021. doi: [10.5281/ZENODO.5579625](https://doi.org/10.5281/ZENODO.5579625).
- [57] Wes McKinney et al. “Data Structures for Statistical Computing in Python”. In: *Proceedings of the 9th Python in Science Conference*. Vol. 445. Austin, TX. SciPy, 2010, pp. 51–56. doi: [10.25080/majora-92bf1922-00a](https://doi.org/10.25080/majora-92bf1922-00a).
- [58] Jeff Reback et al. *pandas-dev/pandas: Pandas 1.3.4*. 2021. doi: [10.5281/ZENODO.5574486](https://doi.org/10.5281/ZENODO.5574486).
- [59] Robert T. McGibbon et al. *quadprog: Quadratic Programming Solver (Python)* v0.1.10. Oct. 1, 2021. url: <https://github.com/quadprog/quadprog> (visited on 10/26/2021).
- [60] Pauli Virtanen et al. “SciPy 1.0: fundamental algorithms for scientific computing in Python”. In: *Nature Methods* 17.3 (Feb. 2020), pp. 261–272. doi: [10.1038/s41592-019-0686-2](https://doi.org/10.1038/s41592-019-0686-2).
- [61] J. D. Watson and F. H. C. Crick. “Molecular Structure of Nucleic Acids: A Structure for Deoxyribose Nucleic Acid”. In: *Nature* 171.4356 (Apr. 1953), pp. 737–738. doi: [10.1038/171737a0](https://doi.org/10.1038/171737a0).
- [62] F. Liang et al. “Homology-directed repair is a major double-strand break repair pathway in mammalian cells”. In: *Proceedings of the National Academy of Sciences* 95.9 (Apr. 1998), pp. 5172–5177. doi: [10.1073/pnas.95.9.5172](https://doi.org/10.1073/pnas.95.9.5172).
- [63] Richard R. Sinden. “Introduction to the Structure, Properties, and Reactions of DNA”. In: *DNA Structure and Function*. Elsevier, 1994, pp. 1–57. doi: [10.1016/b978-0-08-057173-7.50006-7](https://doi.org/10.1016/b978-0-08-057173-7.50006-7).
- [64] J. Craig Venter et al. “The Sequence of the Human Genome”. In: *Science* 291.5507 (Feb. 2001), pp. 1304–1351. doi: [10.1126/science.1058040](https://doi.org/10.1126/science.1058040).

- [65] Colin M. Hammond et al. “Histone chaperone networks shaping chromatin function”. In: *Nature Reviews Molecular Cell Biology* 18.3 (Jan. 2017), pp. 141–158. doi: [10.1038/nrm.2016.159](https://doi.org/10.1038/nrm.2016.159).
- [66] Boyan Bonev and Giacomo Cavalli. “Organization and function of the 3D genome”. In: *Nature Reviews Genetics* 17.11 (Oct. 2016), pp. 661–678. doi: [10.1038/nrg.2016.112](https://doi.org/10.1038/nrg.2016.112).
- [67] Tuguo Tateoka. “A contribution to the taxonomy of the Agrostis mertensii-flaccida complex (Poaceae) in Japan”. In: *The Botanical Magazine Tokyo* 88.2 (June 1975), pp. 65–87. doi: [10.1007/bf02491243](https://doi.org/10.1007/bf02491243).
- [68] R. Trivers and H Hare. “Haplodiploidy and the evolution of the social insect”. In: *Science* 191.4224 (Jan. 1976), pp. 249–263. doi: [10.1126/science.1108197](https://doi.org/10.1126/science.1108197).
- [69] Sarah P. Otto. “The Evolutionary Consequences of Polyploidy”. In: *Cell* 131.3 (Nov. 2007), pp. 452–462. doi: [10.1016/j.cell.2007.10.022](https://doi.org/10.1016/j.cell.2007.10.022).
- [70] Marvin I. Gottlieb et al. “Trisomy-17 syndrome”. In: *The American Journal of Medicine* 33.5 (Nov. 1962), pp. 763–773. doi: [10.1016/0002-9343\(62\)90253-x](https://doi.org/10.1016/0002-9343(62)90253-x).
- [71] Anna Cereda and John C Carey. “Trisomy 18 Syndrome”. In: *Atlas of Genetic Diagnosis and Counseling*. Vol. 7. 1. Humana Press, 2012, pp. 990–996. doi: [10.1186/1750-1172-7-81](https://doi.org/10.1186/1750-1172-7-81).
- [72] Maj A Hultén et al. “On the origin of trisomy 21 Down syndrome”. In: *Molecular Cytogenetics* 1.1 (2008), p. 21. doi: [10.1186/1755-8166-1-21](https://doi.org/10.1186/1755-8166-1-21).
- [73] David M. J. Lilley. “Structures of helical junctions in nucleic acids”. In: *Quarterly Reviews of Biophysics* 33.2 (May 2000), pp. 109–159. doi: [10.1017/s0033583500003590](https://doi.org/10.1017/s0033583500003590).
- [74] William P. Hanage, Christophe Fraser, and Brian G. Spratt. “The impact of homologous recombination on the generation of diversity in bacteria”. In: *Journal of Theoretical Biology* 239.2 (Mar. 2006), pp. 210–219. doi: [10.1016/j.jtbi.2005.08.035](https://doi.org/10.1016/j.jtbi.2005.08.035).
- [75] Ying Kong et al. “Homologous Recombination Drives Both Sequence Diversity and Gene Content Variation in *Neisseria meningitidis*”. In: *Genome Biology and Evolution* 5.9 (July 2013), pp. 1611–1627. doi: [10.1093/gbe/evt116](https://doi.org/10.1093/gbe/evt116).
- [76] Charles Darwin. “On the Origin of Species by Means of Natural Selection, or the Preservation of Favoured Races in the Struggle for Life”. In: *Evolutionary Writings*. Oxford University Press, May 2010. doi: [10.1093/owc/9780199580149.003.0005](https://doi.org/10.1093/owc/9780199580149.003.0005).
- [77] Kathleen Sprouffske et al. “High mutation rates limit evolutionary adaptation in *Escherichia coli*”. In: *PLOS Genetics* 14.4 (Apr. 2018). Ed. by Ivan Matic, e1007324. doi: [10.1371/journal.pgen.1007324](https://doi.org/10.1371/journal.pgen.1007324).

- [78] Ludmil B Alexandrov et al. “Clock-like mutational processes in human somatic cells”. In: *Nature Genetics* 47.12 (Nov. 2015), pp. 1402–1407. doi: [10.1038/ng.3441](https://doi.org/10.1038/ng.3441).
- [79] Luiza Moore et al. “The mutational landscape of human somatic and germline cells”. In: *Nature* (Aug. 2021). doi: [10.1038/s41586-021-03822-7](https://doi.org/10.1038/s41586-021-03822-7).
- [80] Hanan E. Shamseldin et al. “Identification of embryonic lethal genes in humans by autozygosity mapping and exome sequencing in consanguineous families”. In: *Genome Biology* 16.1 (June 2015). doi: [10.1186/s13059-015-0681-6](https://doi.org/10.1186/s13059-015-0681-6).
- [81] Laura Frey et al. “Mammalian VPS45 orchestrates trafficking through the endosomal system”. In: *Blood* 137.14 (Apr. 2021), pp. 1932–1944. doi: [10.1182/blood.2020006871](https://doi.org/10.1182/blood.2020006871).
- [82] Shan Dan et al. “Clinical application of massively parallel sequencing-based prenatal non-invasive fetal trisomy test for trisomies 21 and 18 in 11 105 pregnancies with mixed risk factors”. In: *Prenatal Diagnosis* 32.13 (Nov. 2012), pp. 1225–1232. doi: [10.1002/pd.4002](https://doi.org/10.1002/pd.4002).
- [83] Kypros H. Nicolaides et al. “Noninvasive Prenatal Testing for Fetal Trisomies in a Routinely Screened First-Trimester Population”. In: *Obstetrical & Gynecological Survey* 68.3 (Mar. 2013), pp. 173–175. doi: [10.1097/ogx.0b013e318285bf66](https://doi.org/10.1097/ogx.0b013e318285bf66).
- [84] Frank Diehl et al. “Circulating mutant DNA to assess tumor dynamics”. In: *Nature Medicine* 14.9 (July 2008), pp. 985–990. doi: [10.1038/nm.1789](https://doi.org/10.1038/nm.1789).
- [85] Heidi Schwarzenbach, Dave S. B. Hoon, and Klaus Pantel. “Cell-free nucleic acids as biomarkers in cancer patients”. In: *Nature Reviews Cancer* 11.6 (May 2011), pp. 426–437. doi: [10.1038/nrc3066](https://doi.org/10.1038/nrc3066).
- [86] R. Padmanabhan, E. Jay, and R. Wu. “Chemical Synthesis of a Primer and Its Use in the Sequence Analysis of the Lysozyme Gene of Bacteriophage T4”. In: *Proceedings of the National Academy of Sciences* 71.6 (June 1974), pp. 2510–2514. doi: [10.1073/pnas.71.6.2510](https://doi.org/10.1073/pnas.71.6.2510).
- [87] F. Sanger and A.R. Coulson. “A rapid method for determining sequences in DNA by primed synthesis with DNA polymerase”. In: *Journal of Molecular Biology* 94.3 (May 1975), pp. 441–448. doi: [10.1016/0022-2836\(75\)90213-2](https://doi.org/10.1016/0022-2836(75)90213-2).
- [88] F. Sanger, S. Nicklen, and A. R. Coulson. “DNA sequencing with chain-terminating inhibitors”. In: *Proceedings of the National Academy of Sciences* 74.12 (Dec. 1977), pp. 5463–5467. doi: [10.1073/pnas.74.12.5463](https://doi.org/10.1073/pnas.74.12.5463).
- [89] Eric S. Lander et al. “Initial sequencing and analysis of the human genome”. In: *Nature* 409 (Feb. 15, 2001): *The human genome*, pp. 860–921. doi: [10.1038/35057062](https://doi.org/10.1038/35057062).

- [90] Inc Illumina. *How short inserts affect sequencing performance*. Sept. 2020. url: <https://sapac.support.illumina.com/bulletins/2020/12/how-short-inserts-affect-sequencing-performance.html> (visited on 09/08/2021).
- [91] Elaine R. Mardis. “Next-Generation DNA Sequencing Methods”. In: *Annual Review of Genomics and Human Genetics* 9.1 (Sept. 2008), pp. 387–402. doi: [10.1146/annurev.genom.9.081307.164359](https://doi.org/10.1146/annurev.genom.9.081307.164359).
- [92] Jenny Straiton et al. “From Sanger sequencing to genome databases and beyond”. In: *BioTechniques* 66.2 (Feb. 2019), pp. 60–63. doi: [10.2144/btn-2019-0011](https://doi.org/10.2144/btn-2019-0011).
- [93] G. M. Church and W. Gilbert. “Genomic sequencing.” In: *Proceedings of the National Academy of Sciences* 81.7 (Apr. 1984), pp. 1991–1995. doi: [10.1073/pnas.81.7.1991](https://doi.org/10.1073/pnas.81.7.1991).
- [94] G. Church and S Kieffer-Higgins. “Multiplex DNA sequencing”. In: *Science* 240 (Apr. 1988), pp. 185–188. doi: [10.1126/science.3353714](https://doi.org/10.1126/science.3353714).
- [95] Alexander Payne et al. “BulkVis: a graphical viewer for Oxford nanopore bulk FAST5 files”. In: *Bioinformatics* 35.13 (Nov. 2018). Ed. by Inanc Birol, pp. 2193–2198. doi: [10.1093/bioinformatics/bty841](https://doi.org/10.1093/bioinformatics/bty841).
- [96] Ploy N. Pratanwanich et al. “Identification of differential RNA modifications from nanopore direct RNA sequencing with xPore”. In: *Nature Biotechnology* (July 2021). doi: [10.1038/s41587-021-00949-w](https://doi.org/10.1038/s41587-021-00949-w).
- [97] Nicolas L Bray et al. “Near-optimal probabilistic RNA-seq quantification”. In: *Nature Biotechnology* 34.5 (Apr. 2016), pp. 525–527. doi: [10.1038/nbt.3519](https://doi.org/10.1038/nbt.3519).
- [98] Rob Patro et al. “Salmon provides fast and bias-aware quantification of transcript expression”. In: *Nature Methods* 14.4 (Mar. 2017), pp. 417–419. doi: [10.1038/nmeth.4197](https://doi.org/10.1038/nmeth.4197).
- [99] Brian D. Ondov et al. “Mash: fast genome and metagenome distance estimation using MinHash”. In: *Genome Biology* 17.1 (June 2016). doi: [10.1186/s13059-016-0997-x](https://doi.org/10.1186/s13059-016-0997-x).
- [100] Brian B Luczak, Benjamin T James, and Hani Z Girgis. “A survey and evaluations of histogram-based statistics in alignment-free sequence comparison”. In: *Briefings in Bioinformatics* 20.4 (Dec. 2017), pp. 1222–1237. doi: [10.1093/bib/bbx161](https://doi.org/10.1093/bib/bbx161).
- [101] Heng Li. “Aligning sequence reads, clone sequences and assembly contigs with BWA-MEM”. In: (Mar. 16, 2013). arXiv: [1303.3997 \[q-bio.GN\]](https://arxiv.org/abs/1303.3997).

- [102] Ben Langmead et al. “Scaling read aligners to hundreds of threads on general-purpose processors”. In: *Bioinformatics* 35.3 (July 2018). Ed. by John Hancock, pp. 421–432. doi: [10.1093/bioinformatics/bty648](https://doi.org/10.1093/bioinformatics/bty648).
- [103] Klaus F. X. Mayer et al. “A chromosome-based draft sequence of the hexaploid bread wheat (*Triticum aestivum*) genome”. In: *Science* 345.6194 (July 2014), pp. 1251788–1251788. doi: [10.1126/science.1251788](https://doi.org/10.1126/science.1251788).
- [104] Erik Garrison and Gabor Marth. “Haplotype-based variant detection from short-read sequencing”. In: *arXiv preprint arXiv:1207.3907 [q-bio.GN]* (July 17, 2012). arXiv: <http://arxiv.org/abs/1207.3907v2> [q-bio.GN].
- [105] Zhongwu Lai et al. “VarDict: a novel and versatile variant caller for next-generation sequencing in cancer research”. In: *Nucleic Acids Research* 44.11 (Apr. 2016), e108–e108. doi: [10.1093/nar/gkw227](https://doi.org/10.1093/nar/gkw227).
- [106] Sangtae Kim et al. “Strelka2: fast and accurate calling of germline and somatic variants”. In: *Nature Methods* 15.8 (July 2018), pp. 591–594. doi: [10.1038/s41592-018-0051-x](https://doi.org/10.1038/s41592-018-0051-x).
- [107] David Benjamin et al. “Calling Somatic SNVs and Indels with Mutect2”. In: *bioRxiv* (Dec. 2019). doi: [10.1101/861054](https://doi.org/10.1101/861054).
- [108] Daniel P. Cooke, David C. Wedge, and Gerton Lunter. “A unified haplotype-based method for accurate and comprehensive variant calling”. In: *Nature Biotechnology* 39.7 (Mar. 2021), pp. 885–892. doi: [10.1038/s41587-021-00861-3](https://doi.org/10.1038/s41587-021-00861-3).
- [109] GATK Team. *Somatic calling is NOT simply a difference between two callsets*. Sept. 15, 2021. url: <https://gatk.broadinstitute.org/hc/en-us/articles/360035890491> (visited on 09/23/2021).
- [110] Amaro Taylor-Weiner et al. “DeTiN: overcoming tumor-in-normal contamination”. In: *Nature Methods* 15.7 (June 2018), pp. 531–534. doi: [10.1038/s41592-018-0036-9](https://doi.org/10.1038/s41592-018-0036-9).
- [111] Konrad J. Karczewski et al. “The mutational constraint spectrum quantified from variation in 141,456 humans”. In: *Nature* 581.7809 (May 2020), pp. 434–443. doi: [10.1038/s41586-020-2308-7](https://doi.org/10.1038/s41586-020-2308-7).
- [112] Ali Karimnezhad et al. “Accuracy and reproducibility of somatic point mutation calling in clinical-type targeted sequencing data”. In: *BMC Med Genomics* 13.1 (Oct. 2020). doi: [10.1186/s12920-020-00803-z](https://doi.org/10.1186/s12920-020-00803-z).
- [113] James Henry Breasted. “The Edwin Smith Surgical Papyrus: published in facsimile and hieroglyphic transliteration with translation and commentary in two volumes”. In: (1930).

- [114] Steven I Hajdu. "Greco-Roman thought about cancer". In: *Cancer* 100.10 (2004), pp. 2048–2051. doi: [10.1002/cncr.20198](https://doi.org/10.1002/cncr.20198).
- [115] John Chadwick and William N Mann. *The medical works of Hippocrates*. Oxford Blackwell Scientific Publications, 1950, pp. 124–147.
- [116] Celsus. "De Medicina". In: *British Journal of Surgery* 26.103 (Jan. 1939). With an english translation by W. G. Spencer, M.S. (Lond.), F.R.C.S. (Eng.), pp. 658–659. doi: [10.1002/bjs.18002610338](https://doi.org/10.1002/bjs.18002610338).
- [117] E. G. Browne. *Arabian medicine. the FitzPatrick lectures Delivered at the College of Physicians in November 1919 and November 1920*. Cambridge Library Collection - History of Medicine. Cambridge: Cambridge University Press, 2011. 154 pp. isbn: 9780511709296. doi: [10.1017/cbo9780511709296](https://doi.org/10.1017/cbo9780511709296).
- [118] J. E. Pilcher. "Guy de Chauliac and Henri de Mondeville,-A Surgical Retrospect." In: *Annals of surgery* 21 (1 Jan. 1895), pp. 84–102. issn: 0003-4932.
- [119] Paracelsus (Bombastus von Hohenheim TPA). "De Grandibus, de Compositionibus, et Dosisbus Receptorum ac Naturalium (Libri Septem)". In: (1562).
- [120] Marco Aurelio 1580-1656 Severino. *De recondita abscessuum natura libri VII*. Apud Octavium Beltranum, 1632.
- [121] Zacutus Lusitani. "Praxis Medical Admiranda". In: *Lugduni: J. Hugvetan* (1649).
- [122] Nicolai Tulpia. *Observationes Medicae*. Amstelredami, 1652.
- [123] Claude Deshaies-Gendron. *Recherches sur la nature et la guerison des cancers. Enquiries into the nature, knowledge, and cure of cancers. By Mr. Deshaies Gendron, ... Done out of French*. Print edition. Gale ECCO, 1701. 146 pp. isbn: 978-1385259078.
- [124] Steven I. Hajdu. "The First Printed Case Reports of Cancer. The First Printed Case Reports of Cancer". In: *Cancer* (2010). doi: [10.1002/cncr.25000](https://doi.org/10.1002/cncr.25000).
- [125] James Nooth. *Observations on the treatment of scirrhous tumours, and cancers of the breast*. G. and J. Robinson, 1804, p. 101.
- [126] Michael Etmüller. *ETMULLERUS ABRIDG'D : or, a compleat system of the theory and practice of physic being a ... description of all diseases incident to men, women*. Gale ECCO, 2018. isbn: 1385770074.

- [127] Lorenz Heister. *Kleine Chirurgie, oder, Wund-Artzney: in welcher ein kurzer doch deutlicher Unterricht und Begriff dieser Wissenschaft gegeben ... werden.* German. Nürnberg: Joh. Adam Stein und Gabriel Nicolaus Raspe, 1747.
- [128] Steven I. Hajdu. "A note from history: Landmarks in history of cancer, part 2". In: *Cancer* 117.12 (Dec. 2010), pp. 2811–2820. doi: [10.1002/cncr.25825](https://doi.org/10.1002/cncr.25825).
- [129] Johannes Müller. *Über den feinern Bau und die Formen der krankhaften Geschwülste : in zwei Lieferungen.* German. Reimer, 1838. url: <https://echo.mpiwg-berlin.mpg.de/ECHOdocuView?url=/permanent/library/84U9MMKo/pageimg&start=61&mode=imagepath&pn=66> (visited on 12/07/2021).
- [130] J.H. Bennett. *On Cancerous and Cancroid Growths.* Sutherland and Knox, 1849, pp. vi–viii. url: https://books.google.com.au/books?id=VQg%5C_AAAAcAAJ.
- [131] Rudolf ludwig Carl 10.1002/andp.18983000103 Virchow. *Die Krankhaften Geschwülste. dreissig Vorlesungen, gehalten während des Wintersemesters 1862-1863 an der Universität zu Berlin.* German. 3 vols. Berlin: Verlag von August Hirschwald, 1863. url: <http://resource.nlm.nih.gov/62231840R> (visited on 08/17/2021).
- [132] W. C. Röntgen. "Ueber eine neue Art von Strahlen". In: *Annalen der Physik* 300.1 (1898), pp. 12–17. doi: [10.1002/andp.18983000103](https://doi.org/10.1002/andp.18983000103).
- [133] EAFA Frieben. "Demonstration eines cancroids des rechten handrückens, das sich nach langdauernder einwirkung von roentgenstrahlen entwickelt hatte". In: *Forsch Roentgenstr* 6 (1902), pp. 106–111.
- [134] W Scholtz. "Ueber den Einfluss der Röntgenstrahlen auf die Haut in gesundem und krankem Zustande". In: *Archiv für Dermatologie und Syphilis* 59.3 (1902), pp. 421–446.
- [135] Paul Ehrlich. *Beiträge zur experimentellen Pathologie und Chemotherapie.* German. Germany, Leipzig: Akademische Verlagsgesellschaft, 1909, pp. 167–194. 247 pp. url: <https://id.lib.harvard.edu/curiosity/contagion/36-990061083080203941> (visited on 12/07/2021).
- [136] Otto Warburg. "Photochemie der Eisencarbonylverbindungen und das absolute Absorptionsspektrum des Atmungsferments". In: *Naturwissenschaften* 16.45-47 (1928), pp. 856–861.
- [137] Albert Claude, Keith R. Porter, and Edward G. Pickels. "Electron Microscope Study of Chicken Tumor Cells". In: *Cancer Research* 7.7 (1947), pp. 421–430. issn: 0008-5472. eprint: <https://cancerres.aacrjournals.org/content/7/7/421.full.pdf>. url: <https://cancerres.aacrjournals.org/content/7/7/421>.

- [138] Robert J Huebner and George J Todaro. “Oncogenes of RNA tumor viruses as determinants of cancer”. In: *Proceedings of the National Academy of Sciences* 64.3 (Nov. 1969), pp. 1087–1094. doi: [10.1073/pnas.64.3.1087](https://doi.org/10.1073/pnas.64.3.1087).
- [139] David Baltimore. “Viral RNA-dependent DNA polymerase: RNA-dependent DNA polymerase in virions of RNA tumour viruses”. In: *Nature* 226.5252 (June 1970), pp. 1209–1211. doi: [10.1038/2261209ao](https://doi.org/10.1038/2261209ao).
- [140] Howard M Temin, S Mizutami, et al. “RNA-dependent DNA polymerase in virions of Rous sarcoma virus.” In: *Cold Spring Harbor Symposia on Quantitative Biology* 226.0 (Jan. 1970), pp. 1211–1213. doi: [10.1101/sqb.1970.035.01.100](https://doi.org/10.1101/sqb.1970.035.01.100).
- [141] Frederick P Li and Joseph F Fraumeni Jr. “Rhabdomyosarcoma in children: epidemiologic study and identification of a familial cancer syndrome”. In: *Journal of the National Cancer Institute* 43.6 (1969), pp. 1365–1373.
- [142] Douglas Hanahan and Robert A Weinberg. “The Hallmarks of Cancer”. In: *Cell* 100.1 (Jan. 2000), pp. 57–70. doi: [10.1016/s0092-8674\(00\)81683-9](https://doi.org/10.1016/s0092-8674(00)81683-9).
- [143] Douglas Hanahan and Robert A. Weinberg. “Hallmarks of Cancer: The Next Generation”. In: *Cell* 144.5 (Mar. 2011), pp. 646–674. doi: [10.1016/j.cell.2011.02.013](https://doi.org/10.1016/j.cell.2011.02.013).
- [144] Yousef Ahmed Fouad and Carmen Aanei. “Revisiting the hallmarks of cancer.” In: *American journal of cancer research* 7 (5 2017), pp. 1016–1036. issn: 2156-6976. epublish.
- [145] Douglas Hanahan. “Hallmarks of Cancer: New Dimensions”. In: *Cancer Discovery* 12.1 (Jan. 2022), pp. 31–46. doi: [10.1158/2159-8290.cd-21-1059](https://doi.org/10.1158/2159-8290.cd-21-1059).
- [146] Elizabeth A. Kuczynski et al. “Vessel co-option in cancer.” In: *Nature Reviews Clinical Oncology* 16.8 (Feb. 2019), pp. 469–493. doi: [10.1038/s41571-019-0181-9](https://doi.org/10.1038/s41571-019-0181-9).
- [147] Javad Noorbakhsh et al. “Distribution-based measures of tumor heterogeneity are sensitive to mutation calling and lack strong clinical predictive power”. In: *Scientific Reports* 8.1 (July 2018). doi: [10.1038/s41598-018-29154-7](https://doi.org/10.1038/s41598-018-29154-7).
- [148] Ryan Poplin et al. “Scaling accurate genetic variant discovery to tens of thousands of samples”. In: *bioRxiv* (Nov. 2017). doi: [10.1101/201178](https://doi.org/10.1101/201178).
- [149] Neil A. Miller et al. “A 26-hour system of highly sensitive whole genome sequencing for emergency management of genetic diseases”. In: *Genome Medicine* 7.1 (Sept. 2015). doi: [10.1186/s13073-015-0221-8](https://doi.org/10.1186/s13073-015-0221-8).

- [150] Ryan Poplin et al. “A universal SNP and small-indel variant caller using deep neural networks”. In: *Nature Biotechnology* 36.10 (Sept. 2018), pp. 983–987. doi: [10.1038/nbt.4235](https://doi.org/10.1038/nbt.4235).
- [151] Melanie Schirmer et al. “Illumina error profiles: resolving fine-scale variation in metagenomic sequencing data”. In: *BMC Bioinformatics* 17.1 (Mar. 2016). doi: [10.1186/s12859-016-0976-y](https://doi.org/10.1186/s12859-016-0976-y).
- [152] Nicholas Stoler and Anton Nekrutenko. “Sequencing error profiles of Illumina sequencing instruments”. In: *NAR Genomics and Bioinformatics* 3.1 (Jan. 2021). doi: [10.1093/nargab/lqab019](https://doi.org/10.1093/nargab/lqab019).
- [153] Geraldine van der Auwera Brian O’Connor. *Genomics in the Cloud*. O’Reilly UK Ltd., May 1, 2020. 467 pp. isbn: 1491975199. url: <https://www.oreilly.com/library/view/genomics-in-the/9781491975183/>.
- [154] GATK Team. *Panel of Normals (PON)*. July 23, 2021. url: <https://gatk.broadinstitute.org/hc/en-us/articles/360035890631> (visited on 09/23/2021).
- [155] GATK Team. *Mutect2 multi-sample*. Sept. 25, 2020. url: <https://gatk.broadinstitute.org/hc/en-us/community/posts/360062528691> (visited on 10/23/2020).
- [156] Malvina Josephidou, Andy G. Lynch, and Simon Tavaré. “multiSNV: a probabilistic approach for improving detection of somatic point mutations from multiple related tumour samples”. In: *Nucleic Acids Research* 43.9 (Feb. 2015), e61–e61. doi: [10.1093/nar/gkv135](https://doi.org/10.1093/nar/gkv135).
- [157] Christoffer Flensburg et al. “SuperFreq: Integrated mutation detection and clonal tracking in cancer”. In: *PLOS Computational Biology* 16.2 (Feb. 2020). Ed. by Florian Markowetz, e1007603. doi: [10.1371/journal.pcbi.1007603](https://doi.org/10.1371/journal.pcbi.1007603).
- [158] Sebastian Hollizeck et al. “Custom workflows to improve joint variant calling from multiple related tumour samples: FreeBayesSomatic and Strelka2Pass”. In: *Bioinformatics* (Sept. 2021). Ed. by Can Alkan. doi: [10.1093/bioinformatics/btab606](https://doi.org/10.1093/bioinformatics/btab606).
- [159] Colby Chiang et al. “SpeedSeq: ultra-fast personal genome analysis and interpretation”. In: *Nature Methods* 12.10 (Aug. 2015), pp. 966–968. doi: [10.1038/nmeth.3505](https://doi.org/10.1038/nmeth.3505).
- [160] Brad Chapman et al. *bcbio/bcbio-nextgen: v1.2.4*. 2021. doi: [10.5281/ZENODO.3564938](https://doi.org/10.5281/ZENODO.3564938).
- [161] Brendan A. Veeneman et al. “Two-pass alignment improves novel splice junction quantification”. In: *Bioinformatics* 32 (Oct. 2015), pp. 43–49. doi: [10.1093/bioinformatics/btv642](https://doi.org/10.1093/bioinformatics/btv642).
- [162] Weichun Huang et al. “ART: a next-generation sequencing read simulator”. In: *Bioinformatics* 28.4 (Dec. 2011), pp. 593–594. doi: [10.1093/bioinformatics/btr708](https://doi.org/10.1093/bioinformatics/btr708).

- [163] Adam D. Ewing et al. “Combining tumor genome simulation with crowdsourcing to benchmark somatic single-nucleotide-variant detection”. In: *Nature Methods* 12 (May 2015), pp. 623–630. doi: [10.1038/nmeth.3407](https://doi.org/10.1038/nmeth.3407).
- [164] Benjamin J. Solomon et al. “RET Solvent Front Mutations Mediate Acquired Resistance to Selective RET Inhibition in RET-Driven Malignancies”. In: *Journal of Thoracic Oncology* 15.4 (Apr. 2020), pp. 541–549. doi: [10.1016/j.jtho.2020.01.006](https://doi.org/10.1016/j.jtho.2020.01.006).
- [165] Ismael A. Vergara et al. “Evolution of late-stage metastatic melanoma is dominated by aneuploidy and whole genome doubling”. In: *Nature Communications* 12.1 (Mar. 2021). doi: [10.1038/s41467-021-21576-8](https://doi.org/10.1038/s41467-021-21576-8).
- [166] Zheng Hu et al. “Quantitative evidence for early metastatic seeding in colorectal cancer”. In: *Nature Genetics* 51.7 (June 2019), pp. 1113–1122. doi: [10.1038/s41588-019-0423-x](https://doi.org/10.1038/s41588-019-0423-x).
- [167] N Saitou and M Nei. “The neighbor-joining method: a new method for reconstructing phylogenetic trees.” In: *Molecular Biology and Evolution* (July 1987). doi: [10.1093/oxfordjournals.molbev.ao40454](https://doi.org/10.1093/oxfordjournals.molbev.ao40454).
- [168] Radu Mihaescu, Dan Levy, and Lior Pachter. “Why Neighbor-Joining Works”. In: *Algorithmica* 54.1 (Dec. 2007), pp. 1–24. doi: [10.1007/s00453-007-9116-4](https://doi.org/10.1007/s00453-007-9116-4).
- [169] Robert Reuven Sokal and Charles Duncan Michener. *A Statistical Method for Evaluating Systematic Relationships*. Vol. 38.2. University of Kansas science bulletin 22. University of Kansas, 1958. 30 pp.
- [170] Emile Zuckerkandl and Linus Pauling. “Molecular Disease, Evolution, and Genic Heterogeneity”. In: *Horizons in biochemistry* (1962), pp. 189–225.
- [171] D. Shibata. “Mutation and epigenetic molecular clocks in cancer”. In: *Carcinogenesis* 32.2 (Nov. 2010), pp. 123–128. doi: [10.1093/carcin/bgq239](https://doi.org/10.1093/carcin/bgq239).
- [172] Joseph Felsenstein. “Evolutionary trees from DNA sequences: A maximum likelihood approach”. In: *Journal of Molecular Evolution* 17.6 (Nov. 1981), pp. 368–376. doi: [10.1007/bf01734359](https://doi.org/10.1007/bf01734359).
- [173] Masami Hasegawa, Hirohisa Kishino, and Taka-aki Yano. “Dating of the human-ape splitting by a molecular clock of mitochondrial DNA”. In: *Journal of Molecular Evolution* 22.2 (Oct. 1985), pp. 160–174. doi: [10.1007/bf02101694](https://doi.org/10.1007/bf02101694).
- [174] R. W. Hamming. “Error Detecting and Error Correcting Codes”. In: *Bell System Technical Journal* 29.2 (Apr. 1950), pp. 147–160. doi: [10.1002/j.1538-7305.1950.tb00463.x](https://doi.org/10.1002/j.1538-7305.1950.tb00463.x).

- [175] Benjamin Werner et al. “Measuring single cell divisions in human tissues from multi-region sequencing data”. In: *Nature Communications* 11.1 (Feb. 2020). doi: [10.1038/s41467-020-14844-6](https://doi.org/10.1038/s41467-020-14844-6).
- [176] T. Arai et al. “Tumor doubling time and prognosis in lung cancer patients: evaluation from chest films and clinical follow-up study”. In: *Japanese journal of clinical oncology* 24 (4 Aug. 1994), pp. 199–204. issn: 0368-2811. ppublish.
- [177] Damien M de Vienne. “Tanglegrams Are Misleading for Visual Evaluation of Tree Congruence”. In: 36.1 (Oct. 2018). Ed. by Jeffrey Townsend, pp. 174–176. doi: [10.1093/molbev/msy196](https://doi.org/10.1093/molbev/msy196).
- [178] L. Tan et al. “Prediction and monitoring of relapse in stage III melanoma using circulating tumor DNA”. In: *Annals of Oncology* 30.5 (May 2019), pp. 804–814. doi: [10.1093/annonc/mdz048](https://doi.org/10.1093/annonc/mdz048).
- [179] “ctDNA is a specific and sensitive biomarker in multiple human cancers.” In: *Cancer discovery* 4.4 (4 Apr. 2014), OF8. issn: 2159-8290. doi: [10.1158/2159-8290.CD-RW2014-051](https://doi.org/10.1158/2159-8290.CD-RW2014-051). ppublish.
- [180] Amit G. Deshwar et al. “PhyloWGS: Reconstructing subclonal composition and evolution from whole-genome sequencing of tumors”. In: *Genome Biology* 16.1 (Feb. 2015). doi: [10.1186/s13059-015-0602-8](https://doi.org/10.1186/s13059-015-0602-8).
- [181] Yuchao Jiang et al. “Assessing intratumor heterogeneity and tracking longitudinal and spatial clonal evolutionary history by next-generation sequencing”. In: 113 (Aug. 2016), E5528–E5537. doi: [10.1073/pnas.1522203113](https://doi.org/10.1073/pnas.1522203113).
- [182] Francesco Marass et al. “A phylogenetic latent feature model for clonal deconvolution”. In: *The Annals of Applied Statistics* 10.4 (Dec. 2016). doi: [10.1214/16-aoas986](https://doi.org/10.1214/16-aoas986).
- [183] Sayaka Miura et al. “Predicting clone genotypes from tumor bulk sequencing of multiple samples”. In: (June 2018). Ed. by John Hancock. doi: [10.1093/bioinformatics/bty469](https://doi.org/10.1093/bioinformatics/bty469).
- [184] Mohammed El-Kebir, Gryte Satas, and Benjamin J. Raphael. “Inferring parsimonious migration histories for metastatic cancers”. In: 50.5 (Apr. 2018), pp. 718–726. doi: [10.1038/s41588-018-0106-z](https://doi.org/10.1038/s41588-018-0106-z).
- [185] Giulio Caravagna et al. “The MOBSTER R package for tumour subclonal deconvolution from bulk DNA whole-genome sequencing data”. In: *BMC Bioinformatics* 21.1 (Nov. 2020). doi: [10.1186/s12859-020-03863-1](https://doi.org/10.1186/s12859-020-03863-1).

- [186] Maxime Tarabichi et al. “A practical guide to cancer subclonal reconstruction from DNA sequencing.” In: *Nature methods* 18.2 (2 Feb. 2021), pp. 144–155. issn: 1548-7105. doi: [10.1038/s41592-020-01013-2](https://doi.org/10.1038/s41592-020-01013-2). ppublish.
- [187] Sayaka Miura et al. “Power and pitfalls of computational methods for inferring clone phylogenies and mutation orders from bulk sequencing data”. In: *Scientific Reports* 10.1 (Feb. 2020). doi: [10.1038/s41598-020-59006-2](https://doi.org/10.1038/s41598-020-59006-2).
- [188] Ignaty Leshchiner et al. “Comprehensive analysis of tumour initiation, spatial and temporal progression under multiple lines of treatment”. In: *bioRxiv* (Dec. 2018). doi: [10.1101/508127](https://doi.org/10.1101/508127).
- [189] Moritz Gerstung et al. “The evolutionary history of 2,658 cancers”. In: *Nature* 578.7793 (Feb. 2020), pp. 122–128. doi: [10.1038/s41586-019-1907-7](https://doi.org/10.1038/s41586-019-1907-7).
- [190] Paul P. Gardner et al. “Sustained software development, not number of citations or journal choice, is indicative of accurate bioinformatic software”. In: *Genome Biology* 23.1 (Feb. 2022). doi: [10.1186/s13059-022-02625-x](https://doi.org/10.1186/s13059-022-02625-x).
- [191] Katie A. Fennell et al. “Non-genetic determinants of malignant clonal fitness at single-cell resolution”. In: *Nature* 601.7891 (Dec. 2021), pp. 125–131. doi: [10.1038/s41586-021-04206-7](https://doi.org/10.1038/s41586-021-04206-7).
- [192] Livius Penter, Satyen H. Gohil, and Catherine J. Wu. “Natural Barcodes for Longitudinal Single Cell Tracking of Leukemic and Immune Cell Dynamics”. In: *Frontiers in Immunology* 12 (Jan. 2022). doi: [10.3389/fimmu.2021.788891](https://doi.org/10.3389/fimmu.2021.788891).
- [193] Cathie Sudlow et al. “UK Biobank: An Open Access Resource for Identifying the Causes of a Wide Range of Complex Diseases of Middle and Old Age”. In: *PLOS Medicine* 12.3 (Mar. 2015), e1001779. doi: [10.1371/journal.pmed.1001779](https://doi.org/10.1371/journal.pmed.1001779).
- [194] Cancer Council Victoria. *Victorian Cancer Biobank. Integrity. Excellence. Innovation. Empowering Patients*. 2006. url: viccancerbiobank.org.au (visited on 03/03/2022).
- [195] Go J. Yoshida. “Applications of patient-derived tumor xenograft models and tumor organoids”. In: *Journal of Hematology & Oncology* 13.1 (Jan. 2020). doi: [10.1186/s13045-019-0829-z](https://doi.org/10.1186/s13045-019-0829-z).
- [196] Kathryn Alsop et al. “A community-based model of rapid autopsy in end-stage cancer patients”. In: *Nature Biotechnology* 34.10 (Sept. 2016), pp. 1010–1014. doi: [10.1038/nbt.3674](https://doi.org/10.1038/nbt.3674).
- [197] Rebecca L. Siegel, Kimberly D. Miller, and Ahmedin Jemal. “Cancer statistics, 2018”. In: *CA: A Cancer Journal for Clinicians* 68.1 (Jan. 2018), pp. 7–30. doi: [10.3322/caac.21442](https://doi.org/10.3322/caac.21442).

- [198] Julian R. Molina et al. “Non-Small Cell Lung Cancer: Epidemiology, Risk Factors, Treatment, and Survivorship”. In: *Mayo Clinic Proceedings* 83.5 (May 2008), pp. 584–594. doi: [10.4065/83.5.584](https://doi.org/10.4065/83.5.584).
- [199] Sophie Sun, Joan H. Schiller, and Adi F. Gazdar. “Lung cancer in never smokers—a different disease”. In: *Nature Reviews Cancer* 7.10 (Oct. 2007), pp. 778–790. doi: [10.1038/nrc2190](https://doi.org/10.1038/nrc2190).
- [200] Kenichi Suda et al. “Innate Genetic Evolution of Lung Cancers and Spatial Heterogeneity: Analysis of Treatment-Naïve Lesions”. In: *Journal of Thoracic Oncology* 13 (Oct. 2018), pp. 1496–1507. doi: [10.1016/j.jtho.2018.05.039](https://doi.org/10.1016/j.jtho.2018.05.039).
- [201] Neal I. Lindeman et al. “Updated Molecular Testing Guideline for the Selection of Lung Cancer Patients for Treatment With Targeted Tyrosine Kinase Inhibitors: Guideline From the College of American Pathologists, the International Association for the Study of Lung Cancer, and the Association for Molecular Pathology”. In: *Archives of Pathology & Laboratory Medicine* 142.3 (Jan. 2018), pp. 321–346. doi: [10.5858/arpa.2017-o388-cp](https://doi.org/10.5858/arpa.2017-o388-cp).
- [202] Peter Savas et al. “The Subclonal Architecture of Metastatic Breast Cancer: Results from a Prospective Community-Based Rapid Autopsy Program “CASCADE””. In: *PLOS Medicine* 13.12 (Dec. 2016). Ed. by Marc Ladanyi, e1002204. doi: [10.1371/journal.pmed.1002204](https://doi.org/10.1371/journal.pmed.1002204).
- [203] Marian L. Burr et al. “An Evolutionarily Conserved Function of Polycomb Silences the MHC Class I Antigen Presentation Pathway and Enables Immune Evasion in Cancer”. In: *Cancer Cell* 36.4 (Oct. 2019), 385–401.e8. doi: [10.1016/j.ccr.2019.08.008](https://doi.org/10.1016/j.ccr.2019.08.008).
- [204] Sejoon Lee et al. “NGSCheckMate: software for validating sample identity in next-generation sequencing studies within and across data types”. In: *Nucleic Acids Research* 45.11 (Mar. 2017), e103–e103. doi: [10.1093/nar/gkx193](https://doi.org/10.1093/nar/gkx193).
- [205] Brent S. Pedersen et al. “Somalier: rapid relatedness estimation for cancer and germline studies using efficient genome sketches”. In: *Genome Medicine* 12.1 (July 2020). doi: [10.1186/s13073-020-00761-2](https://doi.org/10.1186/s13073-020-00761-2).
- [206] S. Andrews. *FastQC: A Quality Control Tool for High Throughput Sequence Data*. 2010. url: <http://www.bioinformatics.babraham.ac.uk/projects/fastqc/>.
- [207] Broad Institute. *Picard toolkit*. <http://broadinstitute.github.io/picard/>. Comp. software. Version 2.23.8. 2019.
- [208] Daniel L. Cameron et al. “GRIDSS2: comprehensive characterisation of somatic structural variation using single breakend variants and structural variant phasing”. In: *Genome Biology* 22.1 (July 2021). doi: [10.1186/s13059-021-02423-x](https://doi.org/10.1186/s13059-021-02423-x).

- [209] Ludmil B. Alexandrov et al. “The repertoire of mutational signatures in human cancer”. In: *Nature* 578.7793 (Feb. 2020), pp. 94–101. doi: [10.1038/s41586-020-1943-3](https://doi.org/10.1038/s41586-020-1943-3).
- [210] Maria Moksnes Bjaanæs et al. “Whole genome copy number analyses reveal a highly aberrant genome in TP53 mutant lung adenocarcinoma tumors”. In: *BMC Cancer* 21.1 (Oct. 2021). doi: [10.1186/s12885-021-08811-7](https://doi.org/10.1186/s12885-021-08811-7).
- [211] Xiaohui Ni et al. “Reproducible copy number variation patterns among single circulating tumor cells of lung cancer patients”. In: *Proceedings of the National Academy of Sciences* 110.52 (Dec. 2013), pp. 21083–21088. doi: [10.1073/pnas.1320659110](https://doi.org/10.1073/pnas.1320659110).
- [212] Eric Talevich et al. “CNVkit: Genome-Wide Copy Number Detection and Visualization from Targeted DNA Sequencing”. In: *PLOS Computational Biology* 12.4 (Apr. 2016), e1004873. doi: [10.1371/journal.pcbi.1004873](https://doi.org/10.1371/journal.pcbi.1004873).
- [213] Simone Zaccaria and Benjamin J. Raphael. “Accurate quantification of copy-number aberrations and whole-genome duplications in multi-sample tumor sequencing data”. In: *Nature Communications* 11.1 (Sept. 2020). doi: [10.1038/s41467-020-17967-y](https://doi.org/10.1038/s41467-020-17967-y).
- [214] AmirAli Talasaz et al. *Use of the GUARDANT360 noninvasive tumor sequencing assay on 300 patients across colorectal, melanoma, lung, breast, and prostate cancers and its clinical utility*. 2014.
- [215] Ludmil B. Alexandrov et al. “Signatures of mutational processes in human cancer”. In: *Nature* 500.7463 (Aug. 2013), pp. 415–421. doi: [10.1038/nature12477](https://doi.org/10.1038/nature12477).
- [216] Haojie Jin et al. “EGFR activation limits the response of liver cancer to lenvatinib”. In: *Nature* 595.7869 (July 2021), pp. 730–734. doi: [10.1038/s41586-021-03741-7](https://doi.org/10.1038/s41586-021-03741-7).
- [217] Hongdo Do and Alexander Dobrovic. “Sequence Artifacts in DNA from Formalin-Fixed Tissues: Causes and Strategies for Minimization”. In: *Clinical Chemistry* 61.1 (Jan. 2015), pp. 64–71. doi: [10.1373/clinchem.2014.223040](https://doi.org/10.1373/clinchem.2014.223040).
- [218] Faye M. Johnson et al. “Phase II Study of Dasatinib in Patients With Advanced Non-Small-Cell Lung Cancer”. In: *Journal of Clinical Oncology* 28.30 (Oct. 2010), pp. 4609–4615. doi: [10.1200/jco.2010.30.5474](https://doi.org/10.1200/jco.2010.30.5474).
- [219] Melissa Bersanelli et al. “L718Q Mutation as New Mechanism of Acquired Resistance to AZD9291 in EGFR -Mutated NSCLC”. In: *Journal of Thoracic Oncology* 11.10 (Oct. 2016), e121–e123. doi: [10.1016/j.jtho.2016.05.019](https://doi.org/10.1016/j.jtho.2016.05.019).
- [220] Shuhang Wang et al. “EGFR C797S mutation mediates resistance to third-generation inhibitors in T790M-positive non-small cell lung cancer”. In: *Journal of Hematology & Oncology* 9.1 (July 2016). doi: [10.1186/s13045-016-0290-1](https://doi.org/10.1186/s13045-016-0290-1).

- [221] Alessandro Leonetti et al. “Resistance mechanisms to osimertinib in EGFR-mutated non-small cell lung cancer”. In: *British Journal of Cancer* 121.9 (Sept. 2019), pp. 725–737. doi: [10.1038/s41416-019-0573-8](https://doi.org/10.1038/s41416-019-0573-8).
- [222] Qi Zhang et al. “EGFR L792H and G796R: Two Novel Mutations Mediating Resistance to the Third-Generation EGFR Tyrosine Kinase Inhibitor Osimertinib”. In: *Journal of Thoracic Oncology* 13.9 (Sept. 2018), pp. 1415–1421. doi: [10.1016/j.jtho.2018.05.024](https://doi.org/10.1016/j.jtho.2018.05.024).
- [223] Matthew G. Oser et al. “Transformation from non-small-cell lung cancer to small-cell lung cancer: molecular drivers and cells of origin”. In: *The Lancet Oncology* 16.4 (Apr. 2015), e165–e172. doi: [10.1016/s1470-2045\(14\)71180-5](https://doi.org/10.1016/s1470-2045(14)71180-5).
- [224] Rahul Aggarwal et al. “Clinical and Genomic Characterization of Treatment-Emergent Small-Cell Neuroendocrine Prostate Cancer: A Multi-institutional Prospective Study”. In: *Journal of Clinical Oncology* 36.24 (Aug. 2018), pp. 2492–2503. doi: [10.1200/jco.2017.77.6880](https://doi.org/10.1200/jco.2017.77.6880).
- [225] Michael Offin et al. “Concurrent RB1 and TP53 Alterations Define a Subset of EGFR-Mutant Lung Cancers at risk for Histologic Transformation and Inferior Clinical Outcomes”. In: *Journal of Thoracic Oncology* 14.10 (Oct. 2019), pp. 1784–1793. doi: [10.1016/j.jtho.2019.06.002](https://doi.org/10.1016/j.jtho.2019.06.002).
- [226] David Brown et al. “Phylogenetic analysis of metastatic progression in breast cancer using somatic mutations and copy number aberrations”. In: *Nature Communications* 8.1 (Apr. 2017). doi: [10.1038/ncomms14944](https://doi.org/10.1038/ncomms14944).
- [227] Motoo Kimura. “Evolutionary Rate at the Molecular Level”. In: *Nature* 217.5129 (Feb. 1968), pp. 624–626. doi: [10.1038/217624a0](https://doi.org/10.1038/217624a0).
- [228] Michael Lynch. “Phylogenetic Hypotheses Under the Assumption of Neutral Quantitative-Genetic Variation”. In: *Evolution* 43.1 (Jan. 1989), p. 1. doi: [10.2307/2409160](https://doi.org/10.2307/2409160).
- [229] Vincent L. Cannataro and Jeffrey P. Townsend. “Neutral Theory and the Somatic Evolution of Cancer”. In: *Molecular Biology and Evolution* 35.6 (Apr. 2018). Ed. by Sudhir Kumar, pp. 1308–1315. doi: [10.1093/molbev/msy079](https://doi.org/10.1093/molbev/msy079).
- [230] Adam Eyre-Walker and Peter D. Keightley. “The distribution of fitness effects of new mutations”. In: *Nature Reviews Genetics* 8.8 (Aug. 2007), pp. 610–618. doi: [10.1038/nrg2146](https://doi.org/10.1038/nrg2146).
- [231] Leif S. Ludwig et al. “Lineage Tracing in Humans Enabled by Mitochondrial Mutations and Single-Cell Genomics”. In: *Cell* 176.6 (Mar. 2019), 1325–1339.e22. doi: [10.1016/j.cell.2019.01.022](https://doi.org/10.1016/j.cell.2019.01.022).
- [232] J. N. Harvey and D. Barnett. “Endocrine dysfunction in Kearns-Sayre syndrome”. In: *Clinical Endocrinology* 37.1 (July 1992), pp. 97–104. doi: [10.1111/j.1365-2265.1992.tb02289.x](https://doi.org/10.1111/j.1365-2265.1992.tb02289.x).

- [233] Margaret P. Adam et al. “GeneReviews”. In: (1993). ppublish.
- [234] Michio Hirano et al. “MELAS: An original case and clinical criteria for diagnosis”. In: *Neuromuscular Disorders* 2.2 (Jan. 1992), pp. 125–135. doi: [10.1016/0960-8966\(92\)90045-8](https://doi.org/10.1016/0960-8966(92)90045-8).
- [235] Anders Rodell et al. “Natural selection of mitochondria during somatic lifetime promotes healthy aging”. In: *Frontiers in Neuroenergetics* 5 (2013). doi: [10.3389/fnene.2013.00007](https://doi.org/10.3389/fnene.2013.00007).
- [236] Yuan Yuan et al. “Comprehensive molecular characterization of mitochondrial genomes in human cancers”. In: *Nature Genetics* 52.3 (Feb. 2020), pp. 342–352. doi: [10.1038/s41588-019-0557-x](https://doi.org/10.1038/s41588-019-0557-x).
- [237] Logan W. Cole. “The Evolution of Per-cell Organelle Number”. In: *Frontiers in Cell and Developmental Biology* 4 (Aug. 2016). doi: [10.3389/fcell.2016.00085](https://doi.org/10.3389/fcell.2016.00085).
- [238] Motoo Kimura. “THE NUMBER OF HETEROZYGOUS NUCLEOTIDE SITES MAINTAINED IN A FINITE POPULATION DUE TO STEADY FLUX OF MUTATIONS”. In: *Genetics* 61.4 (Apr. 1969), pp. 893–903. doi: [10.1093/genetics/61.4.893](https://doi.org/10.1093/genetics/61.4.893).
- [239] Monica Hollstein et al. “p53 Mutations in Human Cancers”. In: *Science* 253.5015 (July 1991), pp. 49–53. doi: [10.1126/science.1905840](https://doi.org/10.1126/science.1905840).
- [240] Jill E. Kucab et al. “A Compendium of Mutational Signatures of Environmental Agents”. In: *Cell* 177.4 (May 2019), 821–836.e16. doi: [10.1016/j.cell.2019.03.001](https://doi.org/10.1016/j.cell.2019.03.001).
- [241] Nigel J. O’Neil, Melanie L. Bailey, and Philip Hieter. “Synthetic lethality and cancer”. In: *Nature Reviews Genetics* 18.10 (June 2017), pp. 613–623. doi: [10.1038/nrg.2017.47](https://doi.org/10.1038/nrg.2017.47).
- [242] Adam Auton et al. “A global reference for human genetic variation”. In: *Nature* 526.7571 (Sept. 2015), pp. 68–74. doi: [10.1038/nature15393](https://doi.org/10.1038/nature15393).
- [243] Mahdi Heydari et al. “Illumina error correction near highly repetitive DNA regions improves de novo genome assembly”. In: *BMC Bioinformatics* 20.1 (June 2019). doi: [10.1186/s12859-019-2906-2](https://doi.org/10.1186/s12859-019-2906-2).
- [244] Irena Hudecova et al. “Characteristics, origin, and potential for cancer diagnostics of ultra-short plasma cell-free DNA”. In: *Genome Research* (Dec. 2021), gr.275691.121. doi: [10.1101/gr.275691.121](https://doi.org/10.1101/gr.275691.121).
- [245] Yan Guo et al. “The effect of strand bias in Illumina short-read sequencing data”. In: *BMC Genomics* 13.1 (Nov. 2012). doi: [10.1186/1471-2164-13-666](https://doi.org/10.1186/1471-2164-13-666).

- [246] Christopher T. Saunders et al. “Strelka: accurate somatic small-variant calling from sequenced tumor-normal sample pairs”. In: *Bioinformatics* 28.14 (May 2012), pp. 1811–1817. doi: [10.1093/bioinformatics/bts271](https://doi.org/10.1093/bioinformatics/bts271).
- [247] GATK Team. *StrandBiasBySample*. Sept. 18, 2019. url: <https://gatk.broadinstitute.org/hc/en-us/articles/360040096492> (visited on 12/21/2021).
- [248] Alistair Miles; pyup.io bot; Murillo R.; Peter Ralph; Nick Harding; Rahul Pisupati; Summer Rae; Tim Millar. *scikit-allel: A Python package for exploring and analysing genetic variation data*. June 14, 2021. doi: [10.5281/zenodo.4759368](https://doi.org/10.5281/zenodo.4759368).
- [249] Andy G. Lynch. “Decomposition of mutational context signatures using quadratic programming methods”. In: *F1000Research* 5 (June 2016), p. 1253. doi: [10.12688/f1000research.8918.1](https://doi.org/10.12688/f1000research.8918.1).
- [250] Marie Laure Delignette-Muller and Christophe Dutang. “fitdistrplus: An R Package for Fitting Distributions”. In: *Journal of Statistical Software* 64.4 (2015), pp. 1–34. url: <https://www.jstatsoft.org/v64/i04/>.
- [251] Michael S. Lawrence et al. “Mutational heterogeneity in cancer and the search for new cancer-associated genes”. In: *Nature* 499.7457 (June 2013), pp. 214–218. doi: [10.1038/nature12213](https://doi.org/10.1038/nature12213).
- [252] Tenghui Chen et al. “Hotspot mutations delineating diverse mutational signatures and biological utilities across cancer types”. In: *BMC Genomics* 17.S2 (June 2016). doi: [10.1186/s12864-016-2727-x](https://doi.org/10.1186/s12864-016-2727-x).
- [253] John G Tate et al. “COSMIC: the Catalogue Of Somatic Mutations In Cancer”. In: *Nucleic Acids Research* 47.D1 (Oct. 2018), pp. D941–D947. doi: [10.1093/nar/gky1015](https://doi.org/10.1093/nar/gky1015).
- [254] Wellcome Sanger Institute. *COSMIC database v95*. Nov. 14, 2021. url: <https://cancer.sanger.ac.uk/>.
- [255] R. Barroso-Sousa et al. “Prevalence and mutational determinants of high tumor mutation burden in breast cancer”. In: *Annals of Oncology* 31.3 (Mar. 2020), pp. 387–394. doi: [10.1016/j.annonc.2019.11.010](https://doi.org/10.1016/j.annonc.2019.11.010).
- [256] Federico Abascal et al. “Somatic mutation landscapes at single-molecule resolution”. In: *Nature* 593.7859 (Apr. 2021), pp. 405–410. doi: [10.1038/s41586-021-03477-4](https://doi.org/10.1038/s41586-021-03477-4).
- [257] Miguel Ganuza et al. “The global clonal complexity of the murine blood system declines throughout life and after serial transplantation”. In: *Blood* 133.18 (May 2019), pp. 1927–1942. doi: [10.1182/blood-2018-09-873059](https://doi.org/10.1182/blood-2018-09-873059).

- [258] Julian R. Homburger et al. “Low coverage whole genome sequencing enables accurate assessment of common variants and calculation of genome-wide polygenic scores”. In: *Genome Medicine* 11.1 (Nov. 2019). doi: [10.1186/s13073-019-0682-2](https://doi.org/10.1186/s13073-019-0682-2).
- [259] Ming Chen et al. “Applying low coverage whole genome sequencing to detect malignant ovarian mass”. In: *Journal of Translational Medicine* 19.1 (Aug. 2021). doi: [10.1186/s12967-021-03046-3](https://doi.org/10.1186/s12967-021-03046-3).
- [260] Grace Tiao and Julia Goodrich. *gnomAD v3.1. New Content, Methods, Annotations, and Data Availability*. Oct. 29, 2020. url: <https://gnomad.broadinstitute.org/news/2020-10-gnomad-v3-1-new-content-methods-annotations-and-data-availability/> (visited on 03/04/2023).
- [261] Shixiang Wang et al. “Copy number signature analysis tool and its application in prostate cancer reveals distinct mutational processes and clinical outcomes”. In: *PLOS Genetics* 17.5 (May 2021). Ed. by Dmitry A. Gordenin, e1009557. doi: [10.1371/journal.pgen.1009557](https://doi.org/10.1371/journal.pgen.1009557).
- [262] Mark A DePristo et al. “A framework for variation discovery and genotyping using next-generation DNA sequencing data”. In: *Nature Genetics* 43.5 (Apr. 2011), pp. 491–498. doi: [10.1038/ng.806](https://doi.org/10.1038/ng.806).
- [263] Berke Ç Toptaş et al. “Comparing complex variants in family trios”. In: *Bioinformatics* (June 2018). Ed. by Oliver Stegle. doi: [10.1093/bioinformatics/bty443](https://doi.org/10.1093/bioinformatics/bty443).
- [264] Di Wang et al. “Multiregion Sequencing Reveals the Genetic Heterogeneity and Evolutionary History of Osteosarcoma and Matched Pulmonary Metastases”. In: *Cancer Research* 79.1 (Nov. 2018), pp. 7–20. doi: [10.1158/0008-5472.can-18-1086](https://doi.org/10.1158/0008-5472.can-18-1086).
- [265] Zixi Chen et al. “Systematic comparison of somatic variant calling performance among different sequencing depth and mutation frequency”. In: *Scientific Reports* 10.1 (Feb. 2020). doi: [10.1038/s41598-020-60559-5](https://doi.org/10.1038/s41598-020-60559-5).
- [266] Richard Lupat et al. *Janis: A Python framework for Portable Pipelines*. en. 2021. doi: [10.5281/ZENODO.4427231](https://doi.org/10.5281/ZENODO.4427231).
- [267] H. Li and R. Durbin. “Fast and accurate short read alignment with Burrows-Wheeler transform”. In: *Bioinformatics* 25.14 (May 2009), pp. 1754–1760. doi: [10.1093/bioinformatics/btp324](https://doi.org/10.1093/bioinformatics/btp324).
- [268] Kenneth D. Doig et al. “Canary: an atomic pipeline for clinical amplicon assays”. In: *BMC Bioinformatics* 18.1 (Dec. 2017). doi: [10.1186/s12859-017-1950-z](https://doi.org/10.1186/s12859-017-1950-z).

- [269] Roche Sequencing Solutions, Inc. *AVENIO ctDNA and Tumour Tissue Expanded Panel*. Sept. 2018. url: <https://sequencing.roche.com/content/dam/rochesequence/worldwide/resources/brochure-avenio-ctdna-tumor-tissue-expanded-kit-gene-list-SEQ100327.pdf> (visited on 03/10/2022).
- [270] H. Greulich. “The Genomics of Lung Adenocarcinoma: Opportunities for Targeted Therapies”. In: *Genes & Cancer* 1.12 (Dec. 2010), pp. 1200–1210. doi: [10.1177/1947601911407324](https://doi.org/10.1177/1947601911407324).
- [271] A. El-Telbany and P. C. Ma. “Cancer Genes in Lung Cancer: Racial Disparities: Are There Any?” In: *Genes & Cancer* 3.7-8 (July 2012), pp. 467–480. doi: [10.1177/1947601912465177](https://doi.org/10.1177/1947601912465177).
- [272] The Cancer Genome Atlas Research Network. “Comprehensive molecular profiling of lung adenocarcinoma”. In: *Nature* 511.7511 (July 2014), pp. 543–550. doi: [10.1038/nature13385](https://doi.org/10.1038/nature13385).
- [273] National Comprehensive Cancer Network. *NCCN Guidelines. Non-Small Cell Lung Cancer*. Version 2.2022. July 3, 2022. url: https://www.nccn.org/professionals/physician_gls/pdf/nscl.pdf (visited on 03/15/2022).
- [274] Zhongyi Fan et al. “The risk variant rs884225 within EGFR impairs miR-103a-3p’s anti-tumourigenic function in non-small cell lung cancer”. In: *Oncogene* 38.13 (Nov. 2018), pp. 2291–2304. doi: [10.1038/s41388-018-0576-6](https://doi.org/10.1038/s41388-018-0576-6).
- [275] Jun Jiang et al. “MKRN2 inhibits migration and invasion of non-small-cell lung cancer by negatively regulating the PI3K/Akt pathway”. In: *Journal of Experimental & Clinical Cancer Research* 37.1 (Aug. 2018). doi: [10.1186/s13046-018-0855-7](https://doi.org/10.1186/s13046-018-0855-7).
- [276] Jenny Hötzl et al. “Protein expression of close homologue of L1 (CHL1) is a marker for overall survival in non-small cell lung cancer (NSCLC)”. In: *Journal of Cancer Research and Clinical Oncology* 145.9 (Aug. 2019), pp. 2285–2292. doi: [10.1007/s00432-019-02989-x](https://doi.org/10.1007/s00432-019-02989-x).
- [277] Hyunhee Do et al. “TFAP2C increases cell proliferation by downregulating GADD45B and PMAIP1 in non-small cell lung cancer cells”. In: *Biological Research* 52.1 (July 2019). doi: [10.1186/s40659-019-0244-5](https://doi.org/10.1186/s40659-019-0244-5).
- [278] Zhu-Jun Cheng et al. “THZ1 suppresses human non-small-cell lung cancer cells in vitro through interference with cancer metabolism”. In: *Acta Pharmacologica Sinica* 40.6 (Nov. 2018), pp. 814–822. doi: [10.1038/s41401-018-0187-3](https://doi.org/10.1038/s41401-018-0187-3).
- [279] Lin Ye et al. “Transmembrane-4 L-six family member-1 (TM4SF1) promotes non-small cell lung cancer proliferation, invasion and chemo-resistance through regulating the DDR1/Akt/ERK-mTOR axis”. In: *Respiratory Research* 20 (May 2019). doi: [10.1186/s12931-019-1071-5](https://doi.org/10.1186/s12931-019-1071-5).

- [280] Ying-Gui Yang et al. “Interferon-induced transmembrane protein 1-mediated EGFR/SOX2 signaling axis is essential for progression of non-small cell lung cancer”. In: *International Journal of Cancer* (Dec. 2018). doi: [10.1002/ijc.31926](https://doi.org/10.1002/ijc.31926).
- [281] Siyang Feng et al. “TUSC3 accelerates cancer growth and induces epithelial-mesenchymal transition by upregulating claudin-1 in non-small-cell lung cancer cells”. In: *Experimental Cell Research* 373.1-2 (Dec. 2018), pp. 44–56. doi: [10.1016/j.yexcr.2018.08.012](https://doi.org/10.1016/j.yexcr.2018.08.012).
- [282] Yue Wu et al. “Amplification of USP13 drives non-small cell lung cancer progression mediated by AKT/MAPK signaling”. In: *Biomedicine & Pharmacotherapy* 114 (June 2019), p. 108831. doi: [10.1016/j.biopha.2019.108831](https://doi.org/10.1016/j.biopha.2019.108831).
- [283] Shanshan Sun et al. “KDM4A promotes the growth of non-small cell lung cancer by mediating the expression of Myc via DLX5 through the Wnt/β-catenin signaling pathway”. In: *Life Sciences* 262 (Dec. 2020), p. 118508. doi: [10.1016/j.lfs.2020.118508](https://doi.org/10.1016/j.lfs.2020.118508).
- [284] Thomas Derrien et al. “Fast Computation and Applications of Genome Mappability”. In: *PLoS ONE* 7.1 (Jan. 2012). Ed. by Christos A. Ouzounis, e30377. doi: [10.1371/journal.pone.0030377](https://doi.org/10.1371/journal.pone.0030377).
- [285] Valerie A. Schneider et al. “Evaluation of GRCh38 and de novo haploid genome assemblies demonstrates the enduring quality of the reference assembly”. In: *Genome Research* 27 (Apr. 2017), pp. 849–864. doi: [10.1101/gr.213611.116](https://doi.org/10.1101/gr.213611.116).
- [286] Deanna M. Church et al. “Modernizing Reference Genome Assemblies”. In: *PLoS Biology* 9.7 (July 2011), e1001091. doi: [10.1371/journal.pbio.1001091](https://doi.org/10.1371/journal.pbio.1001091).
- [287] H. Li. “Tabix: fast retrieval of sequence features from generic TAB-delimited files”. In: *Bioinformatics* 27.5 (Jan. 2011), pp. 718–719. doi: [10.1093/bioinformatics/btq671](https://doi.org/10.1093/bioinformatics/btq671).

Appendices

by [Sebastian Hollizeck](#)

[ORCID: oooo-ooo2-9504-3497](#)

contains:

- published manuscripts
- supplementary method
- supplementary figures

A

Custom workflows to improve joint variant calling from multiple related tumour samples: FreeBayesSomatic and Strelka2Pass

This appendix contains the manuscript published at *Bioinformatics* in a non journal style format with the supplementary methods and figures. It can also be found at [10.1093/bioinformatics/btaa606/6361543](https://doi.org/10.1093/bioinformatics/btaa606) for a paper style version.

Hollizeck S.^{1,2}, Wong S.Q.^{1,2}, Solomon B.^{1,2}, Chandrananda D.^{1,2,*}, and Dawson S-J.^{1,2,3,*}

¹ Peter MacCallum Cancer Centre, Melbourne 3000, Victoria, Australia

² Sir Peter MacCallum Department of Oncology, University of Melbourne, Melbourne 3000, Victoria, Australia

³ Centre for Cancer Research, University of Melbourne, Melbourne 3000, Victoria, Australia

* D.C and S.J.D are co-senior authors and contributed equally to this article

Received on 27-Jan-2021; revised on 13-Jul-2021; accepted on 12-Aug-2021

Abstract

Summary:

This work describes two novel workflows for variant calling that extend the widely used algorithms of Strelka2 and FreeBayes to call somatic mutations from multiple related tumour samples and one

matched normal sample. We show that these workflows offer higher precision and recall than their single tumour-normal pair equivalents in both simulated and clinical sequencing data.

Availability and Implementation:

Source code freely available at the following link: <https://atlassian.petermac.org.au/bitbucket/projects/DAW/repos/multisamplevariantcalling> and executable through Janis (<https://github.com/MCC-BioinformaticsCore/janis>) under the GPLv3 licence.

Contact:

Dineika.Chandrananda@petermac.org, Sarah-Jane.Dawson@petermac.org

Supplementary information:

Supplementary data are available at *Bioinformatics* online.

A.1 Introduction

Joint variant calling methods are routinely used to call germline variants by leveraging population-wide information across multiple related samples [262, 263]. This concept is also advantageous for somatic variant calling to potentially overcome the challenges of spatial heterogeneity and low tumour purity. However, there is a critical lack of robust algorithms that allow multi-sample somatic calling. Most studies still rely on variant calling of separate tumour-normal pairs, subsequently combining the results across a sample cohort [166, 3, 264].

There are two major pitfalls for combining variants called from individual tumour samples. First, it is very difficult to differentiate between a false negative result due to "missing data" versus the true absence of a variant. Second, there is limited sensitivity for low allele frequency variants thus, decreasing the ability to detect minor clones, particularly in samples with low tumour purity.

Currently, only three algorithms claim to have the functionality to jointly analyse multiple samples: multiSNV [156], SuperFreq [157], and Mutect2 [107], each presenting different limitations. For instance, multiSNV cannot call indels and along with SuperFreq, is not optimised for analysis of deep coverage whole-genome sequencing (WGS) data. Mutect2 has previously been shown to be disadvantageously conservative as well as computationally inefficient [265].

To enable highly sensitive, fast and accurate variant detection from multiple related tumour samples, we have developed joint variant calling extensions to two widely used single-sample algorithms, FreeBayes [104] and Strelka2 [106]. Using both simulated and clinical sequencing data, we show that these workflows are highly accurate and can detect variants at much lower variant allele frequencies than commonly used methods.

A.2 Materials and methods

A.2.1 FreeBayesSomatic workflow

The original FreeBayes algorithm can jointly evaluate multiple samples but routinely it does not perform somatic variant calling on tumour-normal pairs. We introduce FreeBayesSomatic which allows concurrent analysis of multiple tumour samples by adapting concepts from SpeedSeq [159] which differentiates the likelihood of a variant between tumour and normal samples instead of imposing an absolute filter for all variants called in the normal. Hence, for each genotype (GT) at SNV sites, FreeBayesSomatic first calculates the difference in likelihoods (LOD) between the normal ([Equation A.1](#)) and the tumour ([Equation A.2](#)) samples genotype likelihoods (GL) with g_0 describing the reference genotype.

$$\text{LOD}_{\text{normal}} = \max_{g_i \in \text{GT}} (\text{GL}(g_0) - \text{GL}(g_i)) \quad (\text{A.1})$$

$$\text{LOD}_{\text{tumour}} = \min_{s \in \text{Samples}} \left(\min_{g_i \in \text{GT}} (\text{GL}_s(g_i) - \text{GL}_s(g_0)) \right) \quad (\text{A.2})$$

$$\text{somaticLOD} := (\text{LOD}_{\text{normal}} \geq 3.5 \wedge \text{LOD}_{\text{tumour}} \geq 3.5) \quad (\text{A.3})$$

Next, the variant allele frequencies (VAF) in both the tumour and the normal samples are compared at each site.

$$\text{VAF}_{\text{tumour}} = \max_{s \in \text{Samples}} (\text{VAF}_s) \quad (\text{A.4})$$

$$\begin{aligned} \text{somaticVAF} := & (\text{VAF}_{\text{normal}} \leq 0.001 \vee \\ & (\text{VAF}_{\text{tumour}} \geq 2.7 \cdot \text{VAF}_{\text{normal}})) \end{aligned} \quad (\text{A.5})$$

A variant is classified as somatic when both somaticLOD as well as somatic VAF pass the criteria somaticLOD ([Equation A.3](#)) and somaticVAF ([Equation A.5](#)).

The thresholds chosen for both LOD and VAF calculations were previously fitted by the blue-collar bioinformatics workflow for the DREAM synthetic 3 dataset using the SpeedSeq likelihood difference approach [[160](#)] and were selected to identify high confidence variants.

A.2.2 Strelka2Pass workflow

In contrast to FreeBayes, whilst Strelka2 has a multiple-sample mode for germline analysis and tumour-normal pair somatic variant calling capabilities, it cannot jointly analyse multiple related tumour samples. We enable this feature by adapting a two-pass strategy previously used for RNA-seq data [[161](#)]. First, somatic variants are called from each tumour-normal pair. All detected variants across the cohort are then used as input for the second pass of the analysis where we re-iterate through each tumour-normal pair but assess allelic information for all input genomic sites.

The method re-evaluates the likelihood of each variant, by integrating every genotype from each tumour-normal pair. This step can "call" a variant (v) in a sample that initially did not present enough evidence to pass the Strelka2 internal filtering using two conditions: 1) if this variant was called as a proper "PASS" by Strelka2 in any other tumour sample, or 2) if the integrated evidence for this variant across all tumour-normal pairs reached a sufficiently high level. The second condition was based on the somatic evidence score (SomEVS) reported by Strelka2, which is the logarithm of the probability of the variant v being an artefact.

$$p_{error}(v) = 10^{\left(\frac{-\text{SomEVS}(v)}{10}\right)} \quad (\text{A.6})$$

While the germline sample is shared between all processes, we can approximate these individual probabilities as being independent, since one variant calling process is agnostic of the other. Hence, we derive the following:

$$p_{error}(v_{s_1}, v_{s_2}, \dots, v_{s_n}) = \prod_{s \in \text{Samples}} p_{error}(v_s) \quad (\text{A.7})$$

And therefore:

$$\text{SomEVS}(v_{s_1}, v_{s_2}, \dots, v_{s_n}) = \sum_{s \in \text{Samples}} \text{SomEVS}(v_s) \quad (\text{A.8})$$

This allows the summation (Equation A.8) of the SomEVS score across all supporting variants to assign a "PASS" filter, if it reached a joint SomEVS score threshold. This threshold can be set by the user and is 20 by default, which corresponds to an estimated error rate of 1%. These "recovered" variants need to pass a set of additional quality metrics related to depth of coverage, mapping quality and read position rank sum score.

As an additional improvement, we also built multiallelic support into Strelka2 which originally only reports the most prevalent variant at a specific site. Within the two-pass analysis, we reconstruct the available evidence for a multiallelic variant at a called site from the allele-specific read counts and report the minor allele at this site, if there is sufficient support from other samples. This method allows recovery of minor alleles only if another sample has this variant called by Strelka2, as SomEVS scores are not available for minor alleles.

A.3 Validation

A.3.1 Simulated data

We first simulated a phylogeny with somatic and germline variants from ten tumour samples and one normal (Figure A.1A, Figure A.2A, B) (Section A.5). Germline variants were simulated at a uniform allele frequency of 0.5. Somatic VAFs were sampled from a custom distribution, modelled to favour low allele frequency variants to closely represent real world data (min VAF: 0.001; max VAF: 1; Figure A.2C, D). Paired-end sequencing reads with realistic error profiles were simulated for WGS data at 160X average coverage using the ART-MountRainier software [162]. The simulated reads were aligned to GRCh38 and both germline and somatic variants from the phylogeny were spiked into the aligned reads using Bamsurgeon [163]. We compared the workflows for FreeBayes and Strelka2 with and without our extensions for joint variant calling on the simulated datasets. The performance of Mutect2 joint variant calling was also assessed using its proposed best practice workflow. As both Mutect2 and FreeBayes do not return a verdict for each individual sample, we needed to assign each sample in the multi-sample VCF its own FILTER value. We called a somatic variant as present in a sample, if there were at least two reads supporting it for this sample and

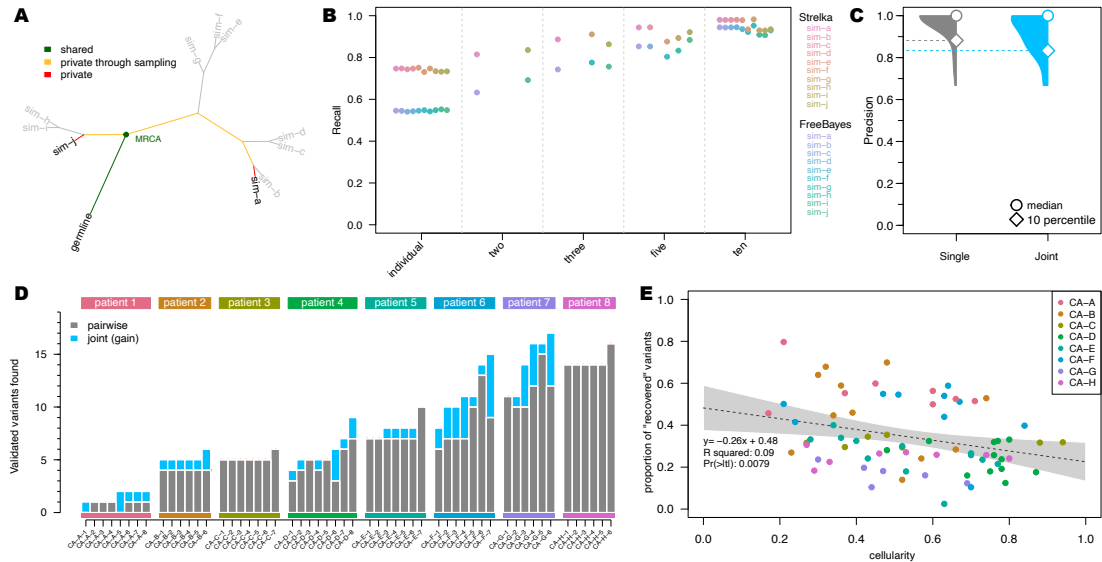


Figure A.1: Comparison of joint multi-sample variant calling and single tumour-normal paired calling methods; A) Simulated phylogeny highlighting two samples with high evolutionary distance (sim-a and sim-j) where MRCA denotes the most recent common ancestor. B) Recall estimates of FreeBayes and Strelka2, run in individual tumour-normal paired and joint calling configurations using two (sim-a and sim-j), three (sim-a, sim-g and sim-j), five (sim-a, sim-c, sim-f, sim-h and sim-j) and all ten tumour samples. C) Precision of Strelka2 and D) Number of variants called by Strelka2 run in both tumour-normal paired (grey) and added with joint calling configurations (blue), which have been validated by targeted amplicon sequencing (TAS). E) Correlation between cellularity and proportion of variants found only with joint calling using Strelka2Pass for clinical samples; grey area shows the "95%" confidence interval for the linear model fit (dotted line).

the overall FILTER showed a “PASS”, which was the same cut-off used in the refiltering step in the Strelka2-pass workflow.

While the precision of each method without our extensions was greater than 99.8%, they all missed at least 25% of all variants in the samples (i.e recall $\leq 75\%$). In contrast, the recall of the modified workflows increased to $\approx 95\%$ with only a minute decrease in the precision for both FreeBayes and Strelka2 (Figure A.3). Mutect2 however, had virtually no change in precision, but the recall actually decreased from $\approx 75\%$ to $\approx 41\%$ when analysing the samples jointly (Figure A.3B). Additionally, with our modified workflows, true positive variants were called with VAFs as low as 0.008 (median detected VAF ≥ 0.14 for joint sample analysis and ≥ 0.21 for single tumour-normal pair analysis), enabling improved distinction between true variants and technical errors (Figure A.4). This improvement in performance for Strelka2 is only achieved after the refiltering step and not just a result of the second pass (Figure A.5) (Section A.5.4).

The performance of joint variant calling in Mutect2 was inferior compared to all other methods (Figure A.3A, B). This was primarily due to the “clustered_events” filter in Mutect2, which excluded

the majority of false negative variants, with negligible contribution to the exclusion of true negative variants ([Figure A.6A, B](#)). This result was unexpected as the simulated variants were evenly distributed along the genome and the corresponding allele frequencies were sampled randomly ([Figure A.2D](#)).

Since the extent of the improvement in our joint calling workflows is bound by the number of shared variants between samples, we sub-sampled the simulated dataset, to show the effect of incomplete sampling on our methods, which is more likely in clinical settings. Furthermore, the evolutionary distance between the related samples in addition to the number of samples, has a major impact on the number of shared variants, as only variants acquired between the germline and the most recent common ancestor (MRCA), will benefit from the joint analysis. Therefore, we selected three sample subsets which included two, three and five samples with high evolutionary distance to show the minimum expected improvement ([Figure A.1A, B](#)). There was a clear linear improvement for both FreeBayesSomatic and Strelka2Pass when increasing the number of samples even if they had a distant evolutionary relationship. In contrast, when using only two samples with a small evolutionary distance, the increase in performance was almost as large as when jointly analysing all 10 available samples. This shows that samples with a high number of shared variants will perform better in joint calling workflows ([Figure A.7](#)).

A.3.2 Clinical data

To validate the performance of our new workflows, we then analysed WGS and whole-exome sequencing (WES) data of multi-region tumour samples from eight patients, with multiple tumour sites (average 7 samples per patient; total number of samples 55), enrolled in a rapid autopsy program conducted at the Peter MacCallum Cancer Centre ([Table A.1](#) and [Section A.5](#)) [[164, 165](#)]. The published studies had multiple somatic variants from the clinical samples orthogonally validated through targeted amplicon sequencing (TAS). We used these TAS-validated variants as the gold standard to evaluate the performance of different workflows, acknowledging that the technical biases inherent to TAS data are different to those present in WGS and WES ([Figure A.8](#)) and that there would be sampling biases depending on different tumour cells analysed in each data type.

In concordance with the results of the simulated data, our improved workflows found additional variants in all but one patient ([Figure A.1D](#), [Figure A.9](#)) (total additional variants Strelka2Pass: 64; FreeBayesSomatic: 85) with only a slight drop in precision for FreeBayesSomatic (mean: 0.94 vs. 0.88) and Strelka2Pass (mean: 0.97 vs. 0.92). Since the panel of variants validated by TAS was

limited (7108 bp for patients CA-B through -H), this increase in detected variants suggests that a high number of shared variants in samples are missed with current approaches, which in turn leads to an overestimation of tumour heterogeneity between samples, as these variants are thought to not be present rather than undetected.

Even though the number of shared variants is a major influencing factor when jointly calling variants, low cellularity samples benefit more from the joint calling, as conventional methods cannot reliably distinguish low allele frequency variants from noise. Through a joint analysis approach, the number of recovered variants is higher in low cellularity samples, which indicates, that especially for clinical samples with variable tumour purity, joint analysis can have a major impact on improving performance ([Figure A.1E](#), [Figure A.10](#)).

Mutect2 in contrast, did not show significant improvement in any sample in its joint calling configuration, but showed inferior performance compared to the tumour-normal pairwise approach in two samples ([Figure A.9E](#)), similar to its decreased performance in the simulated data ([Figure A.3](#)). This was due to true variants being removed by the internal filters of the tool ([Figure A.6C, D](#)). This is in stark contrast to our novel workflows, where the joint analysis preserves all called sites from the pairwise method and finds additional variants. Overall, Mutect2 found less validated variants in all patients than both Strelka2Pass (mean: 2.2) and FreeBayesSomatic (mean: 2.5) with comparable levels of precision ([Figure A.9](#), [Figure A.11](#)) but longer run times ([Table A.2](#)).

Our improved workflow also enabled the discovery of multiallelic variants with Strelka2, which led to the discovery of on average 42 additional variants (min: 1; max: 535) in the analysed WES and 987 additional variants in the WGS (min: 81; max 2329). These variants are strong indicators of sub clonal structure and could be invaluable for the study of evolutionary trajectories in cancer.

A.4 Discussion

Here we present an extension to two widely used variant callers, enabling them to analyse multiple related tumour samples and improve the sensitivity of detecting low allele frequency variants. This is highly relevant in clinical settings where low tumour purities in samples is a common occurrence. These workflows are an important step to satisfy the current unmet need for multi-sample tumour variant calling. While we have showcased their improvements in patient sequencing data, additional validation on larger clinical datasets is warranted to ensure the methodology performs robustly in real world settings. Importantly, these workflows are fully containerised and can be

run through Janis [266] on almost any high-performance computing environment, as well as cloud services. Each workflow is highly optimised and parallelised to facilitate the analysis of the large amount of data joint variant calling requires. The workflow specification also allows the easy adjustment of parameters to enable customisation for the user's needs and priorities, whereas building an ensemble workflow using multiple callers is up to the discretion of the user (Figure A.12).

Acknowledgements

The authors would like to thank all patients who provided tissue samples utilised in this study. The authors acknowledge Dr Lavinia Tan for assistance provided with the collection of patient clinical samples.

Funding

This work was supported by the National Health and Medical Research Council [grant numbers 1196755 to S.J.D, 1158345 to S.J.D and B.J.S, 1194783 to S.Q.W, 1173450 to B.J.S]; and CSL Centenary Fellowship to S.J.D; Victorian Cancer Agency [grant numbers 19008 to D.C, 19002 to S.Q.W]

Conflicts of Interest

S.J.D has been a member of advisory boards for AstraZeneca and Inivata. The S.J.D. lab has received funding from Cancer Therapeutics CRC and Roche-Genentech. B.J.S. has been a member of advisory boards for AstraZeneca, Roche-Genentech, Pfizer, Novartis, Amgen, Bristol Myers Squibb and Merk

Data availability

The simulated data and the respective final variant calling files underlying this article are available from Figshare at <https://melbourne.figshare.com>, and can be accessed with <https://doi.org/10.26188/13635186> for the dataset and <https://doi.org/10.26188/13635187> for the called variants.

The biological data underlying this article are available at the European Genome-Phenome Archive (EGA) at <https://ega-archive.org>, and can be accessed with study id [EGAS00001004023](https://ega-archive.org/study/EGAS00001004023) and [EGAS00001004950](https://ega-archive.org/study/EGAS00001004950).

Supplementary data

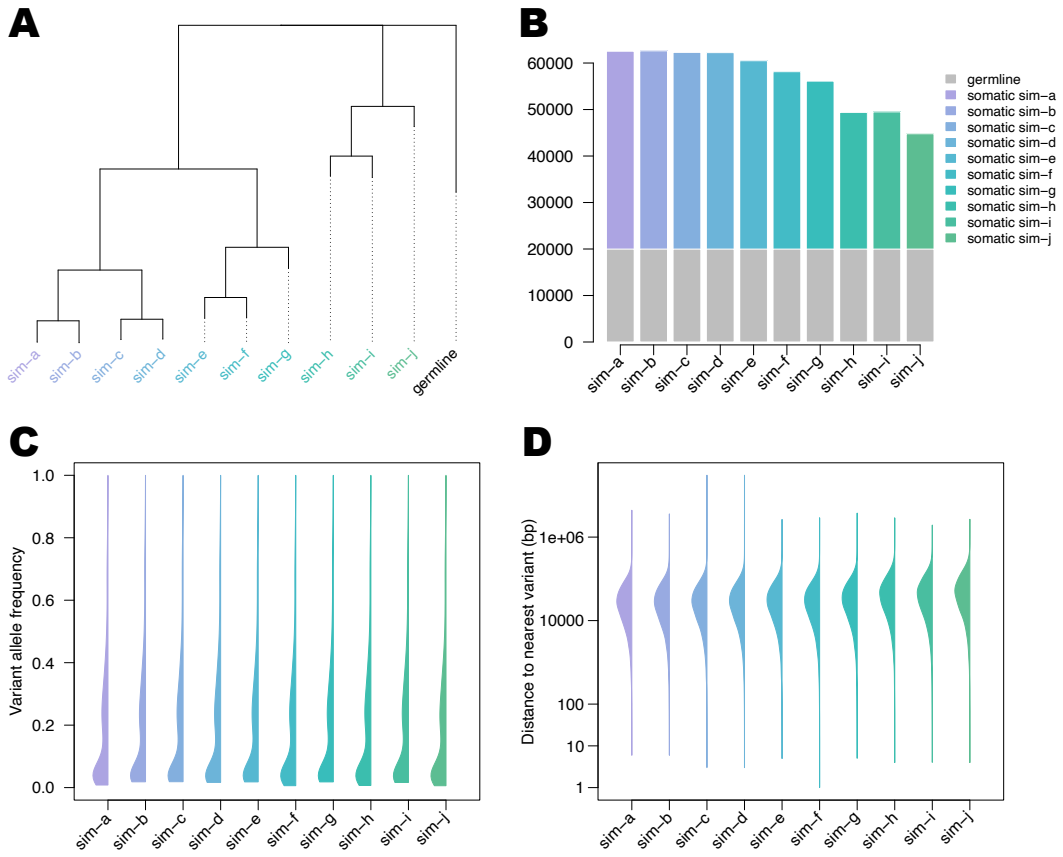


Figure A.2: Characteristics of simulated data: A) Simulated phylogeny of samples B) Number of simulated germline and somatic variants per sample C) Variant allele frequency distribution of simulated variants per sample D) Distance to nearest variant in each sample.

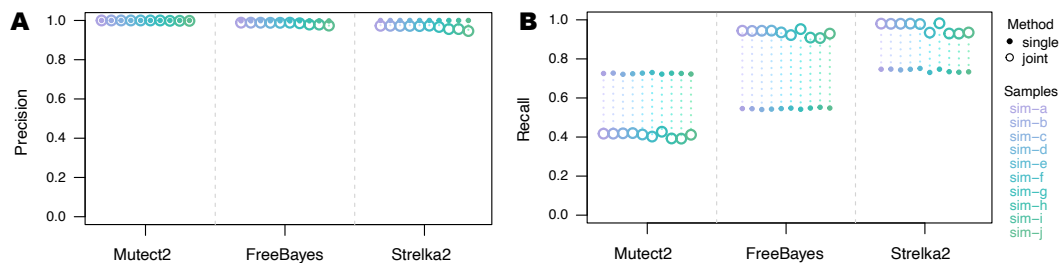


Figure A.3: Performance of workflows using simulated data: A) Precision and B) Recall of Mutect2, FreeBayes and Strelka2, run in single tumour-normal paired and joint calling configurations.

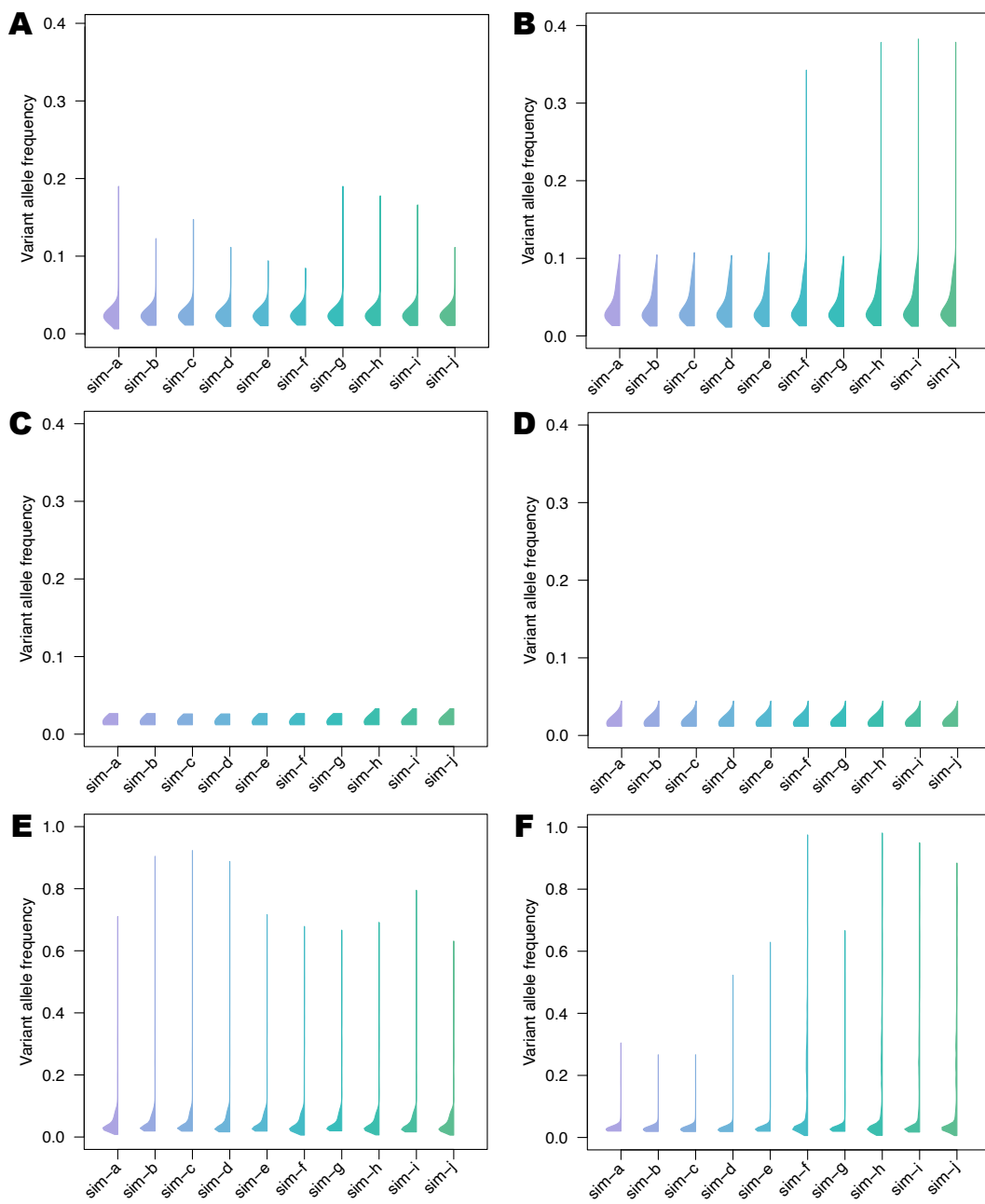


Figure A.4: Variant allele frequencies (VAF) of variants detected by joint sample analysis; A) VAF distribution of true positive variants additionally detected by Strelka2pass B) and FreeBayesSomatic C) VAF distribution of false positive variants additionally detected by FreeBayesSomatic D) and Strelka2pass E) VAF distribution of false negatives not called by FreeBayesSomatic F) and Strelka2pass.

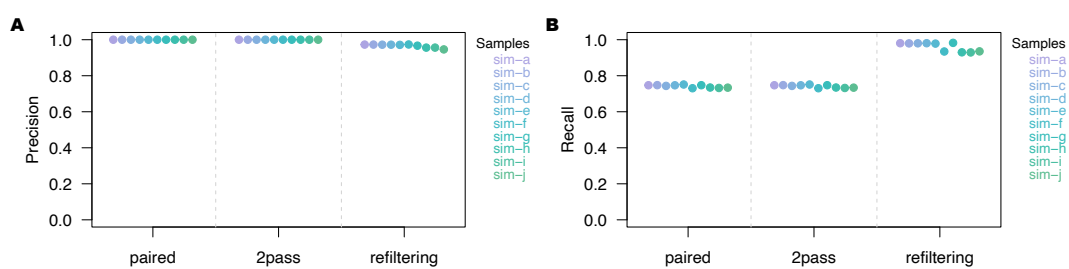


Figure A.5: Performance of individual steps in the Strelka2pass workflow using the simulated data: A) Precision and B) Recall of tumour-normal paired analysis, two-pass step without refiltering (supplying variants from all tumour-normal pairs for evaluation) and two-pass step with refiltering (the final workflow)

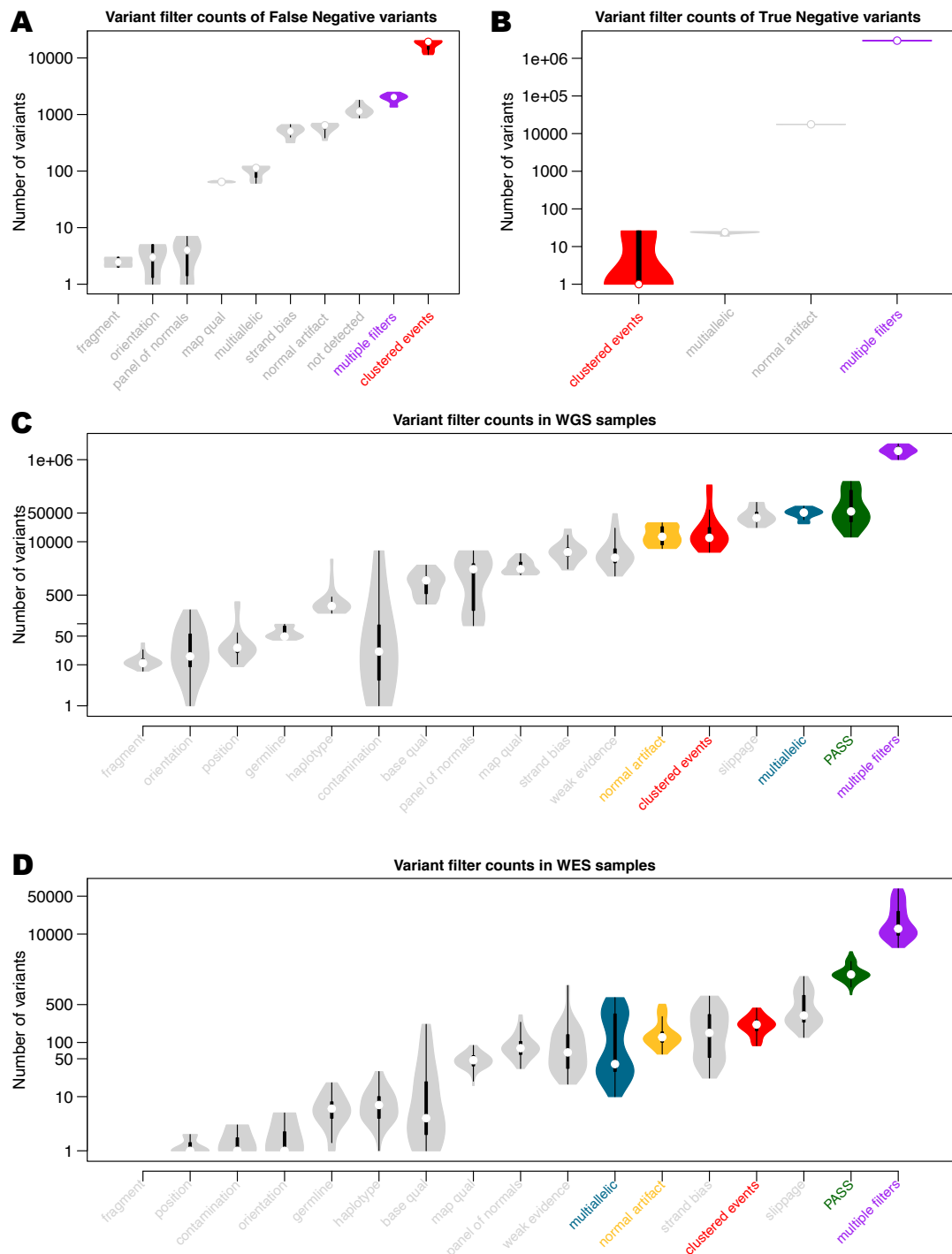


Figure A.6: Summary of variant filters assigned by Mutect2; The counts for each filter type are denoted by black boxplots with white circles depicting the median values. The fitted distribution of variant counts outlines each boxplot; A) Counts of filter assignments for false negative variants and B) true negative variants called by Mutect2 C) Filter assignment for all variants reported for sequenced patient data sequenced with WGS or D) WES.

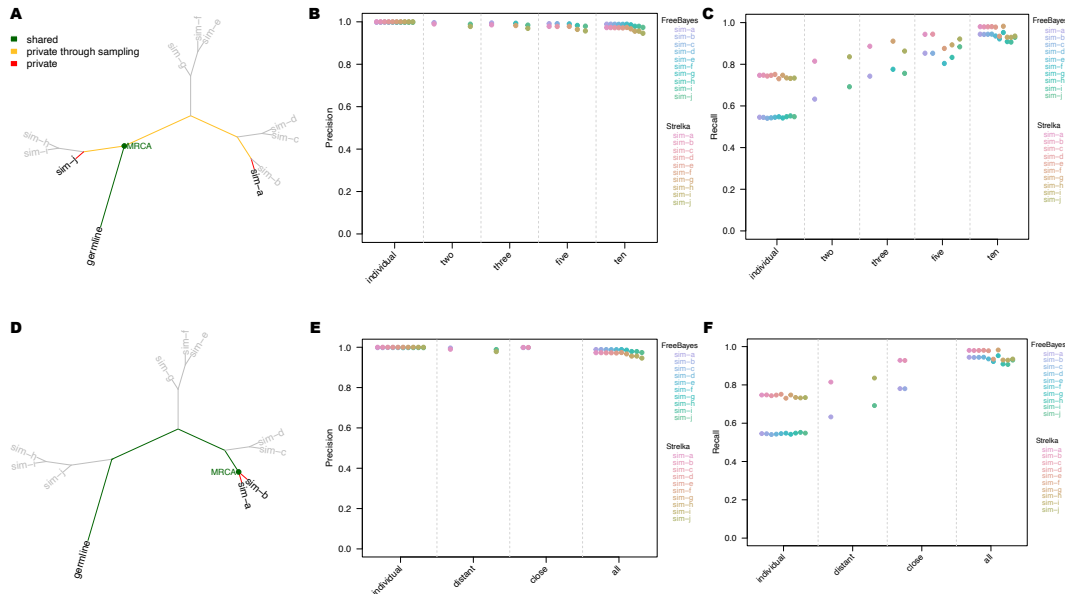


Figure A.7: Assessing the performance of different workflows using tumour samples with different evolutionary relationships in the simulated data; A) Simulated phylogeny highlighting two samples with high evolutionary distance (sim-a and sim-j) where MRCA denotes the most recent common ancestor. B) Precision and C) Recall estimates of FreeBayes and Strelka, run in individual tumour-normal paired and joint calling configurations using two (sim-a and sim-j), three (sim-a, sim-g and sim-j), five (sim-a, sim-c, sim-f, sim-h and sim-j) and all ten tumour samples D) Simulated phylogeny highlighting two samples with low evolutionary distance (sim-a and sim-b). E) Precision and F) Recall estimates for FreeBayes and Strelka run in individual tumour-normal paired and joint calling configurations. The plots compare the performance of these workflows when using two evolutionary distant samples (sim-a and sim-j), two evolutionary close samples (sim-a and sim-b) and all ten tumour samples.

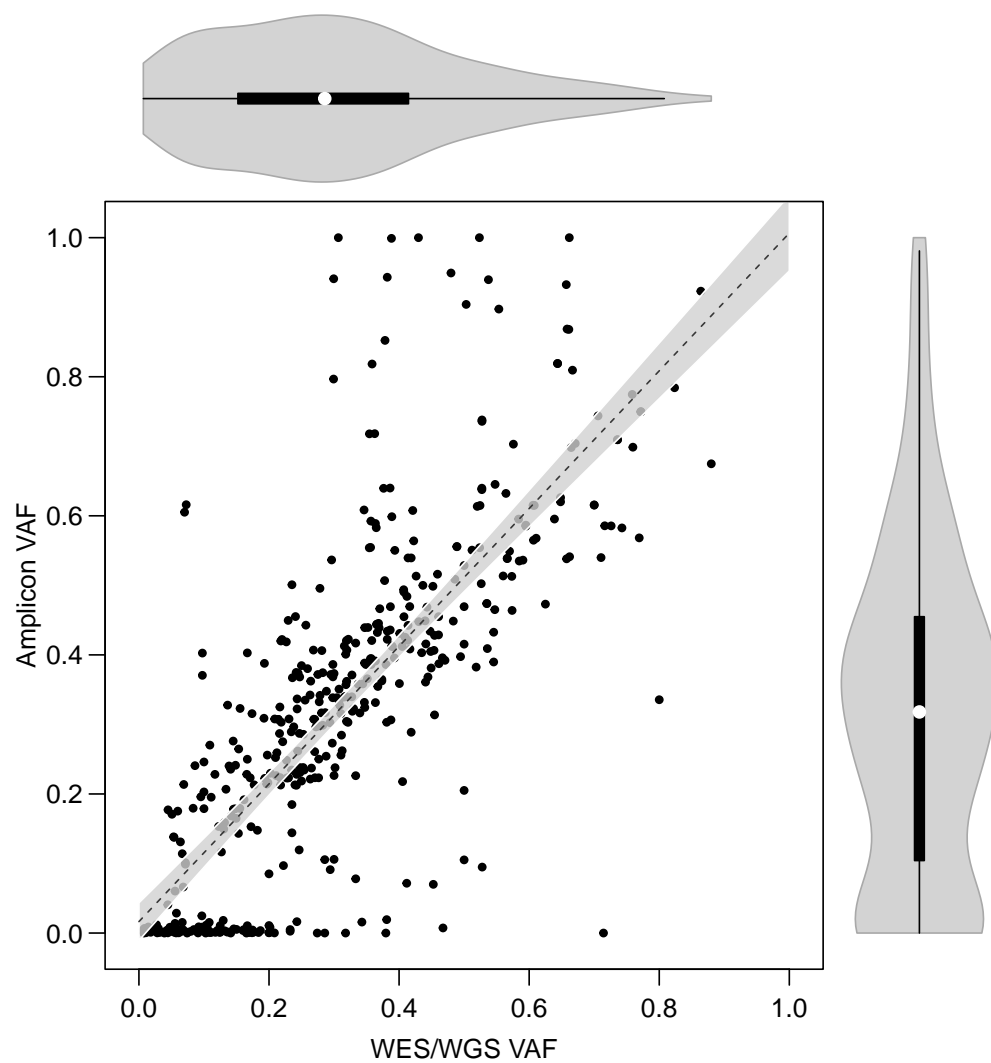


Figure A.8: Correlation of variant allele frequencies (VAF) from WES and WGS data against targeted amplicon sequencing VAF values with fitted violin plots of each individual distribution. Grey background shows 95% confidence interval for the fit of the linear model (dotted line).

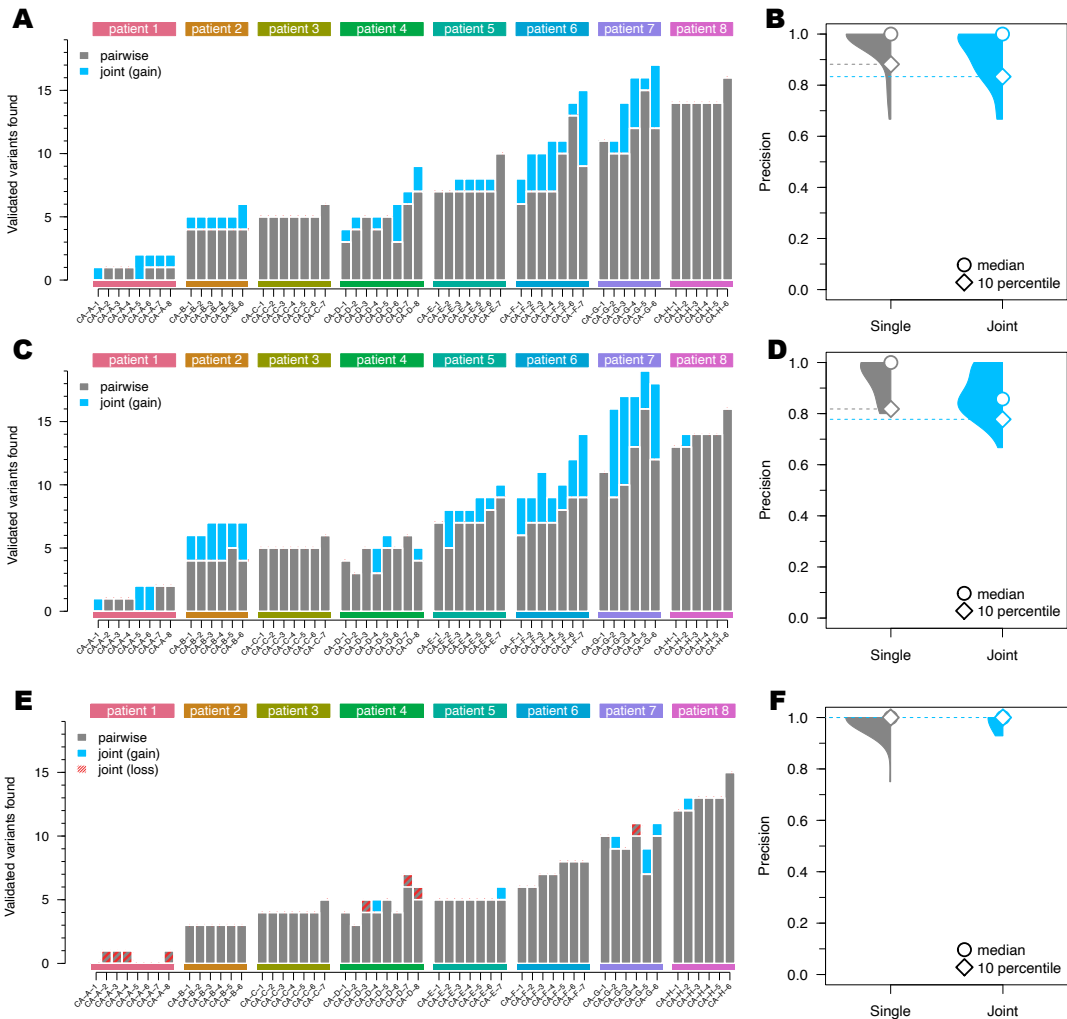


Figure A.9: Performance of the different workflows using clinical samples from eight cancer patients: A) Number of variants called by Strelka2 run in the tumour-normal paired (grey) and joint calling configurations, which have been validated by targeted amplicon sequencing (TAS). The same for C) FreeBayes and E) Mutect2 workflows. Precision of tumour-normal paired and joint analysis of TAS validated clinical data for B) Strelka2, D) FreeBayes and F) Mutect2; Sup. Table 1 provides the sample naming map to the original publications.

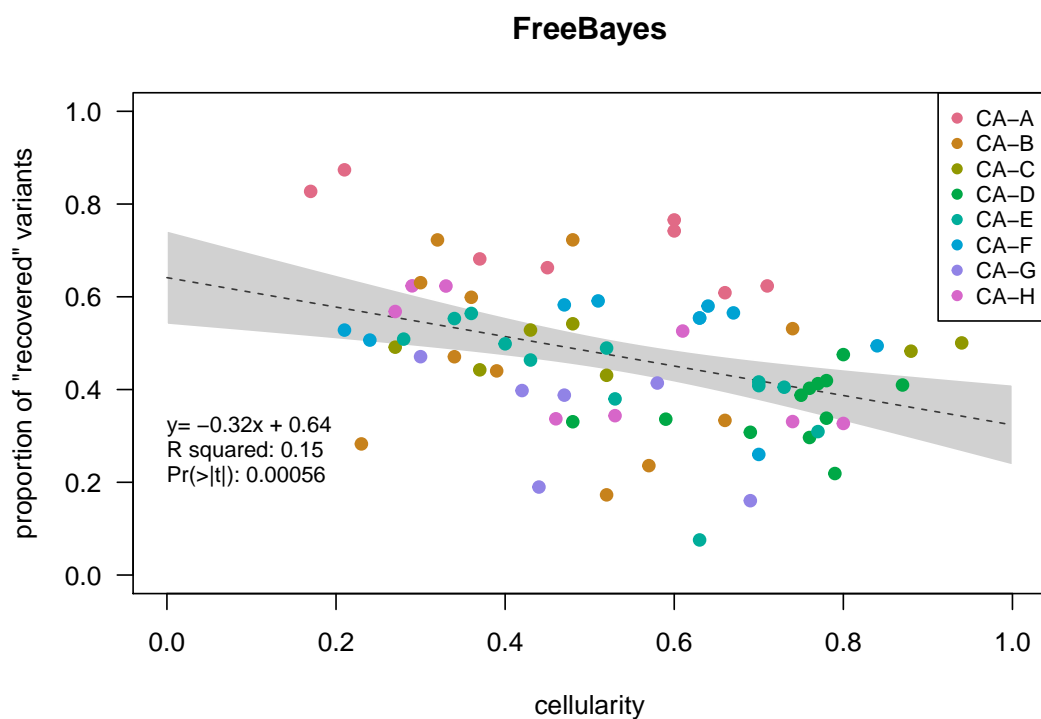


Figure A.10: Correlation between cellularity and proportion of variants found only with joint calling using FreeBayesSomatic. Grey background shows 95% confidence interval for fit of linear model (dotted line)

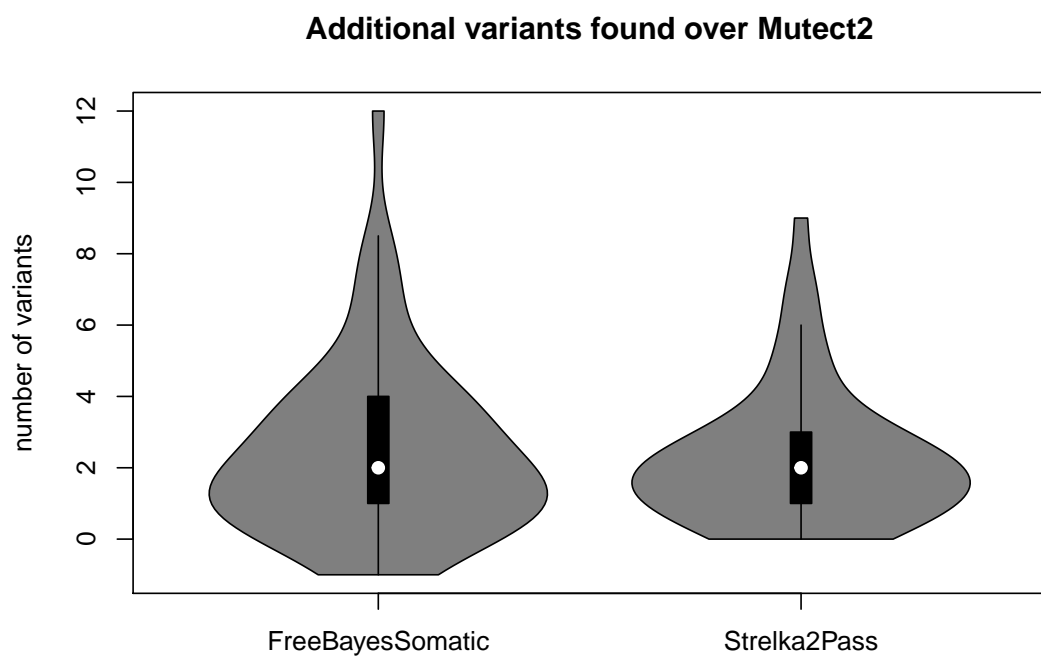


Figure A.11: Improvement in recall using FreeBayesSomatic and Strelka2pass over Mutect2 in the clinical samples.

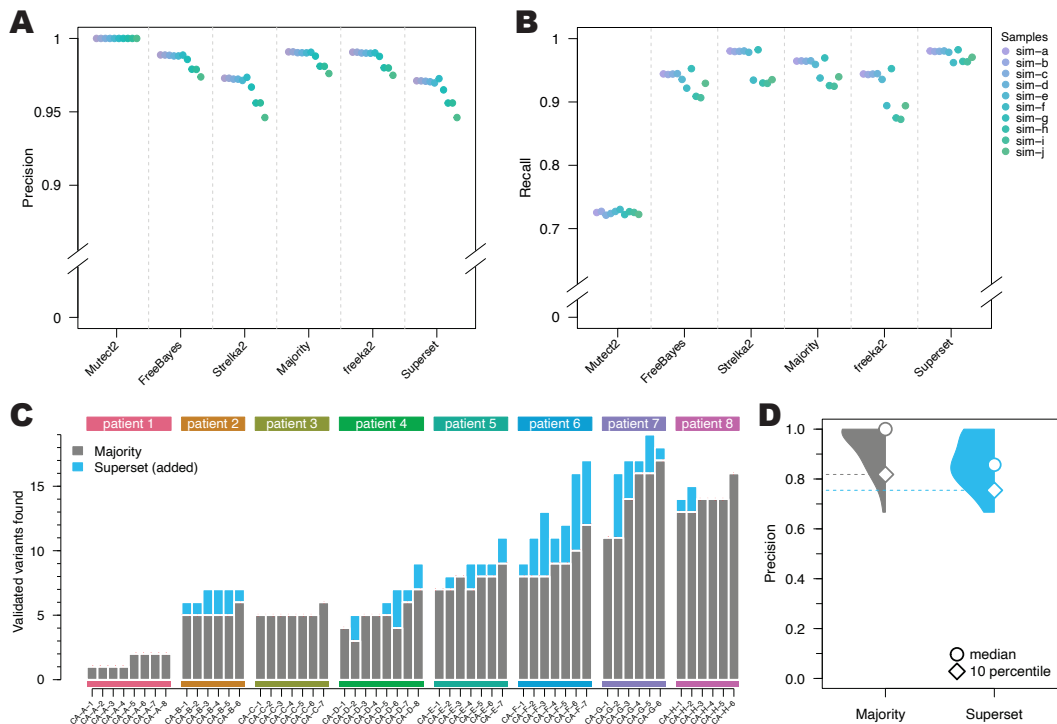


Figure A.12: Performance of ensemble variant calling strategies. A) Precision and B) Recall of variant detection using the joint multi-sample calling of each tool separately and compared to using Majority-vote ensemble calling (variant is called by at least two callers), Freek2 (variant is called by both FreeBayesSomatic and Strelka2pass) and Superset (variant is called by either FreeBayesSomatic or Strelka2pass) for the simulated dataset D) Number of TAS validated variants found in the clinical samples with Majority-vote and Superset methods and the corresponding D) Precision estimates.

Table A.1: Sample naming map relating to previously published datasets. The first column contains sample names as they appear in this work, and the third column denotes how the samples are referred to in the original studies. Forth column shows the type of sequencing WES: whole-exome sequencing; WGS: whole genome sequencing.

SAMPLE NAME	PUBLISHED STUDY	ORIGINAL NAME	SEQUENCING TYPE
CA-A-1	Solomon et al. [164]	Case 1 Left liver 1	WGS
CA-A-2		Case 1 Right occipital	
CA-A-3		Case 1 Right liver 2	
CA-A-4		Case 1 Right pleura	
CA-A-5		Case 1 Left lower lung lobe	
CA-A-6		Case 1 Left liver 5	
CA-A-7		Case 1 Right liver 3	
CA-A-8		Case 1 Left liver 2	
CA-B-1	Vergara et al. [165]	CAS-B-21-L-LUNG	WES
CA-B-2		CAS-B-22-R-LUNG	
CA-B-3		CAS-B-14B37035-1B	
CA-B-4		CAS-B-Primary-1	
CA-B-5		CAS-B-15Bo8317-3A	
CA-B-6		CAS-B-14B37035-1C	
CA-C-1		CAS-A-FRo7935894	WGS
CA-C-2		CAS-A-FRo7935905	
CA-C-3		CAS-A-FRo7935906	
CA-C-4		CAS-A-FRo7935907	
CA-C-5		CAS-A-FRo7935908	
CA-C-6		CAS-A-FRo7935916	
CA-C-7		CAS-A-FRo7935918	
CA-D-1		CAS-G-91-2	WES
CA-D-2		CAS-G-75	
CA-D-3		CAS-G-74	
CA-D-4		CAS-G-71	
CA-D-5		CAS-G-91	
CA-D-6		CAS-G-76	
CA-D-7		CAS-G-94	
CA-D-8		CAS-G-72	
CA-E-1		CAS-D-70	WES
CA-E-2		CAS-D-61-3	
CA-E-3		CAS-D-66	
CA-E-4		CAS-D-68	
CA-E-5		CAS-D-64	
CA-E-6		CAS-D-61-2	
CA-E-7		CAS-D-62	
CA-F-1		CAS-C-41	WES
CA-F-2		CAS-C-40-Fresh	
CA-F-3		CAS-C-37	
CA-F-4		CAS-C-44	
CA-F-5		CAS-C-42-Fresh	
CA-F-6		CAS-C-43-Fresh	
CA-F-7		CAS-C-46-Primary	
CA-G-1		CAS-F-FRo7935922	WGS
CA-G-2		CAS-F-FRo7935915	
CA-G-3		CAS-F-FRo7935913	
CA-G-4		CAS-F-FRo7935909	
CA-G-5		CAS-F-FRo7935904	
CA-G-6		CAS-F-FRo7935903	
CA-H-1		CAS-E-1	WES
CA-H-2		CAS-E-3	
CA-H-3		CAS-E-4	
CA-H-4		CAS-E-10	
CA-H-5		CAS-E-6	
CA-H-6		CAS-E-8	

Table A.2: Runtime of different workflows on simulated data; The runtimes were generated on the Peter MacCallum Cancer Centre HPC cluster with Intel(R) Xeon(R) CPU E5-2660 v3 @ 2.60GHz. The times are displayed in single CPU runtime, but each workflow is highly parallelised, such that the user runtime is far lower.

Method	Number of tumour samples used for joint calling			
	2	3	5	10
FreeBayesSomatic	562h	811h	1185h	2292h
Strelka2Pass	310h	465h	776h	1552h
Mutect2	-	-	-	28 418h

A.5 Supplementary methods

A.5.1 Alignment of clinical data

Detailed information on processing of the clinical sequencing datasets was published previously [164, 165]. Briefly, reads were aligned to GRCh38 for patient CAS-A and GRCh37 for patients CAS-B through CAS-H using BWA version 0.7.17 [267] allowing the use of alternative contigs. Reads were then marked as duplicates with Picard software (v2.17.3).

A.5.2 Validation of clinical data

Detailed information on targeted amplicon sequencing of patient samples can be found in the original publications [164, 165]. A SNV called in WES with any workflow was considered a true positive when the adjusted p-value calculated through an exact binomial test was lower than 0.05 on the TAS data. The probability of success for this test was estimated as the number of bases different from the reference divided by the total number of sequenced bases (0.001) and the number of trials was the read depth covering the variant. For indels, a variant was considered to be validated if either of the panel variant callers primal (in house) or canary [268] called the same variant.

Only amplicons with an average mapping rate of at least 80% over all samples, as well as an average coverage of more than 300 were considered for further analysis. WES variants were first subsetted to be within the area of the respective amplicons.

A.5.3 Purity estimation with sequenza

For CA-A the sequenza-utils python program was used to generate input files for the sequenza R program on the aligned BAM files [13]. Kmin and gamma were set to 100 and 500 respectively to discourage a highly fragmented result. For CA-B through -H the reported tumour purities were used from the publication [165].

A.5.4 Performance of individual steps in Strelka2Pass

As each of the three steps potentially has implications for the performance, we assessed the improvement provided by each step in the Strelka2pass workflow. [Figure A.5](#) shows, that there is no change in either precision or recall just by supplying variants from all tumour-normal pairs for a second round of evaluation. However, there is a >20% improvement in recall when coupling this to the refiltering step that we have built into the workflow.

A.5.5 Ensemble workflows – user suggestions

An overall workflow can contain any number of additional variant callers, when not restricted to callers with joint analysis capability. Importantly, there is no benefit of jointly analysing samples with Mutect2, and it may decrease the performance in some cases. Each of our presented workflows outperformed Mutect2 on the data shown here, so when assembling an ensemble method, these methods, should have a higher confidence assigned to them in joint analysis cases, than tumour-normal pair approaches.

Depending on the end needs of the user, an ensemble workflow can be optimised towards precision or recall. In [Figure A.12](#) we show the performance changes improvement that can be achieved by combining Mutect2 in tumour-normal paired analysis with the two new workflows FreeBayesSomatic and Strelka2Pass. First, in a “best of three” majority vote, where the variant needs to be called by two out of three variant callers, we enhance the precision of each of the individual tools, with slightly lower recall. On the other hand, with the super set approach, where any variant called in either FreeBayesSomatic or Strelka2Pass is included in the end result, this improves the recall even further, but slightly reduces the precision. This approach has the additional benefit of not needing to run Mutect2 which is an order of magnitude slower in our tests, than Strelka2Pass and

FreeBayesSomatic ([Table A.2](#)). The usage of these workflows can be easily integrated into existing workflows and can be customised to the needs of the user.

Additional supplementary data

This section contains supplementary data for the joint somatic variant calling chapter ([Chapter 2](#)) not contains in the published paper but for the work shown in this thesis

Listing A.1: parse strelka VCF

```
1 #this function will parse a strelkaVcf after the joined refiltering put
2   all the
3 #relevant info into a data.table
4 parseStrelkaVcf <- function(vcffilePath=stop("need file as input"),
5   geneList){
6   require(ensemblVEP)
7   vcfObj <- VariantAnnotation::readVcf(vcffilePath)
8   vcfObj <- VariantAnnotation::expand(vcfObj)
9
10  res <- data.table()
11  #add the fixed columns to the result
12  fixed <- .getFixedVcfColumns(vcfObj)
13  res[,c("chr","pos","ref","alt","filter"):=fixed]
14
15  #get the vep annotation
16  vepcolumns <- .getVepAnnotationColumns(vcfObj, geneList)
17  res <- cbind(res,vepcolumns)
18
19  #add additional info, which is interesting but we dont us TUMOR and
20  # NORMAL
21  # because what if the columns were renamed
22  res[, dp:=as.numeric(geno(vcfObj)$DP[,2])]
23  if(is.null(geno(vcfObj)$AF)){
24    res[, freq:=extractStrelkaAD(vcfObj, sample=2)/dp]
25    res[, nfreq:=extractStrelkaAD(vcfObj, sample=1)/dp]
26  }else{
27    res[, freq:=as.numeric(geno(vcfObj)$AF[,2])]
28    res[, nfreq:=as.numeric(geno(vcfObj)$AF[,1])]
29  }
30
31  return(res)
32 }
```

Listing A.2: annotate variants with copy number calls

```
1 for (sample in dnaSamples){
2 }
```

```

3 varName <- paste0("vars", sample)
4 varTmp <- as.data.frame(get(varName))
5
6 segments <- read.table(paste0(pathPrefix, '/dawson_genomics/Projects/
7 CASCADE/ ', .sampleBase, '/analysis/ ', .sampleBase, "-", sample, '/CNV
8 /', .sampleBase, "-", sample, "_segments.txt"), header=T)
9 cnInfo <- apply(varTmp, 1, function(x){
10   # print(x["chr"])
11   cnRow <- segments[(segments$chromosome == x["chr"] & segments$start.
12   pos <= as.numeric(x["pos"]) & segments$end.pos >= as.numeric(x["pos"]))
13   ),]
14   cnCols <- cnRow[,c("CNt", "A", "B")]
15   if (nrow(cnCols) == 0){
16     #no info means we assume its normal
17     cnCols <- data.frame(CNt=2, A=1, B=1)
18   }
19   return(cnCols)
20 })
21
22 cnInfo <- bind_rows(cnInfo)
23 varTmp <- cbind(varTmp, cnInfo)
24
25 #dividing by purity and then dividing by CNt tells us how many cells
26 #have that variant
27 varTmp$vaf <- varTmp$freq / purities[counter] #/ varTmp$CNt
28 #does not help if we have more than 1 in a percentage
29 varTmp$vaf[varTmp$vaf > 1] <- 1
30 assign(varName, as.data.table(varTmp))
31 counter <- counter +1
32
33 }

```

Listing A.3: convert to maf format

```

1 convertToMaf <- function(varTable, chrs=paste0("chr", c(1:22, "X", "Y"))){
2
3   keep <- varTable[chr %in% chrs,]
4
5   ret <- data.table(Hugo_Symbol=keep$symbol,
6                      Chromosome=keep$chr,
7                      Start_position=keep$pos,
8                      Reference_Allele=keep$ref,
9                      Tumor_Seq_Allele2=keep$alt,

```

```

10      t_ref_count=round(keep$dp*(1-keep$freq)),
11      t_alt_count=round(keep$dp*keep$freq),
12      local_cn_a1=keep$A,
13      local_cn_a2=keep$B)

14
15      #if there is no gene annotated, we set it to unknown
16      ret[is.na(ret$Hugo_Symbol), "Hugo_Symbol"] <- "Unknown"
17
18      return(ret)
19
20  }

```

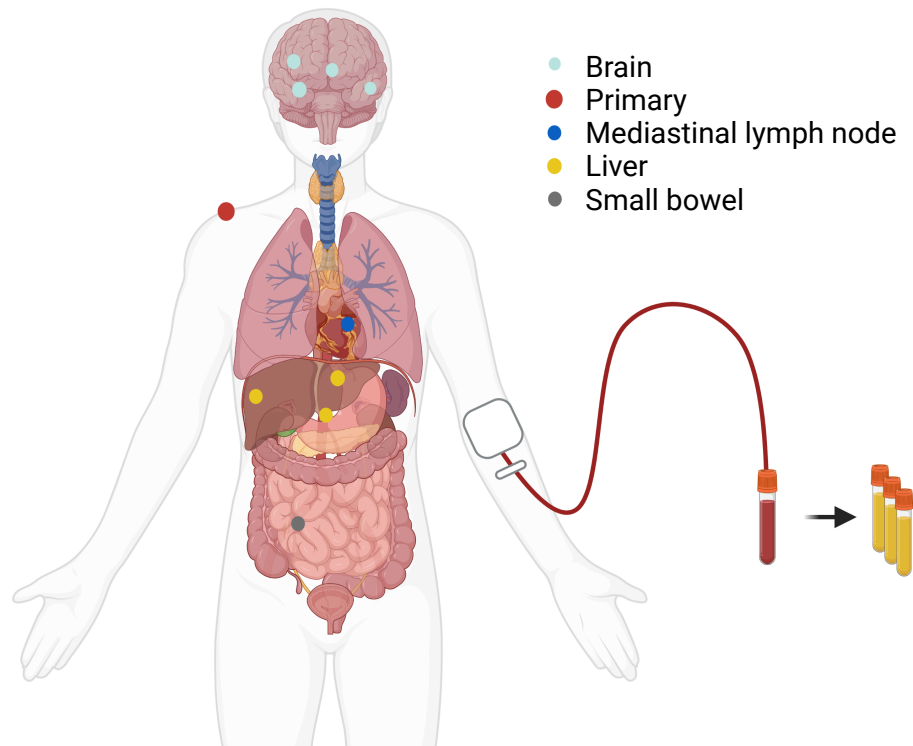


Figure A.13: Schematic of analysed tumour lesions in patient CA-F; Primary (diagnostic) skin sample is shown in red; metastatic sites are shown in blue; From top to bottom: right parietal lobe; left temporal lobe; right cerebellum; posterior mediastinal lymph node; left liver lobe; right liver lobe; liver, hepatic vessel; small bowel; Right side depicts three blood draws with plasma sampling (Figure 2.4)

B

CASCADE - supplementary methods

Listing B.1: Preprocessing of mitochondrial reads and variants for analysis in R

```
1 #!/usr/bin/env bash
2 #
3 # Author: Sebastian Hollizeck
4 # Date: 26/10/2021
5 #
6 # adapts the ideas from Ludwig et al. (https://www.cell.com/
7 #     cell/fulltext/S0092-8674(19)30055-8)
8 # to process mitochondrial reads for phylogenetic reconstruction
9 #
10
11
12 reference="/data/reference/dawson_labs/genomes/GRCh38/GCA_000001405.15
13 _GRCh38_full_analysis_set.fna"
14
15 pileupProg="python /dawson_genomics/0ther/software/mitoGenotyping/01
16 _pileup_counts.py"
17 mergeProg="bash /dawson_genomics/0ther/software/mitoGenotyping/02
18 _merge_pileup_counts.sh"
19 generateRDSProg="Rscript /dawson_genomics/0ther/software/mitoGenotyping
20 /03_makeRDS.R"
21
22 mtChrName="chrM"
23 mtLength=16569
```

```

24
25 #bams in comma seperated array
26 bams=(<bams here>)
27
28 #base name of the patient
29 projectName=""
30
31
32 tmpDir=$(mktemp -d)
33
34 #folder for the temp processed data
35 processedDir=$tmpDir"/processed_data"
36 mkdir $processedDir
37
38
39 outPath="/dawson_genomics/Projects/CASCADE/$sampleName/analysis/joint/
        mito"
40
41
42 for bam in "${bams[@]}"; do
43
44     bamBase=$(basename $bam)
45     end=${bamBase#*_}
46     start=${bamBase%%_*}
47
48     #new tmp bam to write to
49     mtBam=$tmpDir/$start"_MT_"$end
50     #just in case it was a cram in the beginning, we change this to bam
51     mtBam=${mtBam/.cram/.bam}
52
53     #need to only get the MT reads in a bam (and check if we got things)
54     res=$(samtools view -@ 2 -1 -T $reference -o $mtBam -O BAM $bam
      $mtChrName --write-index 2>&1)
55
56     if [[ "$test" =~ "specifies an invalid region or unknown reference.
      Continue anyway." ]]; then
57         echo "Specified mitochondrial chromosome name ($mtChrName) does
      not exist in bam ($bam)"
58         exit 1
59     fi
60

```

```
61 $pileupProg $mtBam $processedDir/$start $mtLength $minBQ $start
62 $minMQ &
63 done
64
65 wait
66
67 #merge everything we generated before
68 $mergeProg $processedDir $projectName
69
70 #generate a only MT reference
71 samtools faidx -o $tmpDir/mtRef.fa $reference $mtChrName
72
73 #convert to an RDS to be readable in R
74 $generateRDSProg $processedDir $tmpDir/mtRef.fa
```

Table B.1: List of lung cancer related genes used for variant effect prioritisation. If no source was listed, the gene is part of the “AVENIO ctDNA and Tumour Tissue extended Panel” [269], the list of commonly mutated genes in lung cancer [270, 271], which were validated through TCGA [272]. Some of the genes are also part of the targets for molecular analysis of the National Comprehensive Cancer Network guidelines for NSCLC [273].

Gene	source	Gene	source
ABL1		KEAP1	
AKT1		KIT	
AKT2		KRAS	
ALK		MAP2K1	
APC		MAP2K2	
AR		MET	
ARAF		miR-103a-3p	Fan et al. [274]
BRAF		MKRN2	Jiang et al. [275]
BRCA1		MLH1	
BRCA2		MSH2	
CCND1		MSH6	
CCND2		MTOR	
CCND3		NF2	
CD274		NFE2L2	
CDK4		NRAS	
CDK6		NTRK1	
CDKN2A		PDCD1LG2	
CHL1	Hötzl et al. [276]	PDGFRA	
CSF1R		PDGFRB	
CTNNB1		PIK3CA	
DDR2		PIK3R1	
DPYD		PMAIP1	Do et al. [277]
EGFR		PMS2	
ERBB2		PTCH1	
ESR1		PTEN	
EZH2		RAF1	
FBXW7		RB1	
FGFR1		RET	
FGFR2		RNF43	
FGFR3		ROS1	
FLT1		SMAD4	
FLT3		SMO	
FLT4		STK11	
GADD45B	Do et al. [277]	TERT	
GATA3		TFAP2C	Do et al. [277]
GNA11		THZ1	Cheng et al. [278]
GNAQ		TM4SF1	Ye et al. [279]
GNAS		TP53	
IDH1		TSC1	
IDH2		TSC2	
IFITM1	Yang et al. [280]	TUSC3	Feng et al. [281]
JAK2		UGT1A1	
JAK3		USP13	Wu et al. [282]
KDM4	Sun et al. [283]	VHL	
KDR			

CASCADE - supplementary figures

B.1 Patient CA-A



Figure B.1: Circos plot of patient CA-A sample 26 with somatic structural variants with allele frequency > 0.2 : outer first ring shows the canonical chromosomes with gaps (centromere, heterochromatin,...) highlighted as darker areas; second ring visualises all somatic SNVs corrected for tumour purity and scaled from 0 to 1, the colour representing the base change of SNV like in Alexandrov et al. [215]; vertical lines directly under the SNVs symbolise InDels, with yellow for insertions and red for deletions; the third ring shows the total copy number alterations, with green showing a copy number gain and red a loss, dots at the outer border show a copy number greater than four; the last ring shows the minor copy number, with blue depicting a gain and orange a loss, this ring allows the detection of copy number neutral changes, like loss of heterozygosity; the center shows all structural variants: translocations in blue, deletions in red, insertions in yellow, tandem duplications in green and inversions in black.

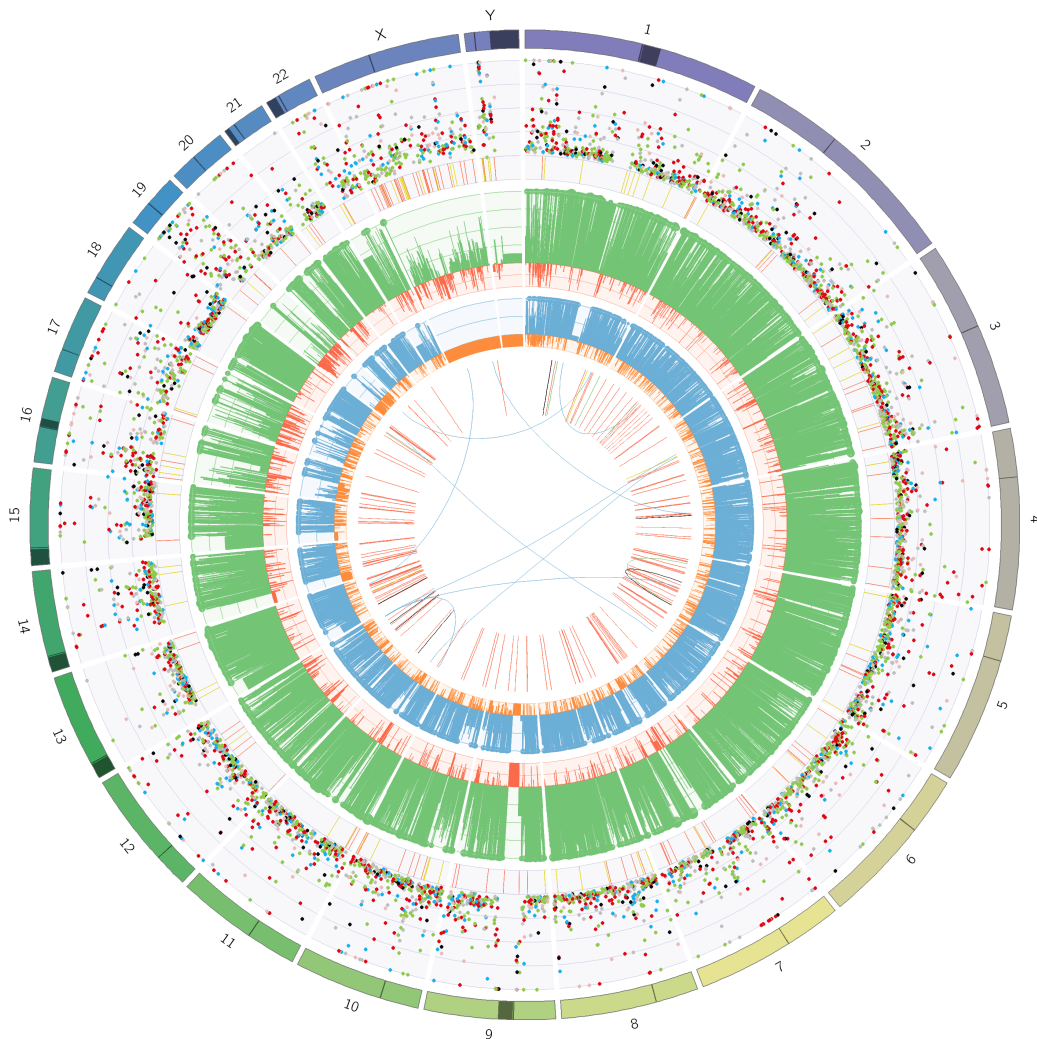


Figure B.2: Circos plot of patient CA-A sample 31 with somatic structural variants with allele frequency > 0.2 : outer first ring shows the canonical chromosomes with gaps (centromere, heterochromatin,...) highlighted as darker areas; second ring visualises all somatic SNVs corrected for tumour purity and scaled from 0 to 1, the colour representing the base change of SNV like in Alexandrov et al. [215]; vertical lines directly under the SNVs symbolise InDels, with yellow for insertions and red for deletions; the third ring shows the total copy number alterations, with green showing a copy number gain and red a loss, dots at the outer border show a copy number greater than four; the last ring shows the minor copy number, with blue depicting a gain and orange a loss, this ring allows the detection of copy number neutral changes, like loss of heterozygosity; the center shows all structural variants: translocations in blue, deletions in red, insertions in yellow, tandem duplications in green and inversions in black.

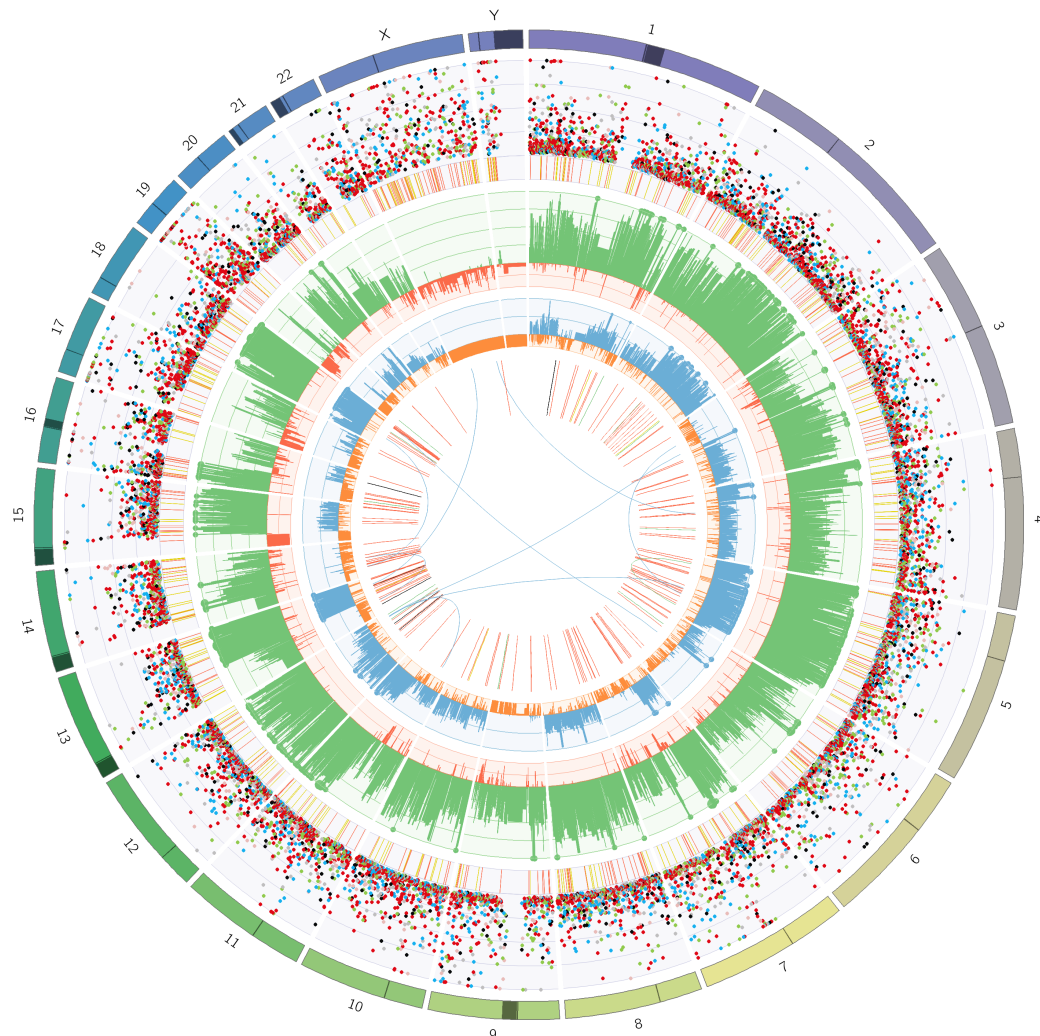


Figure B.3: Circos plot of patient CA-A sample 41 with somatic structural variants with allele frequency > 0.2: outer first ring shows the canonical chromosomes with gaps (centromere, heterochromatin,...) highlighted as darker areas; second ring visualises all somatic SNVs corrected for tumour purity and scaled from 0 to 1, the colour representing the base change of SNV like in Alexandrov et al. [215]; vertical lines directly under the SNVs symbolise InDels, with yellow for insertions and red for deletions; the third ring shows the total copy number alterations, with green showing a copy number gain and red a loss, dots at the outer border show a copy number greater than four; the last ring shows the minor copy number, with blue depicting a gain and orange a loss, this ring allows the detection of copy number neutral changes, like loss of heterozygosity; the center shows all structural variants: translocations in blue, deletions in red, insertions in yellow, tandem duplications in green and inversions in black.



Figure B.4: Circos plot of patient CA-A sample 47 with somatic structural variants with allele frequency > 0.2 : outer first ring shows the canonical chromosomes with gaps (centromere, heterochromatin,...) highlighted as darker areas; second ring visualises all somatic SNVs corrected for tumour purity and scaled from 0 to 1, the colour representing the base change of SNV like in Alexandrov et al. [215]; vertical lines directly under the SNVs symbolise InDels, with yellow for insertions and red for deletions; the third ring shows the total copy number alterations, with green showing a copy number gain and red a loss, dots at the outer border show a copy number greater than four; the last ring shows the minor copy number, with blue depicting a gain and orange a loss, this ring allows the detection of copy number neutral changes, like loss of heterozygosity; the center shows all structural variants: translocations in blue, deletions in red, insertions in yellow, tandem duplications in green and inversions in black.

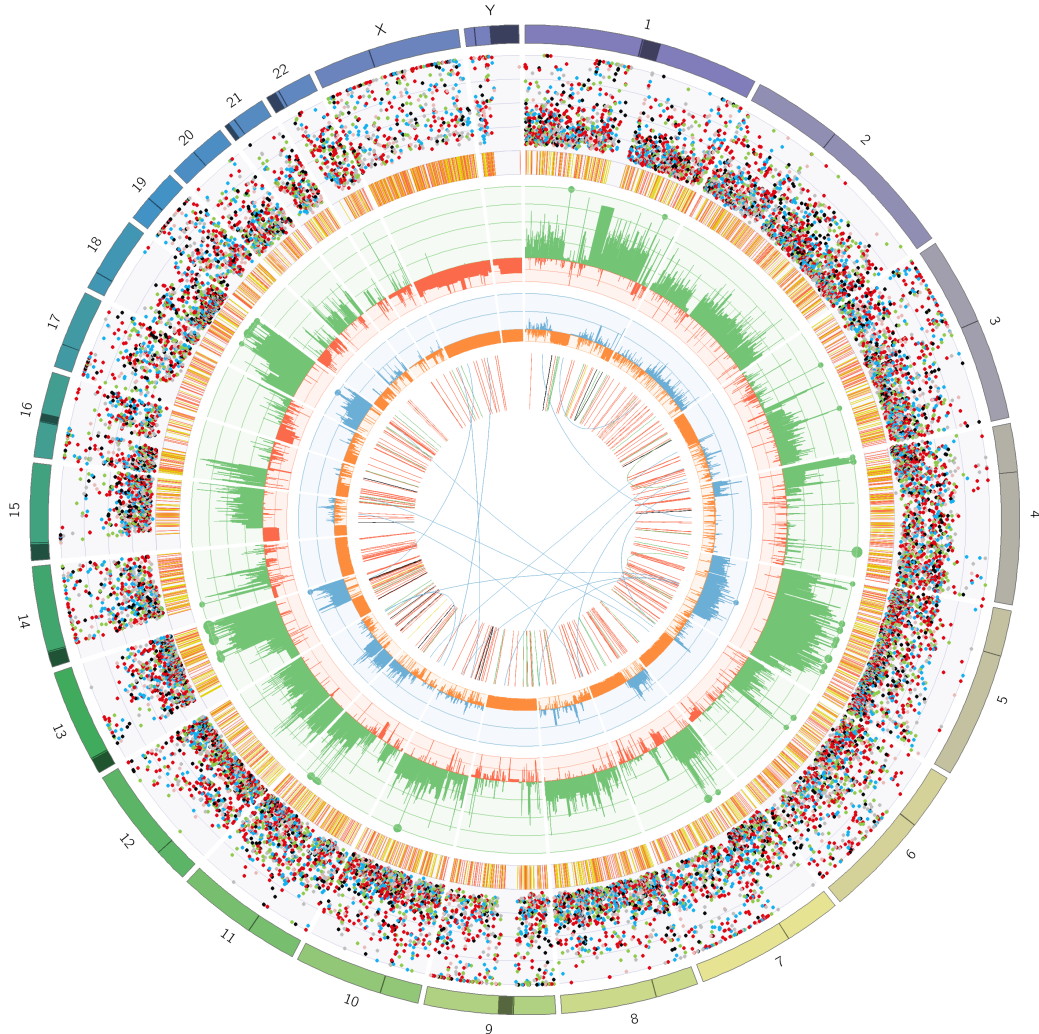


Figure B.5: Circos plot of patient CA-A sample 55 with somatic structural variants with allele frequency > 0.2: outer first ring shows the canonical chromosomes with gaps (centromere, heterochromatin,...) highlighted as darker areas; second ring visualises all somatic SNVs corrected for tumour purity and scaled from 0 to 1, the colour representing the base change of SNV like in Alexandrov et al. [215]; vertical lines directly under the SNVs symbolise InDels, with yellow for insertions and red for deletions; the third ring shows the total copy number alterations, with green showing a copy number gain and red a loss, dots at the outer border show a copy number greater than four; the last ring shows the minor copy number, with blue depicting a gain and orange a loss, this ring allows the detection of copy number neutral changes, like loss of heterozygosity; the center shows all structural variants: translocations in blue, deletions in red, insertions in yellow, tandem duplications in green and inversions in black.

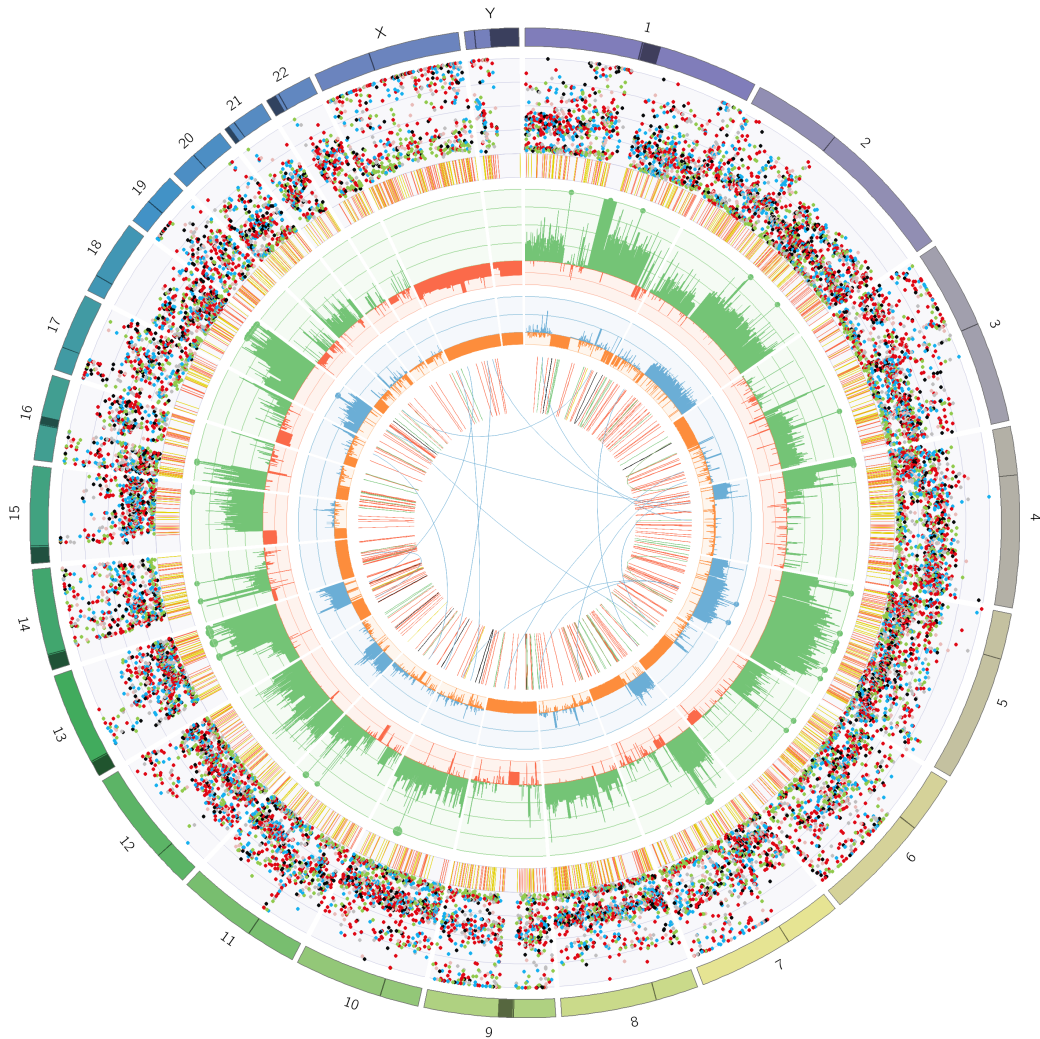


Figure B.6: Circos plot of patient CA-A sample 57 with somatic structural variants with allele frequency > 0.2 : outer first ring shows the canonical chromosomes with gaps (centromere, heterochromatin,...) highlighted as darker areas; second ring visualises all somatic SNVs corrected for tumour purity and scaled from 0 to 1, the colour representing the base change of SNV like in Alexandrov et al. [215]; vertical lines directly under the SNVs symbolise InDels, with yellow for insertions and red for deletions; the third ring shows the total copy number alterations, with green showing a copy number gain and red a loss, dots at the outer border show a copy number greater than four; the last ring shows the minor copy number, with blue depicting a gain and orange a loss, this ring allows the detection of copy number neutral changes, like loss of heterozygosity; the center shows all structural variants: translocations in blue, deletions in red, insertions in yellow, tandem duplications in green and inversions in black.



Figure B.7: Circos plot of patient CA-A sample 59 with somatic structural variants with allele frequency > 0.2 : outer first ring shows the canonical chromosomes with gaps (centromere, heterochromatin,...) highlighted as darker areas; second ring visualises all somatic SNVs corrected for tumour purity and scaled from 0 to 1, the colour representing the base change of SNV like in Alexandrov et al. [215]; vertical lines directly under the SNVs symbolise InDels, with yellow for insertions and red for deletions; the third ring shows the total copy number alterations, with green showing a copy number gain and red a loss, dots at the outer border show a copy number greater than four; the last ring shows the minor copy number, with blue depicting a gain and orange a loss, this ring allows the detection of copy number neutral changes, like loss of heterozygosity; the center shows all structural variants: translocations in blue, deletions in red, insertions in yellow, tandem duplications in green and inversions in black.

B.2 Patient CA-I

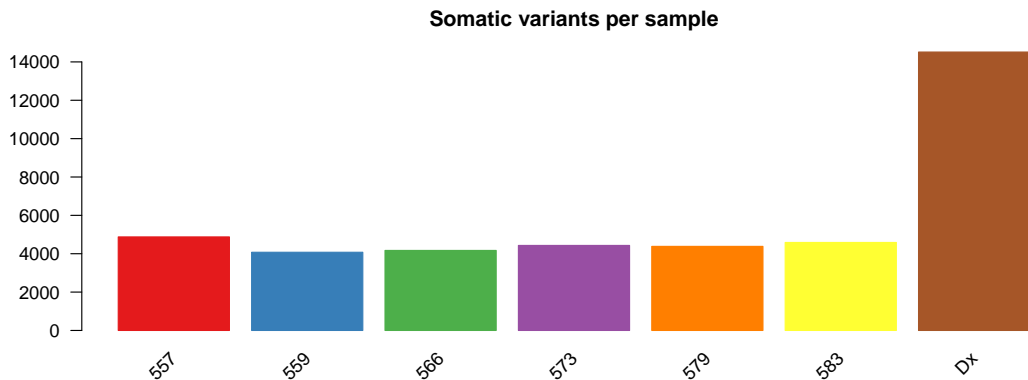


Figure B.8: Number of high confidence somatic variants per sample in patient CA-I; variants were called with the Strelka2Pass workflow and restricted to *PASS* only

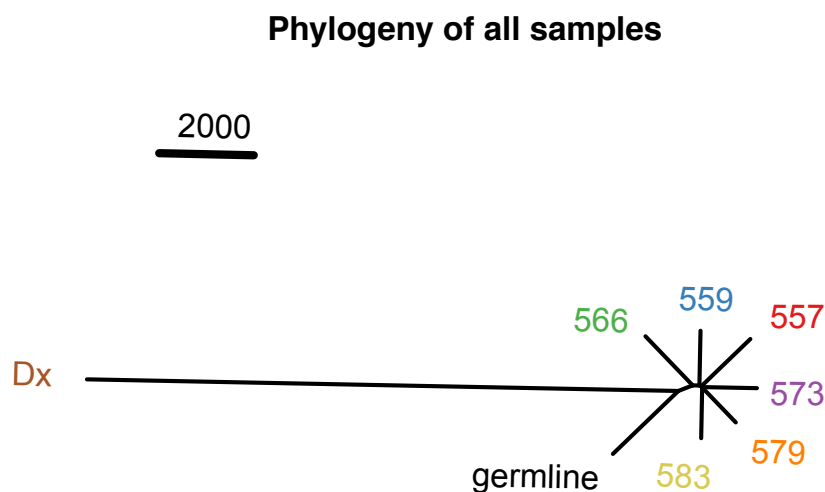


Figure B.9: Phylogeny of samples from patient CA-I with diagnostic sample

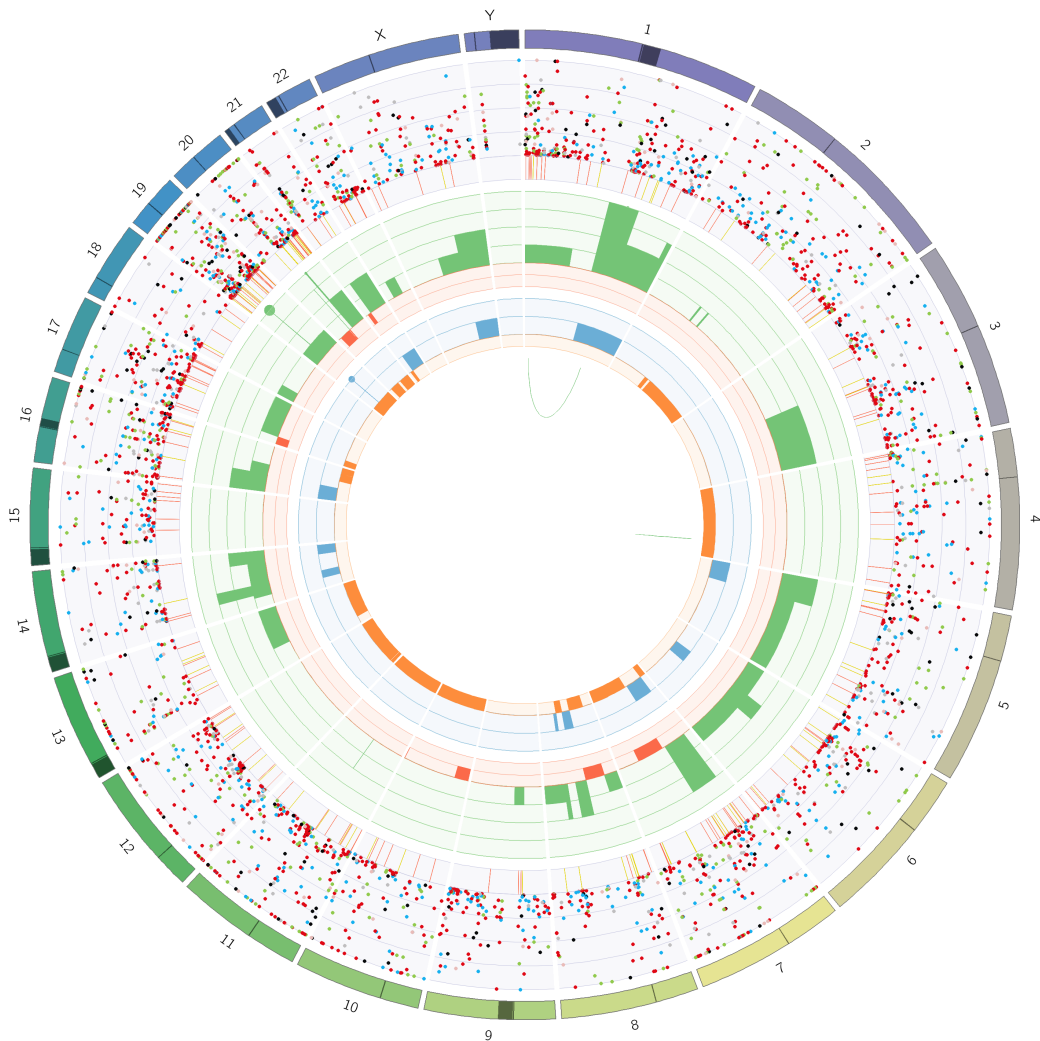


Figure B.10: Circos plot of patient CA-I sample 559 with somatic structural variants with allele frequency > 0.2 : outer first ring shows the canonical chromosomes with gaps (centromere, heterochromatin,...) highlighted as darker areas; second ring visualises all somatic SNVs corrected for tumour purity and scaled from 0 to 1, the colour representing the base change of SNV like in Alexandrov et al. [215]; vertical lines directly under the SNVs symbolise InDels, with yellow for insertions and red for deletions; the third ring shows the total copy number alterations, with green showing a copy number gain and red a loss, dots at the outer border show a copy number greater than four; the last ring shows the minor copy number, with blue depicting a gain and orange a loss, this ring allows the detection of copy number neutral changes, like loss of heterozygosity; the center shows all structural variants: translocations in blue, deletions in red, insertions in yellow, tandem duplications in green and inversions in black.

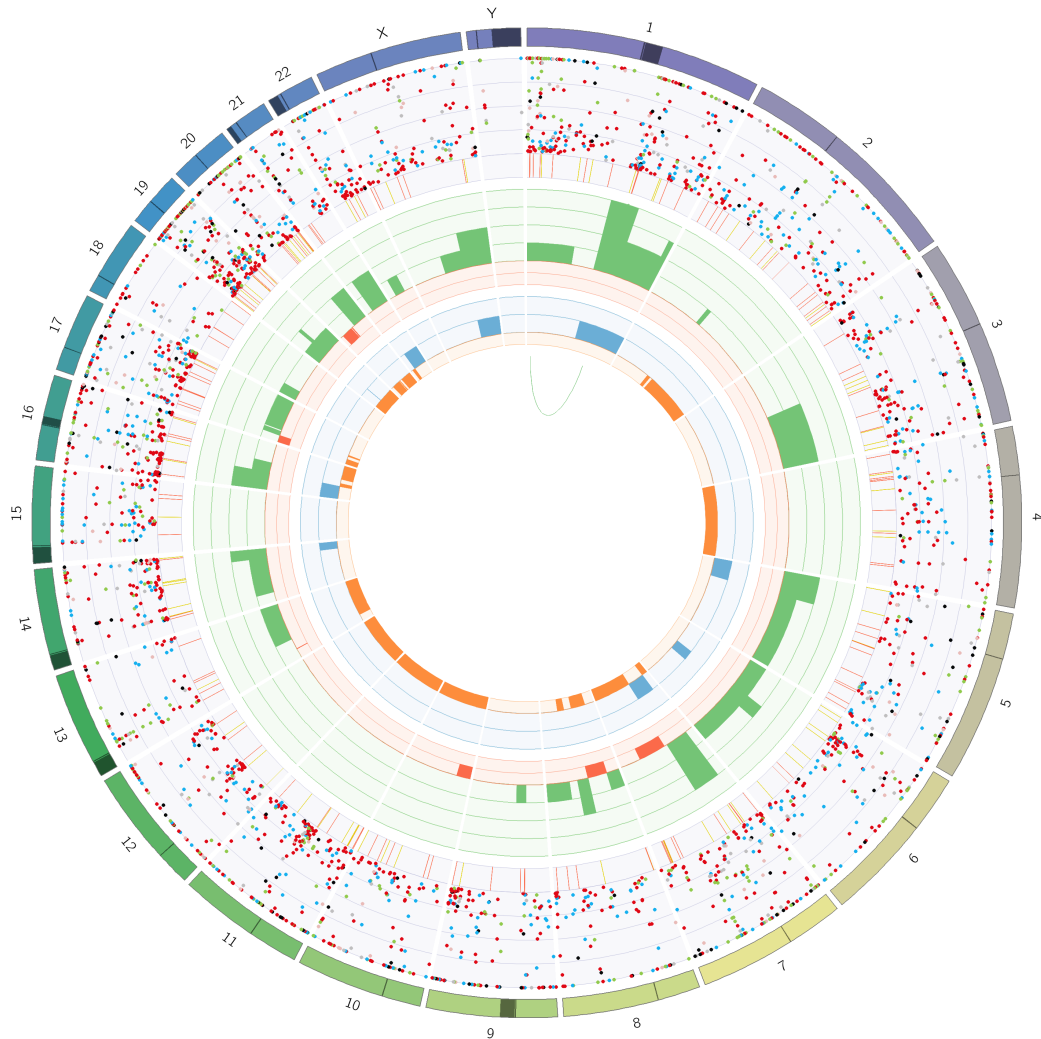


Figure B.11: Circos plot of patient CA-I sample 566 with somatic structural variants with allele frequency > 0.2 : outer first ring shows the canonical chromosomes with gaps (centromere, heterochromatin,...) highlighted as darker areas; second ring visualises all somatic SNVs corrected for tumour purity and scaled from 0 to 1, the colour representing the base change of SNV like in Alexandrov et al. [215]; vertical lines directly under the SNVs symbolise InDels, with yellow for insertions and red for deletions; the third ring shows the total copy number alterations, with green showing a copy number gain and red a loss, dots at the outer border show a copy number greater than four; the last ring shows the minor copy number, with blue depicting a gain and orange a loss, this ring allows the detection of copy number neutral changes, like loss of heterozygosity; the center shows all structural variants: translocations in blue, deletions in red, insertions in yellow, tandem duplications in green and inversions in black.

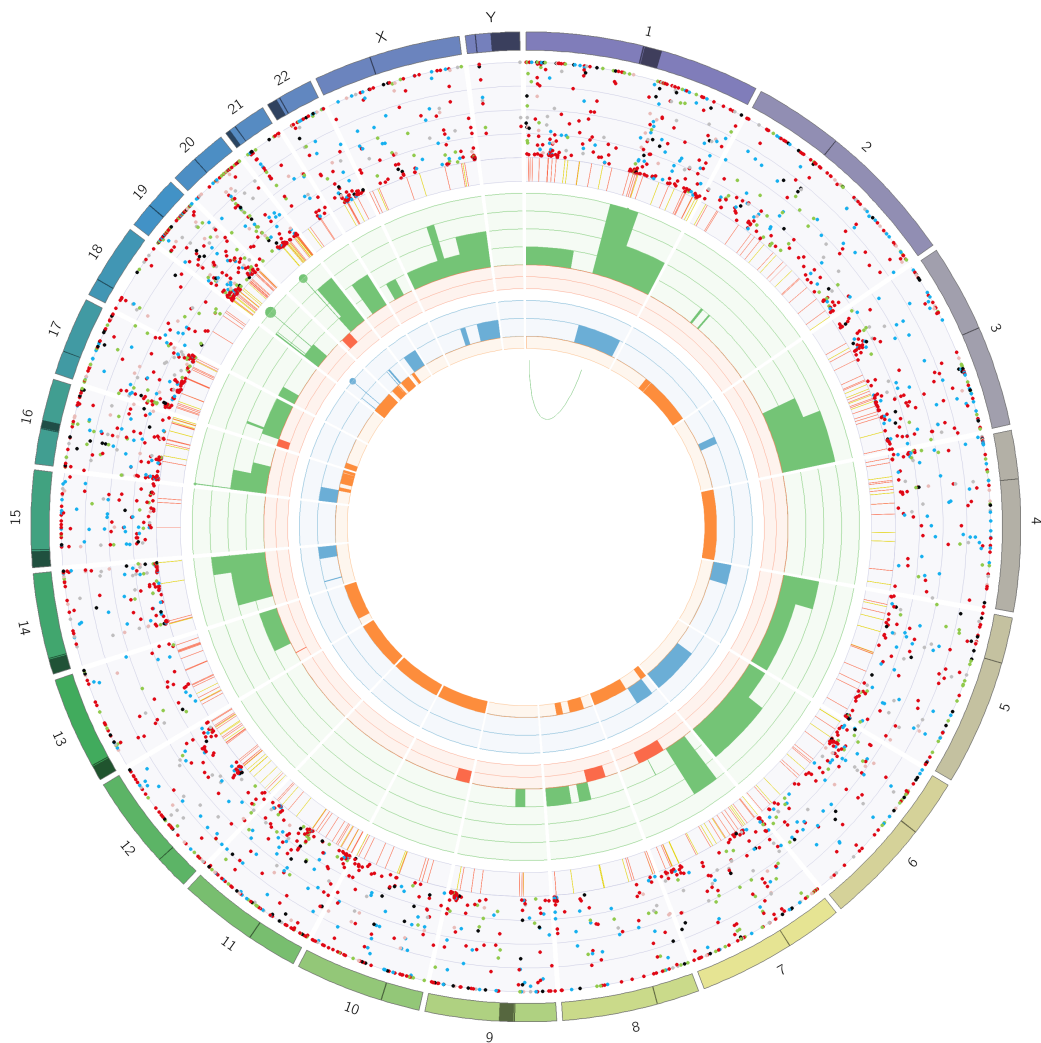


Figure B.12: Circos plot of patient CA-I sample 573 with somatic structural variants with allele frequency > 0.2 : outer first ring shows the canonical chromosomes with gaps (centromere, heterochromatin,...) highlighted as darker areas; second ring visualises all somatic SNVs corrected for tumour purity and scaled from 0 to 1, the colour representing the base change of SNV like in Alexandrov et al. [215]; vertical lines directly under the SNVs symbolise InDels, with yellow for insertions and red for deletions; the third ring shows the total copy number alterations, with green showing a copy number gain and red a loss, dots at the outer border show a copy number greater than four; the last ring shows the minor copy number, with blue depicting a gain and orange a loss, this ring allows the detection of copy number neutral changes, like loss of heterozygosity; the center shows all structural variants: translocations in blue, deletions in red, insertions in yellow, tandem duplications in green and inversions in black.

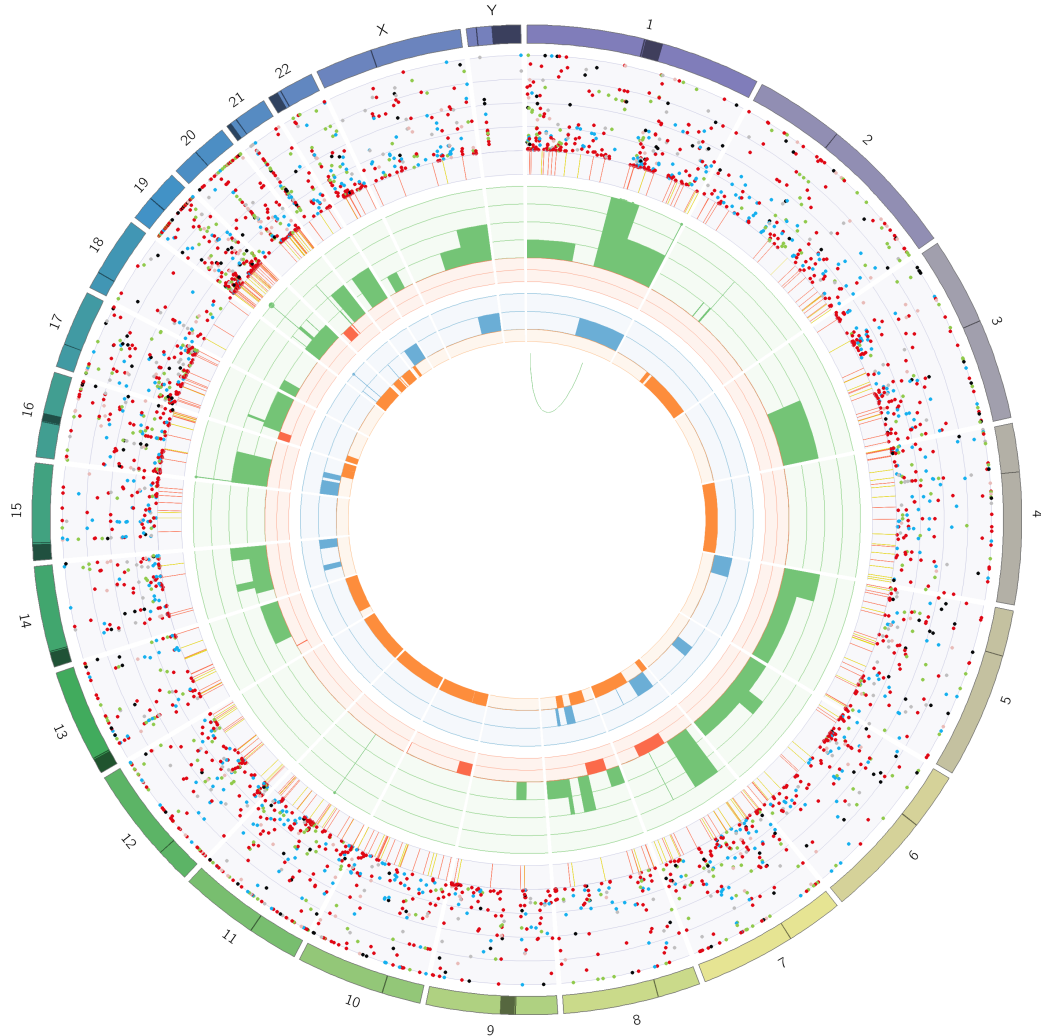


Figure B.13: Circos plot of patient CA-I sample 579 with somatic structural variants with allele frequency > 0.2 : outer first ring shows the canonical chromosomes with gaps (centromere, heterochromatin,...) highlighted as darker areas; second ring visualises all somatic SNVs corrected for tumour purity and scaled from 0 to 1, the colour representing the base change of SNV like in Alexandrov et al. [215]; vertical lines directly under the SNVs symbolise InDels, with yellow for insertions and red for deletions; the third ring shows the total copy number alterations, with green showing a copy number gain and red a loss, dots at the outer border show a copy number greater than four; the last ring shows the minor copy number, with blue depicting a gain and orange a loss, this ring allows the detection of copy number neutral changes, like loss of heterozygosity; the center shows all structural variants: translocations in blue, deletions in red, insertions in yellow, tandem duplications in green and inversions in black.

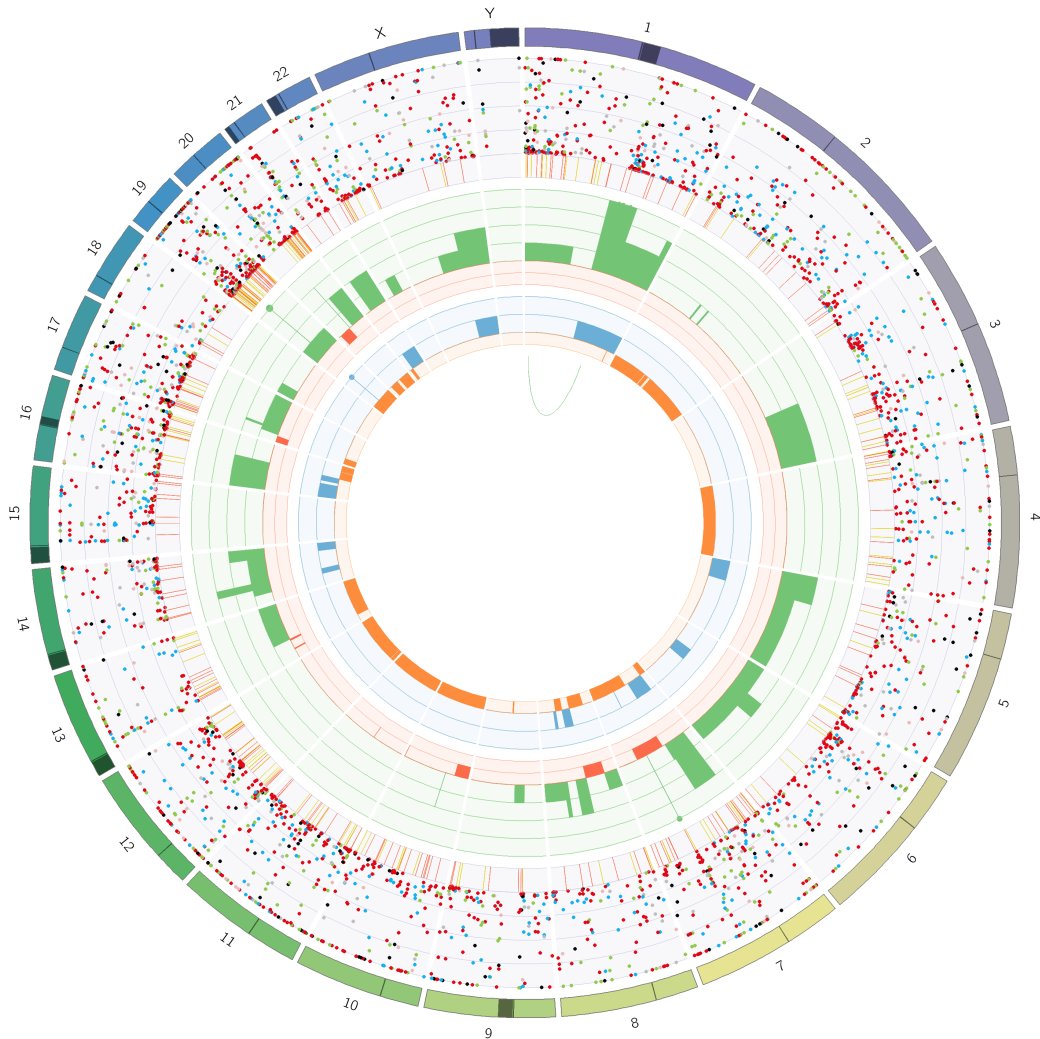


Figure B.14: Circos plot of patient CA-I sample 583 with somatic structural variants with allele frequency > 0.2 : outer first ring shows the canonical chromosomes with gaps (centromere, heterochromatin,...) highlighted as darker areas; second ring visualises all somatic SNVs corrected for tumour purity and scaled from 0 to 1, the colour representing the base change of SNV like in Alexandrov et al. [215]; vertical lines directly under the SNVs symbolise InDels, with yellow for insertions and red for deletions; the third ring shows the total copy number alterations, with green showing a copy number gain and red a loss, dots at the outer border show a copy number greater than four; the last ring shows the minor copy number, with blue depicting a gain and orange a loss, this ring allows the detection of copy number neutral changes, like loss of heterozygosity; the center shows all structural variants: translocations in blue, deletions in red, insertions in yellow, tandem duplications in green and inversions in black.

B.3 Patient CA-J

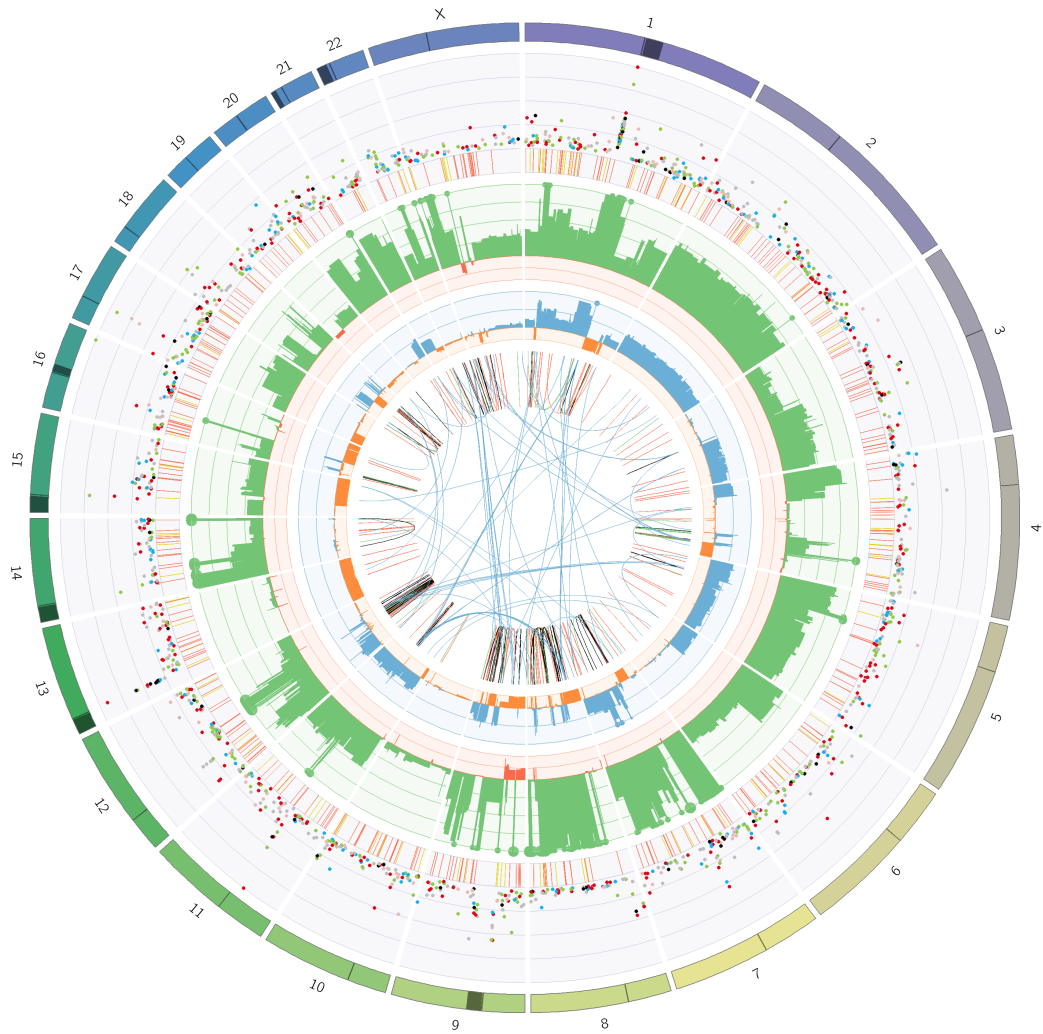


Figure B.15: Circos plot of patient CA-J sample 24 with somatic structural variants with allele frequency ≥ 0.10 : outer first ring shows the canonical chromosomes with gaps (centromere, heterochromatin,...) highlighted as darker areas; second ring visualises all somatic SNVs corrected for tumour purity and scaled from 0 to 1, the colour representing the base change of SNV like in Alexandrov et al. [215]; vertical lines directly under the SNVs symbolise InDels, with yellow for insertions and red for deletions; the third ring shows the total copy number alterations, with green showing a copy number gain and red a loss, dots at the outer border show a copy number greater than four; the last ring shows the minor copy number, with blue depicting a gain and orange a loss, this ring allows the detection of copy number neutral changes, like loss of heterozygosity; the center shows all structural variants: translocations in blue, deletions in red, insertions in yellow, tandem duplications in green and inversions in black.

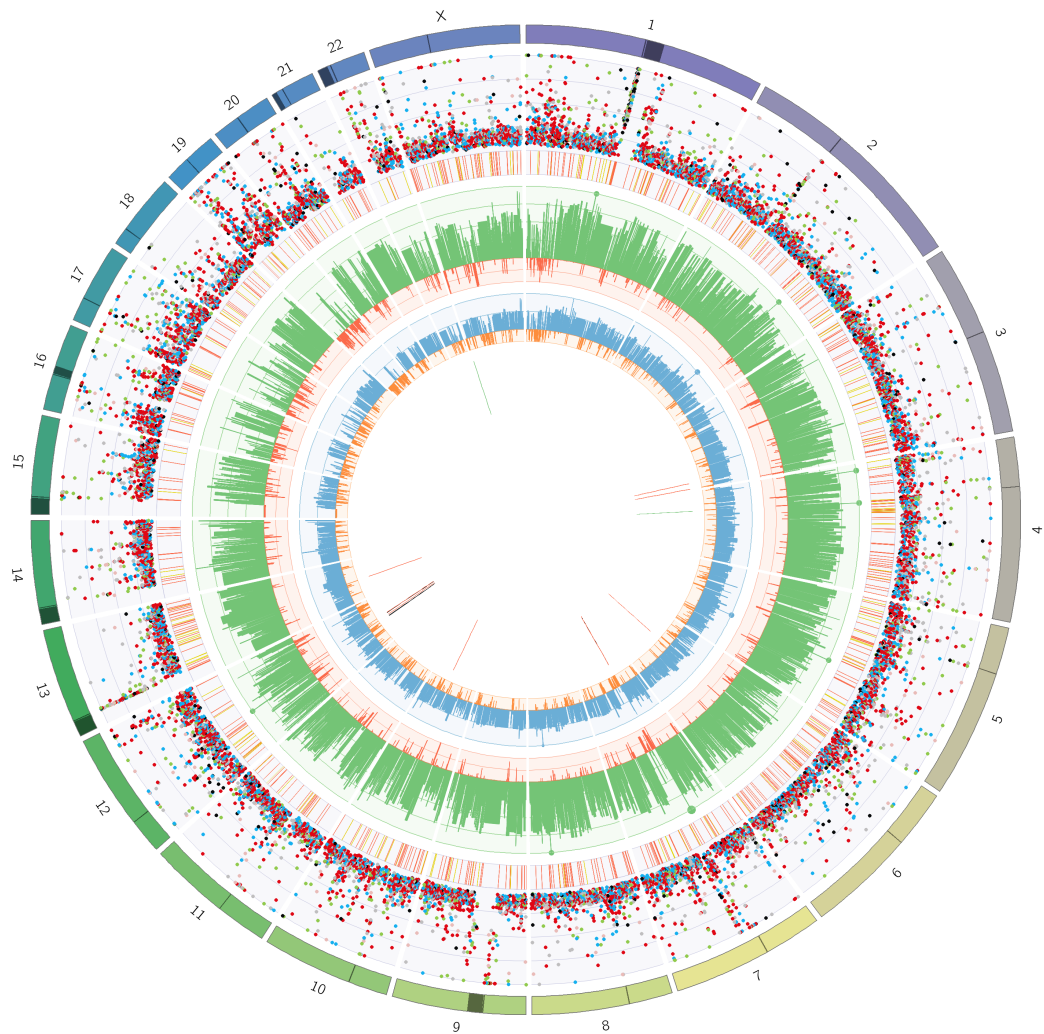


Figure B.16: Circos plot of patient CA-J sample 28 with somatic structural variants with allele frequency ≥ 0.10 : outer first ring shows the canonical chromosomes with gaps (centromere, heterochromatin,...) highlighted as darker areas; second ring visualises all somatic SNVs corrected for tumour purity and scaled from 0 to 1, the colour representing the base change of SNV like in Alexandrov et al. [215]; vertical lines directly under the SNVs symbolise InDels, with yellow for insertions and red for deletions; the third ring shows the total copy number alterations, with green showing a copy number gain and red a loss, dots at the outer border show a copy number greater than four; the last ring shows the minor copy number, with blue depicting a gain and orange a loss, this ring allows the detection of copy number neutral changes, like loss of heterozygosity; the center shows all structural variants: translocations in blue, deletions in red, insertions in yellow, tandem duplications in green and inversions in black.



Figure B.17: Circos plot of patient CA-J sample 32 with somatic structural variants with allele frequency ≥ 0.10 : outer first ring shows the canonical chromosomes with gaps (centromere, heterochromatin,...) highlighted as darker areas; second ring visualises all somatic SNVs corrected for tumour purity and scaled from 0 to 1, the colour representing the base change of SNV like in Alexandrov et al. [215]; vertical lines directly under the SNVs symbolise InDels, with yellow for insertions and red for deletions; the third ring shows the total copy number alterations, with green showing a copy number gain and red a loss, dots at the outer border show a copy number greater than four; the last ring shows the minor copy number, with blue depicting a gain and orange a loss, this ring allows the detection of copy number neutral changes, like loss of heterozygosity; the center shows all structural variants: translocations in blue, deletions in red, insertions in yellow, tandem duplications in green and inversions in black.



Figure B.18: Circos plot of patient CA-J sample 42 with somatic structural variants with allele frequency ≥ 0.10 : outer first ring shows the canonical chromosomes with gaps (centromere, heterochromatin,...) highlighted as darker areas; second ring visualises all somatic SNVs corrected for tumour purity and scaled from 0 to 1, the colour representing the base change of SNV like in Alexandrov et al. [215]; vertical lines directly under the SNVs symbolise InDels, with yellow for insertions and red for deletions; the third ring shows the total copy number alterations, with green showing a copy number gain and red a loss, dots at the outer border show a copy number greater than four; the last ring shows the minor copy number, with blue depicting a gain and orange a loss, this ring allows the detection of copy number neutral changes, like loss of heterozygosity; the center shows all structural variants: translocations in blue, deletions in red, insertions in yellow, tandem duplications in green and inversions in black.

B.4 Patient CA-K

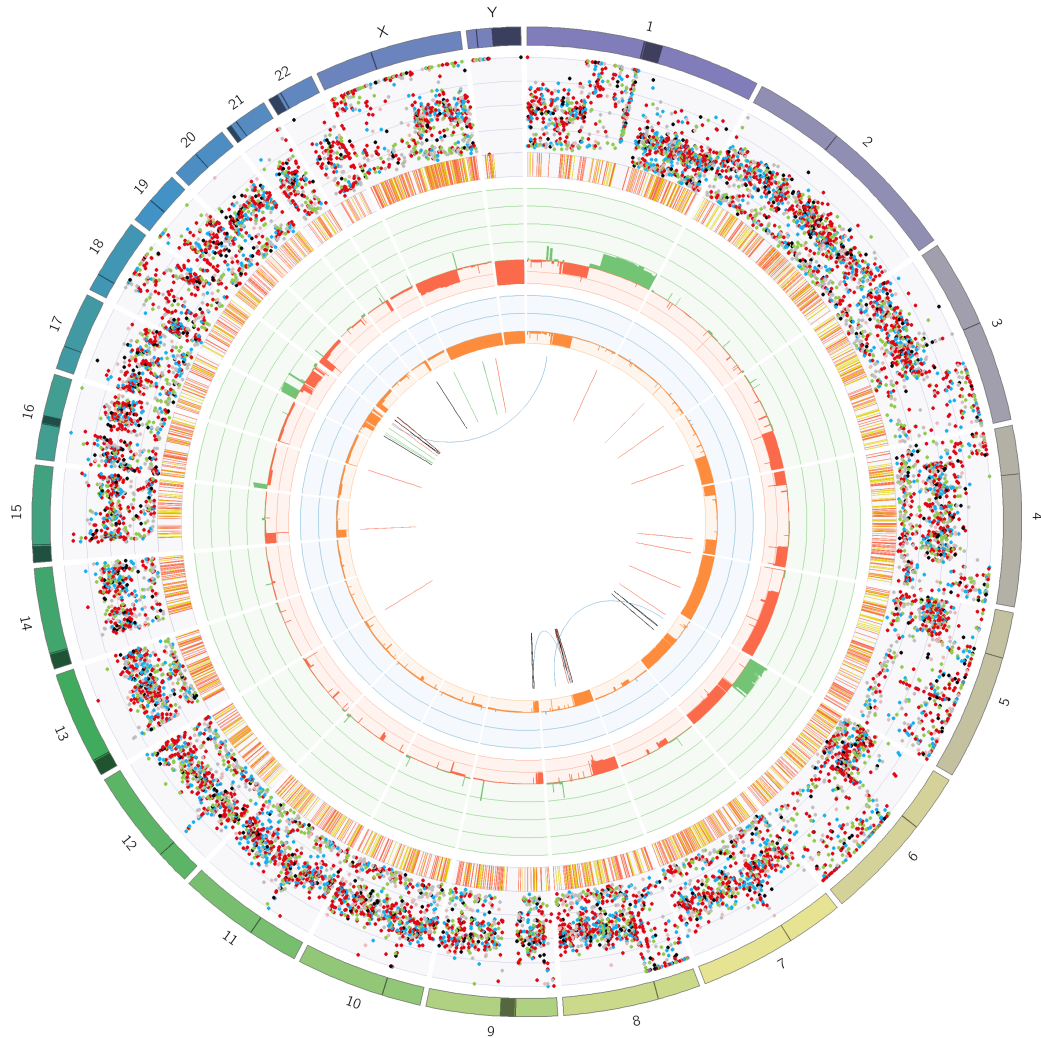


Figure B.19: Circos plot of patient CA-K sample 4: outer first ring shows the canonical chromosomes with gaps (centromere, heterochromatin,...) highlighted as darker areas; second ring visualises all somatic SNVs corrected for tumour purity and scaled from 0 to 1, the colour representing the base change of SNV like in Alexandrov et al. [215]; vertical lines directly under the SNVs symbolise InDels, with yellow for insertions and red for deletions; the third ring shows the total copy number alterations, with green showing a copy number gain and red a loss, dots at the outer border show a copy number greater than four; the last ring shows the minor copy number, with blue depicting a gain and orange a loss, this ring allows the detection of copy number neutral changes, like loss of heterozygosity; the center shows all structural variants: translocations in blue, deletions in red, insertions in yellow, tandem duplications in green and inversions in black.

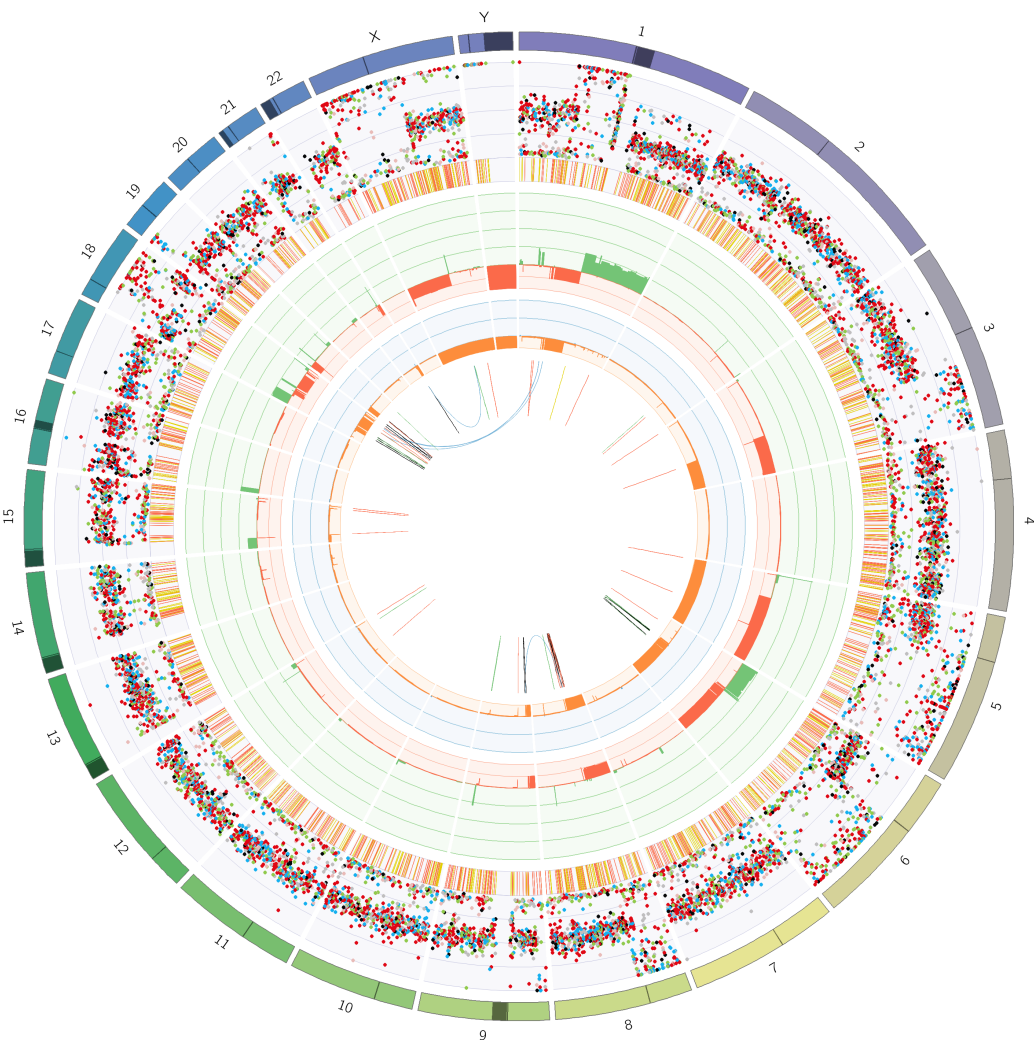


Figure B.20: Circos plot of patient CA-K sample 5: outer first ring shows the canonical chromosomes with gaps (centromere, heterochromatin,...) highlighted as darker areas; second ring visualises all somatic SNVs corrected for tumour purity and scaled from 0 to 1, the colour representing the base change of SNV like in Alexandrov et al. [215]; vertical lines directly under the SNVs symbolise InDels, with yellow for insertions and red for deletions; the third ring shows the total copy number alterations, with green showing a copy number gain and red a loss, dots at the outer border show a copy number greater than four; the last ring shows the minor copy number, with blue depicting a gain and orange a loss, this ring allows the detection of copy number neutral changes, like loss of heterozygosity; the center shows all structural variants: translocations in blue, deletions in red, insertions in yellow, tandem duplications in green and inversions in black.

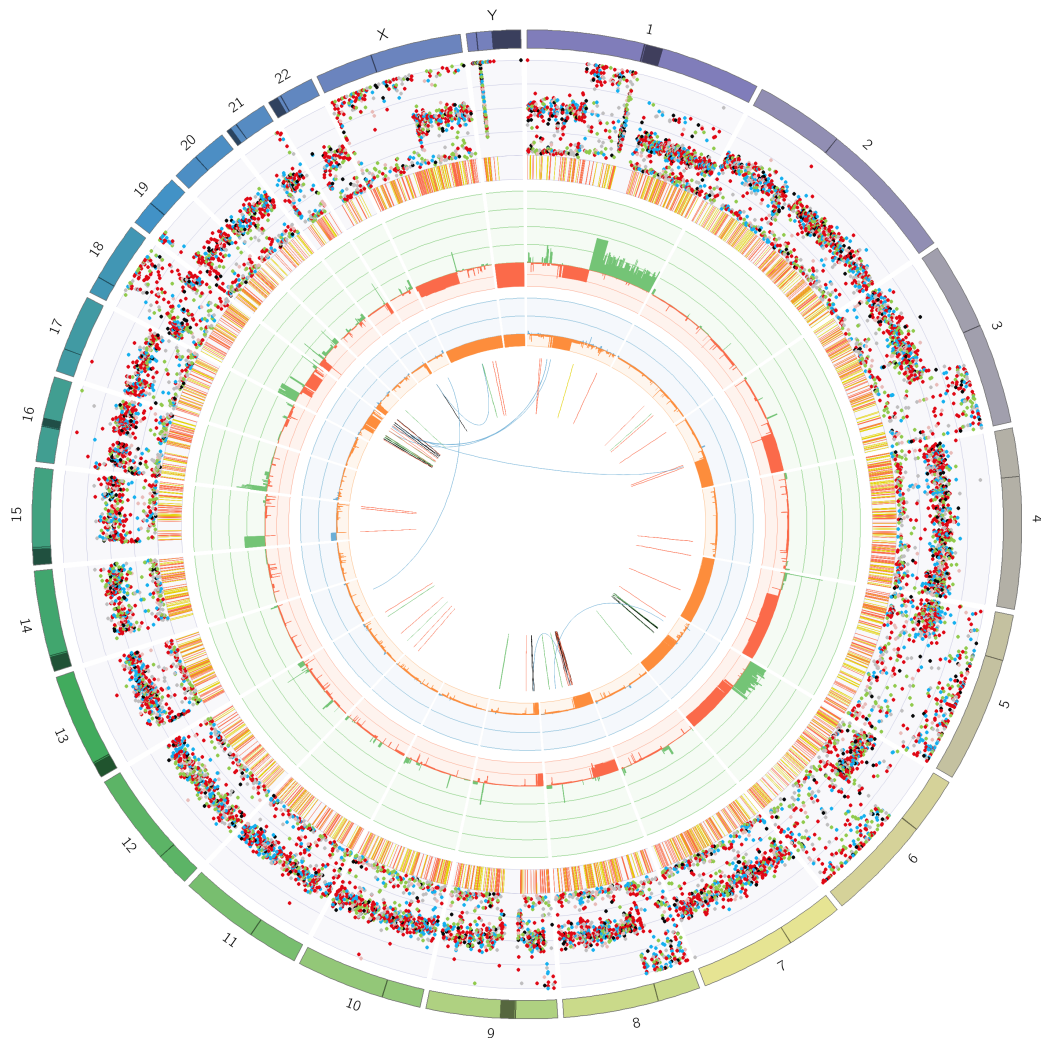


Figure B.21: Circos plot of patient CA-K sample 6: outer first ring shows the canonical chromosomes with gaps (centromere, heterochromatin,...) highlighted as darker areas; second ring visualises all somatic SNVs corrected for tumour purity and scaled from 0 to 1, the colour representing the base change of SNV like in Alexandrov et al. [215]; vertical lines directly under the SNVs symbolise InDels, with yellow for insertions and red for deletions; the third ring shows the total copy number alterations, with green showing a copy number gain and red a loss, dots at the outer border show a copy number greater than four; the last ring shows the minor copy number, with blue depicting a gain and orange a loss, this ring allows the detection of copy number neutral changes, like loss of heterozygosity; the center shows all structural variants: translocations in blue, deletions in red, insertions in yellow, tandem duplications in green and inversions in black.



Figure B.22: Circos plot of patient CA-K sample 9: outer first ring shows the canonical chromosomes with gaps (centromere, heterochromatin,...) highlighted as darker areas; second ring visualises all somatic SNVs corrected for tumour purity and scaled from 0 to 1, the colour representing the base change of SNV like in Alexandrov et al. [215]; vertical lines directly under the SNVs symbolise InDels, with yellow for insertions and red for deletions; the third ring shows the total copy number alterations, with green showing a copy number gain and red a loss, dots at the outer border show a copy number greater than four; the last ring shows the minor copy number, with blue depicting a gain and orange a loss, this ring allows the detection of copy number neutral changes, like loss of heterozygosity; the center shows all structural variants: translocations in blue, deletions in red, insertions in yellow, tandem duplications in green and inversions in black.

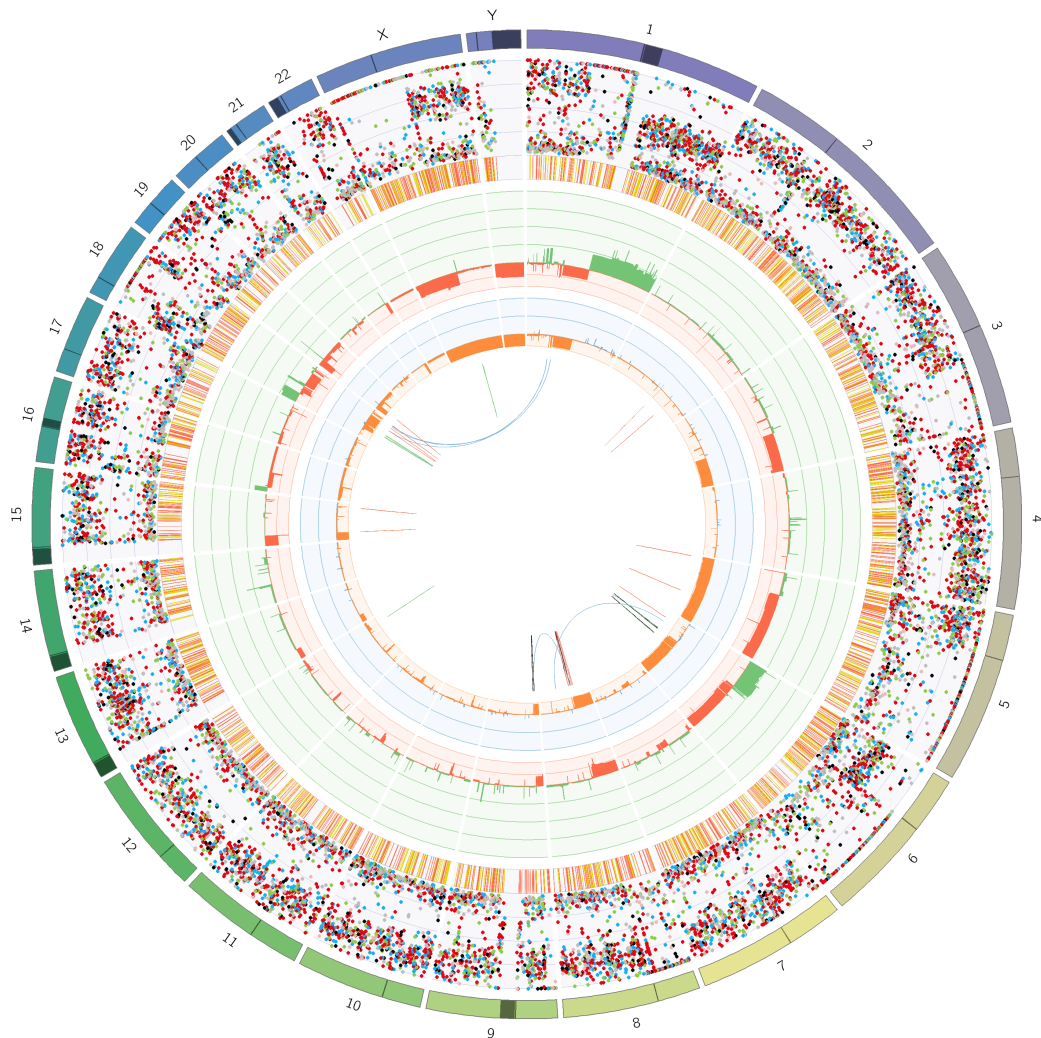


Figure B.23: Circos plot of patient CA-K sample 13; outer first ring shows the canonical chromosomes with gaps (centromere, heterochromatin,...) highlighted as darker areas; second ring visualises all somatic SNVs corrected for tumour purity and scaled from 0 to 1, the colour representing the base change of SNV like in Alexandrov et al. [215]; vertical lines directly under the SNVs symbolise InDels, with yellow for insertions and red for deletions; the third ring shows the total copy number alterations, with green showing a copy number gain and red a loss, dots at the outer border show a copy number greater than four; the last ring shows the minor copy number, with blue depicting a gain and orange a loss, this ring allows the detection of copy number neutral changes, like loss of heterozygosity; the center shows all structural variants: translocations in blue, deletions in red, insertions in yellow, tandem duplications in green and inversions in black.

B.5 Patient CA-L



Figure B.24: Circos plot of patient CA-L sample 8: outer first ring shows the canonical chromosomes with gaps (centromere, heterochromatin,...) highlighted as darker areas; second ring visualises all somatic SNVs corrected for tumour purity and scaled from 0 to 1, the colour representing the base change of SNV like in Alexandrov et al. [215]; vertical lines directly under the SNVs symbolise InDels, with yellow for insertions and red for deletions; the third ring shows the total copy number alterations, with green showing a copy number gain and red a loss, dots at the outer border show a copy number greater than four; the last ring shows the minor copy number, with blue depicting a gain and orange a loss, this ring allows the detection of copy number neutral changes, like loss of heterozygosity; the center shows all structural variants: translocations in blue, deletions in red, insertions in yellow, tandem duplications in green and inversions in black.

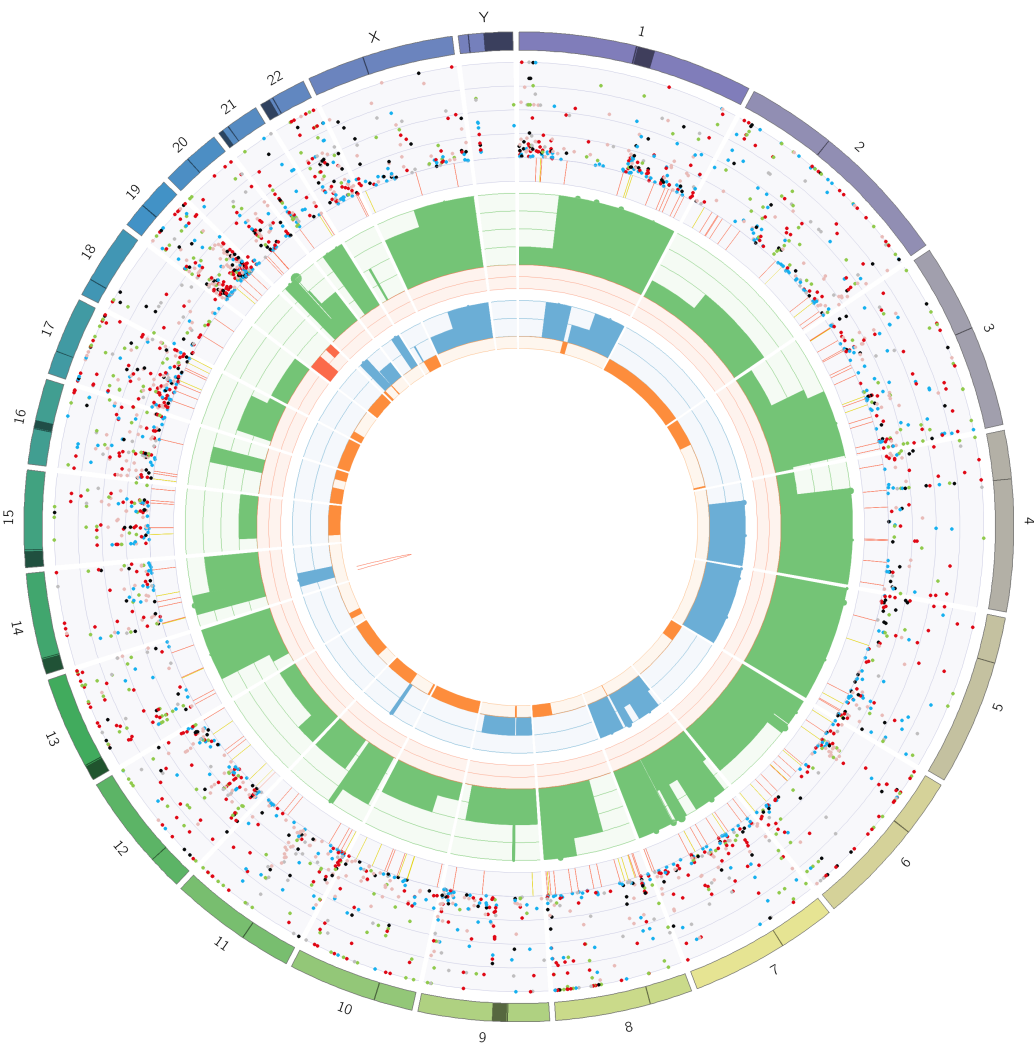


Figure B.25: Circos plot of patient CA-L sample 17A: outer first ring shows the canonical chromosomes with gaps (centromere, heterochromatin,...) highlighted as darker areas; second ring visualises all somatic SNVs corrected for tumour purity and scaled from 0 to 1, the colour representing the base change of SNV like in Alexandrov et al. [215]; vertical lines directly under the SNVs symbolise InDels, with yellow for insertions and red for deletions; the third ring shows the total copy number alterations, with green showing a copy number gain and red a loss, dots at the outer border show a copy number greater than four; the last ring shows the minor copy number, with blue depicting a gain and orange a loss, this ring allows the detection of copy number neutral changes, like loss of heterozygosity; the center shows all structural variants: translocations in blue, deletions in red, insertions in yellow, tandem duplications in green and inversions in black.

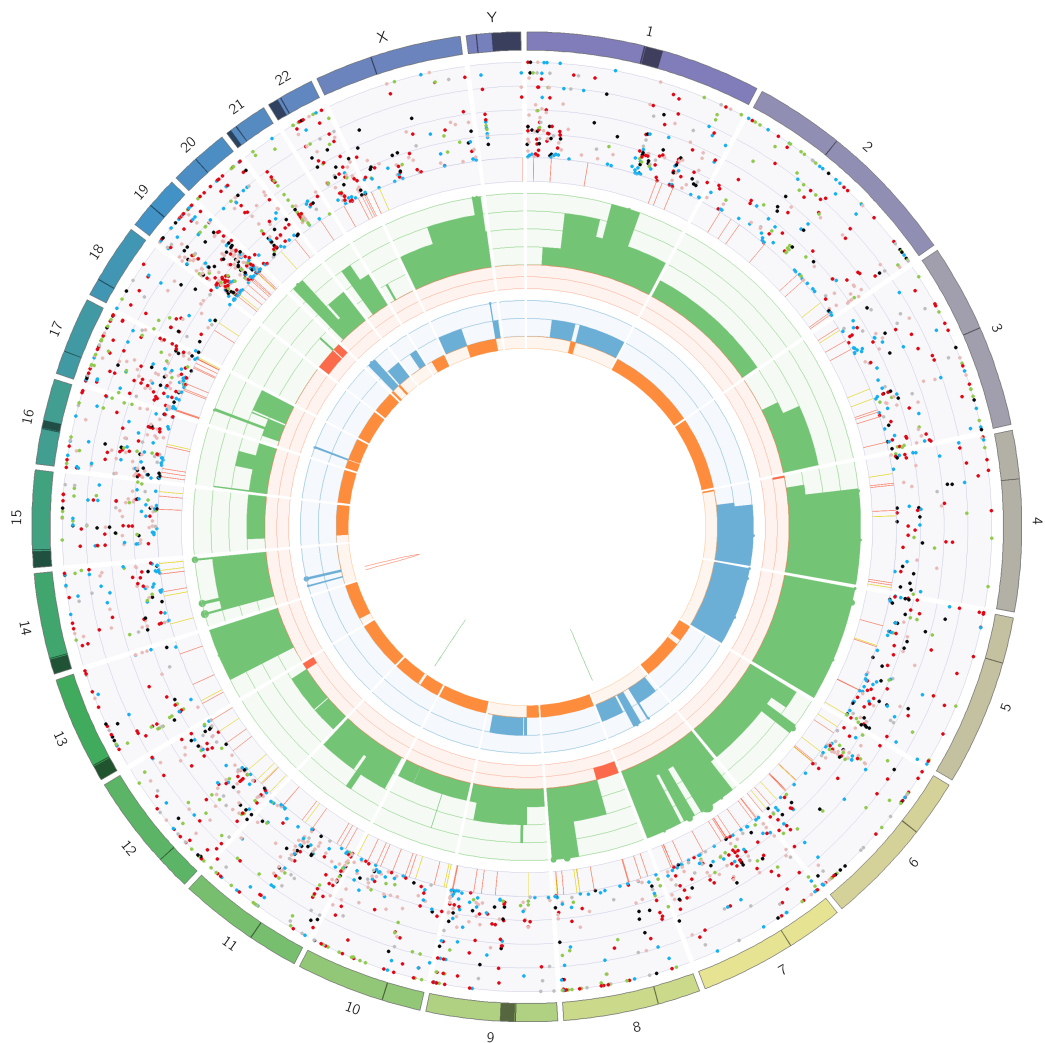


Figure B.26: Circos plot of patient CA-L sample 26: outer first ring shows the canonical chromosomes with gaps (centromere, heterochromatin,...) highlighted as darker areas; second ring visualises all somatic SNVs corrected for tumour purity and scaled from 0 to 1, the colour representing the base change of SNV like in Alexandrov et al. [215]; vertical lines directly under the SNVs symbolise InDels, with yellow for insertions and red for deletions; the third ring shows the total copy number alterations, with green showing a copy number gain and red a loss, dots at the outer border show a copy number greater than four; the last ring shows the minor copy number, with blue depicting a gain and orange a loss, this ring allows the detection of copy number neutral changes, like loss of heterozygosity; the center shows all structural variants: translocations in blue, deletions in red, insertions in yellow, tandem duplications in green and inversions in black.

C

MisMatchFinder - supplementary methods

C.1 ROI bed files generation

To ensure optimal mapping rates and no mapping related mismatches, the analysis was restricted to high mappability areas of the genome. These areas were defined as regions, where a k-mer of 100bp had a 85% or higher unique mappability rate. The mappability tracks were first computed with GEM [284] and then collated converted to a bed file with R just like in the best practice instructions of QDNAseq [37] for creating a new bin annotation. This method was only required for GRCh38 [285] as so far, the UCSC mappability data track was only available for GRCh37 [286].

C.2 Oligo-nucleotide context normalisation

The ROI restriction of the analysis from [Section C.1](#) automatically led to a different tri- and di-nucleotide context frequency in the analysed regions, than the rest of the genome, which was used to generate the original signatures [209]. For this reason, MisMatchFinder analyses the oligo-nucleotide composition of the analysed regions and generates weighted counts by adjusting for the differences.

The baseline frequencies of both di- and tri-nucleotides were generated with the function *oligonucleotideFrequency* from the “Biostrings” library [34] using the hg38 BSgenome [36]. The raw counts of the di- and tri-nucleotides can be seen in [Table C.1](#) and [Table C.2](#) respectively.

Table C.1: Dinucleotide counts generated with Biostrings [34] for GRCh38

DINUCLEOTIDE	COUNT
AA	287 025 139
AC	148 150 331
AG	205 752 406
AT	226 225 785
CA	212 880 749
CC	151 236 932
CG	29 401 795
CT	205 524 144
GA	175 847 498
GC	124 732 844
GG	152 432 158
GT	148 502 457
TA	191 400 248
TC	174 923 630
TG	213 928 532
TT	289 690 054

Table C.2: Trinucleotide counts generated with Biostrings [34] for GRCh38

TRINUCLEOTIDE	COUNT	TRINUCLEOTIDE	COUNT
AAA	112 465 943	GAA	58 990 420
AAC	43 532 050	GAC	27 737 004
AAG	58 439 928	GAG	49 560 877
AAT	72 587 151	GAT	39 559 024
ACA	59 305 516	GCA	42 481 943
ACC	33 784 390	GCC	34 497 599
ACG	7 584 302	GCG	7 078 395
ACT	47 476 086	GCT	40 674 873
AGA	65 552 680	GGA	46 022 042
AGC	41 073 623	GGC	34 474 720
AGG	51 723 263	GGG	38 148 838
AGT	47 402 783	GGT	33 786 518
ATA	60 308 591	GTA	33 265 786
ATC	39 076 747	GTC	27 466 578
ATG	53 548 035	GTG	44 578 403
ATT	73 292 370	GTT	43 191 653
CAA	55 220 609	TAA	60 348 082
CAC	44 001 434	TAC	32 879 810
CAG	59 791 771	TAG	37 959 659
CAT	53 866 888	TAT	60 212 654
CCA	53 293 160	TCA	57 800 075
CCC	38 036 593	TCC	44 918 305
CCG	8 026 845	TCG	6 712 244
CCT	51 880 303	TCT	65 492 835
CGA	6 511 692	TGA	57 760 931
CGC	7 021 552	TGC	42 162 935
CGG	8 229 568	TGG	54 330 453
CGT	7 638 969	TGT	59 674 158
CTA	37 666 053	TTA	60 159 779
CTC	49 481 013	TTC	58 899 235
CTG	59 039 769	TTG	56 762 262
CTT	59 337 262	TTT	113 868 707

C.3 Germline filtering with zarr

As shown in [Figure 4.4A](#), the amount of mismatches found in a 10x coverage sample can easily exceed 3 million. In addition to that, the current gnomAD database contains ≈ 707 million variants. This means a normal merge for two datasets based on chromosomal position is not feasible for a normal compute resource in an acceptable time frame. To allow an easy query of mismatch positions against the full database, a zarr [56] representation of the gnomAD VCF was generated. However in contrast to the out of the box indexing function shipped with scikit-allel [248] which was used to convert the vcf to zarr, the program uses its own index built with ncls, which is available through PyRanges [52]. The sections below outline first the conversion process with scikit-allel ([Section C.3.1](#)) and then details the filtering in the MisMatchFinder program ([Section C.3.2](#))

C.3.1 Zarr conversion with scikit-allel

While it is easy to access a zarr archive, both for reading and writing, once it is created, the generation requires time. The time is mostly computational and not so much development, as the scikit-allel package contains the function '*allel.vcf_to_zarr*', which allows the direct conversion of VCF to zarr with only a few prerequisites.

Importantly, tabix [287] can be used to split the conversion into multiple parts by restricting the process to specific regions.

[Listing C.1](#) shows the code used to convert chromosome 'chr1' from the downloaded gnomad vcf

Listing C.1: scikit-allel conversion vcf_to_zarr

```

1 import scikit-allel as allel
2
3 allel.vcf_to_zarr(input="gnomad.genomes.r3.1.2.sites.vcf.bgz", output="/
    out/put/folder/", group="chr1", region="chr1", fields="*")

```

When MisMatchFinder is installed on your system, the function '*generateZarrStorage*' is a wrapper, which allows the parallel conversion as well to resume a failed or incomplete attempt. It is equivalent to the above code and has only usability and ease of access as priorities. This automated version will convert all fields, which include fields never used in MisMatchFinder to optimise the memory footprint of the zarr representation, the option fields in [Listing C.1](#) can be set to the value shown in [Listing C.2](#).

Listing C.2: field options for reduced memory

```
1 fields="['variants/CHROM', 'variants/POS', 'variants/REF', 'variants/ALT',
   , 'variants/AF', 'variants/FILTER_PASS']"
```

Which contains only the information used in MisMatchFinder. The same result can be achieved with adding the option ‘*–mandatoryOnly*’ to the supplied wrapper.

actually implement the wrapper i am talking about here

C.3.2 MisMatchFinder filtering - the zarr API

C.3.3 Data simulation

This section contains all the additional information required to replicate the simulation of data used in the MisMatchFinder chapter ([Chapter 4](#))

C.3.4 Signature simulation - we can spike this punch

This section describes the signature spike-in simulation. The full code of the variant selection is available in [Listing C.3](#) with the bamsurgeon code shown in [Listing C.4](#).

For the selection of variants to spike-in with bamsurgeon, I use the fully annotated “CosmicMutantExport.tsv” from <https://cancer.sanger.ac.uk/cosmic/download>, then restrict the list to SNPs. These are loaded into R and annotated with their tri-nucleotide context. Because the signatures are based on the pyrimidine nucleotides, the reverse complement is generated for variants with a purine in the center position.

The sampling amount is calculated by using the intended signatures percentages (e.g. [Figure 4.1](#), [Figure C.1](#)) and multiplying with the desired amount of variants, which can be derived from the chosen mutation rate in per million ([Equation C.1](#)).

$$n(\text{variants}) = \frac{\text{mutation rate}}{1 \cdot 10^6 \cdot \text{genome length}} \quad (\text{C.1})$$

For our data, we assume a genome length of $3 \cdot 10^9$ and use four different mutations rates (0.1, 5, 25, 50 and 100). For the final sampling I used “data.table” and finally variants are assigned an allele frequency of 0.1.

Listing C.3: spike-in variant selection

```

1 #get the snps
2 bed <- data.table(read.table("/data/reference/dawson_labs/COSMIC/v92/
3 CosmicMutantSNPs.bed", sep="\t"))
4 colnames(bed) <- c("chr", "start", "end", "ref", "alt", "cancer", "status
5 ")
6
7
8 #get the surrounding variants
9 varTriNuc <- GRanges(seqnames=bed$chr, IRanges(start=(bed$start-1), end=(

10 bed$end+1)))
11
12 #select the right genome
13 genome <- BSgenome.Hsapiens.UCSC.hg38::BSgenome.Hsapiens.UCSC.hg38
14
15 #get trinucs
16 seq <- Biostrings::getSeq(genome, varTriNuc)
17
18 # if we dont have a C or a T as the ref, we build the reverse complement,
19 # because thats
20 # what the signatures are based on
21 seq[bed$ref %in% c("G", "A")] <- Biostrings::reverseComplement(seq[bed$ref %
22 %in% c("G", "A")])
23
24 #put the trinucs with the variants
25 bed[,tri:= as.character(seq) ]
26 #add in the trinuc alt, so that we know where things are going
27 bed[,triAlt:=ifelse(ref %in% c("C", "T"), alt, as.character(Biostrings::
28 complement(Biostrings::DNAStringSet(bed$alt))))]
29
30 #now we build the name of the trinuc change as it is used in COSMIC
31 bed[,cosmicName:=paste(tri,triAlt)]
32 bed[,cosmicName:=gsub(pattern="(.)().(.) (. )", replacement =
33 "\\1[\\2>\\4]\\3", cosmicName)]
34
35 #read in the signatures profile
36 sig7a <- data.table(read.table("/home/shollizeck/workspace/myDawsonRep/
37 TMB/v3.2_SBS7a_PROFILE.txt", header=T, sep="\t"))
38
39 # mutations per megabase
40 rate <- 100
41
42

```

```

33 nVars <- rate/1E6*3E9
34
35 #get the number of each trinucChange we need
36 numCols <- colnames(sig7a)[-1]
37 sig7a[, (numCols)]:=lapply(.SD, function(x) round(x*nVars)), .SDcols=
38   numCols]
39
40 #merge the two tables together to enable sampling
41 sampleTableSBS7a <- merge(bed, sig7a, by.x="cosmicName", by.y="X")
42
43 selectionSBS7a <- sampleTableSBS7a[,.SD[sample(.N, size=SBS7a_GRC38)], by=
44   ="cosmicName"]
45
46 #add in the frequency (VAF) of the variants which is a uniform 10%
47 selectionSBS7a[, vaf:=0.1]

```

With the generated bed, bamsurgeon can be used to create the final mutated BAM. As we are using low coverage WGS as input, some parameters need to be adjusted to allow variants to be generated. Mostly, we need to allow bamsurgeon to even mutate regions with very low coverage ('*-mindepth 1*'), ignore the pileup of the original ('*-ignorepileup*'), allow a higher coverage difference ('*-d 0.7*') and lastly allow bamsurgeon to NOT mutate a position ('*-minmutreads 0*'). To make the data creation reproducible, we also assign a seed of 1234.

After the BAM generation, the actually spiked-in variants are generated sorted and indexed.

Lastly, the bam needs to be postprocessed to be in line with the SAM specifications ([Listing C.4](#)).

Listing C.4: bamsurgeon spike-in

```

1 bamsurgeon addsnv.py -d 0.7 --ignorepileup --mindepth 1 --minmutreads 0 -
2   v mutations.bed -r $reference -o mutated.bam --aligner mem --seed 1234
3   -f input.bam
4
5 bamsurgeon makevcf.py addsnv_logs_mutated.bam | vcfstreamsrt -a |
6   bcftools view -o variants.vcf.gz -O z && bcftools index -t variants.
7   vcf.gz
8
9 bamsurgeon postprocess.py -f ${reference}.fai mutated.bam

```

C.3.5 Patient data subsampling

Subsampling of high depth WGS data was done with samtools (v1.13) supplying random seeds, but stable sampling rates. Sampling rates were selected, such that the output file would have an average coverage of 10x to be comparable with other sequencing data.

MisMatchFinder - supplementary figures

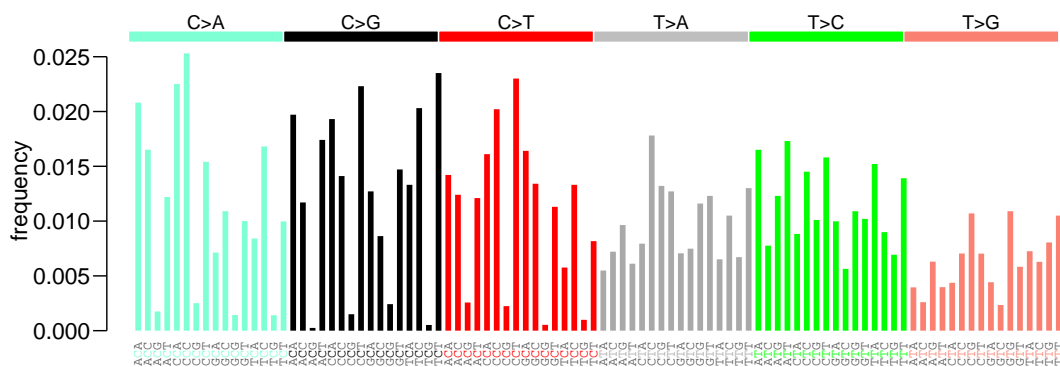


Figure C.1: Trinucleotide count contributions for SBS signature 3 (Defective homologous recombination-based DNA damage repair); values taken from Alexandrov et al. [209]

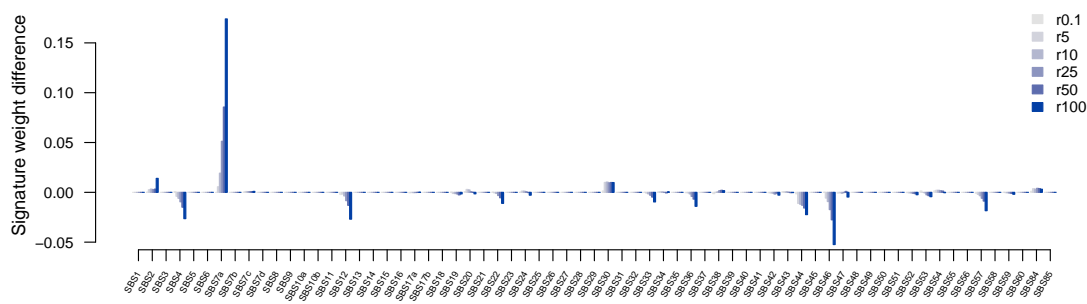


Figure C.2: Signature weights differences from normal for SBS7a spike-in; Weights were deconstructed with QP method in MisMatchFinder and the weights assigned to the normal sample used for the spike-in were subtracted; r0.1 corresponds to 0.1 mutations per megabase (287 variants) and r100 is the equivalent of 100 mutations per megabase (286974 variants)

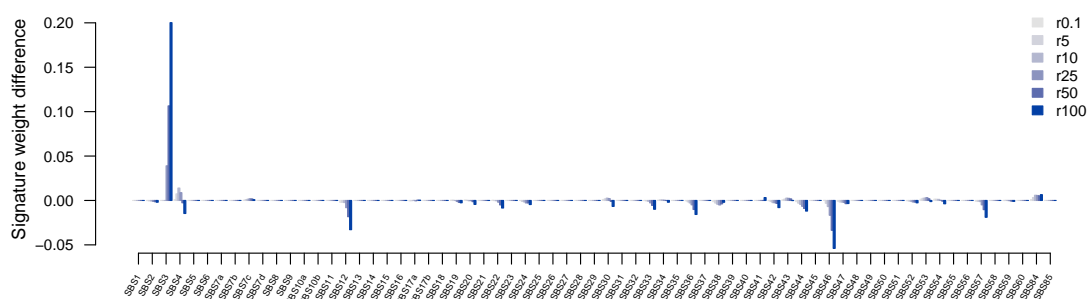


Figure C.3: Signature weights differences from normal for SBS3 spike-in; Weights were deconstructed with QP method in MisMatchFinder and the weights assigned to the normal sample used for the spike-in were subtracted; r0.1 corresponds to 0.1 mutations per megabase (264 variants) and r100 is the equivalent of 100 mutations per megabase (285367 variants)

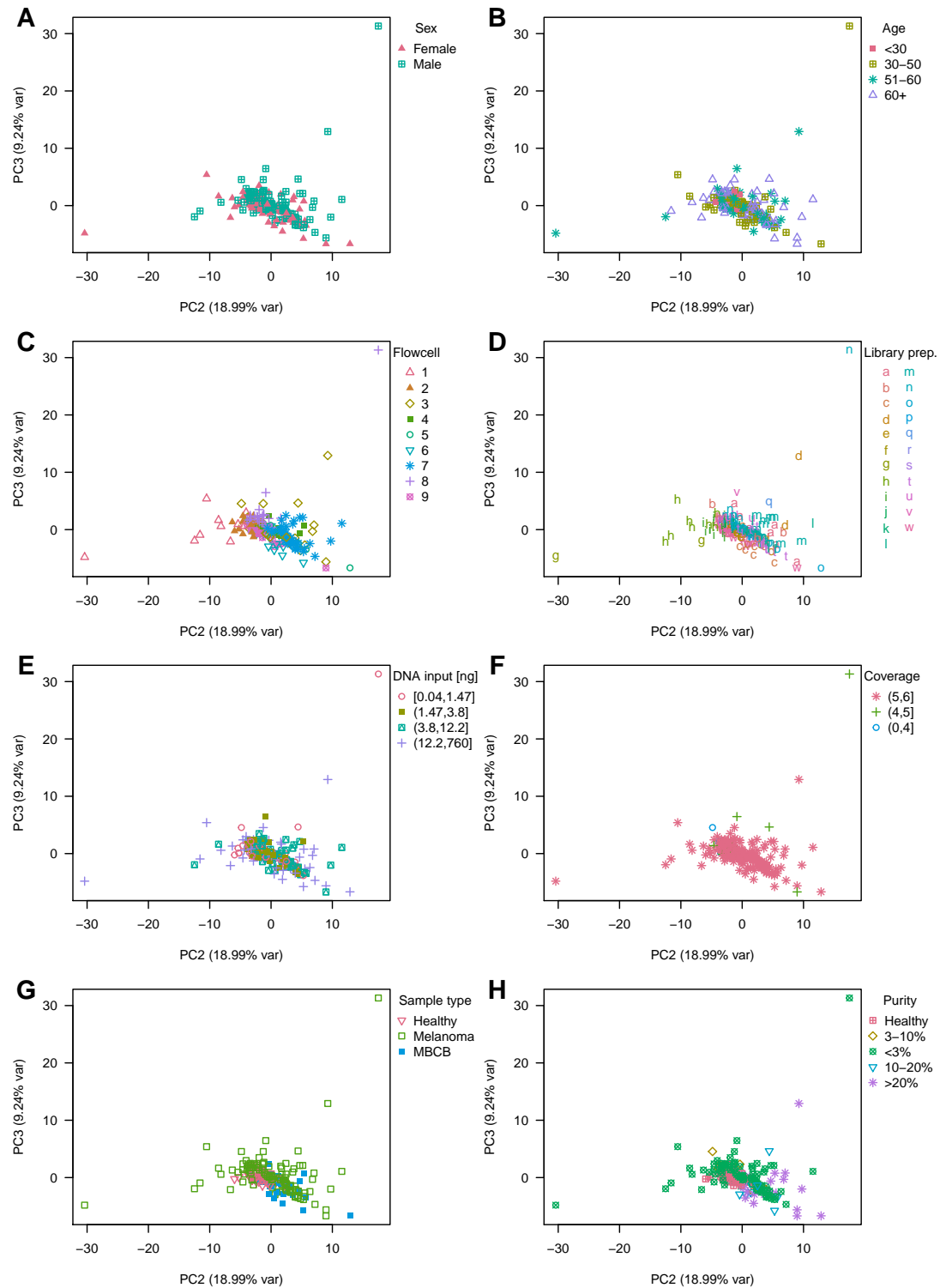


Figure C.4: PCA (PC2 and PC3) of tri-nucleotide mismatch counts of healthy donor and tumour samples (melanoma and metastatic breast cancer) of varying purity; PCA was conducted on scaled and centered data

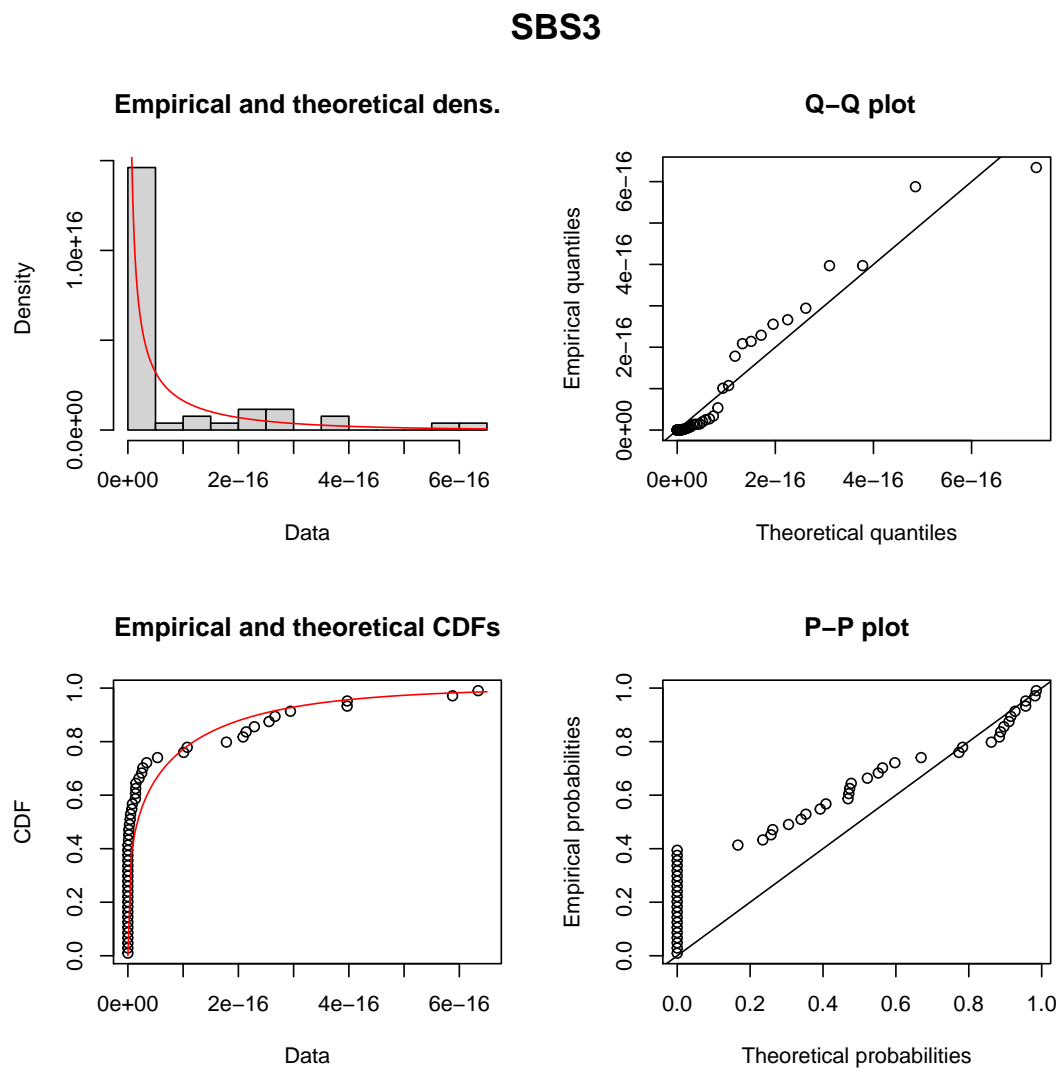


Figure C.5: Fitted beta distribution for Signature SBS3 in healthy samples

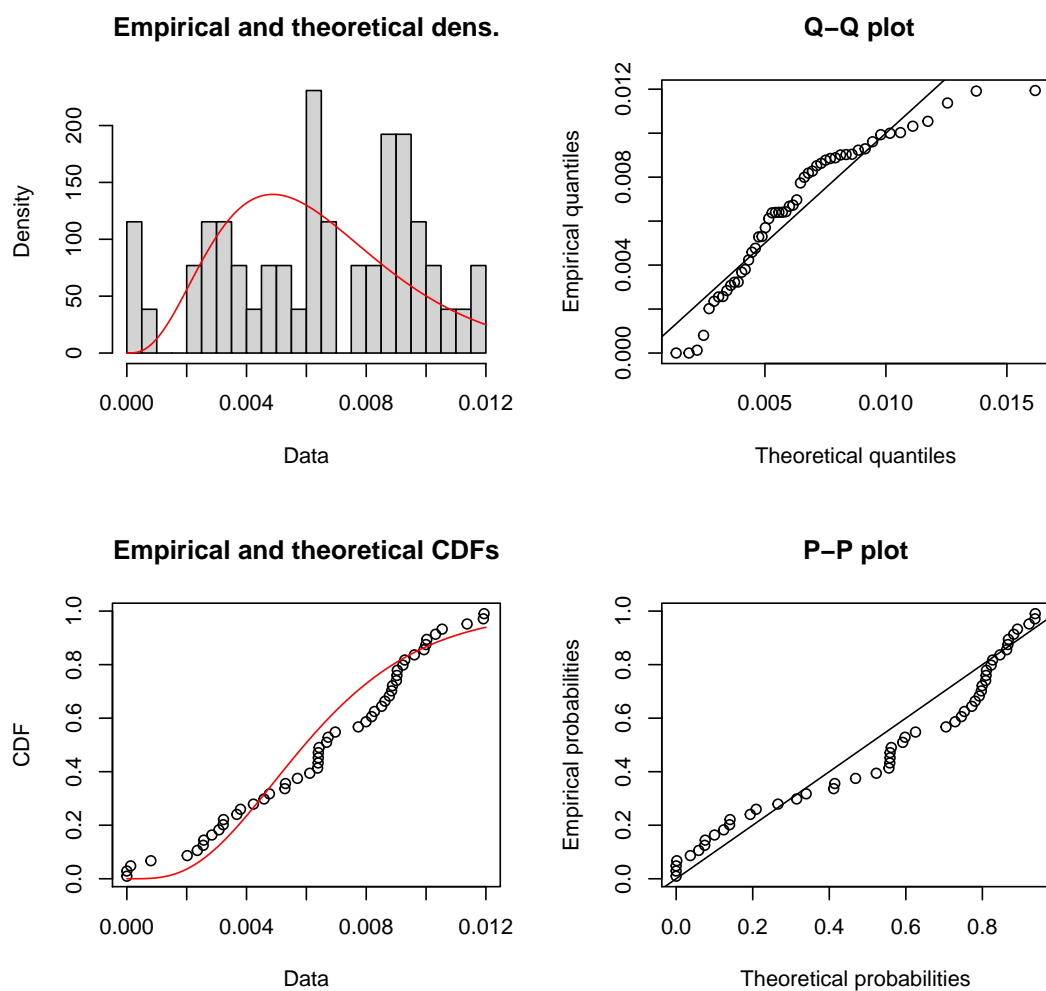
SBS17a

Figure C.6: Fitted beta distribution for Signature SBS17a in healthy samples

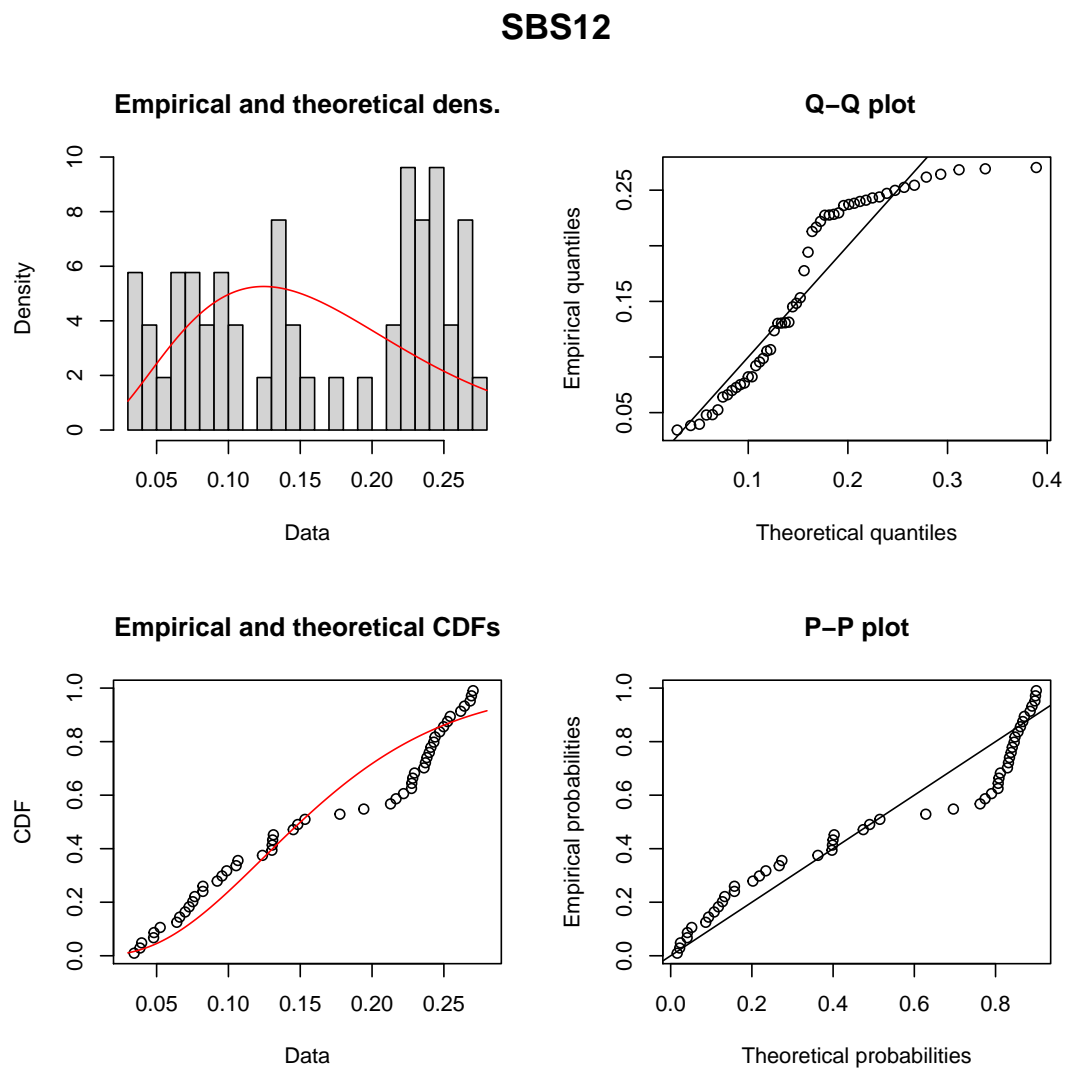


Figure C.7: Fitted beta distribution for Signature SBS12 in healthy samples

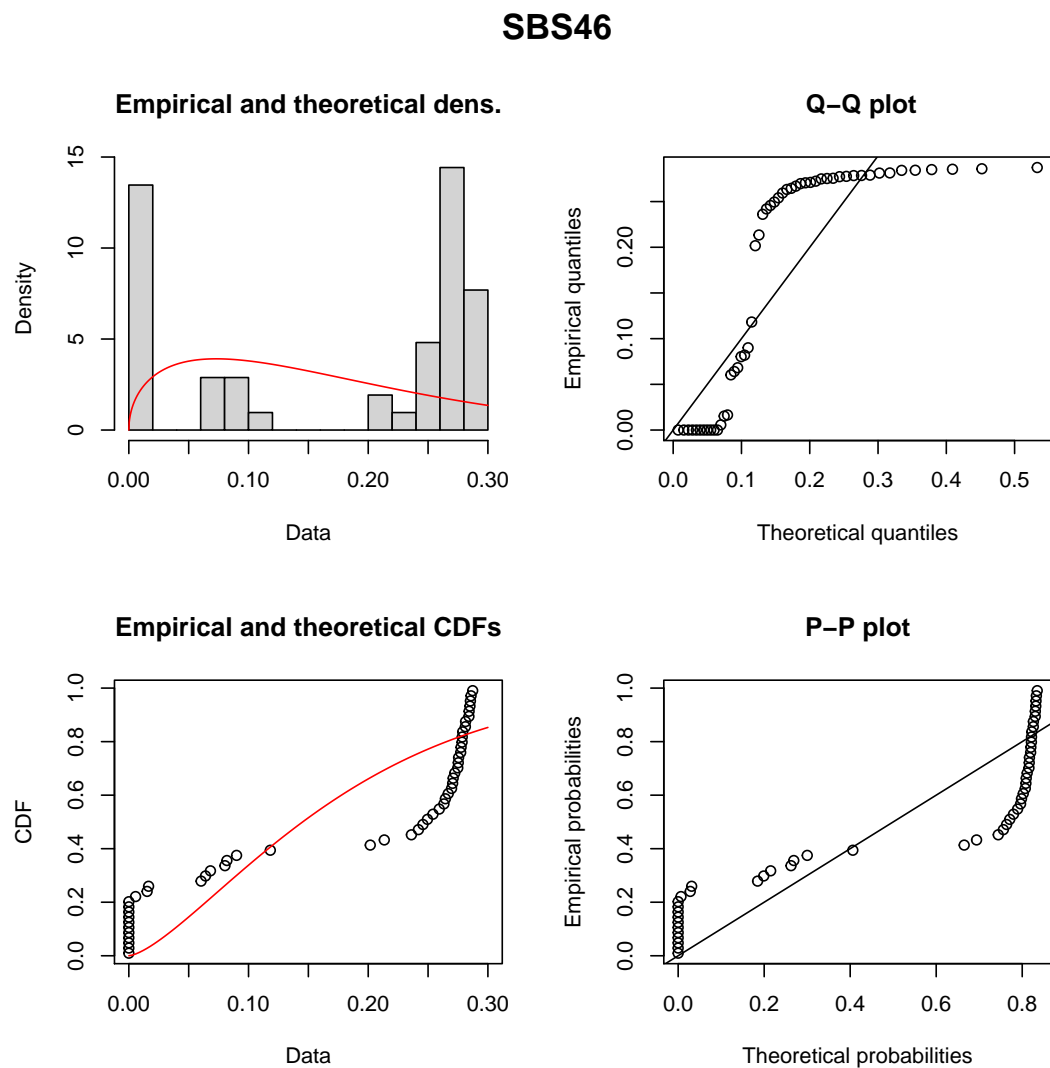


Figure C.8: Fitted beta distribution for Signature SBS46 in healthy samples